# Analysis of flow phenomena inside moonpools in operational and transit conditions


vorgelegt von
Dipl.-Ing.
Jan Löhrmann
geb. in Berlin


von der Fakultät V - Verkehrs- und Maschinensysteme
der Technischen Universität Berlin
zur Erlangung des akademischen Grades

Doktor der Ingenieurwissenschaften
- Dr.-Ing. -

genehmigte Dissertation

Promotionsausschuss:

| | |
|---|---|
| Vorsitzender: | Prof. Dr.-Ing. Henning Jürgen Meyer |
| Gutachter: | Prof. Dr.-Ing. Andrés Cura Hochbaum |
| Gutachter: | Prof. Dr.-Ing. Bettar Ould el Moctar |

Tag der wissenschaftlichen Aussprache: 17.08.2018

Berlin 2018

# Acknowledgement

First of all, I would like to thank Prof. Dr.-Ing. Andrés Cura Hochbaum for his personal and professional support during the last six years at his department. His constant backup and the numerous possibilities to visit conferences, going to the University of Iowa as Visiting Researcher, or enabling me to perform experimental tests for my thesis encouraged me to keep on working on this topic. Furthermore, I want to thank Prof. Dr.-Ing. Bettar Ould el Moctar for being advisor and agreeing on that, even on short notice. His efforts have been highly appreciated. Furthermore, I'm deeply thankful for all the support from Prof. Pablo Carrica during the last years. I always felt personally welcome by him, his family and his colleagues during my time in Iowa. He also generously granted me the resources for my simulations, was open for discussions and eager to help me when I was facing problems. Therefore, I want to express my deep gratitude. At last, I also want to thank Prof. Dr.-Ing. Henning Jürgen Meyer for being the chairman of the doctoral committee.

The thesis would not have been possible at this scope, without the fruitful discussions, support and friendship with my colleagues. Therefore, I would like to thank every single one of whom I have been working with during the last years. I want to express my gratitude especially to Sebastian Uharek, for his constant technical and non-technical support in numerous areas, Lars Koopmann for valuable advices and discussions and Antonio Lengwinat for his introduction to the experimental measuring devices. I received a lot of help during the experimental tests and especially want to thank Karsten Rieck, Verena Hertzsch, Barbara Blum, Gerrit Aßbrock, Conrad Jentzsch, Xin Gao, Sebastian Sperling and Karsten Kowalski each for their individual support. Furthermore, I want to thank Kornelia Tietze for her constant support in daily tasks and her cheerful spirit.

In the end, I want to thank the most important persons in my life, being friends and family, for constantly supporting and encouraging me, as well as distracting me in times of need.

# Contents

# List of Figures

# Kurzfassung

In dieser Dissertation wurden Strömungsphänomene in Moonpools unter verschiedensten Zuständen untersucht. Das Verhalten der Wassersäulenoszillation wurde für Moonpools von unterschiedlicher Größe und Längen- Breitenverhältnis, sowie für das Schiff in Fahrt mit variierenden Froudezahlen, als auch für das Schiff ohne Fahrt analysiert. Die Untersuchungen fanden für Glattwasserzustände, als auch für harmonische Wellen unterschiedlicher Länge und Richtung statt. Hierfür wurden sowohl Experimente mit einem Schiffsmodel, als auch numerische Simulation mit einem viskosen Verfahren durchgeführt. Zusätzlich wurde der dämpfende Einfluss von Lochblechgittern in Moonpools experimentell analysiert. Das numerische Verfahren wurde dahingehend weiterentwickelt um diesen Einfluss zu Berücksichtigen, ohne jedoch der Notwendigkeit von komplexen Gittern. Zur Validierung dieses Verfahrens wurden eigens angefertigte, vergleichbare experimentelle Daten herangezogen. Der numerische Dämpfungsansatz erzielt sehr zufriedenstellende Ergebnisse und kann bspw. für hochgenaue Simulationen verwendet werden, bei gleichzeitiger Vermeidung von rechenintensiven Gittern.

Die Oszillation der Wassersäule von Moonpools wird generell in eine Hub-Bewegung und Sloshing-Bewegung unterteilt. Es ist gängige Praxis die Frequenz der Hub-Bewegung durch vorhandene empirische oder semi-analytische Methoden zu bestimmen. Die durchgeführten Untersuchungen in dieser Arbeit zeigten eine signifikante Abhängigkeit dieser Frequenz von der Schiffsgeschwindigkeit. Daher wurde ein empirisches Model entwickelt, welches die Frequenz in Abhängigkeit der Schiffsgeschwindigkeit bestimmt und zur Verbesserung der Genauigkeit bisheriger Methoden abzielt. Die neu entwickelte Methode erzielt zufriedenstellende Ergebnisse für das untersuchte Schiff und die jeweiligen Moonpool Geometrien, sollte jedoch anhand weiterer Daten anderer Schiffsmodelle und Moonpools erweitert werden, um dessen generelle Einsetzbarkeit zu stärken.

# Abstract

The flow phenomena inside moonpools under different conditions have been analysed within this thesis. The water oscillation behaviour was investigated for moonpool geometries of different size and length to breadth ratio for the ship in transit condition at different Froude numbers, as well as for operational condition with the ship at rest. Calm water, as well as regular waves of different wave directions were included in the test matrix. Investigations have been performed experimentally and numerically using a viscous flow solver. Additionally, the damping performance of perforated bulkheads inside moonpools was experimentally analysed. A numerical damping approach, which mimics the effect of perforated bulkheads without the need for highly complex grids, has been implemented into the numerical solver and validated against experimental data. The overall performance of this new approach is very satisfactory and can be used for accurate numerical simulations, while avoiding high computational costs.

The water column motion in moonpools can be characterised by piston or sloshing type. It is common practice to determine the natural piston type motion by different empirical or semi-analytical methods. The investigation within this thesis revealed a significant dependency of the frequency on the forward ship speed. A new empirical model for a velocity dependent piston type frequency has been developed, which aims at improving the accuracy of existing methods. The new model performs satisfactory for the investigated ship type and moonpool geometries. The model should however be enhanced using more data of different ships and moonpools, to strengthen its general applicability.

# Nomenclature

| | |
|---|---|
| $(\phi, \theta, \psi)$ | Euler angles (roll,pitch,yaw) |
| $(\xi, \eta, \zeta)$ | Earth fixed cartesian coordinates |
| $(F_x, F_y, F_z)$ | Ship fixed force vector components |
| $(M_x, M_y, M_z)$ | Ship fixed moment vector components |
| $(p, q, r)$ | Ship fixed angular velocity components |
| $(u, v, w)$ | Earth fixed cartesian velocity components |
| $(U_0, V_0, W_0)$ | Velocity components of the origin of the ship fixed frame of reference |
| $(x, y, z)$ | Ship fixed cartesian coordinates |
| $(x^*, y^*, z^*)$ | Hybrid cartesian coordinates |
| $(x_G, y_G, z_G)$ | Ship fixed coordinates for centre of gravity |
| $\alpha$ | Distance function |
| $\Delta C_{mp}$ | Added resistance coefficient due to the moonpool |
| $\Delta t$ | Time step |
| $\delta_{99}$ | Boundary layer thickness |
| $\delta_{ij}$ | Kronecker symbol |
| $\epsilon$ | Phase shift |
| $\Lambda$ | Logarithmic decrement |
| $\lambda$ | Scale |
| $\lambda_W$ | Wave length |
| $\lambda_{max}$, $\lambda_{min}$ | Maximum/minimum wave length |
| $\mu$ | Linear viscous damping coefficient |
| $\mu_W$ | Wave direction |
| $\nu$ | Kinematic viscosity |
| $\nu_t$ | Eddy viscosity |
| $\omega$ | Specific dissipation rate |
| $\omega_W$ | Angular wave fequency |
| $\overline{GM}$ | Metacentric height |
| $\Phi$ | Phase shift |
| $\phi_{ls}$ | Level set function |
| $\rho$ | Water density |
| $\sigma$ | Variance |
| $\tau_{ij}$ | Reynolds stress tensor |
| $\zeta_d$ | Damping ratio |

$\zeta_I$ .............. Initial amplitude
$\zeta_R$ .............. Reflected amplitude
$\zeta_W$ .............. Wave amplitude
$\zeta_{0-WG}$ .......... Oscillation amplitude at piston mode frequency
$\zeta_{W-WG}$ ......... Oscillation amplitude at wave frequency
$\zeta_{WG}$ ............ Wave gauge amplitude
$A$ .............. Horizontal moonpool area
$b_{mp}$ ............ Breadth moonpool
$b_{opening}$ ......... Breadth moonpool opening at keel
$c$ ............... Damping constant
$C_F$ ............. Frictional resistance coefficient
$c_k$ .............. Fourier transform coefficients
$C_P$ ............. Pressure resistance coefficient
$C_T$ ............. Total resistance coefficient
$C_{M-z}$ ........... Yaw moment coefficient
$d$ ............... Damping term
$D/Dt$ .......... Material derivative
$D^k$ ............. Dissipative turbulent kinetic energy transport term
$E$ .............. Energy spectra
$f$ ............... Frequency
$f_0$ .............. Piston mode frequency
$f_1$ .............. First sloshing mode frequency
$F_1, F_2$ .......... Blending functions
$f_{\text{shedding}}$ ........ Shedding frequency
$f_W$ ............. Wave frequency
$f_{0,emp}$ .......... Empirical piston mode frequency
$Fr$ ............. Froude number
$Fr_{mp}$ .......... Moonpool Froude number
$G$ .............. Filter function for LES model
$g$ ............... Gravity constant
$h$ ............... Water depth
$h_l$ .............. heeling lever
$H_s$ ............. Significant wave height
$H_W$ ............ Wave height
$h_{basin}$ ........... Basin water depth
$H_{max}$, $H_{min}$ .... Maximum/minimum wave height

$I_{ij}$ .............. Inertia tensor components
$k$ ............... Turbulent kinetic energy
$k_W$ ............. Wave number
$k_{xx}, k_{yy}, k_{zz}$ ..... Gyradii components
$l_{DDES}$ .......... Length scale DDES model
$l_{DES}$ ............ Length scale DES model
$l_{mp}$ ............. Length moonpool
$l_{opening}$ .......... Length moonpool opening at keel
$L_{PP}$ ............ Length between perpendicular
$l_{RANS}$ .......... Length scale RANS model
$L_{ref}$ ............ Reference length
$L_{SL}$ ............ Sponge layer length
$m$ .............. Mass
$M_h$ ............. Heeling moment
$M_{st}$ ............ Stabilising moment
$n_i$ .............. Normal vector
$p$ ............... Pressure
$R$ .............. Reflection coefficient
$R_G$ ............. Grid convergence ratio
$r_G$ .............. Grid refinement ratio
$R_t$ .............. Timestep convergence ratio
$Re$ ............. Reynolds number
$Re_{\mathrm{eff}}$ ........... Effective Reynolds number
$S$ ............... Amplitude spectra
$S_i$ .............. Length of distance sensors
$s_i$ .............. Source term
$S_w$ ............. Static wetted surface
$Sr_{mp}$ ........... Moonpool Strouhal number
$T$ .............. Period
$t$ ............... time
$T_{add}$ ............ Added draught coefficient
$u^+$ ............ Dimensionless velocity in viscous sublayer
$u_{i,\mathrm{target}}$ ......... Desired/target cartesian earth fixed velocity components
$u_{i,inf}$ ........... Cartesian earth fixed freestream velocity components
$u_{i,wave}$ .......... Cartesian earth fixed wave velocity components
$u_{ref}$ ............ Reference velocity

$y^+$ .............. Dimensionless wall distance

# 1. Introduction

In the past decades, exploration of resources, research, and construction took place more and more offshore. Whenever critical equipment needs to be handled for these operations, a safe environment is sought onside the ship. Handling sideways or even at the aft of the ship may imply larger relative ship motions and being exposed to waves, wind and current. It is therefore beneficial to perform the operations towards the centre of the ship, where especially motions due to ship rotations are at a minimum and where a protected place from environmental conditions is granted. This has been achieved by construction of moonpools, which have an opening at the keel and vertical walls above the water line. They are typically of rectangular or sometimes of circular shape and need to be large enough to allow a safe operation of the individual equipment. Common ship types making use of moonpools are drilling-, diving-, dredging-, research- and sometimes pleasure vessels. Drill ships have in general large moonpools, which increased in length during the past decades to allow for dual operation of drilling equipment (van 't Veer & Tholen [80]).

Unfortunately, moonpools have also disadvantages, as they usually increase the resistance during transit conditions. Moreover, the water column can perform severe resonant-like behaviour under different circumstances, leading to conditions where equipment operation needs to be cancelled or green water on deck endangers workers. To reduce operational downtime, resistance increase and risk of green water, different measures can be taken to avoid violent water column motions, which are explained in chapter 1.1.

Water motion excitation can occur for two different reasons. At first, one can think of the ship being under operational conditions (zero ship speed) and exposed to waves. Orbital velocity and pressure fluctuations due to waves reach below the keel and induce fluctuations inside the moonpool. Furthermore, ship motions due to waves cause local flow acceleration and flow separation at the moonpool opening edge, which induce vortices and leading to disturbances. This excitation can reach resonant behaviour if the wave frequency coincides with the resonant frequency of the moonpool water column, which will be explained in chapter 6.1.1. Moreover, Aalbers [1] stated that due to non-linearities, excitation at half the natural water column frequency can lead to resonant-like behaviour as well. The second reason of water column excitation can occur during transit conditions (ship with forward velocity), where no sea state needs to be present. If assuming a ship fixed observation of the fluid, the water inside the moonpool is at rest, while the ship hull is experiencing a flow velocity correlating to the ship speed. This causes a flow separation at the moonpool leading edge at the keel. A shear-layer rollup develops and vortices, generated at the leading edge, reach the impingement edge at the aft wall of the moonpool. Two possible possible scenarios can develop from that situation. Either the vortices have no significant upward directed velocity and are shed below the keel, which causes almost no disturbances inside the moonpool, but might influence propulsion devices at the aft of the ship. More critical is the situation if the vortices hit the aft wall and travel upwards inside the moonpool. This leads to severe disturbances and can cause violent water column motions. The water column rises with separation at the leading edge, which further creates and upward direction of the shear-layer. Pressure fluctuations due to impingement of vortices at the aft wall travel back to the leading edge and are causing again disturbances in the shear-layer. This in itself could cause new vortex shedding and lead to a self-sustained oscillation cycle, which has been described by Rockwell & Naudascher [62] as 'phase locking'. The mentioned authors thoroughly investigated cavity flows, which can be compared to a moonpool being closed at the free surface, such that no water column motions are allowed. Due to the vertical motion in an open moonpool, vortex shedding is however strongly influenced by the oscillating frequency of the water column. An exemplary half oscillation cycle is shown in figure 1.1, where a combination of piston and sloshing motion is visualised from an experimental case at Froude number $Fr = 0.15$ and a relative wave length of $\lambda_W/L_{PP} = 1.0$. Flow direction is from right to left. At $t/T = 0.00$ the cycle starts and the vortex is fully developed. Due to the inclination of the free surface the water travels towards the front wall and hits this in $t/T \approx 0.20$ and $t/T \approx 0.30$, where the free surface already starts to sink. The water column reaches its minimum at $t/T \approx 0.50$. Afterwards the surface rises again with an inclination until it reaches the state of $t/T = 0.00$ and the cycle starts all over again. Note that this cycle is still dominated by the piston mode frequency, although a sloshing type of motion is present.

The water column motion in moonpools is typically classified between piston modes and sloshing modes. At piston mode, the free surface has a dominating vertical motion direction and no, respectively little phase differences exists between locations inside the moonpool. Sloshing modes are characterised by water motions travelling between the moonpool walls. They hence exhibit larger phase differences between different locations and furthermore have a significant horizontal motion. Molin [56] and Fukuda [32] thoroughly investigated these motion modes for rectangular and in case of Fukuda also for circular shapes of moonpools and individually derived formulations to approximate the resonant frequencies. While Fukuda's investigations where based on experiments, Molin derived his equations by applying linearised potential flow theory for 2D and 3D cases


(a) t/T=0.00

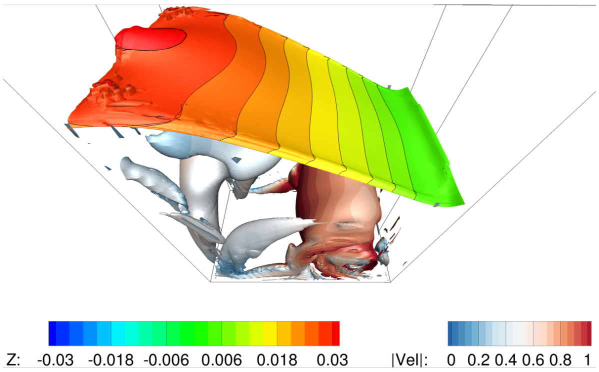


(b) t/T=0.00

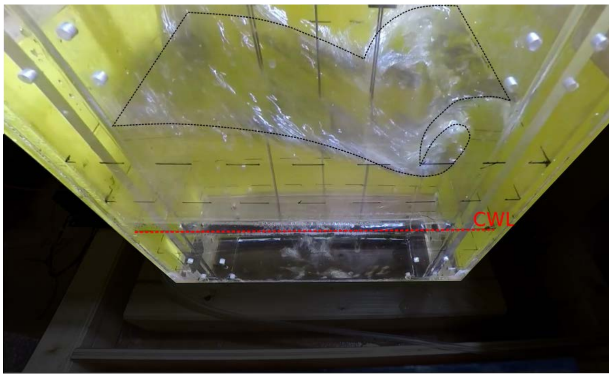


(c) t/T≈0.20

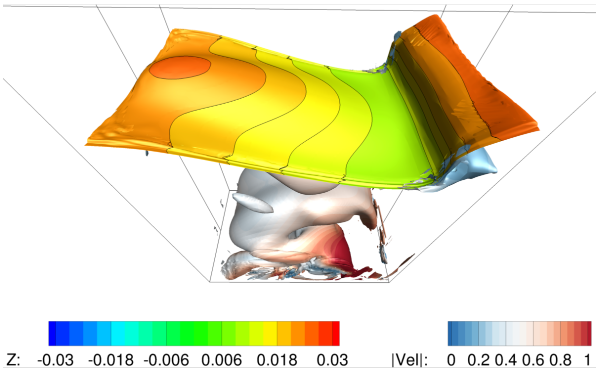


(d) t/T≈0.20

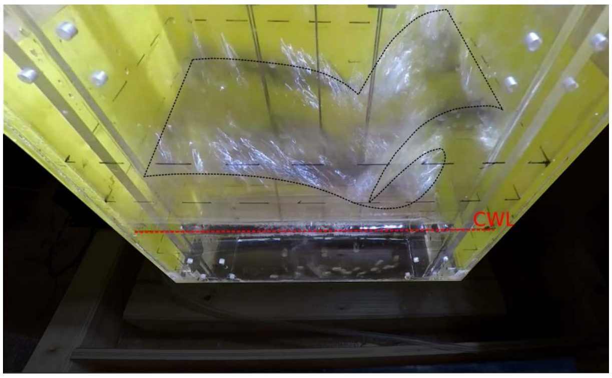


(e) t/T≈0.30

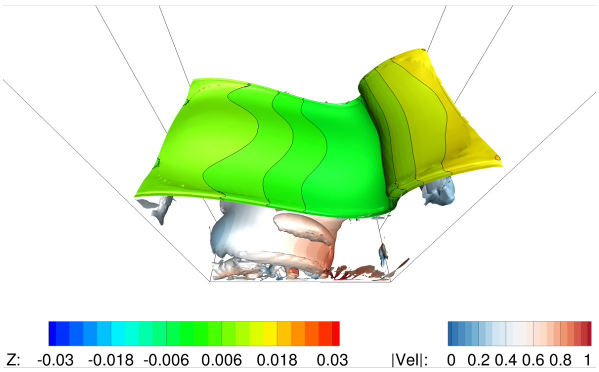


(f) t/T≈0.30

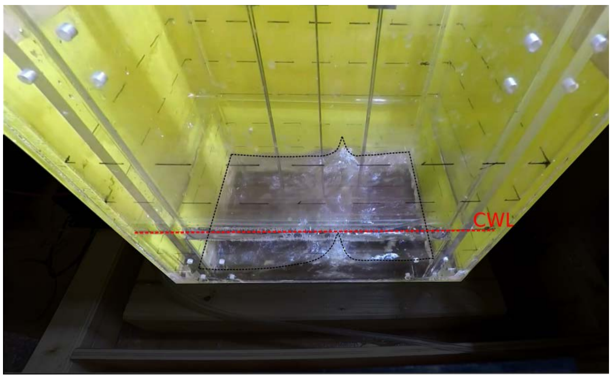


(g) t/T≈0.50

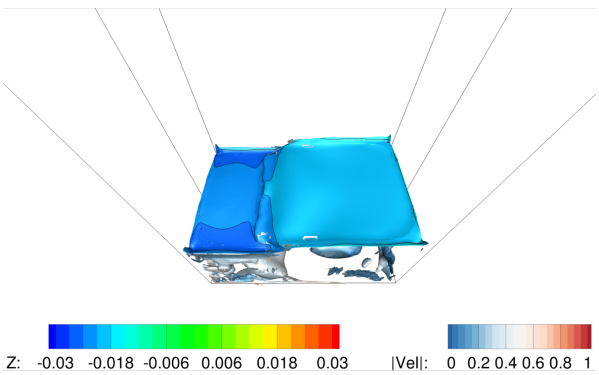


(h) t/T≈0.50

**Figure 1.1.:** Oscillating cycle of dominating piston mode frequency with superposed sloshing motion

under the assumption of the ship being motionless. Furthermore, the case was simplified by assuming infinite water depth and infinite length and breadth of the ship. Both of their approximations are further discussed in chapter 6.1.1. Molin [57] recently extended his approach to moonpools with recesses, which are explained in chapter 1.1.2. Faltinsen [26] mentioned that natural frequencies for two-dimensional cases are over-predicted by Molin for low ratios of moonpool draught to length, as infinite water depth has been assumed.

Several researchers used numerical methods to investigate flow phenomena inside moonpools within the past. Viscous damping due to vortex shedding is important to consider, as otherwise the water motion is severely over-estimated at resonance condition. This significantly complicates the numerical prediction, as pure potential theory based methods, which have the advantage of fast computational time, would fail. Either viscous methods are applied, which come at a higher computational cost, or empirical modifications need to be applied to potential theory codes.

Aalbers [1] developed a simple mathematical 1D model for the relative water column motion. As potential theory was used, experiments were necessary to determine quadratic viscous damping terms. Newman [58] showed results with a diffraction/radiation code, where artificial damping has been applied at the free surface of the moonpool to overcome the mentioned over-estimation. The same method has been later on applied by Chalkias & Krijger [11]. de Vries et al. [19] used radiation/diffraction boundary element method (BEM) and viscous methods to investigate the flow in turret moonpools and mentioned that particularly the piston mode natural period is not captured with sufficient accuracy, when using BEM. Faltinsen & Timokha [27] presented a potential theory method, which has been extended to modify the free surface boundary condition by making use of pressure drop coefficients derived from similarity of piston type motions with the flow through a slot of slatted screens. This method circumvents determination of external damping coefficients, which would normally have to be derived from experiments. A hybrid numerical code, which couples a potential theory method to resolve far field waves and a viscous method for the moonpool and the surrounding of the opening has been developed (Kristiansen et al. [47] and Fredriksen et al. [30, 31]). Reduction of computational time of three magnitudes have been reported, compared to fully viscous methods. Viscous methods have been used for moonpool flow investigations among others by Sauder et al. [63], van der Heiden et al. [79], de Vries et al. [19], Krijger & Chalkias [46].

Fredriksen et al. [30] conducted experiments for a moonpool at low forward speed ($Fr \leq 0.8$). As the influence of forward velocities will be discussed in detail in chapter 6.1.2, it needs to be emphasised at this point that the authors mentioned no significant change in natural periods for the investigated velocities. Fukuda [32] and Fukuda & Yoshii [33] however showed a dependency of the oscillation frequency on forward velocities, but did not further quantify the influence.

The resistance increase due to moonpools has been investigated by many of the previous mentioned authors. van 't Veer & Tholen [80] introduced a simple empirical method to predict the added resistance. A linear increase of added resistance with significant surface elevation amplitude over moonpool draught has been found. The increase is generally found to be stronger for piston mode motions than sloshing mode motions.

## 1.1. Approaches to reduce oscillations in the moonpools

Numerous devices exist in order to reduce the water motion amplitude inside moonpools. The following chapter gives an overview about the most common methods. Typical designs to reduce the amplitude are shown in figure 1.2 with a) being the moonpool without any modification. The individual design changes, highlighted in red, will be explained in the following subsections. These devices can be generally divided in two categories. One, are measurements to deflect separated vortices and prevention of entering into the moonpool and the others are to create an additional damping of the water column oscillation, once the vortices entered the moonpool.

### 1.1.1. Perforated Bulkheads

A very common method is the construction of perforated bulkheads along the walls of the moonpool. The original moonpool size is being reduced by a chosen distance, at which a perforated bulkhead is installed. A sketch of such a perforated bulkhead can be seen in figure 1.2b).

The basic absorption principle of perforated bulkheads is illustrated in figure 1.3. If the holes, shown in figure 1.3a are sufficiently sharp and the water motion horizontal, flow separation takes place at the holes and jets are being formed when passing the perforations. These collide with jets from neighbouring perforations, leading to a highly turbulent flow and energy dissipation. Purely vertical motion, illustrated in figure 1.3b, does not result in a direct damping. It causes however indirectly an absorption, as the void fraction behind the perforated walls are being filled once the water column rises, which causes a horizontal flow through the perforations.

The damping (respectively reflection) at these perforated walls has been studied by several authors. Clauss & Chen [14] investigated multiple perforated walls in order to reduce the tank wall reflection at stationary experiments in a towing tank. Sheets of different

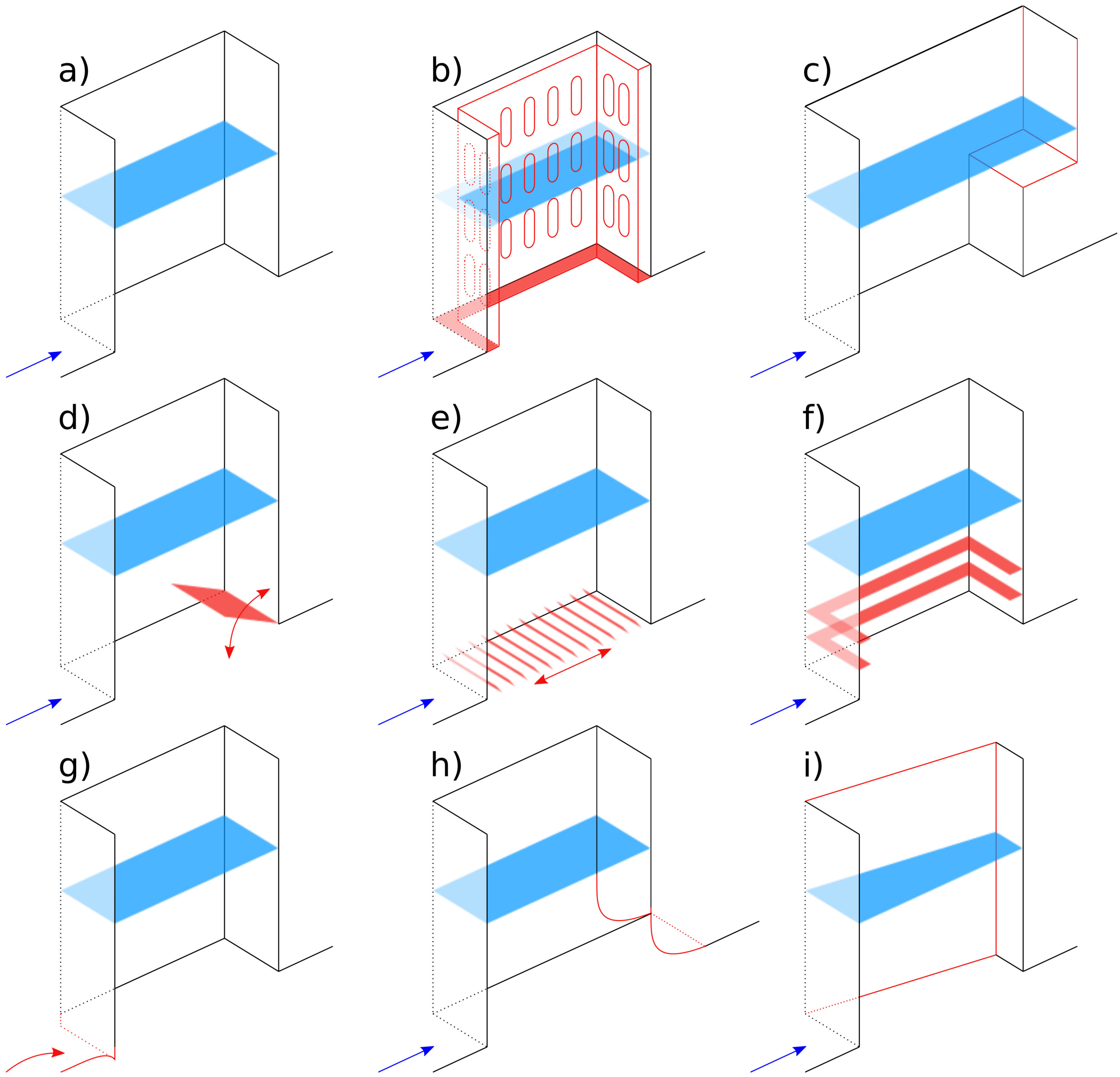


**Figure 1.2.:** Schematic overview of typical moonpool damping devices

numbers, porosities, hole sizes and arrangements have been experimentally investigated and reflection coefficients (which are defined in chapter 2.8.5) given for the individual configurations over varying wave length to absorber length ratios. One finding was that the hole size does have only a minor effect on the damping characteristics. Furthermore, lower porosities showed a superior behaviour over high porosities in terms of absorption efficiency. At last, higher waves are less dependent on the number of perforated sheets, whereas smaller waves are being absorbed better with increasing number of sheets.

Plessers [60] came to similar conclusions by investigating multiple perforated walls, using linear wave theory. He also developed a numerical method to determine the reflection coefficients of arbitrary perforated sheets without the necessity of performing experimental test. This method is however based on coefficients, which need to be determined else wise. He also gave indications for optimum length of the (multiple) sheets before the solid wall of $1/5$ to $1 \cdot \lambda_{max}$, with $\lambda_{max}$ being the maximum wave length to absorb.

Theoretically, this system can be designed to damp one wave at an optimum, or to damp a bandwidth of waves with still good efficiencies, as shown e.g. in Plessers [60]. It should be kept in mind though, that this assumes linear waves, which are not the case inside moonpools, where a rather complex flow takes place. Findings of the previous authors can therefore not be transformed directly to the problem of damping the motion inside moonpools.

Advantages of this system are high reliability, as there are no moving parts and easy installation. Furthermore, the perforated walls extend from top to bottom, which reduces the danger of accidentally hitting the damping device with equipment being handled inside the moonpool. The major disadvantage is the reduced size of the moonpool.

Because of its popularity in moonpools, this damping device was chosen to further investigate within this work. It is therefore used within experiments and numerical simulations. The latter are however performed with a numerical approach in order to avoid a highly complex grid of the exact geometry of perforated walls. This is being further discussed in chapter 2.8.

### 1.1.2. Recesses

Recesses (figure 1.2c)) are another common measurement to avoid high oscillation amplitudes. The horizontal area in vicinity of the free surface at rest is typically enlarged, compared to the area of the moonpool opening at the keel. They are however also used to assemble drilling equipment as stated by Son et al. [67]. The recess can be of different type, as it might be placed in the front or aft side of the moonpool or even on both sides.

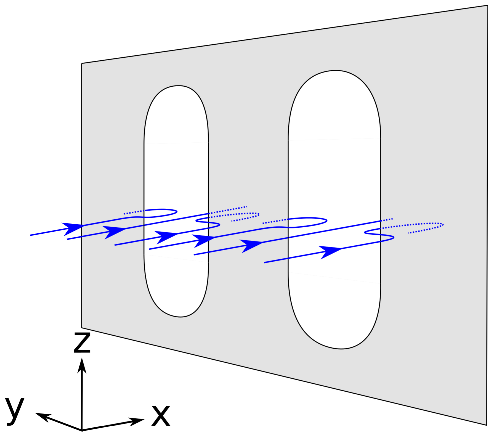


**(a)** Horizontal motion

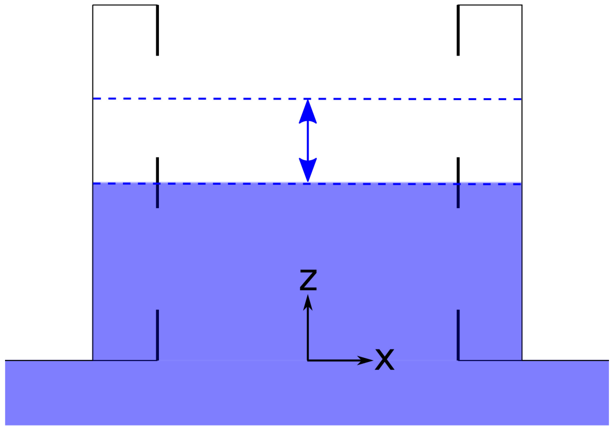


**(b)** Vertical motion

**Figure 1.3.:** Damping mechanism in perforated bulkheads

The natural modes of moonpools using recesses has been recently analysed by Molin [57]. Similar to his approach to model natural modes for simple rectangular moonpools, he used linearised potential flow theory to determine natural frequencies and modal shapes of the free surface for moonpools with recesses. Variation of recess length showed drastic decreasing of natural piston mode frequency with increasing length. Furthermore, maximum free surface elevation occurs at the wall of the recess and reduces on the opposite site (which is where the moonpool opening is located and hence of benefit for equipment handling). Variation of water height above the recess showed that the water elevation opposite the recess wall is lowered, when decreasing the water height above the recess. It needs to be mentioned though that non-linearities are likely to become important with decreasing water height, which are not covered with the chosen approach. Finally the effect of two recesses opposing each other was investigated, which does not seem to be beneficial for piston motions, but has slightly positive effects in terms of modal shape for sloshing motions. Recesses have been studied studied by Son et al. [67] and Yoo et al. [86].

### 1.1.3. Flaps and grids

Different setups of flaps and grids can be used to avoid separated vortices to move upwards into the moonpool. Examples are illustrated in figure 1.2d) and e). They can consist of a single hinged flap covering a part or the whole bottom opening of the moonpool, or be split into a grid of flaps, which needs to be retractable in order open the moonpool for operations. As the upwelling of vortices takes place towards the trailing edge of the moonpool, these flaps or grids are most efficient if placed in that region. Gaillarde

& Cotteleer [34] reported identical results with flaps only placed at the aft part of the moonpool opening, compared to a full coverage with flaps. Single flaps of 30% and 50% moonpool coverage and different inclination angles were tested as well and gave good results in terms of oscillation behaviour.

### 1.1.4. Horizontal plates

Horizontal plates can be placed inside the moonpool, as shown in figure 1.2f). These create additional vortices at their corners, if a vertical water motion is present. This device has been investigated by e.g. Fukuda [32], where the vertical position has been varied. Positioning at the keel proved to be least efficient, as the corners of the moonpool opening already produce vortices and the amplification due to the plates is lowest, if placed there. Positioning at the free surface at rest was more effective but slightly below the free surface proved to be most effective in terms of damping the oscillation amplitude. Similar findings are reported by Aalbers [1], who mentioned an increase in damping of 30% when placing the plates above the keel level.

### 1.1.5. Wedges and cut-outs

Wedges and cut-outs are measurements belonging to the category to deflect possible vortices and avoid entering into the moonpool. A wedge is shown in figure 1.2g) and the general idea of cout-outs in figure 1.2h). Gaillarde & Cotteleer [34] mentioned typical wedge lengths of around 20% moonpool length and inclination angles between 5° - 15°. While wedges direct the flow at the leading edge, cut-outs do the same at the trailing edge. The principal is similar to single flaps, which try to avoid an upwelling of vortices through an inclined aft wall. van 't Veer & Tholen shared their experience that wedges are beneficial only for smaller moonpool lengths but fail for longer ones and that the additional resistance due to the wedge is not balancing the reduced resistance through moonpool oscillations. Other investigations of cut-outs are presented by Krijger & Chalkias [46, 11]

### 1.1.6. Convergent moonpools

Convergent moonpool openings have been tested by English [24] and van 't Veer & Tholen [80], who reported significant oscillation amplitude reductions. The basic idea is to reduce the amount of water entering the moonpool through the geometry. Such a layout is shown in figure 1.2i).

Note that from the discussed mitigation devices, only perforated bulkheads, recesses and horizontal plates have a damping effect in transit and in operational conditions, whereas the others only work at forward speed. The latter hence aim at reducing the added resistance through the moonpool, rather than improve operational conditions.

## 1.2. Contribution of this work

This work contributes on different aspects of moonpool characteristic investigations. Several moonpool geometries are analysed through numerical simulations with a viscous flow solver, as well es experimentally in a seakeeping basin. The variety of moonpool geometries will give insights into the characteristic moonpool behaviour and their dependence on geometry parameters.

Perforated bulkheads are a typical measure to damp oscillating water motions inside the moonpool and will be therefore considered appropriately within this work. A numerical damping approach will be implemented and applied inside a moonpool to mimic the effect of previously mentioned perforated bulkheads. Numerical results are compared and validated with experiments. The numerical approach is beneficial as the need of complex grids and large numbers of cell size can be circumvented and hence computational costs for such simulations improved.

Another focus is laid upon the investigation of moonpool water column oscillation frequencies. The dependency of oscillating frequencies on the vessel forward speed will be discussed and their relevance explained. Numerical and experimental investigations are conducted and an empirical model to determine a velocity dependent natural piston mode frequency proposed.

Different influences on numerical results, such as the choice of turbulence model or individual motion restrictions are analysed and recommendations given. These investigations will be valuable for further numerical research on moonpools, in order to conduct efficient simulations.

At last forces, moments, motions and moonpool surface elevations are investigated for transit and operational conditions including their influence of different wave directions, or closure of the moonpool. The results will be of interest for shipbuilders dealing with moonpools, as well as captains in order to prevent undesired extreme moonpool behaviours leading to e.g. high added resistance or endangerment of operational safety.

# 2. Numerical method

The finite differences method based code *REX*, which is being developed at the University of Iowa / Iowa Institute of Hydraulic Research (IIHR), was used for all simulations in this work. *REX* uses multi-block structured body-fitted curvilinear grids, typically created by using hyperbolic grid generators. Several individual grids can be combined to analyse complex geometries with an overset grid technique, using the commercial software *Suggar++*. The free surface is captured with a single-phase level set approach. Turbulence is modelled with a blended $k$-$\epsilon$/$k$-$\omega$ model with the capability of using DES/DDES (Detached Eddy Simulation, respectively Delayed Detached Eddy Simulation). Implementations of the most important aspects of the previous mentioned numerical methods into *REX* is described in e.g. Carrica et al. [7, 9], Xing et al. [84], Bhushan et al. [3], Ismail et al. [39], Li et al. [50] and relevant references therein.

## 2.1. Governing equations

The description of the governing equations for fluid dynamic investigations can e.g. be found in textbooks like Ferziger & Perić [28]. Common conservation principles of mass and momentum are used. The conservation of mass, also known as the continuity equation, describes the rate of change of mass and has to be zero in all cases. Considering incompressible fluids, the conservation of mass can be written in cartesian coordinates $\xi_i$ and inertial frame of reference in tensor notation as:

$$\frac{\partial u_j}{\partial \xi_j} = 0, \tag{1}$$

with $u_j$ being the cartesian velocity components of the fluid with index $j = 1, 2, 3$ representing the three coordinate directions. The momentum conservation describes the rate of change of the momentum due to forces acting on the considered fluid. Written for incompressible fluids in cartesian coordinates, the momentum equation per volume unit yields

$$\frac{\partial u_i}{\partial t} + \frac{\partial (u_i u_j)}{\partial \xi_j} = -\frac{\partial p}{\partial \xi_i} + \frac{\partial}{\partial \xi_j}\left[\nu\left(\frac{\partial u_i}{\partial \xi_j} + \frac{\partial u_j}{\partial \xi_i}\right)\right] + s_i, \tag{2}$$

The right hand side of equation (2) consists of all acting forces, namely the surface forces composed by pressure $p$ and shear stresses using the kinematic viscosity $\nu$ and body forces which are included in the source term $s_i$.

*REX* uses a non-dimensional form of the governing equations with $u_{ref}$ and $L_{ref}$ used as the reference velocity and length to non-dimensionalise all quantities. These are further marked with superscript $'$. The non-dimensional form of the momentum equation can then be written as:

$$\frac{\partial u_i^{'}}{\partial t'} + \frac{\partial \left(u_i^{'} u_j^{'}\right)}{\partial \xi_j^{'}} = -\frac{\partial p^{'}}{\partial \xi_i^{'}} + \frac{\partial}{\partial \xi_j^{'}} \left[ \frac{1}{Re} \left( \frac{\partial u_i^{'}}{\partial \xi_j^{'}} + \frac{\partial u_j^{'}}{\partial \xi_i^{'}} \right) \right] + s_i^{'} \tag{3}$$

and $Re$ being the Reynolds number defined as

$$Re = \frac{u_{ref} L_{ref}}{\nu} \tag{4}$$

The above shown piezometric pressure $p^{'}$ is a combination of the gravitational force and dimensionless pressure, which can be written as

$$p^{'} = \frac{p_{abs}}{\rho u_{ref}^2} + \frac{\zeta^{'}}{Fr^2} \tag{5}$$

with $p_{abs}$ being the absolute pressure, $\rho$ the density, $\zeta'$ the non-dimensional vertical cartesian coordinate and

$$Fr = \frac{u_{ref}}{\sqrt{L_{ref} \cdot g}} \tag{6}$$

being the Froude number.

The derived set of equation cannot be solved analytically and is hence treated numerically. Differential equations are approximated using suitable schemes. Time derivatives are discretised in *REX* using a second-order backward differencing scheme. A second order central scheme is used for the discretisation of the diffusion and pressure terms. Convection terms can be discretised by numerous schemes such as first-order upwind, second-order linear upwind, quadratic biased and cubic biased interpolation and a hybrid formulation of the second-order linear upwind and the fourth-order cubic interpolation approach. As mentioned in Ismail et al. [39] the advantage of the cubic interpolation, although being only of second-order accuracy, is the reduced numerical diffusion. Coupling of the momentum and continuity equation is done using either the pressure implicit split operator (PISO) algorithm by Issa [41], or the projection method by Bell [2], which has been used in this work.

## 2.2. Turbulence model

The majority of flows in ship hydrodynamic aspects is turbulent. Turbulent flows can briefly be characterised as highly unsteady, 3-dimensional, containing high vorticity with a broad range of length and time scales. The above described general form of Navier-Stokes equations is principally able to solve these turbulences. Direct turbulence solving is known as Direct Numerical Simulation (DNS) where the spatial resolution needs to be very high and time resolution very small, so that the smallest eddies can be resolved directly, without using any model. Hence, the only source of errors results from numerical discretisation, which can be kept small. This method obviously gives the highest possible accuracy regarding turbulence prediction but at immense computational costs as the numerical grids are extremely large and the time step very small. Solving such simulations is until now and the foreseeable future restricted to simple problems with low Reynolds numbers and has almost solely been used to produce validation data for turbulence models in simple cases.

To overcome this, different turbulence models were developed, which are modelling the turbulence through different methods instead of directly resolving it. The most popular and widely used model for engineering purposes are the Reynolds-Averaged Navier-Stokes (RANS) equations. In between DNS and RANS are other methods like DES, DDES and LES (Large Eddy Simulations), as well as other hybrid models, which usually combine a RANS model with an LES model. As a RANS and DDES model has been used within this work, they will be briefly discussed in the following.

### 2.2.1. RANS

RANS methods provide a good level of accuracy for most engineering applications. The underlying approach is to average all turbulent fluctuations. The averaging approach was firstly introduced by Reynolds with the assumption, that a turbulent flow can be described as an average value ($\overline{\ }$) and a fluctuation about that value ($^*$) for any variable $\chi$.

$$\chi(\xi_i, t) = \overline{\chi}(\xi_i) + \chi^*(\xi_i, t) \tag{7}$$

The averaging interval must be large enough compared to the fluctuation frequency to give an accurate value. Unsteady turbulence phenomena can be handled using ensemble averaging (see e.g. Schlichting [64]), where equation (7) changes, such that $\overline{\chi}(\xi_i, t)$ becomes time dependent as well. Averaging linear terms of the Navier-Stokes equation simply returns the identical term of the averaged value as $\overline{\chi^*} = 0$. On the other hand, averaging a non-linear term of the Navier-Stokes equation yields

$$\overline{u_i \chi} = \overline{(\overline{u}_i + u_i^*)(\overline{\chi} + \chi^*)} = \overline{u}_i \overline{\chi} + \overline{u_i^* \chi^*} \tag{8}$$

The second term would only be zero if these quantities are uncorrelated, which is rarely the case.

Substituting equation (7) into the momentum conservation equation results in

$$\frac{\partial \overline{u}_i}{\partial t} + \frac{\partial}{\partial \xi_j}\left(\overline{u}_i \overline{u}_j + \overline{u_i^* u_j^*}\right) = -\frac{\partial \overline{p}}{\partial \xi_i} + \frac{\partial}{\partial \xi_j}\left[\frac{1}{Re}\left(\frac{\partial \overline{u}_i}{\partial \xi_j} + \frac{\partial \overline{u}_j}{\partial \xi_i}\right)\right] + \overline{s}_i \tag{9}$$

Note that the superscript $'$, indicating a non-dimensional variable, has been left aside for the sake of clarity. The general formulation of momentum conservation remains the same, with the exemption of the newly introduced term $\overline{u_i^* u_j^*}$, which is called Reynolds-stress tensor. This tensor is typically written on the right hand side of the equation and included in the viscous stress tensor. As the Reynolds-stress tensor contains six unknown terms, but no additional equations have been stated through the averaging approach, a closure problem of the equations results. Boussinesq [6] was the first to introduce the concept of 'eddy viscosity', where the Reynolds stresses are modelled by an increased viscosity:

$$\tau_{ij} = -\overline{u_i^* u_j^*} = \nu_t \left(\frac{\partial \overline{u}_i}{\partial \xi_j} + \frac{\partial \overline{u}_j}{\partial \xi_i}\right) - \frac{2}{3}\delta_{ij} k \tag{10}$$

In eq.(10) $k = \frac{1}{2}\overline{u_i^* u_i^*}$ and $\nu_t$ describe the unknown turbulent kinetic energy and the eddy viscosity respectively and $\delta_{ij}$ the Kronecker symbol which is 1 for $i = j$ and zero else wise. Once a modelling of $k$ and $\nu_t$ has been stated, the conservation of momentum equation contains only mean quantities of velocities and pressure. Equation (3) remains identical with the exemption of the Reynolds number and pressure changing to the following description, as is e.g. shown in Bhushan et al. [3].

$$Re_{\text{eff}} = \frac{u_{ref} L_{ref}}{\nu + \nu_t} \tag{11}$$

$$p' = \frac{p_{abs}}{\rho u_{ref}^2} + \frac{\zeta'}{Fr^2} + \frac{2k'}{3} \tag{12}$$

There are numerous turbulence models based on eddy viscosity modelling of the Reynolds-stress which present a solution to the closure problem. Examples of these models are one-equation models like Spalart-Allmaras [70] or two-equation models like $k$-$\omega$ from Wilcox [81] or $k$-$\epsilon$ described in Launder & Spalding [48].

A widely used model, which was also applied in this work, is the blended $k$-$\epsilon$/$k$-$\omega$ turbulence model with the extension of the modification of the eddy viscosity to take account of shear stress transport, originally based on Menter [54]. The $k$-$\omega$ model by Wilcox [81] is specifically suitable for the sublayer of the boundary layer, but is also used for the logarithmic part of the boundary layer. It does not involve damping functions and allows simple Dirichlet boundary conditions. As this model shows a strong sensitivity to the freestream value $\omega_f$ outside the boundary layer, it is being turned off in favour for the $k$-$\epsilon$ model which is superior to the $k$-$\omega$ model in freestream areas. The coupling between those two models is achieved through a blending function $F_1$, which is designed to be one in the sublayer and logarithmic region and zero elsewhere. The original $k$-$\omega$ model is multiplied with $F_1$ and the $k$-$\epsilon$ model is being transformed into a $k$-$\omega$ formulation and multiplied with $(1 - F_1)$ as shown in eq. (16). This way, the $k$-$\omega$ model is active in the sublayer and logarithmic boundary layer region and the $k$-$\epsilon$ model in the free shear flow.

Additional to the simple blending of the two mentioned turbulence models (which is called baseline model), Menter also proposed a modification of the eddy viscosity to take account of the shear stress transport (SST). This modification was introduced due to the effect, that the $k$-$\omega$ model fails to accurately predict pressure-induced separation. Again, a blending function $F_2$ is being used to distinguish between boundary layer flows and free shear-layers to specify the respective eddy viscosity. This modification is supposed to work much better in areas of adverse pressure gradients. The exact definition of the blending function $F_1$ and $F_2$ can be seen in Menter [54].

The transport equation of the turbulent kinetic energy $k$ and the specific dissipation rate $\omega$ can be described for the baseline model of Menter by

$$\frac{\partial k}{\partial t} + \overline{u}_j \frac{\partial k}{\partial \xi_j} = \tau_{ij} \frac{\partial \overline{u}_i}{\partial \xi_j} - \beta^* k\omega + \frac{\partial}{\partial \xi_j}\left[\left(\nu + \sigma_k \nu_t\right) \frac{\partial k}{\partial \xi_j}\right] \tag{13}$$

$$\frac{\partial \omega}{\partial t} + \overline{u}_j \frac{\partial \omega}{\partial \xi_j} = \frac{\gamma}{\nu_t} \tau_{ij} \frac{\partial \overline{u}_i}{\partial \xi_j} - \beta\omega^2 + \frac{\partial}{\partial \xi_j}\left[\left(\nu + \sigma_\omega \nu_t\right) \frac{\partial \omega}{\partial \xi_j}\right] + 2\left(1 - F_1\right) \sigma_{\omega 2} \frac{1}{\omega} \frac{\partial k}{\partial \xi_j} \frac{\partial \omega}{\partial \xi_j} \tag{14}$$

with $\nu_t$ being the turbulent viscosity defined as:

$$\nu_t = \frac{k}{\omega} \tag{15}$$

As two turbulence models are used, two sets of constants need to be provided. The constants according to the $k$-$\omega$ and the $k$-$\epsilon$ model can be found in equation (17) respectively

(18) and are blended using the function $F_1$, where $\phi$ represents every single individual constant.

$$\phi = F_1\phi_1 + (1 - F_1)\phi_2 \tag{16}$$

$$\sigma_{k1} = 0.5,\ \ \sigma_{\omega 1} = 0.5,\ \ \beta_1 = 0.075,\ \ \beta^* = 0.09,\ \ \kappa = 0.41,\ \ \gamma_1 = \frac{\beta_1}{\beta^*} - \frac{\sigma_{\omega 1}\kappa^2}{\sqrt{\beta^*}} \tag{17}$$

$$\sigma_{k2} = 1.0,\ \ \sigma_{\omega 2} = 0.856,\ \ \beta_2 = 0.0828,\ \ \beta^* = 0.09,\ \ \kappa = 0.41,\ \ \gamma_2 = \frac{\beta_2}{\beta^*} - \frac{\sigma_{\omega 2}\kappa^2}{\sqrt{\beta^*}}. \tag{18}$$

**Law of the wall**

Wall functions have been investigated within this work, which is why they are briefly explained in the following. The boundary layer is characterised through a velocity profile, leading from $u_i = 0$ at the wall to the freestream velocity $u_i = u_\infty$ outside of the boundary layer. The boundary layer thickness is a function of the Reynolds number and decreases with increasing Reynolds number. The viscous sublayer is typically very small and the dimensionless velocity $u^+ = \frac{u_{||}}{u_\tau}$ increases linearly with the dimensionless wall distance $y^+ = \frac{y u_\tau}{\nu}$. Here, $u_{||}$ describes the mean velocity parallel to the wall, $y$ is the distance normal to the wall, and $u_\tau = \sqrt{\frac{\tau_w}{\rho}}$ the shear velocity with $\tau_w$ being the wall shear stress. The viscous sublayer region is shown in figure 2.1 for $y^+ < 5$.

Outside the viscous sublayer a logarithmic law describes well the velocity profile (see e.g. Schlichting [64]), which is shown from $30 < y^+$ and can be generally described by

$$u^+ = \frac{1}{\kappa}\log\left(y^+\right) + B \tag{19}$$

The von Karman constant $\kappa = 0.41$ and an empirical constant $B$ which may vary depending on the wall roughness are used for description of the logarithmic law. Two different parameters are implemented into *REX*, taking account of wall roughness influence ($\Delta B$) and pressure gradient effects ($P^+$). Details on these parameters can be seen in Bhushan et al. [3], but have not been used in this work.

In between the linear and logarithmic region is a buffer layer, where a transition from linear to logarithmic form takes place.

When assuring a dimensionless wall distance of $y^+ < 1$, the standard momentum and turbulence transport equations can be used right up to the wall.

If a high grid resolution at the wall should be avoided, one can make use of wall functions which model the near wall region instead of resolving it. The velocity in the first, respectively second point away from the wall is derived using equation (19) in case

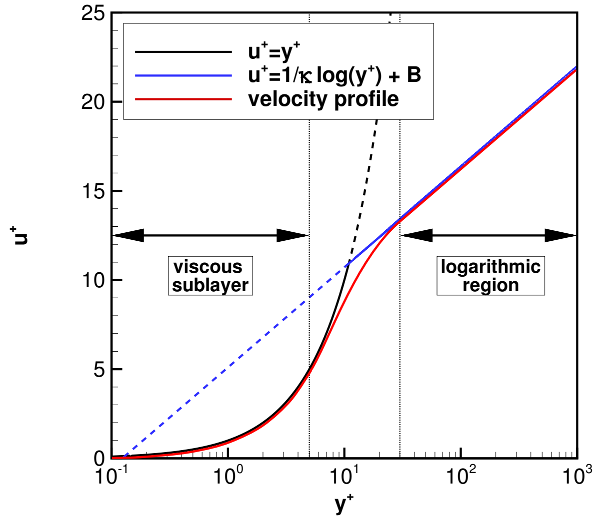


**Figure 2.1.:** Turbulent boundary layer velocity profile

of $y^+_{2,3} > 11.67$ or with $u^+ = y^+$ for $y^+_{2,3} \leq 11.67$. As this is inaccurate inside the buffer region ($5 < y^+ < 30$), those dimensionless wall distances should be avoided. Nevertheless, a multi layer approach has been implemented into *REX*, which treats the buffer layer between $5 < y^+ < 30$ separately and improving accuracy for this region (Bhushan et al. [3]).

The definition of $k$ and $\omega$ when using wall functions is based on Wilcox [81] when using the two layer approach, respectively Kalitzin's [44] and Esch & Menter [25], when using the multi layer approach.

### 2.2.2. LES

The large-eddy simulation is part of DES/DDES models and is therefore briefly explained in the following, as DDES has been investigated within this work. LES can be described as a filtering of DNS, as only large eddies are being resolved in space and time and smaller eddies are being modelled. This approach states its validity, as smaller eddies provide only a small portion to the energy cascade, whereas large eddies provide the biggest part. The velocity is defined using a filter $G$ as shown in eq. (20) which is a localised function and dependent on a length scale $\Delta$ and the difference of the location $\xi_i - \tilde{\xi}_i$. A discussion of common filters can be found in Blazek [4]. The definition of $\Delta$ is still subject to discussions, as different approaches are used (e.g. $\Delta = (\Delta\xi\Delta\eta\Delta\zeta)^{1/3}$ or $\Delta = \max(\Delta\xi, \Delta\eta, \Delta\zeta)$). Eddies smaller than $\Delta$ need to be modelled and eddies larger are resolved directly. The velocity field $u_i$ is decomposed into the large scale eddies $\overline{u}_i$, which are being resolved and the sub-filter part $\tilde{u}_i$ which needs to be modelled.

$$\overline{u}_i(\xi_i) = \int G(\xi_i, \tilde{\xi}_i, \Delta) u_i(\tilde{\xi}_i) d\tilde{\xi}_i \tag{20}$$

Filtering of the Navier-Stokes equation results in similar expressions as found in the RANS equations, where only the large scale eddies are considered:

$$\frac{\partial\left(\overline{u}_i\right)}{\partial t} + \frac{\partial\left(\overline{u_i u_j}\right)}{\partial \xi_j} = -\frac{\partial \overline{p}}{\partial \xi_i} + \frac{\partial}{\partial \xi_j}\left[\nu\left(\frac{\partial \overline{u}_i}{\partial \xi_j} + \frac{\partial \overline{u}_j}{\partial \xi_i}\right)\right] + s_i \tag{21}$$

Prediction of $\overline{u_i u_j}$ is being done by modelling the difference of the inequality $\overline{u_i u_j} \neq \overline{u}_i \overline{u}_j$ defined by the so-called sub-grid scale (SGS) Reynolds stress $\tau_{ij}^S$

$$\tau_{ij}^S = -\left(\overline{u_i u_j} - \overline{u}_i \overline{u}_j\right) \tag{22}$$

SGS models need to simulate the energy transfer from large to sub-grid scales. A common SGS model is the Smagorinsky model [65] which functions as an eddy viscosity model with

$$\tau_{ij}^S - \frac{1}{3}\tau_{kk}^S \delta_{ij} = \nu_t \left(\frac{\partial \overline{u}_i}{\partial \xi_j} + \frac{\partial \overline{u}_j}{\partial \xi_i}\right) = 2\nu_t \overline{S}_{ij}, \tag{23}$$

where $\overline{S}_{ij}$ is the strain rate of the large scale and $\tau_{kk}^S$ represents the isotropic part of the SGS stresses (Blazek [4]). The eddy viscosity is defined as

$$\nu_t = C_S^2 \Delta^2 |\overline{S}|, \tag{24}$$

with $C_S$ being a model parameter which is approximately 0.2 but unfortunately not necessarily constant in the flow field, as explained by Blazek [4]. $|\overline{S}|$ is the magnitude of strain rate tensor and defined as $|\overline{S}| = (2\overline{S}_{ij}\overline{S}_{ij})^{1/2}$.

To resolve the eddies efficiently, an isotropic grid with equal spacings $\Delta$ in every direction ($\Delta\xi \approx \Delta\eta \approx \Delta\zeta$) is strongly advised as the maximum spacing defines the smallest possible eddy being resolved (Spalart [68]). Pure LES hence requires a large amount of cells to resolve the boundary layer as stated by Spalart et al. [72] with approximately $1.3 \cdot 10^7$ cells in the boundary layer region alone for a single wing of an air plane or roughly $10^{11}$ grid points and $10^7$ time steps for an airborne or ground vehicle. The underlying Reynolds number for this estimation has been approx. $Re = 10^7$. Hence, similar magnitudes could be expected for hydrodynamic simulations of ships and would lead to enormous computational times. Also, traditional grid convergence is more subtle compared to RANS or DNS, as the partial differential equations in LES depend on the grid spacing through the filtering process, defined by $\Delta$.

### 2.2.3. DES

The detached-eddy simulation (DES) was primarily introduced by Spalart et al. [72] in 1997. 'Detached' refers to eddies outside boundary layers in contrast to 'attached' eddies inside the boundary layers. DES can be described as 'a three-dimensional unsteady numerical solution using a single turbulence model, which functions as a sub-grid scale model in regions where the grid density is fine enough for a large-eddy simulation, and as a Reynolds-averaged model in regions where it is not' (Travin et al. [76]). Hence, attached eddies will be modelled and detached eddies will be resolved. The idea to use a RANS model within the boundary layer has its origins in the requirement of high numbers of cells, if these regions would need to be handled using LES. Typically, attached eddies are of less interest and smaller scale than detached eddies, which might have a significant influence on following parts. This approach hence is aimed at fluid mechanical problems at high Reynolds numbers and severe separation. In contrast to RANS simulations, DES is able to resolve the three-dimensionality of the turbulence in a more accurate manner when refining the grids, whereas RANS largely, but not completely, suppresses three-dimensionality. Figure 2.2 shows the resolved vorticity isosurfaces of Q=100 (refer to chapter 3.1) using a RANS method and DDES on the same grid. It can be clearly seen, that DDES is able to resolve more vortical structures than RANS. Figure 2.2a and 2.2b show the beginning of the vortex shedding cycle and figure 2.2c and 2.2d an intermediate step of the cycle.

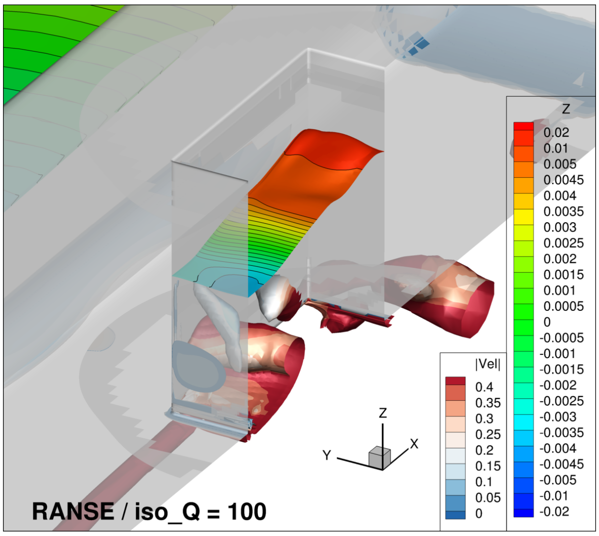


**(a)** $t/T = 0$ with RANS

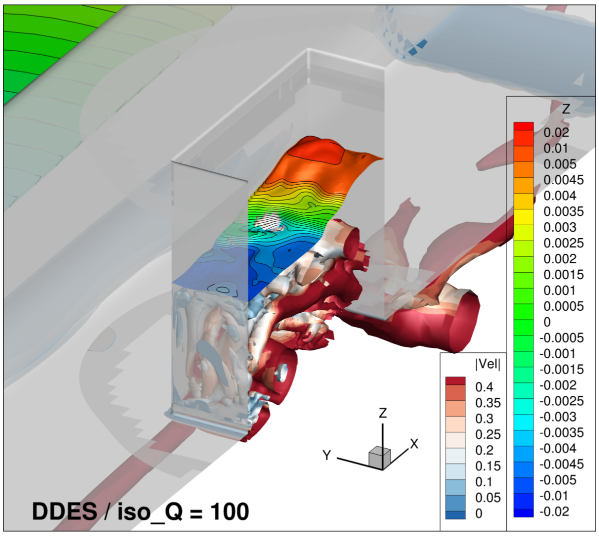


**(b)** $t/T = 0$ with DDES

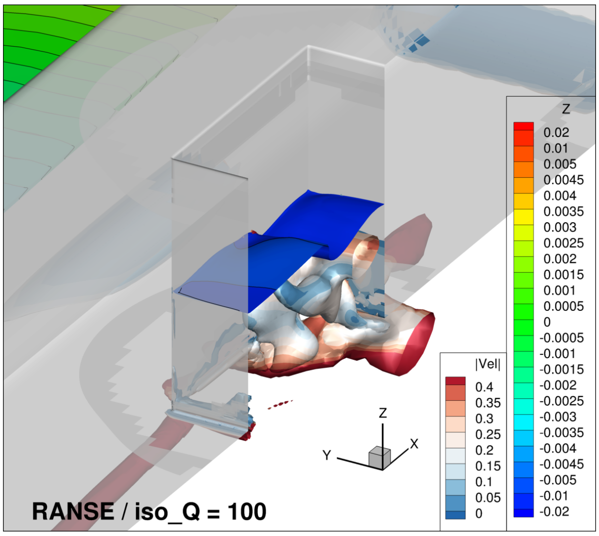


**(c)** $t/T \approx 0.5$ with RANS

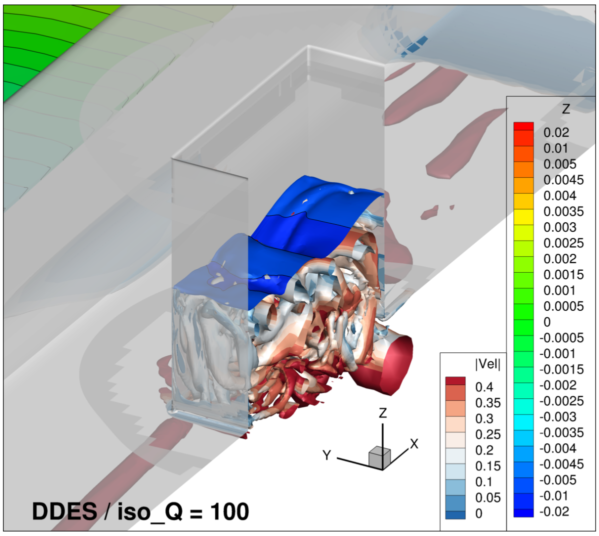


**(d)** $t/T \approx 0.5$ with DDES

**Figure 2.2.:** Comparison of vortex resolution inside the moonpool using RANS and DDES at the beginning (upper pictures) and end (lower pictures) of a half vortex shedding cycle.

DES can be implemented with the use of almost any RANS turbulence model, when appropriately modifying the used length scale. The length scales $l_{RANS}$ respectively $l_{DES}$ describe the scale of the local vortical structures and are defined to be

$$l_{RANS} = \frac{\sqrt{k}}{\beta^* \omega} \tag{25}$$

$$l_{DES} = \min\left(l_{RANS}, C_{DES}\Delta\right). \tag{26}$$

The constant $C_{DES}$ can again be blended between the $k$-$\epsilon$ and $k$-$\omega$ model, using the approach from Menter [54]. Therefore, $C_{DES}$ is defined the following way:

$$C_{DES} = (1 - F_1)C_{DES}^{k-\epsilon} + F_1 C_{DES}^{k-\omega}, \tag{27}$$

with $C_{DES}^{k-\epsilon}$ chosen as 0.61 and $C_{DES}^{k-\omega}$ as 0.78 according to Travin et al. [75]. It was noted, that these values are valid for a hybrid upwind-central differencing scheme and that schemes with higher dissipation may require lower values.

To finally extend the blended $k$-$\omega/k$-$\epsilon$ turbulence model into a DES model, the dissipative term of the $k$-transport $D_{RANS}^k$ is being modified by substituting $l_{DES}$ for $l_{RANS}$ the following way

$$D_{RANS}^k = \beta^* k\omega = \frac{k^{3/2}}{l_{RANS}} \tag{28}$$

$$D_{DES}^k = \frac{k^{3/2}}{l_{DES}} \tag{29}$$

Xing et al. [85] extensively validated turbulent flows around a surface-piercing NACA0024, comparing surface-tracking methods and level set methods using RANS and DES with the code *CFDShip-Iowa*. He concluded, that although RANS is able to resolve most of the vortical structures and instabilities, DES offers a broader range of frequencies, which matched very well the experimental data.

### 2.2.4. DDES

A major problem using DES is the possible failure of grid convergence due to the so called modelled-stress depletion (MSD) or grid-induced separation (GIS) (see e.g. Caruelle [10], Deck et al. [20] and Menter & Kuntz [55]). The source of the problem can be visualised in figure 2.3, where the upper grid corresponds to a boundary layer grid where the wall-parallel spacing $\Delta_{||}$ is much larger than the boundary thickness $\delta_{99}$. This is a suitable grid for the RANS mode in DES. The lower right grid can be described as isotropic with an equal grid spacing in all directions and much smaller than $\delta_{99}$. This grid is suitable for the LES mode in DES. Spalart et al. [71] recommends a value of at least $\Delta \approx \delta_{99}/10$ or better $\Delta \approx \delta_{99}/20$. The problem occurs in the lower left grid, which can be described as ambiguous and has wall-parallel grid spacings which are smaller than $\delta_{99}$. These grids activate the DES limiter ($l_{DES} = C_{DES}\Delta$) prematurely, without being fine enough to resolve the velocity fluctuations in the boundary layer using LES. The premature activation of the DES limiter leads to a reduction of the eddy viscosity

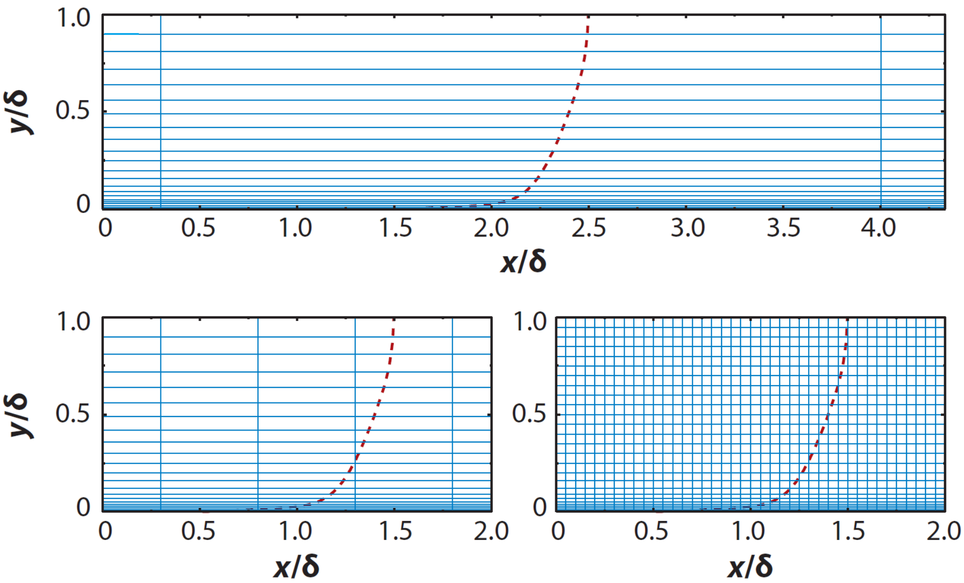


**Figure 2.3.:** Types of grid in boundary layers (Spalart [69])

without being balanced by LES resolved stresses.

Ambiguous grids mainly occur in three cases: First, when the grid is being refined in order of seeking a grid convergence, second, when the distortion of the geometry requires a high wall-parallel grid spacing and third, when the boundary layer thickens and approaches separation. Several approaches have been made to circumvent MSD such as scale-adaptive simulation (SAS) and turbulence resolved RANS (TRRANS) which do not use the grid spacing in order to switch from RANS to LES (Travin et al. [77], Menter & Kuntz [55]). Other approaches are zonal and hence rely on the manual definition of boundary layers by the user, in which the DES limiter is switched off (Deck [21]). This obviously is prone to errors and limited to simple problems. Another method is based on using cell aspect ratios larger than unity as an indicator for boundary layers. This however did not turn out to be robust enough, as e.g. grids in ship hydrodynamics use high aspect ratios to resolve the free surface.

The delayed detached-eddy simulation (DDES) is based on the idea of Menter & Kuntz [55], who are using the $F_2$ or $F_1$ blending function of the SST model to define the boundary layer and 'delay' the LES mode. These functions are one in the boundary layer region and decrease to zero at the edge. The argument of the functions is proportional to $\sqrt{k}/\omega y$ and describes the ratio of the internal length scale $\sqrt{k}/\omega$ of the turbulence model in RANS mode (here being the $k$-$\omega$ model) and the wall distance $y$. This results in a modification of the length scale:

$$l_{DDES} = l_{RANS} - F_1 \cdot \max\left(0, l_{RANS} - l_{DES}\right) \tag{30}$$

Using $l_{DDES}$ instead of $l_{DES}$ results in the significant change, that the length scale is now dependent on the eddy viscosity additionally to the grid spacing, which makes it time-dependent. This not only prevents the use of LES in boundary layers but also leads to a more abrupt change from RANS to LES following separation.

## 2.3. Level set method

The free surface is modelled using a single-phase level set approach, which has been discussed in Carrica et al. [9].

This approach has some advantages over multi-phase level set methods, as the interface remains sharp and does not need a smoothing across the interface due to the jump in density. Furthermore, the computation is performed within a single fluid with uniform properties and the air phase only requires minor computational effort, leading to more robust and often faster simulations. Stresses in the air phase are not captured, which is why these should be of minor importance, as is usually the case in ship hydrodynamics.

The level set function $\phi_{ls}$ is used to describe the signed distance to the captured interface, which is located at $\phi_{ls} = 0$. The function is positive in water and negative in air. The following transport equation is solved:

$$\frac{\partial \phi_{ls}}{\partial t} + u_j \frac{\partial \phi_{ls}}{\partial \xi_j} = 0. \tag{31}$$

The normal vector pointing into the water is defined as

$$n_i = -\frac{\partial \phi_{ls}/\partial \xi_i}{\left|\partial \phi_{ls}/\partial \xi_i\right|}, \tag{32}$$

A jump condition at the interface needs to be enforced in the single-phase approach, in contrast to multi-phase level set methods. The dimensionless pressure at the fluid interface reduces to $p' = \zeta'_{int}/Fr^2$ when considering the interface jump condition and neglecting surface tensions, as shown in Carrica et al. [9]. $\zeta'_{int}$ represents the non-dimensional vertical component of the earth fixed cartesian coordinates at the interface. The pressure is set to be constant for the air phase as an approximation.

Re-initialisation is important to accurately determine the normal at the interface, which is used in the boundary condition and to extend velocities into the air phase. Re-initialisation is done by applying equation (33).

$$n_i \frac{\partial \phi_{ls}}{\partial \xi_i} = sign\left(\phi_{0,ls}\right), \tag{33}$$

with $\phi_{0,ls}$ being the level set function prior to re-initialisation and $n_i$ the normal pointing to the fluid being re-initialised. Due to the dependence of $n_i$ from $\phi_{ls}$, equation (33) is non-linear and requires and iterative approach to converge.

## 2.4. Rigid body motions

Simulations in *REX* can be performed in an earth fixed or ship fixed frame of reference. The earth fixed system is considered to be inertial, which is a valid simplification for most marine hydrodynamic applications. The cartesian earth fixed reference frame $(\xi, \eta, \zeta)$ can move at a constant velocity, which could be used for simulations of passing ships. In combination with use of overset grids, which are described in chapter 2.5, this gives full freedom over the type of simulations being performed.

Every body being investigated holds a body fixed coordinate system $(x_i,y_i,z_i)$, being non-inertial for moving bodies. Index $i$ relates to the number of objects and is one in this work, which is why it is being neglected in further notations. Note that the following description can be applied to each body individually, if multiple objects are investigated.

Vector transformation from cartesian ship fixed to cartesian earth fixed frame of reference can be obtained through

$$\begin{pmatrix} \xi \\ \eta \\ \zeta \end{pmatrix} = \begin{pmatrix} \xi_0 \\ \eta_0 \\ \zeta_0 \end{pmatrix} + T \begin{pmatrix} x \\ y \\ z \end{pmatrix}, \tag{34}$$

where $(\xi_0, \eta_0, \zeta_0)^T$ are coordinates of the origin of the ship fixed frame of reference, described in the earth fixed frame of reference. $T$ is the transformation matrix, composed by three rotations using the Euler angles and is shown in equation (35). Derivation of the transformation matrix can e.g. be seen in Fossen [29]. The Euler angles are defined such that the ship is rotated with a yaw angle $\psi$ around the vertical inertial coordinate axis $\vec{\zeta}$, pitch angle $\theta$ around a hybrid axis and roll angle $\phi$ around the longitudinal ship fixed coordinate axis $\vec{x}$. The hybrid axis is formed by the normalised cross product of $\vec{\zeta}$ and $\vec{x}$.

The hybrid coordinate system is denoted with $(x^*, y^*, z^*)$.

$$T = \begin{pmatrix} \cos\psi\cos\theta & -\cos\phi\sin\psi + \sin\phi\sin\theta\cos\psi & \sin\phi\sin\psi + \cos\phi\sin\theta\cos\psi \\ \sin\psi\cos\theta & \cos\phi\cos\psi + \sin\phi\sin\theta\sin\psi & -\sin\phi\cos\psi + \cos\phi\sin\theta\sin\psi \\ -\sin\theta & \sin\phi\cos\theta & \cos\phi\cos\theta \end{pmatrix} \quad (35)$$

Translational and rotational ship motions are described by the vector

$$(\xi_0, \eta_0, \zeta_0, \phi, \theta, \psi)^T , \quad (36)$$

Components of the angular velocity vector are defined in the ship fixed coordinate system by:

$$\begin{pmatrix} p \\ q \\ r \end{pmatrix} = \begin{pmatrix} \dot{\phi} - \dot{\psi}\sin\theta \\ \dot{\psi}\cos\theta\sin\phi + \dot{\theta}\cos\phi \\ \dot{\psi}\cos\theta\cos\phi - \dot{\theta}\sin\phi \end{pmatrix} \quad (37)$$

Parameters with a dot represent time derivatives of the respective quantity. Forces and moments are denoted with

$$(F_x, F_y, F_z, M_x, M_y, M_z)^T. \quad (38)$$

The forces are computed in the inertial system, where the momentum equations are solved and hence stresses known. After completion of force determination, they are transformed into the ship fixed coordinate system, where needed to solve the rigid body equations. Details on this procedure can be found in Xing et al. [84].

The rigid body equations can be derived from momentum and angular momentum equations and are generally described for non-inertial systems by (see e.g. Fossen [29]):

$$F_x = m \left[ \left( \dot{U}_0 + qW_0 - rV_0 \right) \underbrace{-x_G \left( q^2 + r^2 \right)}_{=0} \underbrace{-y_G \left( \dot{r} - pq \right)}_{=0} \underbrace{+z_G \left( \dot{q} + pr \right)}_{=0} \right] \tag{39}$$

$$F_y = m \left[ \left( \dot{V}_0 - pW_0 + rU_0 \right) \underbrace{+x_G \left( \dot{r} + pq \right)}_{=0} \underbrace{-y_G \left( p^2 + r^2 \right)}_{=0} \underbrace{-z_G \left( \dot{p} - qr \right)}_{=0} \right] \tag{40}$$

$$F_z = m \left[ \left( \dot{W}_0 + pV_0 - qU_0 \right) \underbrace{-x_G \left( \dot{q} - pr \right)}_{=0} \underbrace{+y_G \left( \dot{p} + qr \right)}_{=0} \underbrace{-z_G \left( p^2 + q^2 \right)}_{=0} \right] \tag{41}$$

$$\begin{aligned} M_x = {} & I_{xx}\dot{p} - \left( I_{yy} - I_{zz} \right) qr \underbrace{-I_{xy} \left( \dot{q} - pr \right)}_{=0} \underbrace{-I_{yz} \left( q^2 - r^2 \right)}_{=0} \underbrace{-I_{xz} \left( \dot{r} + pq \right)}_{\approx 0} \\ & + m \left[ \underbrace{y_G \left( \dot{W}_0 + pV_0 - qU_0 \right)}_{=0} \underbrace{-z_G \left( \dot{V}_0 - pW_0 + rU_0 \right)}_{=0} \right] \end{aligned} \tag{42}$$

$$\begin{aligned} M_y = {} & I_{yy}\dot{q} - \left( I_{zz} - I_{xx} \right) pr \underbrace{-I_{xy} \left( \dot{p} + qr \right)}_{=0} \underbrace{-I_{yz} \left( \dot{r} - pq \right)}_{=0} \underbrace{-I_{xz} \left( r^2 - p^2 \right)}_{\approx 0} \\ & + m \left[ \underbrace{z_G \left( \dot{U}_0 + qW_0 - rV_0 \right)}_{=0} \underbrace{-x_G \left( \dot{W}_0 + pV_0 - qU_0 \right)}_{=0} \right] \end{aligned} \tag{43}$$

$$\begin{aligned} M_z = {} & I_{zz}\dot{r} - \left( I_{xx} - I_{yy} \right) pq \underbrace{-I_{xy} \left( p^2 - q^2 \right)}_{=0} \underbrace{-I_{yz} \left( \dot{q} + pr \right)}_{=0} \underbrace{-I_{xz} \left( \dot{p} - qr \right)}_{\approx 0} \\ & + m \left[ \underbrace{x_G \left( \dot{V}_0 - pW_0 + rU_0 \right)}_{=0} \underbrace{-y_G \left( \dot{U}_0 + qW_0 - rV_0 \right)}_{=0} \right] \end{aligned} \tag{44}$$

Terms with an under-brace are zero, if the inertia tensor $I_{ij}$ with $i = j = [x, y, z]$, has only entries at the diagonal and the ship fixed coordinate system is placed in the centre of gravity $(x_G, y_G, z_G)^T$. $U_0, V_0$ and $W_0$ are the velocity components of the origin of ship fixed frame of reference.

Solution of rigid body motion equations is done using a predictor/corrector implicit approach, shown in Wilson et al. [83].

## 2.5. Overset grids

A dynamic overset grid approach is implemented into *REX*. The computational domain consists of typically multiple block-structured grids, whose cells overlap each other. Every grid point is either marked as 'active', 'interpolated', or 'hole'. Hole points are excluded (blanked) from computations as these belong to grids which lay inside of a body, or out of the domain. Each grid with hole and active points is having interpolated points located in between these regions, where interpolation of solutions between overlapping grids takes place. The so called domain connectivity information (DCI) is re-computed at run time, as the relative grid positioning changes for arbitrary body motions. The determination of DCI is done using the code *Suggar++* (Noack et al. [59]). The overlapping region can be reduced by *Suggar++* by blanking unnecessary points, which improves computational time.

Special care needs to be taken when interpolating at the single-phase free surface. This has been further discussed in Carrica et al. [7].

The grids follow a hierarchical structure of a parent-child approach, which e.g. allows rudders to move along with the ship mounted to, while performing rotations around its axis.

The grids which have been assembled and the domain connectivity information computed for in this work are shown in chapter 5.2. Only single body simulations have been performed and no moving appendages were present.

Note that each block-structured grid, used for the grid assembly, needs to be assigned to a new processor. Reducing the number of blocks hence reduces the need of higher number of processors. Furthermore, the number of cells in each block should be a multiple of other block cell numbers. This ensures that after domain decomposition, each processor has a similar number of cells assigned to, which improves parallel computation efficiency.

## 2.6. Boundary conditions

This section briefly describes the boundary conditions, which have been applied in the numerical simulations. Table 2.1 presents an overview of the respective boundary conditions. A description, where these conditions are used, is given in chapter 5.3. The boundary condition of the level set equation at no-slip boundaries is defined with $\partial\phi/\partial n = 0$. This is under certain conditions, such as submerged walls parallel to the free surface, imprecise but especially for the geometry used within this work of minor importance and is therefore seen as an acceptable assumption.

### 2.6.1. Wave boundary condition

If waves are being investigated, they can be already initialised in the computational domain from the first iteration on. This can save computational time, especially if the computational domain is large and the propagation of waves from the inlet on would take long to pass the investigated object. In these cases, the development of the flow field and ship wave system will be quicker, than waiting for the generated waves to pass. However, it would be also possible to initialise the domain using the solution of a calm water simulation, generate the waves at the inlet and wait until the first developed waves will pass the object. The former approach has been used within this work.

In both cases, the wave properties are only given at the inlet face, by superposition of earth fixed orbital velocities and the flow velocity:

$$u_i = u_{i,inf} + u_{i,W}, \tag{45}$$

with $u_{i,inf}$ being e.g. the ship speed and $u_{i,W}$ being the orbital velocities due to the chosen wave theory. $u_{i,inf}$ is defined by vector $[\text{ufullspd}, \text{vfullspd}, \text{wfullspd}]^T$ from table 2.1. The simulations in this work consisted either of the ship at forward velocity or the ship at rest. For forward velocities, ufullspd was set to 1 and the Froude number defined the velocity. For the ship at rest, $u_{i,inf}$ was set to 0 and a fictitious Froude number of $Fr = 0.15$ was chosen to perform the simulations. Only regular waves according to linear theory have been used in this work, whose boundary conditions can be described for deep water in a non-dimensional way as follows (see Carrica et al. [8]):

$$u_W = \zeta_W \frac{\sqrt{k_W}}{Fr} e^{k_W \zeta} \cos\left( k_W \left(\xi \cos(\mu_W) - \eta \sin(\mu_W)\right) - \frac{\sqrt{k_W}}{Fr} \cdot t + \Phi \right) \cos(\mu_W) \tag{46}$$

$$v_W = -\zeta_W \frac{\sqrt{k_W}}{Fr} e^{k_W \zeta} \cos\left( k_W \left(\xi \cos(\mu_W) - \eta \sin(\mu_W)\right) - \frac{\sqrt{k_W}}{Fr} \cdot t + \Phi \right) \sin(\mu_W) \tag{47}$$

$$w_W = \zeta_W \frac{\sqrt{k_W}}{Fr} e^{k_W \zeta} \sin\left( k_W \left(\xi \cos(\mu_W) - \eta \sin(\mu_W)\right) - \frac{\sqrt{k_W}}{Fr} \cdot t + \Phi \right) \tag{48}$$

$$\tag{49}$$

$\zeta_W$ represents the wave amplitude, $\sqrt{k_W}/Fr$ the non-dimensional wave frequency using the wave number $k_W = 2\pi/\lambda_W$, $\mu_W$ is the wave direction, $\Phi$ the phase shift and $\xi$ respectively $\eta$ the horizontal coordinates.

**Table 2.1.:** Boundary conditions

| | $\phi_{ls}$ | $p$ | $k$ | $\omega$ | $u$ | $v$ | $w$ |
|---|---|---|---|---|---|---|---|
| (far) inlet | $\phi_{ls} = -z$ | $p = 0$ | $k_f = 10^{-7}$ | $\omega_f = 9$ | ufullspd | vfullspd | wfullspd |
| waves | $\phi_{ls}(t)^1$ | $p(t)^1 = 0$ | $k_f = 10^{-7}$ | $\omega_f = 9$ | $u(t)^1$ | $v(t)^1$ | $w(t)^1$ |
| exit | $\frac{\partial \phi_{ls}}{\partial n} = 0$ | $\frac{\partial p}{\partial n} = 0$ | $\frac{\partial k}{\partial n} = 0$ | $\frac{\partial \omega}{\partial n} = 0$ | $\frac{\partial^2 u}{\partial n^2} = 0$ | $\frac{\partial^2 v}{\partial n^2} = 0$ | $\frac{\partial^2 w}{\partial n^2} = 0$ |
| far-field | $\frac{\partial \phi_{ls}}{\partial n} = 0$ | $\frac{\partial p}{\partial n} = 0$ | $\frac{\partial k}{\partial n} = 0$ | $\frac{\partial \omega}{\partial n} = 0$ | $\frac{\partial u}{\partial n} = 0$ | $\frac{\partial v}{\partial n} = 0$ | $\frac{\partial w}{\partial n} = 0$ |
| very far-field | $\phi_{ls} = 0$ | $p = 0$ | $\frac{\partial k}{\partial n} = 0$ | $\frac{\partial \omega}{\partial n} = 0$ | $\frac{\partial u}{\partial n} = 0$ | $\frac{\partial v}{\partial n} = 0$ | $\frac{\partial w}{\partial n} = 0$ |
| no-slip | $\frac{\partial \phi_{ls}}{\partial n} = 0$ | - | $k = 0$ | $\omega = \frac{60}{Re\beta {y^+}^2}$ | $\frac{\partial \xi}{\partial t}$ | $\frac{\partial \eta}{\partial t}$ | $\frac{\partial \zeta}{\partial t}$ |
| no-slip (wall func.) | $\frac{\partial \phi_{ls}}{\partial n} = 0$ | - | wall func.[2] | wall func.[2] | wall func.[2] | wall func.[2] | wall func.[2] |
| zero gradient | $\frac{\partial \phi_{ls}}{\partial n} = 0$ | $\frac{\partial p}{\partial n} = 0$ | $\frac{\partial k}{\partial n} = 0$ | $\frac{\partial \omega}{\partial n} = 0$ | $\frac{\partial u}{\partial n} = 0$ | $\frac{\partial v}{\partial n} = 0$ | $\frac{\partial w}{\partial n} = 0$ |
| symmetry | $\frac{\partial \phi_{ls}}{\partial n} = 0$ | $\frac{\partial p}{\partial n} = 0$ | $\frac{\partial k}{\partial n} = 0$ | $\frac{\partial \omega}{\partial n} = 0$ | $\frac{\partial u}{\partial n} = 0$ | $v = 0$ | $\frac{\partial w}{\partial n} = 0$ |
| averaged multi-block | aver. on face | aver. on face | aver. on face | aver. on face | aver. on face | aver. on face | aver. on face |

[1] defined in chapter 2.6.1

[2] defined in chapter 2.2.1

The approach of defining superposed values from freestream velocity and orbital wave components has often been successfully applied, e.g. by Cura Hochbaum & Vogt [18], el Moctar et al. [23], or Wilson et al. [82]. An alternative approach would be to directly numerically model the deflection of the wave generator. This is only beneficial if experiments have been conducted in close proximity to the wave generator and waves were not fully developed yet, which could be reproduced within the numerical simulations.

The boundary conditions for waves are adjusted if numerical wave damping towards a freestream condition is applied, as further explained in chapter 2.8. The boundary face is then treated as without waves being present. This ensures that conditions at the boundary face and in the sponge layer are consistent.

## 2.7. Moonpool field initialisation

The initialisation of the field values within the computational domain is being done at the very beginning of the computation and can be seen as a first guess of the solution in every cell. The initial velocity is uniformly distributed and assigned in the whole grid. If waves are applied, the appropriate wave theory is being used to initially deflect the free surface. Furthermore, the pressure and orbital velocities due to waves are being addressed to every cell.

For this study, the initialisation of the field has been modified, to take account of the moonpool in a more efficient way. No modification, especially of the velocity field, would result in a momentum of the entrapped water in the moonpool. The non-zero velocity and the deflected free surface would cause a strong sloshing and also piston type motion of the entrapped water and hence strongly oscillating forces and motions, which would be damped only slowly during the subsequent time iterations. Therefore, the moonpool boundaries are prescribed in the input file for *REX* and the field values within the moonpool treated differently than for the rest of the initialised field. These modifications can be seen in figure 2.4. Figure 2.4a shows a solution after the first iteration, if the initialisation inside the moonpool is not treated differently than the rest of the domain ($u_i = u_{i,inf} + u_{i,W}, p = p_W, \phi = -\zeta + \zeta_W$). Figure 2.4b on the other hand shows the initialisation of the moonpool with $u_i = 0$, $p = 0$ and no free surface deflection ($\phi = -\zeta$), which is the flow field initialisation inside the moonpool that has been chosen for all simulations.

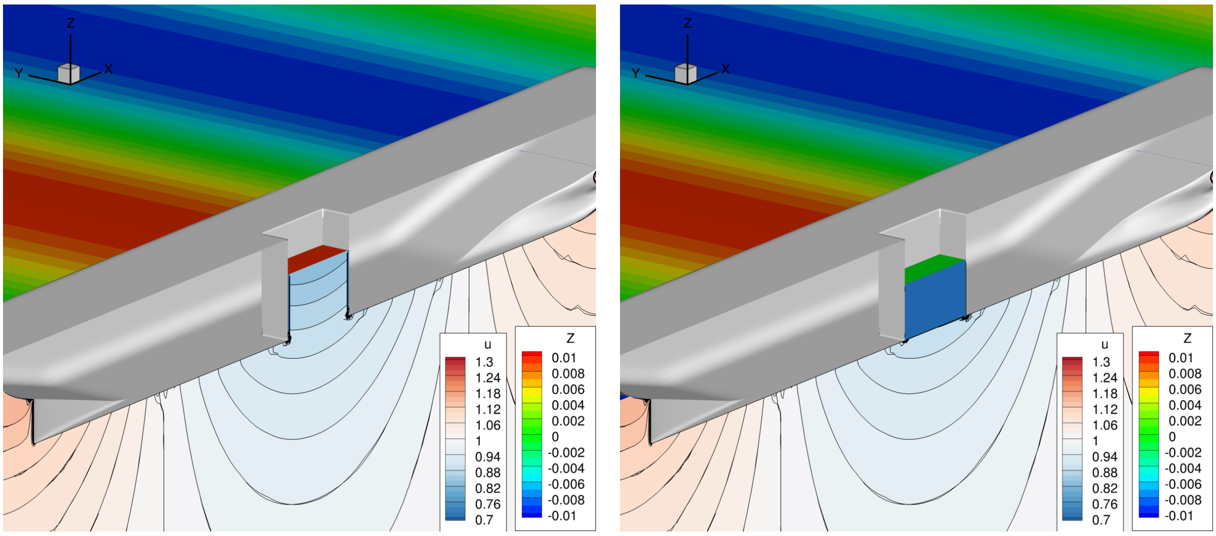


**(a)** Unmodified initialisation in the moonpool **(b)** Modified initialisation in the moonpool

**Figure 2.4.:** Different initialisation of flow field inside the moonpool

## 2.8. Wave damping

There are two areas of application, where the damping of waves should be considered in the simulations performed during this work. First, one needs to define if the solution domain is representing a finite or infinite region. Finite regions in seakeeping simulations are almost non-existent, as either the domain would need to be very large, which is due to computational reasons practically impossible, or the actual problem would need to deal in a very restricted region around the ship. The latter problem is rarely the case, if at all for manoeuvring investigations, but especially not when doing a seakeeping analysis. Therefore, although an infinite region is considered, the domain needs to be restricted to a finite domain, which results in the necessity for suitable boundary conditions. This especially applies to the inlet and outlet face of the computational domain. The wave properties regarding the free surface elevation and the orbital velocities need to be defined at the inlet face. This has been explained in chapter 2.6. Important for the stability of the simulation, but in cases of simulations with longer time durations also for the accuracy of the numerically generated wave, is the handling of the outlet boundary condition. The outlet boundary condition can be, similar to the inlet boundary condition, seen as an artificial boundary condition and hence needs to ensure, that the flow travels through the face undisturbed and unreflected. The best way to avoid reflections at the outlet and hence to avoid computational instabilities and affection of the desired wave elevation, is to ensure that the flow field at the outlet has purely horizontal components of the velocity and that the free surface elevation is zero. Therefore, the flow field needs to be modified which can be achieved with a suitable damping approach.

A second application of wave damping in the case of investigating the flow field in a moonpool is due to the strongly 3-dimensional flow within the moonpool. This causes severe vortices due to separation at the leading edge of the moonpool opening at the bottom of the ship, as well as strong surface elevations in the moonpool, even in calm water conditions. There are several approaches to circumvent or reduce especially the latter phenomenon as has been discussed in chapter 1.1. A common way is to install perforated sheets before the wall of the moonpool, causing a damping of the horizontal velocities. Modelling these perforated sheets cannot be done in a practical manner using *REX*, as this would lead to an immense increase in cells and a highly complicated grid, especially with the requirement of body-fitted block structured grids. Therefore, a suitable approach in terms of artificial boundary conditions should be applied to consider the effect of perforated sheets in a numerical manner.

### 2.8.1. Dissipation due to cell elongation

One of the most simple and also very effective ways to damp the wave field in a certain region is to smoothly expand the cell lengths in wave travelling direction. Cell elongation can be done solely in the horizontal plane or on all three dimensions. This results in numerical dissipation especially of the surface elevation, as the grid gets too coarse to further resolve waves. This strategy has e.g. been successfully applied by Cura Hocbaum & Vogt [18]. One might argue that a disadvantage is the increase of the computational domain due to the elongation of the cells. This usually only affects the size of the domain, which is in most cases not critical, rather than an increasing number of cells, which would be more difficult to justify. The approach is especially suitable for the outlet of a domain, as one is usually not interested in the flow field far behind the ship. It can however not be applied in the moonpool, as the boundary layer resolution at the walls prescribe the cell size. Attention has to be paid to the factor by which the cells are elongated, as a too rapid increase of the cell size can again lead to reflection effects. Cell elongation at the domain outlet has been used in this work for all simulations in order to achieve a good wave dissipation and hence little wave reflections.

### 2.8.2. Damping terms in the momentum equation

One solution of the radiation problem of waves is based on Sommerfeld's method [66]. Sommerfeld argued, that the radiation problem could be modified by applying a small damping term which leads in infinity to the desired radiation boundary condition. The damping could be applied by adding the terms $-du_i - \mu\frac{\partial^2 u_i}{\partial \xi_i^2}$ to the momentum equation. These terms are dependent on $u$ and the second-order derivatives with $d$ and $\mu > 0$. $\mu$ is called by Israeli & Orszag [40] a linear viscous damping coefficient and $d$ a linear 'Newton cooling' or 'friction' coefficient. It needs to be emphasised, that in this description, $d$ and $\mu$ are constants and not depended on the coordinates $\xi_i$.

This leads to a continuous damping of the desired term. The problem with this approach is that the damping term needs to be small enough to ensure the accuracy of the desired wave field at the area of interest. This however results in the necessity for a very large domain, to ensure that the wave is being damped effectively towards the outlet. Israeli and Orszag [40] stated that in this way more than 99% of the computational domain is wasted outside the area of interest, which makes it highly ineffective.

### 2.8.3. Sponge layers

The general idea of sponge layers are based on Chan's [12] method and have been primarily introduced by this name in Israeli & Orszag [40]. The main idea is that the above mentioned terms $d$ and $\mu$ are allowed to vary with $\xi_i$. This enables that damping terms can be set to zero in the area of interest, to ensure a non-affected computation and non-zero within the sponge layer to apply an efficient damping towards the outlet. If the damping term is changed abruptly, severe reflections will be caused. Having a constant damping term across the sponge layer hence requires a small term. Israeli and Orszag [40] stated that choosing a constant $\mu$ and $d$ in the sponge layer leads to a minimum width of the sponge layer of 15 wave lengths to ensure a reflection coefficient of 1%. This is a significant improvement compared to the steady damping mentioned above, but still requires an undesirable large size of the domain for the damping.

It is therefore necessary to vary the magnitude of the damping terms within the sponge layer to allow higher damping terms. This is achieved by using the distance function $\alpha$, which is zero at the beginning of the sponge layer and one at the end. Multiplication of the damping constant $c$ with $\alpha$ leads to a gradually increasing damping term $d$ in the sponge layer. The 'Newton cooling' damping term is more dissipative than the 'viscous damping'. Hence, only the damping term $d(\xi_i)$ is considered in the further investigations. Israeli & Orszag suggested a damping term with a potential distance function, which has been extended in this work to the choice of a cosine distance function:

$$0 \leq \xi_i < \xi_{i,\text{start}} \qquad d(\xi_i) = 0 \tag{50}$$

$$\xi_{i,\text{start}} \leq \xi_i \leq \xi_{i,\text{end}} \begin{cases} d(\xi_i) = c \cdot \overbrace{(n+1) \cdot \dfrac{(\xi_i - \xi_{i,\text{start}})^n}{(\xi_{i,\text{end}} - \xi_{i,\text{start}})^n}}^{\text{potential distance function}} \\ d(\xi_i) = c \cdot \underbrace{\cos\left[\dfrac{\pi}{2}\left(\dfrac{\xi_i - \xi_{i,\text{start}}}{\xi_{i,\text{end}} - \xi_{i,\text{start}}} + 1\right)\right]^2}_{\text{cosine distance function}} \end{cases} \tag{51}$$

$\xi_{i,\text{start}}$ is the beginning of the sponge layer, $\xi_{i,\text{end}}$ the end, $n$ the order of the distance function and $c$ is the damping constant, defining the total magnitude of $d$. The order $n$ can be chosen e.g. between $n = 1, \ldots, 4$, which leads to the distance functions shown in figure 2.5. Note that $d$ is a function of the horizontal directions $\xi$ and $\eta$, whereas it remains constant within a given zone in vertical direction $\zeta$. A time dependence is usually not necessary, but may be required if the grid inside the sponge layer changes. The chosen

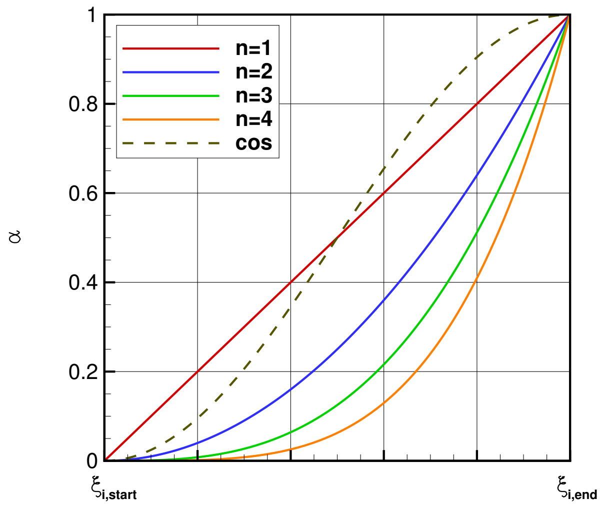


**Figure 2.5.:** Distance functions for different orders $n$

potential description of $d$ has the advantage that the integral over the length of the sponge layer equals the damping constant $c$ for all $n$

$$\int_{\xi_{i,\text{start}}}^{\xi_{i,\text{end}}} d(\xi_i) d\xi_i = c. \tag{52}$$

Hence, the same damping strength dependent on $c$ is applied for every choice of order equivalently.

Israeli and Orszag have shown that, using this method, the reflection of waves can be reduced significantly (in general by less than 5%) for sponge layer lengths up to one wave length at a damping constant of $c = 1$ or slightly higher. Smaller sponge layer lengths lead to more reflections of approximately 25% or less.

The approach of Israeli and Orszag has been implemented into *REX*. The source term which is applied to the momentum equation consists of a multiplication of the damping term $d$ and the respective velocity difference between the 'actual' velocity $u_i$ and the 'desired' velocity $u_{i,\mathrm{target}}$. The term $u_i$ contains all velocity contributions such as the flow velocity, orbital velocities of the waves and grid velocity. The desired velocity can be zero, which would be the case when applying the approach in the moonpool, or a velocity field such as freestream or orbital velocities, when applying at the domain outlet. When choosing the freestream velocity as target velocity, all orbital wave velocity components will be dissipated. Using the superposed freestream and orbital wave velocity as target velocity leads to a conservation of the undisturbed wave. Undesired velocities will be dissipated following this approach. Undesired velocities are deviations of the target/desired velocity. The momentum equation is then modified in the following manner:

$$\frac{Du_i}{Dt} = -\frac{\partial p}{\partial \xi_i} + \frac{\partial}{\partial \xi_j}\left[\frac{1}{Re_{\mathrm{eff}}}\left(\frac{\partial u_i}{\partial \xi_j} + \frac{\partial u_j}{\partial \xi_i}\right)\right] + s_i \boldsymbol{- d(\xi, \eta, \zeta, t)\,(u_i - u_{i,\mathrm{target}})} \tag{53}$$

$D/Dt$ is representing the material derivative. Note that due to the non-dimensional description of equations within *REX*, the damping constant of unit [1/s] is made non-dimensional using $c' = c \cdot L_{\mathrm{ref}}/u_{\mathrm{ref}}$.

It should be mentioned that only velocities are being damped. No modification of the level set approach to damp the wave elevation is applied.

Furthermore, the damping terms are treated implicitly. This is achieved, by splitting the damping term and adding $d(\xi_i)$ to the diagonal of the algebraic system of equation and subtracting $d(\xi_i)\,(-u_{i,\mathrm{target}})$ from the source terms.

A visualisation of the sponge layers for the outlet and moonpool can be seen in figure 2.6. The achieved results of this damping approach are discussed in chapter 2.8.6.

### 2.8.4. Analytical far field solution

Another approach to treat wave damping has been described in detail by Jacobsen et al. [42]. The idea is very similar to the above mentioned sponge layer approach with the difference that no modification of the momentum equation is being done in a direct manner. Sponge layers are defined where the computational solution ('$\phi_{\mathrm{computed}}$') of the

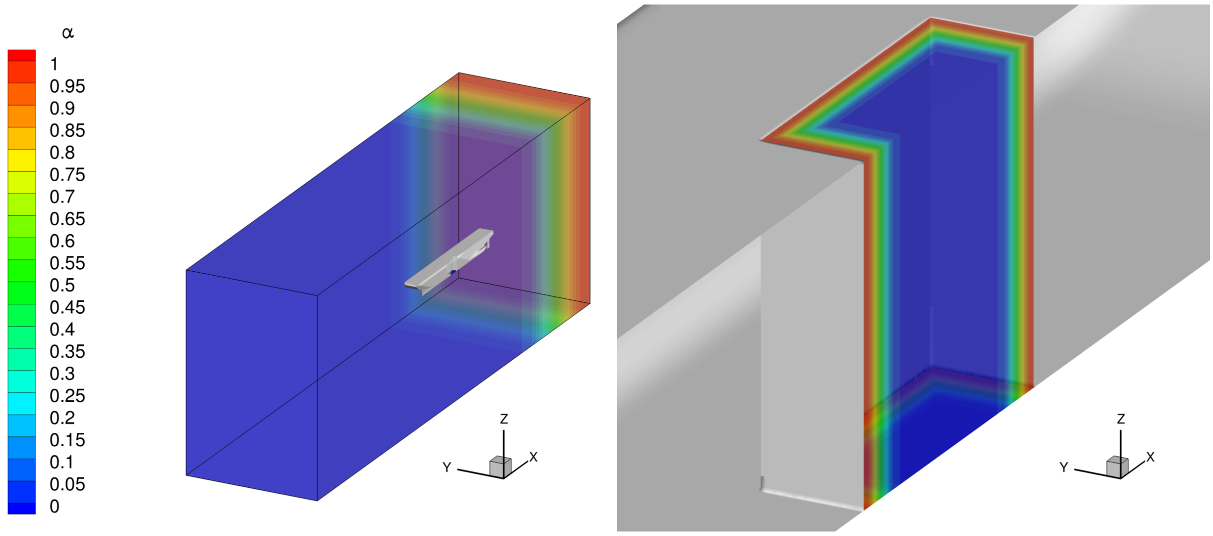


**(a)** Visualisation of the distance function at the domain outlet

**(b)** Visualisation of the distance function in the moonpool

**Figure 2.6.:** Different applications of sponge layers for the wave damping

velocities and phase elevation are mixed with the analytical solution ('$\phi_{\text{target}}$'), determined by the appropriate wave theories. This is being shown in eq. (54). The mixing is being done using the distance function $\alpha$ to avoid a rapid change in the solution and hence improve the stability of the computation.

$$\phi = (1 - \alpha)\,\phi_{target} + \alpha \cdot \phi_{computed} \tag{54}$$

The generation and absorption of waves for harmonic and natural waves has e.g. been investigated on ship hydrodynamical aspects by Löhrmann & Cura Hochbaum [52] using the flow solver OpenFoam-2.3.0. Good results have been achieved using this method and solver for incoming waves. A similar approach has been implemented into *REX*, but was not successful as the damping of waves happened too fast in space, causing artificial reflections. Therefore, the original approach of Israeli & Orszag has been used for all further simulations.

## 2.8.5. Reflection coefficient

To determine the effectiveness of damping waves through the above mentioned methods, it is necessary to define a suitable criteria for the reflection. It is almost impossible to damp all of the generated waves. The effectiveness of the damping respectively the amount of reflection is characterised through the reflection coefficient $R$, which is defined as

$$R = \frac{\zeta_R}{\zeta_I}, \tag{55}$$

with $\zeta_R$ being the amplitude of the reflected waves and $\zeta_I$ the amplitude of the initial waves. It is therefore necessary to determine these two amplitudes from the time signals of one or more probes. There are a number of different methods for this purpose, which will be discussed in the following.

**Regular waves**

The easiest way of determining the reflection coefficient is, when only regular waves are considered. The reflection of a regular wave results in an envelop of superposed waves, namely the incident wave travelling in the forward direction and the reflected wave travelling in the opposite direction as shown in equation (56) and (57).

$$\zeta_I(\xi, t) = \zeta_I \cdot \cos\left(k_W \xi - \omega_W t + \Phi_I\right) \tag{56}$$

$$\zeta_R(\xi, t) = \zeta_R \cdot \cos\left(k_W \xi + \omega_W t + \Phi_R\right) \tag{57}$$

$\xi$ is the coordinate, $\omega_W$ the circular wave frequency, $t$ the time and $\Phi_I$ and $\Phi_R$ are the phase angles of the incident and reflected wave respectively. Superposition of these waves can simply be expressed as:

$$\zeta(\xi, t) = \zeta_I(\xi, t) + \zeta_R(\xi, t), \tag{58}$$

which forms an envelope such as exemplary shown in figure 2.7. It can be seen, that the envelop has a maximum and minimum amplitude respectively height, named $H_{max}$ and $H_{min}$. This can be explained by the superposition and distinguishing of the amplitudes, depending on the phase shift of the two travelling waves. Hence $H_{max}$ respectively $H_{min}$ can be expressed as:

$$H_{max} = 2 \cdot (\zeta_I + \zeta_R) \tag{59}$$

$$H_{min} = 2 \cdot (\zeta_I - \zeta_R) \tag{60}$$

and the reflection coefficient results in:

$$R = \frac{\zeta_R}{\zeta_I} = \frac{H_{max} - H_{min}}{H_{max} + H_{min}}. \tag{61}$$

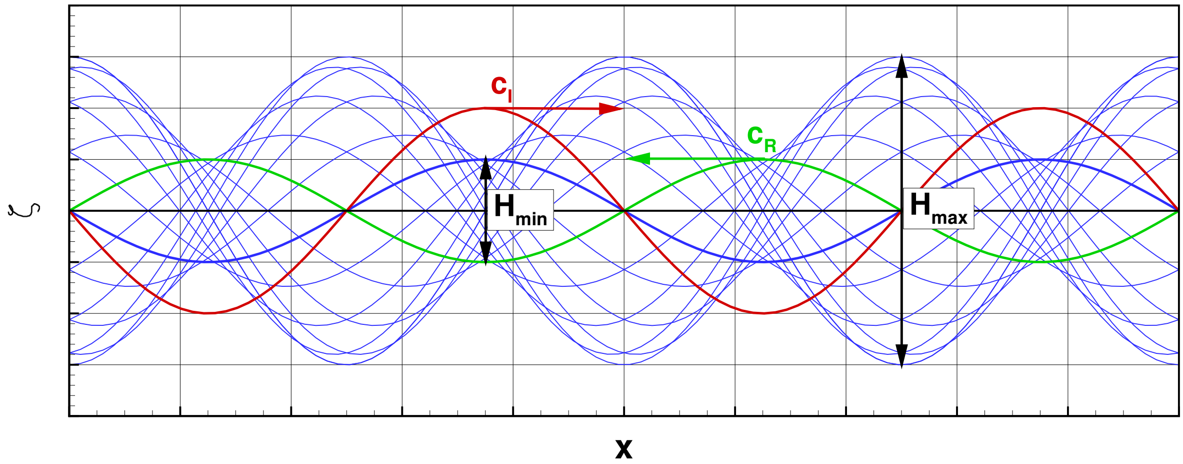


**Figure 2.7.:** Incident wave with amplitude $\zeta_I = 1$ in red and a reflected wave of amplitude $\zeta_R = 0.5$ in green resulting in a envelope of the superposed wave in blue

Note that a regular wave, which is reflected and travels in the opposite direction can be re-reflected where it has been generated. The re-reflected wave is now propagating forward again and hence forms a new initial wave which is a superposition of the generated wave and the re-reflected wave. Hence it is important to distinguish between reflected and multi-reflected waves.

### 2-point-method

When having an irregular wave to be analysed, more complex approaches need to be applied. Such methods have been introduced by Thornton & Calhoun [74] or Goda & Suzuki [35], where the latter used a Fast-Fourier-Transformation to determine the incident and reflected spectra. The wave elevation is measured at two probes of known positions which are in line with the direction of wave propagation. The basic principle is similar to the above mentioned approach

The main assumption is, that irregular waves are linear superpositions of a discrete number of regular wave components, propagating at their own frequency, amplitude and random phase. The phase velocity is described by the dispersion relation. Equation (58) applies here in the same way, only that equation (56) and (57) are rewritten for an irregular wave having $j$ harmonical components

$$\zeta_I(\xi,t) = \sum_{j=1}^{N} \left[\zeta_{I,j}\cos(k_{W,j}\xi - \omega_{W,j}t + \Phi_{I,j})\right] \tag{62}$$

$$\zeta_R(\xi,t) = \sum_{j=1}^{N} \left[\zeta_{R,j}\cos(k_{W,j}\xi + \omega_{W,j}t + \Phi_{R,j})\right]. \tag{63}$$

The signal at two wave probes is Fourier analysed and their respective coefficients can be used to describe the energy spectra of the initial and reflected waves $E_I(\omega_W)$ and $E_R(\omega_W)$. The energy spectra is derived from integration of the respective amplitude spectra $S_I$ and $S_R$ over the frequency range. Derivation of the respective energy spectra from the Fourier coefficients is shown in detail in appendix A.1. Setting the spectra into relation, the overall reflection coefficient $R$ can be expressed to be:

$$R = \sqrt{\frac{E_R}{E_I}}. \tag{64}$$

The frequency range for a given probe spacing is recommended as:

$$f_{min} = \Delta x/\lambda_{max} = 0.05 \tag{65}$$

$$f_{max} = \Delta x/\lambda_{min} = 0.45 \tag{66}$$

The method is sensitive to errors due to:

1. Transversal waves and other disturbances
2. The interaction of incident and reflected waves, which can cause non-linearities and are not covered by the linear approach.
3. Non-linear harmonic terms which do not apply to the general dispersion relation $\omega_W^2 = k_W g \tanh(k_W h)$, with $h$ being the water depth.
4. Signal noise or other measurement errors.

**3-point-method**

To overcome some of the uncertainties with the 2-point-method, Mansard & Funke [53] proposed using a least squares method, based on analysing three or more probes and minimising the error to determine the incident and reflected spectra. A detailed derivation of the 3-point-method is shown in appendix A.2.

The following probe spacings are recommended for this method:

$$\xi_{12} = \lambda_W/10 \tag{67}$$

$$\lambda_W/6 < \xi_{13} < \lambda_W/3 \quad \text{and} \quad \xi_{13} \neq \lambda_W/5 \quad \text{and} \quad \xi_{13} \neq 3\lambda_W/10 \tag{68}$$

Compared to the 2-point-method, the 3-point-method provides a broader range of frequencies due to fewer critical probe spacings and less sensitivity due to noise signals and other discrepancies as mentioned above.

The working principle is shown in figure 2.8, where the method has been tested for an analytical solution. Five harmonic wave components with different frequencies, amplitudes and reflecting amplitudes (upper left picture) are composing an irregular wave train at three different probes (upper right picture). All three signals are being Fourier transformed (lower left picture) and using the relationship mentioned in the appendix, the initial amplitudes, reflected amplitudes and the reflection coefficients are determined (lower right picture). The initial and reflected amplitudes, as well as the reflection coefficients and their respective errors compared to the input signal are given in table 2.2. It can be seen, that the method is able to determine accurately all the desired values out of a random irregular signal.

**Table 2.2.:** Results from the 3-point-method

| | Input | | | Output | | | |
|---|---|---|---|---|---|---|---|
| f [Hz] | $\zeta_I$ | $\zeta_R$ | R | $\zeta_I$ | $\zeta_R$ | R | $1-\Delta R$ [%] |
| 0.2 | 0.200 | 0.0200 | 0.100 | 0.198 | 0.0197 | 0.0993 | 99.3 |
| 0.5 | 1.000 | 0.4850 | 0.485 | 1.000 | 0.4850 | 0.4850 | 100 |
| 1.3 | 0.400 | 0.1000 | 0.250 | 0.399 | 0.0998 | 0.2500 | 100 |
| 2.0 | 0.300 | 0.0375 | 0.125 | 0.300 | 0.0372 | 0.1240 | 99.2 |
| 3.0 | 0.100 | 0.0075 | 0.075 | 0.100 | 0.0074 | 0.0735 | 98.0 |

### Problems with the 2-point-method / 3-point-method

Comparing the accuracy of the results from the 2-point-method and the 3-point-method, only minor differences can be detected for the irregular signal used in figure 2.8. Nevertheless, due to its nature, the 2-point-method can only examine a much smaller bandwidth of frequency compared to the 3-point-method, as has been mentioned before. This however very much depends on the chosen probe spacing.

It has to be noted, that the results in table 2.2 have been reached using an irregular

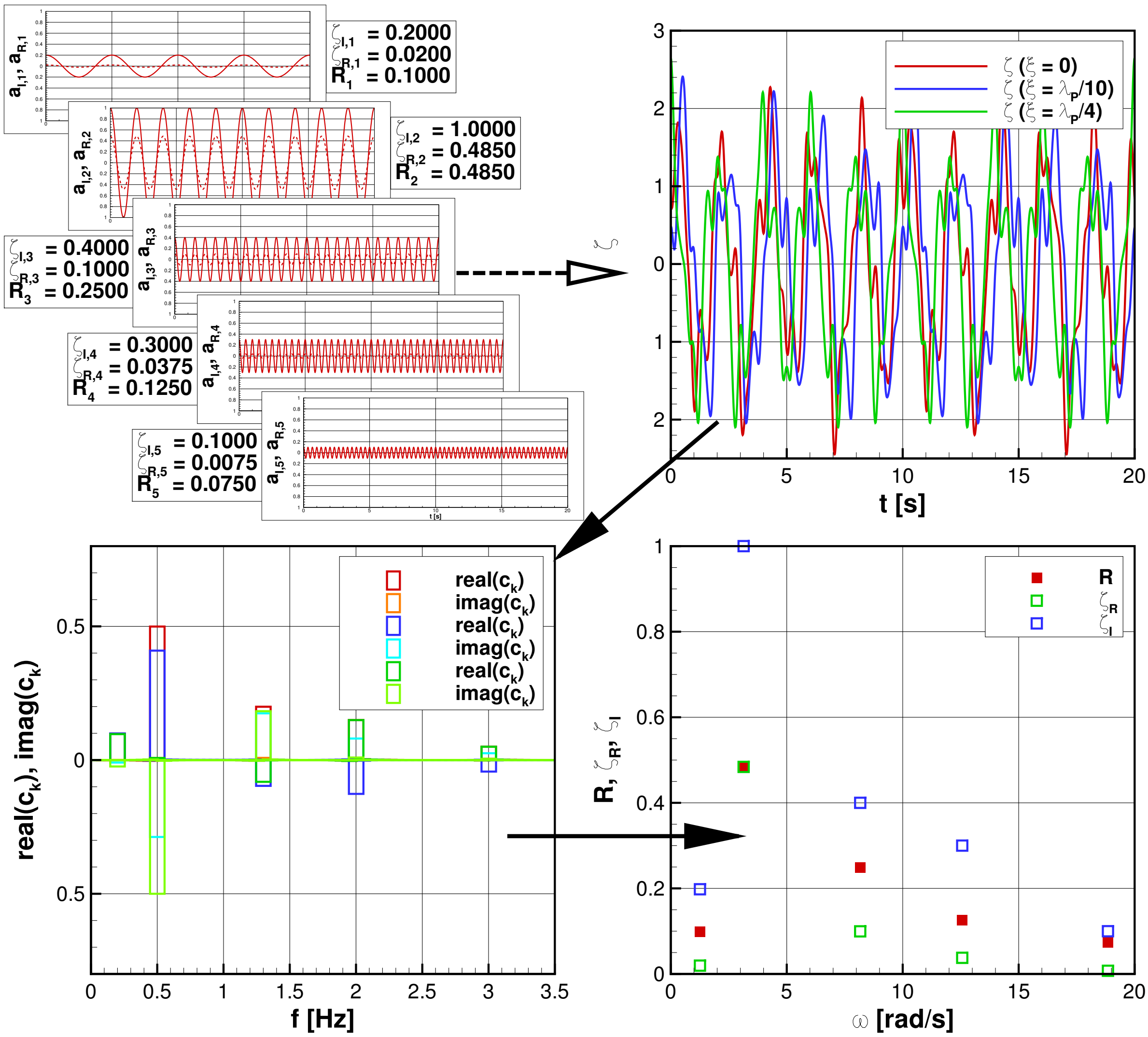


**Figure 2.8.:** Working principle of the 3-point-method

signal, which is periodically over the examined time frame. This is ideal for the Fourier transformation and yields accurate results with errors of less than 2.5%. When using the same signal, but setting the boundaries of the signal to be non-periodic, the results become much less reliable, as can be seen in figure 2.9, where the reflection coefficients have been determined with the same signal from figure 2.8, but cut of at 19.6s. The reflection coefficients from the fully periodic signal are shown in grey. When focusing on the known frequencies (indicated in figure 2.9 with dashed lines), the deviation of the determined amplitudes and reflection coefficients is acceptable compared to the periodic signal. Only the lowest and highest frequencies show larger deviations. Nevertheless, for unknown signals and hence unknown main frequencies, this result cannot be seen as satisfying. Reason for the inaccuracy is the side lobe leakage, which can be seen when comparing the Fourier transform of figure 2.9 and 2.8. Circumvention of this effect would be necessary to achieve acceptable results. Solutions for this might be e.g. window averaging, which smooths the spectra but comes at cost of a reduced resolution. In general, smoothing should be applied with caution, which has also been stated by Riekert [61].

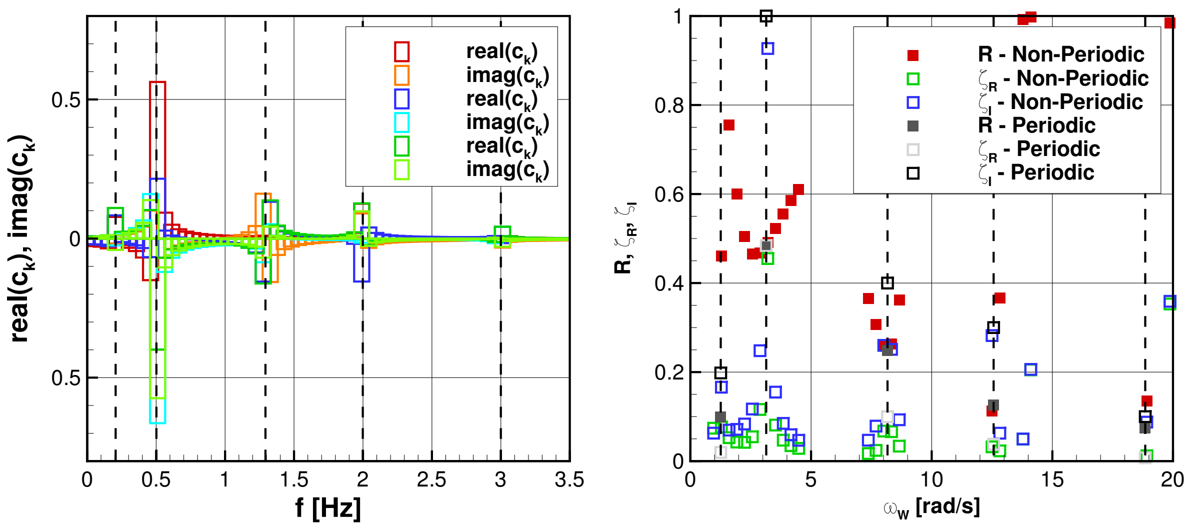


**Figure 2.9.:** Results of 3-point-method for non-periodic signal

### Comparison of energies

A third method is introduced which is much less detailed as the previously mentioned methods, but can give an indication of the reflection, once the other methods fail. The biggest problem of the above mentioned 2-point/3-point-methods is seen to be the error source due to side lobe leakage when using non-periodic signals.

Therefore, a simpler method has been introduced, which determines the energy of a wave train according to its elevation by

$$E_{actual}(t) = \int_{\xi}\int_{\eta} \zeta_{actual}^2 d\xi d\eta, \tag{69}$$

where $\zeta_{actual}$ describes the measured elevation in the x-y-plane and corresponds to $\zeta_{actual} = \zeta_I + \zeta_R$. This can be compared against the target energy $E_{target}$ corresponding to $\zeta_I$ and a reflection coefficient can be determined:

$$E_{target}(t) = \int_{\xi}\int_{\eta} \zeta_I^2 d\xi d\eta \tag{70}$$

$$R(t) = \sqrt{\frac{E_{actual}(t)}{E_{target}(t)}} - 1. \tag{71}$$

Note that to get the correct energy, equation (69) and (70) would need to be multiplied with $(1/2\rho \cdot g)$, which can be left away, due to comparison of both equations in (71). The result is a, depending on the number of periods within the considered plane, fluctuating energy $E_{actual}$ and $E_{target}$ as well as a hence fluctuating reflection coefficient $R$ over time. A good indication of the reflection coefficient is the maximum value of $R$ over time, once the first reflecting waves arrived fully within the considered plane.

A differentiation of initial and reflected amplitude for different frequencies is not possible with this method. Furthermore, the reflection coefficient cannot be assigned to individual frequencies. It has to be noted as well that for the determination of the reflection coefficient, an ideal target wave is assumed to calculate $E_{target}$. This method cannot distinguish if the actual measured initial amplitude deviates from the desired target amplitude, which can have an influence on the accuracy of the reflection coefficient.

### 2.8.6. Results of the implemented wave damping approach

Within this section, the implemented method of sponge layers into the flow solver is verified using suitable methods for determining the reflection coefficient. Therefore, a matrix with variations of damping constant $c$, length of the sponge layer $L_{SL}$ and different distance functions using a cosine function or the exponential functions recommended by Israeli & Orszag [40] with different orders $n$ has been simulated. Simulations were conducted in a numerical wave flume with generation of waves on one side and a solid wall on the opposite site. Conservation of energy requires that the reflected wave amplitude is of the same height as the initial wave amplitude if no damping is applied and no

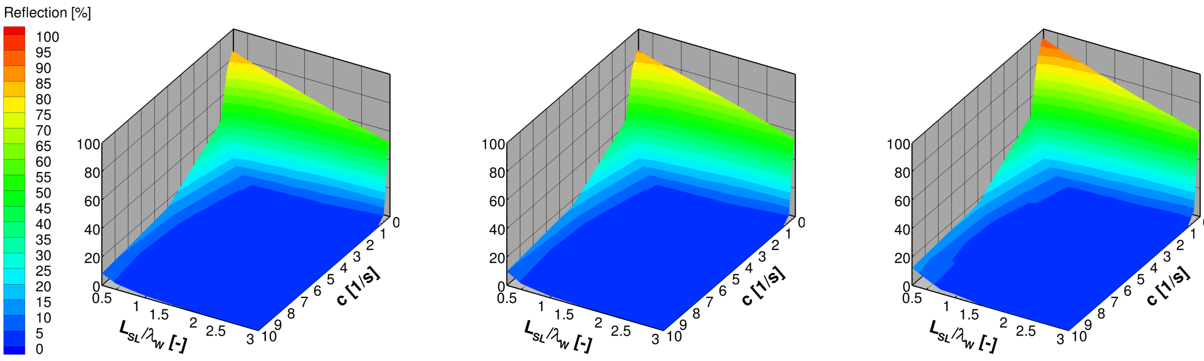


**(a)** 3-point-method **(b)** 2-point-method **(c)** Comparison of energies

**Figure 2.10.:** Reflection depending on $c$ and $L_{SL}/\lambda$ for cosine weighting function

dissipation takes place. Note that this investigation only focused on damping the waves towards a zero amplitude, as this is required when using the damping approach inside the moonpool. The option of damping the waves towards an undisturbed wave elevation has been implemented at the end of this work and hence was not included into this test matrix.

Before discussing the results of this matrix, the chosen method to determine the reflection coefficient needs to be explained. As already mentioned, the 3-point-method should be the most accurate one and being preferred over the 2-point-method and the comparison of energies. Caution needs to be taken though, when applying the method to the respective signal, due to inaccuracies because of side lobe leakage. Applying this method generally provides good results. Nevertheless, problematic are the resulting reflection coefficients at low frequencies, as will be shown later. The same applies to the 2-point-method. Despite being the simplest and less detailed method, the comparison of energies provides plausible results, which coincide well with the observations. Figure 2.10 shows the interrelations between the damping constant $c$ and the non-dimensional sponge layer length $L_{SL}/\lambda_W$ for the cosine distance function and for all three methods. The following damping constants have been investigated:

$$c = 0.1, 0.5, 1, 5, 10 \tag{72}$$

It can be seen, that all three methods yield similar results. Especially the 2-point method and 3-point-method only differ in details. The largest difference is observed when comparing the peak of the reflection coefficient of the 2 and 3-point-method with the comparison of energies. The ideal reflection of 100% is almost reached using the comparison of energies, whereas the 2 and 3-point-method only reach about 86%. The value of the reflection coefficient for high reflections is strongly dependent on the lower boundary of the frequency range. For this investigation $\omega_{W,min}$ was set to $2\,\mathrm{rad\,s^{-1}}$. For higher reflections, the lower frequencies contribute significant initial and reflected amplitudes to the spectrum and hence to the overall reflection coefficient, when integrating the amplitude spectra over the frequency range. A comparison of the result for low reflection and high reflection is shown in figure 2.11. It can be seen, that for the case with low reflection (left figure), reflection is correctly determined at the initial frequency, indicated by the dashed line. For the case with higher reflection (right figure) significant reflection coefficients are predicted at low frequencies. Furthermore, reflection also occurs in the neighbouring frequencies of the initial frequency (dashed line). The latter is to some extend plausible, as the reflection phenomena can likely lead to a transfer of its energy to neighbouring frequencies, whereas reflection at low frequencies seems less plausible. Also note that reflection coefficients higher than 1 are being determined, which is implausible.

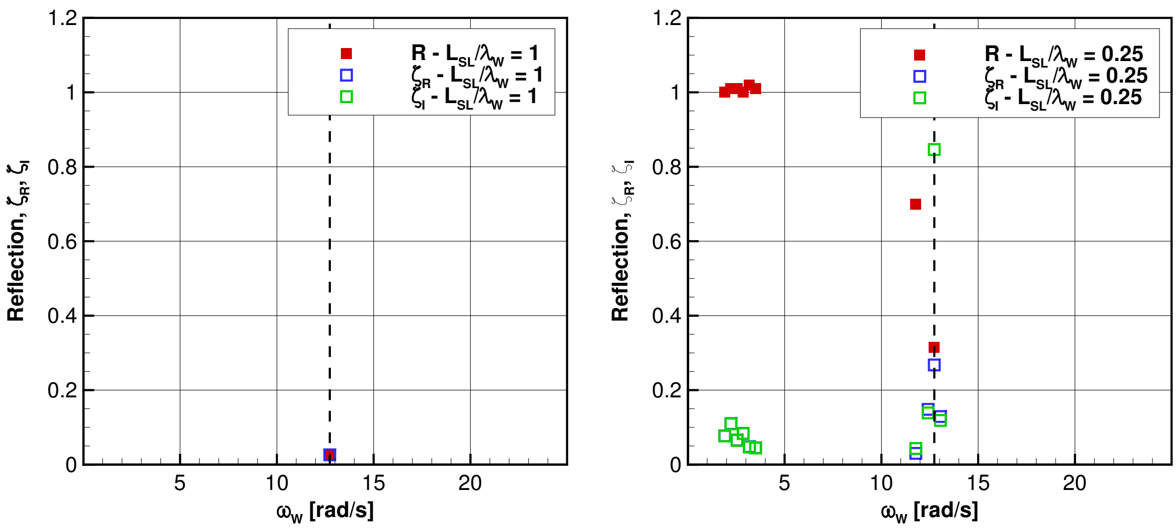


**Figure 2.11.:** Results of 3-point-method for different sponge layer lengths

Due to these uncertainties, the comparison of energies is used for the determination of reflection coefficients. Although this method yields an integrated value and does not distinguish between different frequencies nor distinguishes between an initial and reflected amplitude, results are more plausible for all cases and corresponds well with observations.

It can be seen from figure 2.10, that a damping constant of 5 seems to be ideal to

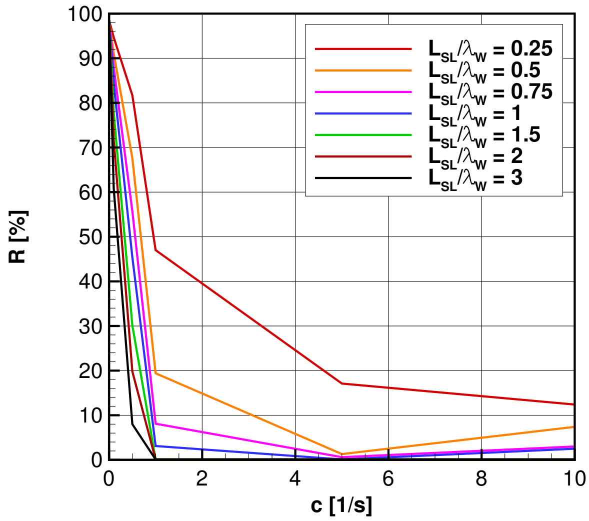


**(a)** Reflection depending on $c$ and $L_{SL}/\lambda_W$ for the cosine distance function

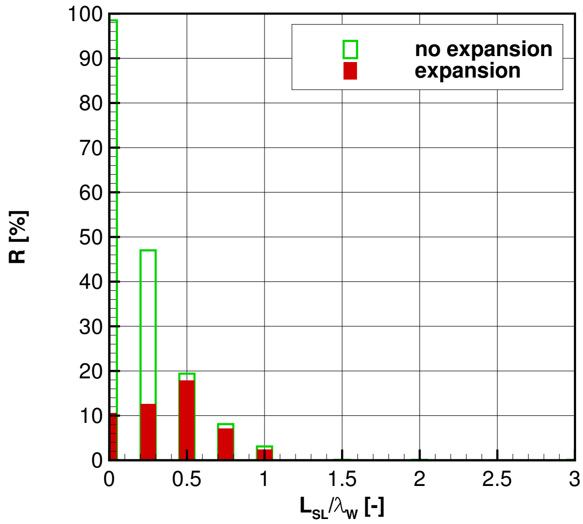


**(b)** Reflection for a combined damping approach using expanded cell lengths and sponge layers of different lengths with a damping constant of $c = 1/\mathrm{s}$

**Figure 2.12.:** Reflection depending on $c$ and sponge layer length for the cosine distance function

damp almost any wave length. Smaller damping constants especially smaller than 1 are less effective and lead to partially severe reflections. Damping constants larger than 5 are still effective, although the reflection can increase again for some wave lengths. This can be seen more clearly in figure 2.12a where the reflection for a damping constant of 10 increases for the cases $L_{SL}/\lambda_W = 0.5, 0.75$ and 1 compared to the next smaller damping constant of 5.

Looking at the length of the sponge layer, a general trend can be seen. The longer the sponge layer, the fewer reflections occur. One wave length seems to be the minimum length of the sponge layer, to damp the waves in an efficient way. If the length becomes shorter, the momentum equations are changed rapidly over space and the solution would need to be changed radically. Hence, waves are only damped partially and reflected more severely for short sponge layer lengths. Longer sponge layers than 1.5 wave lengths seem to be not necessary, as the reflection is already at a minimum. The results regarding the minimum damping constant $c$ and minimum length of the sponge layer agrees very well with the results from Israeli & Orszag [40].

For these investigations, the length of the cells in $\xi$-direction (direction of wave travelling) has been kept constant. Therefore sponge layers longer than 1.5 wave lengths would lead to an unnecessary high amount of grid cells.

An investigation of a combined damping approach using expanded grid cells and sponge layers has been conducted additionally. The grid, which has been used for the previous study has been modified, such that the cell length in wave travelling direction at the outlet was expanded. The expansion factor was set to 1.2 and the expansion started one wave length before the outlet. The influence of this expansion for different sponge layer lengths has been compared to the results of the non-expanded grid and is shown in figure 2.12b.

When expanding the cell lengths, the reflection can be significantly reduced, especially in combination with only short sponge layer lengths. Interestingly, the reflection increases slightly for sponge layer lengths of $L_{SL}/\lambda_W = 0.25$ & $0.5$, compared to no sponge layer ($L_{SL}/\lambda_W = 0$ in figure 2.12b). It needs to be emphasised, that the combined damping approach is obviously only possible at e.g. an outlet of a domain, which is not a solid wall. It can therefore not be used in the moonpool.

# 3. Description of ship & moonpool characteristics

This chapter is describing the difficulty in defining the characteristic of moonpool flows and presents suitable measures, which have been used within this work. Also, non-dimensional parameters such as forces or motions are defined, which will be used later on.

## 3.1. Vortex identification

The disturbance of the flow field within the moonpool is greatly influenced by separation at the leading edge of the moonpool, creating vortices which are deflected at the backward wall. These vortices are highly 3-dimensional and travel through the moonpool creating deformation of the free surface, as well as velocity gradients in the flow field of the moonpool, which can be disadvantageous when lifting equipment. Therefore, the mathematical definition of vortices and suitable visualisation of the flow field within the moonpool needs to be defined.

Although all relevant variables like velocities, pressure and turbulence parameters are known through the computation using a RANS code, the definition of vortical structures remains in the interpretation of the user. In general the understanding of a vortex in this case is the rotation of a fluid around a centre. This however does not define the strength of the vortex, neither the beginning nor end of a vortical structure. As the investigated flow is turbulent in all areas of interest, there will be numerous small vortices depending on the scale of which vortices are resolved.

Numerous methods have been established to describe vortical structures such as the $\Delta$- (Chong et al. [13]), $\lambda_2$- (Jeong and Hussain [43]), or $Q$-criterion (Hunt et al. [37]). The latter has been used for vortex visualisation within this work and is therefore briefly explained in the following section. General description of vortex identification methods can e.g. be found in Kolář [45], Haller [36] or Zhou et al.[87].

All mentioned methods to identify a vortex are based on the definition of the velocity gradient tensor with $\vec{v}$ being the velocity vector

$$\nabla\vec{v} = S + \Omega, \tag{73}$$

which can be decomposed into a symmetric and skew-symmetric part.

$$S = \frac{1}{2}\left[\nabla\vec{v} + (\nabla\vec{v})^T\right] \tag{74}$$

$$\Omega = \frac{1}{2}\left[\nabla\vec{v} - (\nabla\vec{v})^T\right]. \tag{75}$$

$S$ is called the rate-of strain tensor and $\Omega$ the vorticity tensor.

The $Q$-criterion has first been introduced by Hunt et al. [37] and defines a vortex if the second invariant of $\nabla\vec{v}$ is positive, meaning the vorticity magnitude dominating over the rate-of-strain magnitude. Hence eq. (76) forms the first requirement of the existence of a vortex.

$$Q = \frac{1}{2}\left[||\Omega||^2 - ||S||^2\right] > 0, \tag{76}$$

This description uses the definition of the norm of any tensor $G$, which is defined by $||G|| = \left[tr\left(GG^T\right)\right]^{1/2}$. A second assumption is, that the pressure in the vortex needs to be smaller than the ambient pressure, which ensures that if the flow is rotational, the streamlines are curved (Hunt et al. [37]). In this way, straight shear-layers can be excluded from the solution. The isosurfaces of $Q$ can then be used to visualise the vortex. A suitable magnitude of $Q$ which provides a good visualisation of the main vortical structures needs to be found by the user. $Q = 100$ has been used in this work for all isosurfaces, as can e.g. be seen in figure 2.2. Note that this procedure can only be applied to numerical simulations where the exact flow field is known. It is unfortunately not suitable for experiments, due to lack of informations on the flow field.

## 3.2. Moonpool water column oscillation

In order to describe the oscillation inside the moonpool, the free surface has been measured at three locations. These locations are denoted with index 'WG1-3'. As will be further explained in chapter 6.1.1, each moonpool has its own natural frequency at which it might oscillate. These can be of piston type, denoted with index '0' or of sloshing type, denoted with index 'm'. Furthermore, if the ship is exposed to waves, their respective wave frequencies, denoted with index 'W', can define the oscillation. For each frequency, a respective amplitude can be assigned. It varies a lot, which amplitude is dominating or if they are of equal size. It can be already mentioned that the amplitude corresponding to the sloshing frequency was by far the smallest, if even present. Hence, the wave gauge signal mainly consisted of a natural piston mode frequency and if present of a wave frequency

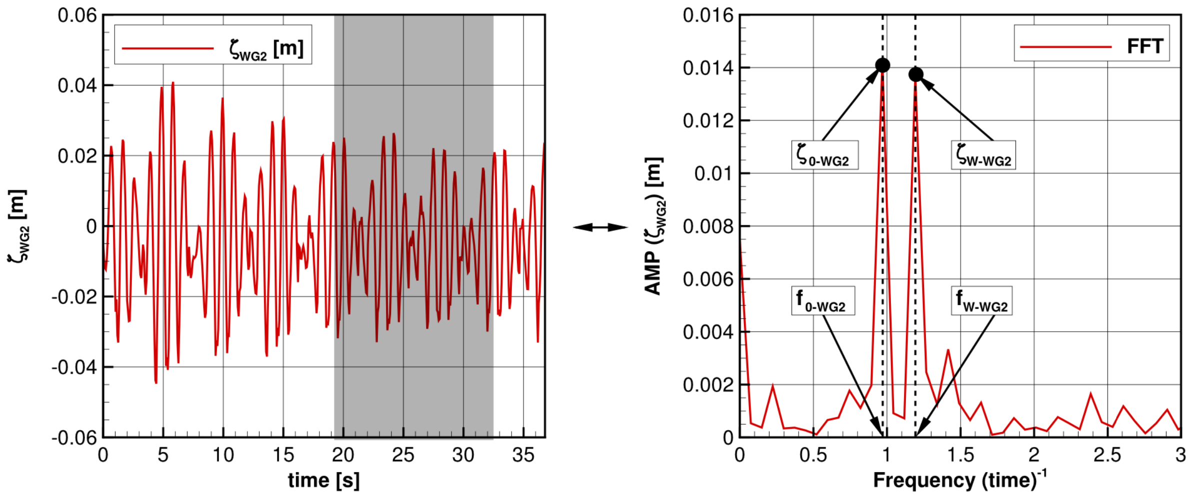


**Figure 3.1.:** Determination of mean oscillation amplitudes from Fourier analysis

and their respective amplitudes. Figure 3.1 shows on the left side the signal of the free surface elevation for WG2 ($\zeta_{WG2}$) for an exemplary simulation in waves at forward speed 'RW075_0_015_MD' (refer to chapter 4.5 for case name denotion). This signal is then cut into a periodic one, shown in the shaded area and then Fourier transformed. This results in the right figure, where two pronounced amplitudes are visible. One corresponds to the known wave frequency and the other to the piston mode frequency, which can be estimated using e.g. the method proposed by Molin [56]. All three wave gauge signals are processed in this manner and a mean amplitude $\zeta_{0-WG}$ respectively $\zeta_{W-WG}$ determined by averaging the amplitudes of the three wave gauges. The respective frequencies at all three wave gauges are identical. This procedure can be applied to experiments and numerical simulations equally, therefore providing a good comparability.

## 3.3. Moonpool forces

The numerical simulations have been performed in such a way that hydrodynamic forces on ship and moonpool surfaces where determined separately. An example is shown in figure 3.2, where the longitudinal force component is plotted for the moonpool (green line) and the hull (red line). The left figure shows a calm water case, where the force amplitude on moonpool surfaces is relatively large, compared to an almost steady force on the hull. Note that the force oscillation on the hull stems from an interaction with the moonpool water column oscillation. The right figure shows the same moonpool geometry and Froude number, but in regular waves of $\lambda_W/L_{PP} = 0.5$ and $\mu_W = 0°$. The force amplitude on

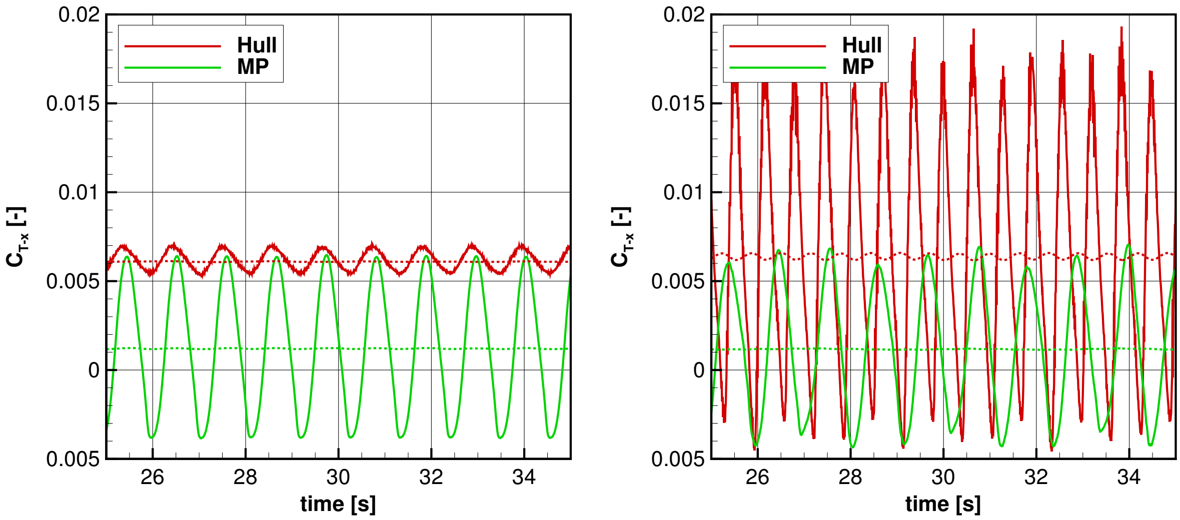


**(a)** Calm water case for moonpool 'MP' at $Fr = 0.15$

**(b)** Regular wave of $\lambda_W/L_{PP} = 0.5$ at $Fr = 0.15$ for moonpool 'MP'

**Figure 3.2.:** Total longitudinal hydrodynamic force components on hull an moonpool surfaces separately

the moonpool remains similar, while the force amplitude on the hull increases drastically due to the presence of waves. Note that both figures show the moving average in the respective coloured dashed lines. The moving average of the calm water case has been averaged once with the piston mode period and the case with regular waves twice (using the piston mode period and wave period), as will be further explained in chapter 6.1.5. The same procedure of determining forces individually has been used in chapter 6.1.7 to examine forces on the lid, when the moonpool has been closed at the free surface. Again this procedure is only applicable to numerical simulations and could not be used for experiments.

## 3.4. Definition of dimensionless parameters

This chapter contains a brief overview of dimensionless coefficients, which will be used when analysing the results of experiments and numerical simulations. All parameters starting with a $C$ or having a $'$ attached to it are made dimensionless. Other parameters refer to the dimensional form.

### 3.4.1. Forces & moments

Forces are usually given as mean values, determined over full periods, which might be defined by piston motion frequencies, wave frequencies, or a combination of both. The latter case can lead to ambiguous signals which might be difficult to cut properly, in order to create a periodic time series. A Fourier analysis can help to understand which frequencies are contained in the time signal and what source they are related to. Further description of treatment of forces, especially referring to experimentally measured forces, is given in chapter 4.3.2.

All forces $F_{i,j}$ (for calm water and waves) are made dimensionless using the dynamic pressure and static wetted surface $S_w$ of the ship (varying slightly with the moonpool geometry).

$$C_{i,j} = \frac{F_{i,j}}{\rho/2u_{ref}^2 S_w}, \tag{77}$$

with $i = T, F, P$ for total, frictional and pressure resistance and $j = x, y, z$ representing the coordinate direction. Index $j$ is often skipped for investigations of calm water or head seas, as transverse and vertical forces are not of interest for these cases.

Yaw moment is made dimensionless using the squared wave amplitude $\zeta_W^2$ and characteristic length $L_{ref}^2$.

$$C_{m,z} = \frac{M_{T,z}}{\rho g \zeta_w^2 \cdot L_{ref}^2} \tag{78}$$

Others moments have not been analysed within this work.

### 3.4.2. Ship motions

Motions of the ship have been analysed similarly as described in section 3.2. The time series of the ship motions where periodically cut, Fourier transformed and the dominant amplitude of the respective degrees of freedom determined. Although an amplitude at piston mode frequency existed in some degrees of freedom, the dominant amplitude has usually been found at the wave frequency and is therefore shown.

Translational motions of the ship are made dimensionless using response amplitude operators (RAO), which relates the response with the wave amplitude $\zeta_W$.

$$RAO(j_{AMP}) = \frac{j_{AMP}}{\zeta_W}, \tag{79}$$

with $_{AMP}$ referring to the motion amplitude, determined by Fourier analysis and $j = x, y, z$. Rotational motions are always shown in degrees.

### 3.4.3. Moonpool oscillations

Moonpool oscillation amplitudes $\zeta_{WG}$ are either shown in dimensional form or in non-dimensional form using the RAO again:

$$RAO(\zeta_{WG}) = \frac{\zeta_{WG}}{\zeta_W}, \tag{80}$$

Otherwise, they are given in dimensional form in metre and refer to the model scale.

If frequencies are shown in a non-dimensional form, relation of $u_{ref}$ and $L_{ref}$ is used:

$$f' = f \cdot \frac{L_{ref}}{u_{ref}} \tag{81}$$

Mostly, frequencies are given however in dimensional form in Hertz and correspond to model scale.

# 4. Experiments

Experiments have been conducted for a ship model in order to validate the numerical simulations. The experiments also allowed a larger test matrix, e.g. a variation of ship speed in waves. These results would not have been possible to determine numerically, in an acceptable amount of time. This chapter contains a description of all experimental facilities used, the respective measurement techniques including their individual characteristics, the ship model and its outfitting, as well as initial tests to determine the model characteristics. Results of the experiments are shown, together with the results of numerical simulations, in chapter 6.

## 4.1. Experimental facility

All experiments have been conducted at the facilities of the Technical University of Berlin, operated by the Department of Dynamics of Maritime Systems.

The major part of the experiments has been conducted at the shallow water basin. The basin main dimensions and the wave generator capabilities are listed in table 4.1. The

**Table 4.1.:** Shallow water basin main characteristics

| Basin | | |
|---|---|---|
| Length | 120 | m |
| Breadth | 8 | m |
| Depth | 0.2 - 1.1 | m |
| **Wave Generator** | | |
| Wave length | 0.4 - 20.0 | m |
| Wave height | 0.05 - 0.30 | m |
| Piston or flap type | | |

water depth has been kept constant at 1.0 m for all experiments and the electrical wave generator was set up to piston mode. The wave generator consists of three single flaps, placed next to each other and which are running synchronously, producing long crested waves of regular or irregular type. Only regular waves have been investigated in this work, in order to simplify the understanding of the effects inside the moonpool. The carriage is equipped with all necessary measuring equipment and reaches velocities of up to $4\,\mathrm{m\,s^{-1}}$.

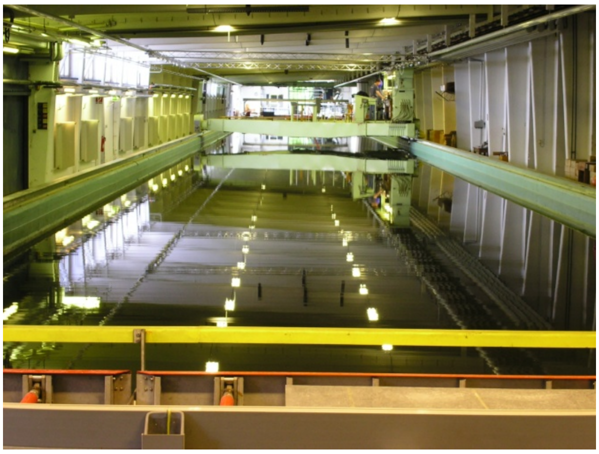

(a) Seakeeping basin

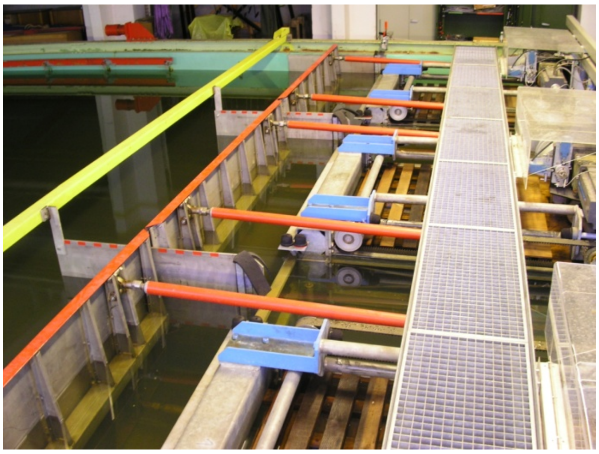

(b) wave generator

**Figure 4.1.:** Seakeeping basin (left) and wave generator (right)

The measuring platform, which is attached to the carriage, will be described in detail in chapter 4.3. The carriage is running with pneumatic tires on T-beams.

There are two drawbacks which come along with the shallow water facility. The first is the water depth which can be set at most to $h_{basin} = 1.1$ m. This implies that wave lengths of more than 2.2 m will have shallow water effects, as the ratio for deep water waves of $h_{basin}/\lambda_W > 0.5$ will be violated. The ship model had a length of 3 m and relative wave lengths between $\lambda_W/L_{PP} = 0.5 - 1.25$ were investigated. Hence, only the shortest wave has been a purely deep water wave. The wave with a ratio of $\lambda_W/L_{PP} = 0.75$ was right on the edge to transitional water characteristics and the two longest waves of $\lambda_W/L_{PP} = 1.0$ and 1.25 had more pronounced shallow water effects. The major effect is that the wave frequency is slightly shifted, compared to deep water waves of the same wave length.

The second drawback is due to the construction of the carriage using pneumatic tires and T-beams as well as the control system. This results in slightly non-constant carriage velocities and vibrations, especially at low speed. Hence, comparison of time series for low speeds is more difficult, but does not have a major effect when investigating mean values.

Some experiments have been conducted in the deep water towing tank, which is collaboratively used by several departments of the TU Berlin. This basin has a more modern towing carriage and control mechanism and is significantly longer (250 m) and deeper (4.5 m) which improves the testing conditions for calm water. The tank has been used for experiments with all degrees of freedom restricted, as will be discussed in chapter 6.1.3. However, no wave generator exists in this towing tank, which is why the shallow water basin has mainly been used. Furthermore, the newly developed measuring device to determine motions and mean forces simultaneously, which will be further explained in chapter 4.3, currently only exists in the shallow water basin.

## 4.2. Ship model

The investigated ship geometry has been specifically designed for this purpose and does not represent an existing ship. The hull is designed to allow for a simple construction and building of the model. The ship model has been designed to consist of as little three-dimensionally curved surfaces as possible, as no milling machine has been available for the manufacturing process. The ship is shaped similar to a barge with a moonpool at the centre. A forefoot at the bow of the ship, a stern bulb with a propeller shaft, and a spade rudder with a rudder dome are rigidly attached to the hull. Construction took place at the facilities of the Department of Dynamics of Maritime Systems. The bare hull is build out of a wooden framework and planked with wooden plates. The edges have been manually shaped. The radii (especially of the bilge keel) have been carefully reviewed using template plates. Although much effort has been done to build the model as accurately as possible, one has to bear in mind that this procedure causes more geometry deviations than high fidelity milling machines. The forefoot, stern bulb and rudder, which contain significant three-dimensional surfaces, have been manufactured using a 3-axis milling machine and connected to the bare hull. One deviation from the computer model geometry is that the spade rudder and rudder dome are separated in the numerical model, while they are joined in the experimental model. This however should not cause significant differences in the respective results.

A sand strip turbulence stimulator has been placed at the bow, according to the ITTC recommendations [38], which can be seen on figure 4.2c. Note that the original (yellow) coating caused some problems, which is why the model has been grinded and recoated, as can be seen on figures 4.2b-4.2c.

The full scale and model scale dimensions are listed in table 4.2. The dimensions resemble a drill ships main dimension.

### 4.2.1. Moonpool dimensions for experimental investigations

Several different moonpools have been investigated in this work and will be described in this section. Moonpool variation is done to investigate their characteristics and the dependence on geometrical parameters. The idea of the experimental model was to allow for

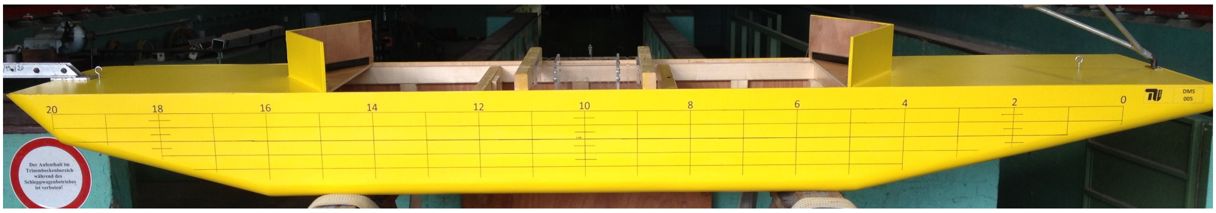


**(a)** Ship model (with original coating) without forefoot, sternbulb, rudder and rudder dome

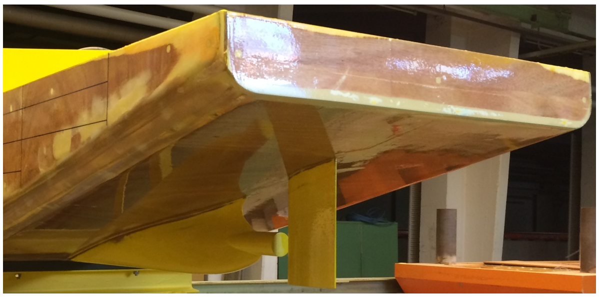

**(b)** Sternbulb and rudder

**(c)** Forefoot and sand strip

**Figure 4.2.:** Ship model

investigation of different moonpool geometries. This was accomplished by rigidly placing a relatively large moonpool in the ship model, which will be called 'outer-moonpool' if combined with an insertion. When investigating e.g. different moonpol dimensions, insertions with the respective dimensions can be mounted inside the outer-moonpool. These insertions define the new moonpool geometry. Both, the outer-moonpool, as well as the insertions have been made of plexiglass in order to ensure a high visibility.

There are in general two types of experiments, which have been conducted. One is experiments without any damping device and the other with a damping device mounted (perforated bulkheads in case of this work). The different setups of these two type of experiments is discussed in the following.

If no damping device was investigated but different moonpool sizes, insertions with a closed wall were placed inside the outer-moonpool. As can be seen exemplary in figure 4.3, these insertions have a bottom which not only reduces the moonpool dimensions but also the moonpool opening at the keel. The insertions can be mounted from top. As the edge between the insertion and the ship model has not been sealed in each individual setup, water was able to flow between the closed wall of the insertion and outer-moonpool wall. This had no effect other than a slightly different displacement. The flow inside the moonpool was not affected due to the trapped water.

If damping was to be investigated, one of the insertions in figure 4.3 were placed inside the outer-moonpool, as is shown in figure 4.3d. In this case the water was able to flow through the wall of the insertion into the damping chamber which leads to a damping

**Table 4.2.:** Main dimensions of full scale and model scale

| | | Full scale | Model scale | Unit |
|---|---|---|---|---|
| Scale | $\lambda$ | 1 | 65 | – |
| Length over all | $L_{OA}$ | 221.00 | 3.400 | m |
| Length betw. perp. | $L_{PP}$ | 195.00 | 3.000 | m |
| Breadth waterline | $B_{WL}$ | 42.25 | 0.650 | m |
| Draught | $T$ | 11.05 | 0.170 | m |
| Height | $H$ | 20.00 | 0.308 | m |
| Block coef. | $C_B$ | 0.758 | 0.758 | – |
| Displacement | $V$ | 70,659 | 0.251 | $m^3$ |
| Static wetted surface ('MP') | $S_w$ | 12,372 | 2.928 | $m^2$ |
| Metacentre above keel | $\overline{KM}$ | 23.90 | 0.368 | m |
| Metacentric height | $\overline{GM}$ | 7.50 | 0.115 | m |
| Centre of gravity above keel | $\overline{KG}$ | 16.40 | 0.252 | m |
| Long. centre of gravity from FP | $LCG$ | 95.53 | 1.470 | m |
| Long. gyradii | $k_{xx}$ | 18.73 | 0.288 | m |
| Transv. gyradii | $k_{yy}$ | 49.46 | 0.761 | m |
| Vertical gyradii | $k_{zz}$ | 49.46 | 0.761 | m |
| Density | $\rho$ | 1,025 | 999.1 | $kg\,m^{-3}$ |
| Viscosity | $\nu$ | $1.19 \cdot 10^{-6}$ | $1.14 \cdot 10^{-6}$ | $m^2\,s^{-1}$ |
| Design speed | $v$ | 12.25 | 1.58 | kn |
| Design Froude number | $Fr$ | 0.15 | 0.15 | – |
| Design Reynolds number | $Re$ | $1.076 \cdot 10^9$ | $2.144 \cdot 10^6$ | – |

effect, as has been explained in chapter 1.1.1. These insertions are in the following denoted by two numbers, characterising the porosity and dimension. The first two digits represent the porosity of the perforated bulkhead in percent, while the last two digits represent the reduction of length and breadth of the original moonpool size. Table 4.3 contains an overview of the three insertions. The dimension of the full scale moonpool has been chosen according to an average value of existing drillships, listed in van't Veer & Tholen [80].

Note that additionally to the moonpool dimensions investigated in the experiments, two more moonpool geometries were investigated in the numerical simulations. These had a variation of length to beam ratio. This ratio was constant in the experiments and had a value of $l_{mp}/b_{mp} = 1.59$.

Each moonpool configuration was investigated in the experiments using a camera, which visually recorded the oscillation behaviour through the plexiglass. A set of horizontal lines with a distance of 4 cm upwards and downwards, starting at the calm water line, is used to visually detect the surface elevation. Accurate measurement of the water oscillation has been done using three wave gauges, which are placed identically in each moonpool

**Table 4.3.:** Main dimensions of moonpools in the experiments

| | | Model scale | Porosity | | | Model scale | Porosity |
|---|---|---|---|---|---|---|---|
| MP | $l_{mp}$ | 0.300 m | - | 40-40 | $l_{opening}$ | 0.180 m | 40% |
| | $b_{mp}$ | 0.189 m | | | $b_{opening}$ | 0.113 m | |
| MD | $l_{mp}$ | 0.240 m | - | 60-40 | $l_{opening}$ | 0.180 m | 60% |
| | $b_{mp}$ | 0.151 m | | | $b_{opening}$ | 0.113 m | |
| SD | $l_{mp}$ | 0.180 m | - | 60-20 | $l_{opening}$ | 0.240 m | 60% |
| | $b_{mp}$ | 0.113 m | | | $b_{opening}$ | 0.151 m | |

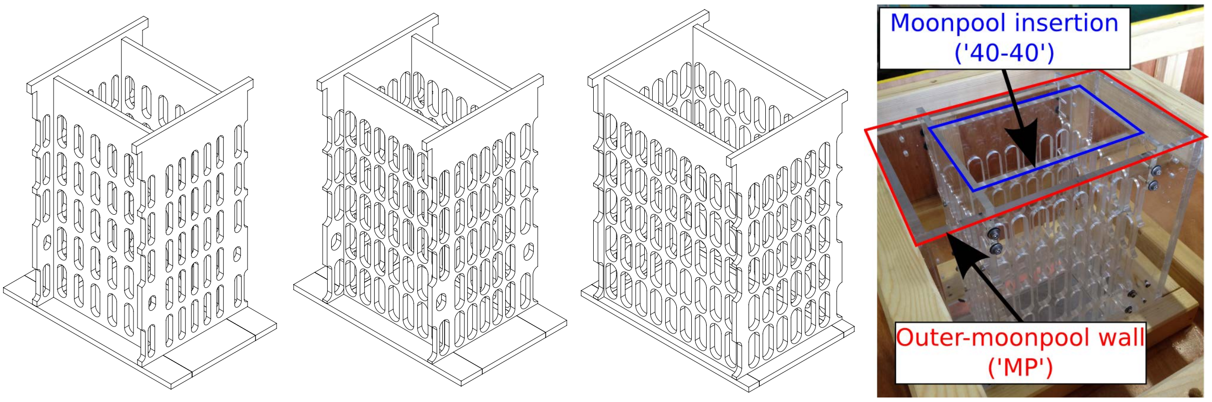


**(a)** 40-40 **(b)** 60-40 **(c)** 60-20 **(d)** Insertion mounted

**Figure 4.3.:** Different moonpool insertions

configuration. Wave gauge # 2 (further described by index 'WG2') is placed at the longitudinal and transversal centre of the moonpool opening. 'WG1' is placed 4.5 cm upstream and 'WG3' downstream. Note that the wave gauges were always placed along the longitudinal ship direction and not in wave direction in case of quartering or beam seas. Identical measurement points have been chosen in the numerical simulations.

## 4.3. Measuring device

The measuring device which is used in this work to determine forces and motions has been developed at the TU Berlin and is described in full detail in Cura Hochbaum et al. [17] and Cura Hochbaum & Lengwinat [16]. The general idea of this device was to simultaneously measure forces and motions with high accuracy, while avoiding restrictions in free motion of the model. To achieve this, a platform has been constructed consisting of two individually moving $\Delta y$-slides, two $\Delta x$-slides which are nested in the $\Delta y$-slides and two heave rods. The slides are running on semi open linear ball bearings and are connected to springs. The heave rods are running in closed linear bearings, which are mounted to the front and aft $\Delta x$-slide. The construction view of the platform can be seen in figure 4.4. The $\Delta y$-slides are highlighted in blue, $\Delta x$-slides in green and the heave rods in orange.

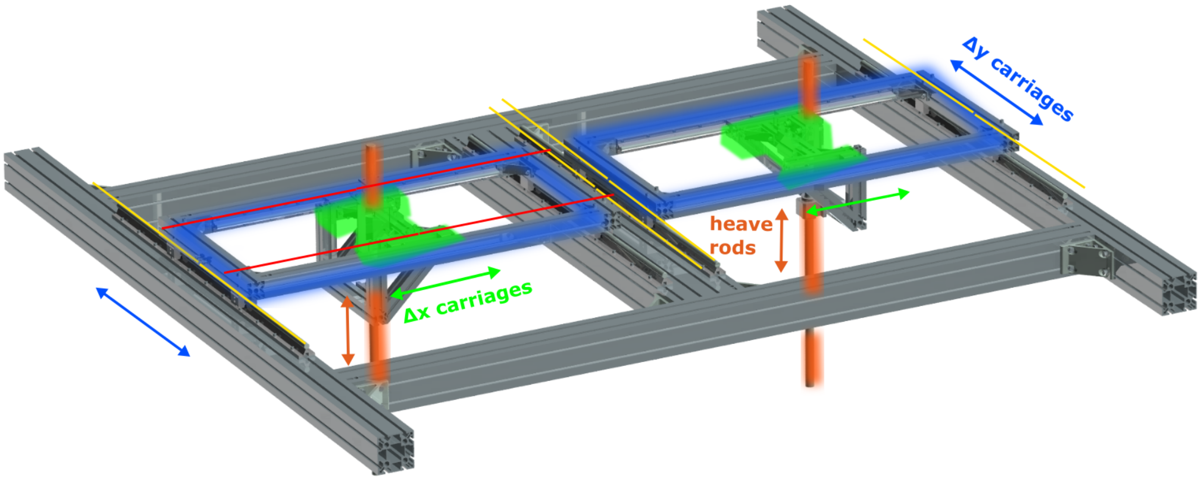


**Figure 4.4.:** Construction view of measuring platform (Cura Hochbaum & Lengwinat [16])

The model is connected to the heave rods through rod ends, allowing free pitch and roll motion as illustrated in figure 4.5. Below each rod end, a force gauge is placed, which measures the forces at each connection in the ship fixed frame of reference. Due to the construction, the ship is able to move freely in roll, pitch and heave, while surge, sway and yaw are allowed to move in a certain manner and are only restricted through the springs. The springs are marked in yellow and red respectively in figure 4.4. Several different spring rates have been tested to determine their influence on the ship model, which is further discussed in chapter 4.3.1. The maximum amplitude of the slides and rods is approximately 0.2 m.

Theoretically, this construction ensures a free motion in every degree of freedom and therefore an unrestricted point of rotation. Nevertheless, it is advised to place the rod end to the vertical centre of gravity, as has been done in this work, or better to the mean roll axis. The latter however is only an estimation, as there exists no (fixed) roll axis.

If oblique waves are to be investigated, the measuring platform can be rotated manually, which causes a static yaw angle. If the carriage velocity is not equal zero, the drift angle of the ship would coincide with the wave inclining angle.

The coordinate system is visualised in figure 4.5. The origin is placed in the centre of gravity (COG). The origin of coordinates of the numerical simulations is placed at the forward perpendicular, but motions are determined for the centre of gravity and hence coinciding with the system shown in figure 4.5. The wave heading $\mu_W$ is defined as 0° for head seas, 90° for waves coming from starboard and 180° for following seas.

The approach using a spring system on slides mimics to a certain degree real conditions with a self-propelled and self-controlled ship. The main reason for using this system is however the accurate determination of mean forces, moments as well as motions, which would be partly at least very complicated to determine for a self-propelled ship. Behaviour in surge motion with a propelled model can be approximated with springs. Decreasing ship speed would lead to an increase in advance ratio $J$ and hence an increase in thrust coefficient which can be seen as a comparable behaviour as an increase in spring force in longitudinal direction. This does not apply for the spring force in transversal direction when encountering beam or quartering seas. The spring system keeps the ship model on course, while in real conditions the ship would keep course through a static drift angle by rudder steering. This situation is hence less comparable. It should be however noted that this simplification is expected to be of negligible importance for determining moonpool characteristics. A propulsion system would have significantly complicated building the model and was hence disregarded, although numerical simulation with e.g. a simple body-force model for the propeller would have been feasible. Furthermore, although controller options for the rudder would have been available in the flow solver, the experimental setup with a self-controlled model would have been to complicated for the purpose. To make a comparison between experimental and numerical simulations, the spring system is also used in the numerics. The exact same spring coefficients in surge, sway and yaw motion direction are applied in both methods. There are however two simplifications within the numerical spring system. First, the additional mass of the slides has not been taken account for. As shown in Cura Hochbaum et al. [17], this affects the amplitude of forces in time series but not the magnitude of the mean force. As mainly mean forces are compared in the following, this simplification can hence be seen as justifiable. Second, the exact point of acting force through the springs was treated differently. The springs act in the experimental measuring device at the rod ends. The numerical spring forces are subtracted from the integral force of the respective directions and hence act in the hydrodynamic force application point. This could cause a difference in yaw moment, which should be kept in mind. However, the influence of this uncertainty is assumed to be negligible.

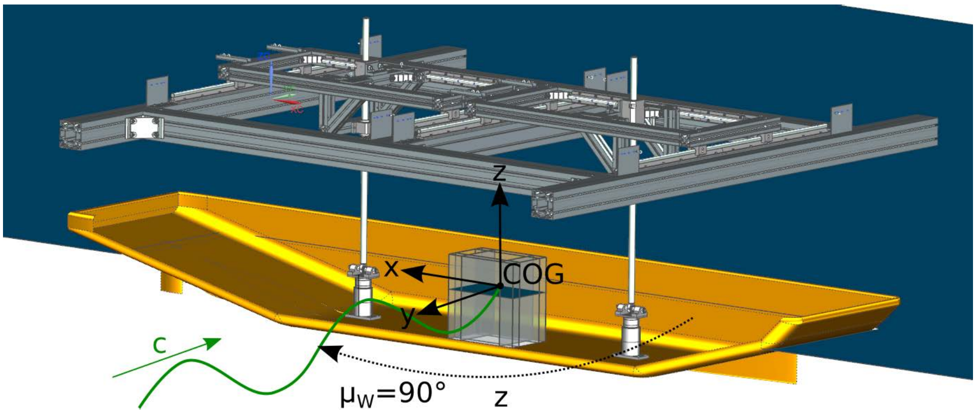


**Figure 4.5.:** Orientation of coordinate system

### 4.3.1. Motion determination

The motion of the model is determined using in total 10 cable actuated distance sensors. Although less sensors would be sufficient to determine the motion, the arrangement was chosen such that the cables are acting symmetrically on the slides, respectively the model and hence minimising artificial forces respectively moments. A sketch of the placed sensors is shown in figure 4.6. Two sensors are placed opposed to each other on the aft $\Delta x$-slide in longitudinal direction (W1 & W2) as well as on each $\Delta y$-slide in transversal direction (W3 - W6). Furthermore, four sensors mounted on the $\Delta x$-slides are connected to the ship model in vertical direction (W7 - W10). Three of these sensors are needed to determine heave, roll and pitch and the fourth is used to achieve a symmetric acting of forces induced through the cables, albeit being small.

It is now required to determine the ship fixed motion through these sets of distance sensors. A detailed description can be found in Cura Hochbaum, Uharek & Lengwinat [17] and Cura Hochbaum & Lengwinat [16] but will be briefly explained in the following.

The position of the aft rod end is chosen as reference point $P$. W1 can be used to directly determine $\Delta\xi_P$ and W3 for $\Delta\eta_P$, both in an inertial frame of reference. The yaw angle $\psi$ directly follows from W3 & W5 and the known distance between both heave rods.

The remaining degrees of freedom roll, pitch and heave are determined by using three of the vertical distance sensors W7 - W10. The length $S_i$ of each distance sensor can be defined using the known earth fixed coordinates of the start points (index $_S$) and earth fixed coordinates of the end points (index $_E$), which can be derived from the known ship

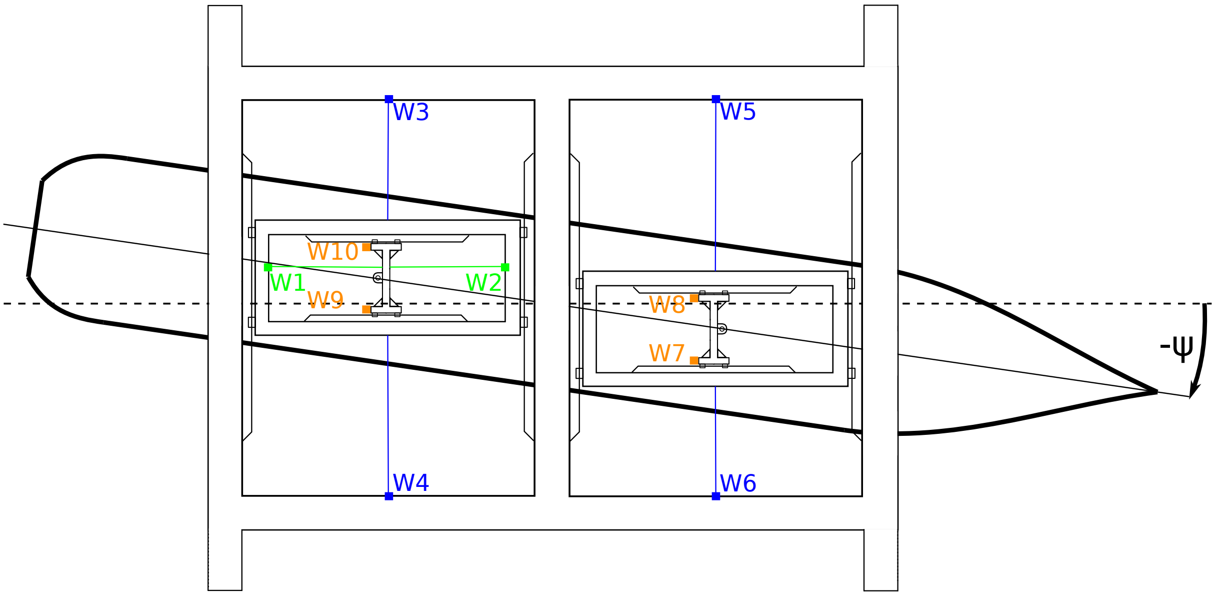


**Figure 4.6.:** Drawing of distance sensors on the measuring platform

fixed coordinates of the end points using the transformation matrix $T$ (equation (83)).

$$S_i = |\vec{\xi}_E - \vec{\xi}_S| = \sqrt{(\xi_{Ei} - \xi_{Si})^2 + (\eta_{Ei} - \eta_{Si})^2 + (\zeta_{Ei} - \zeta_{Si})^2} \tag{82}$$

$$\begin{pmatrix} \xi_{E,i} \\ \eta_{E,i} \\ \zeta_{E,i} \end{pmatrix} = \begin{pmatrix} \xi_0 \\ \eta_0 \\ \zeta_0 \end{pmatrix} + T(\phi, \theta, \psi) \begin{pmatrix} x_{E,i} \\ y_{E,i} \\ z_{E,i} \end{pmatrix} \tag{83}$$

The same transformation matrix can be used to derive the earth fixed points of $P$:

$$\begin{pmatrix} \xi_P \\ \eta_P \\ \zeta_P \end{pmatrix} = \begin{pmatrix} \xi_0 \\ \eta_0 \\ \zeta_0 \end{pmatrix} + T(\phi, \theta, \psi) \begin{pmatrix} x_P \\ y_P \\ z_P \end{pmatrix} \tag{84}$$

Subtraction of equation (84) from (83) and insertion into equation (82) yields a description, where only $\zeta_P, \phi$ and $\theta$ are unknown.

$$\begin{pmatrix} \xi_{E,i} \\ \eta_{E,i} \\ \zeta_{E,i} \end{pmatrix} = \begin{pmatrix} \xi_P \\ \eta_P \\ \zeta_P \end{pmatrix} + T(\phi, \theta, \psi) \begin{pmatrix} x_{E,i} - x_P \\ y_{E,i} - y_P \\ z_{E,i} - z_P \end{pmatrix} \tag{85}$$

This coupled non-linear system of equations can be e.g. solved iteratively at every time step using a Newton-Raphson method.

After all coordinates of reference point $P$ and the Euler angles are known, motions at every point such as the origin of coordinates (index $_O$) for the ship reference frame can be calculated:

$$\begin{pmatrix} \xi_0 \\ \eta_0 \\ \zeta_0 \end{pmatrix} = \begin{pmatrix} \xi_P \\ \eta_P \\ \zeta_P \end{pmatrix} - T(\phi, \theta, \psi) \begin{pmatrix} x_P \\ y_P \\ z_P \end{pmatrix} \tag{86}$$

**Influence of motion sensors**

The use of cable actuated distance sensors for motion determination has been validated in Cura Hochbaum et al. [17] using an optical measurement system and manual distance measurements in static conditions. The system had an overall good performance and can be seen as validated.

As the horizontal cable sensors are counteracting each other, their influence on the motion prediction is non-existent. However, the vertical cable sensors cannot be opposed and hence may influence the motion of the model. The heave and pitch motion are seen to be non-affected by the cables, as their restoring forces are high, compared to the relatively small force induced through the cables. The roll motion on the other hand is significantly affected by the cables. A roll decay test has been conducted once using the measuring device with the four cable sensors attached to the model and once using an inertia motion unit (IMU) where the model was completely free to move. The model was fully equipped and the moonpool closed. A weight has been used until a heeling angle of approximately 11° was reached. Afterwards, the weight was lifted rapidly and the roll decay measured with the individual systems. The result of these experiments is shown in figure 4.7. It can be clearly seen that both measuring systems predict the same roll frequency. However, the roll amplitudes when measuring with cable sensors are significantly more damped, than with the IMU. In Cura Hochbaum et al. [17] more detailed experiments have been conducted to investigate this effect. Measurements with a variation of number of attached cables was compared to optical motion measurements with a ship connected to the heave rods and a completely free floating ship. The conclusion of this investigation was that the damping of roll amplitudes drastically increases with the number of attached cables. The connection of the model to the heave rods has no influence on the amplitudes, but a very small influence on the roll frequency, as the weight of the heave rods was replaced by weights in the model, which slightly changed the gyradii.

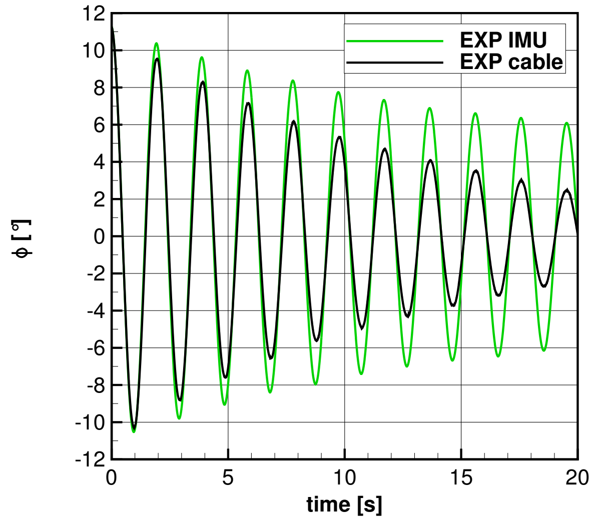


**Figure 4.7.:** Comparison of roll amplitudes using cable sensors and IMU

The additional damping due to cable actuated distance sensors should be kept in mind, when comparing numerical simulation with experimental data. Therefore, this topic will be further discussed in chapter 5.9.

### Influence of slide systems

Another influence on the motion of the ship can be assigned to the construction of the measuring device, which uses slides. These have different effects, which need to be understood, when postprocessing experimental data.

Time series of the force signal is typically oscillating with different frequencies, when using the measurement platform. Despite the exciting frequency, which is usually the wave frequency or in this case may also be the moonpool resonant frequency, the time series shows higher frequencies, which at first cannot be directly assigned. Such a signal is shown in figure 4.8 for the exemplary case RW125_0_015_MP (see chapter 4.5 for description of case denotion). These higher frequencies have been explained in Cura Hochbaum et al. [17] and are due to frictional effects in the slides and tolerances in the bearings. The friction inside the horizontal bearings causes a break loose force, which prevents the slide initially to move, once e.g. a wave hits the model. Instead, due to the tolerance of the linear bearings, the vertical heave rods are able to pitch approximately 0.2°. Once the maximum tolerance angle is reached, the force on the horizontal linear bearings increases and the slide moves rapidly. Friction and springs decelerate the slides again and the process is repeated at higher frequencies than the exciting frequency.

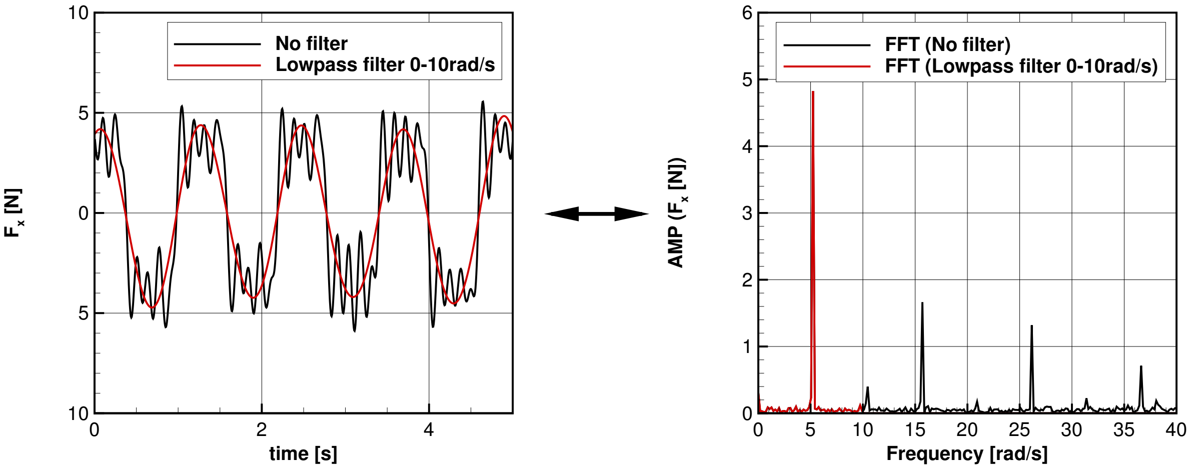


**Figure 4.8.:** Comparison of lowpass-filtered and non-filtered signal of longitudinal force

Tests using an electric motor to pull the individual slides at a constant speed and a force gauge to measure the break loose force and the constant frictional force were performed in Cura Hochbaum et al. [17]. A typical break loose force of approximately 12 N for the $\Delta x$-slide and a mean friction force of around 2 N for the $\Delta x$-slide respectively 4 N for the $\Delta y$-slide were measured. These forces are independent on the slide velocity, but of Coulomb type (proportional to the mass of the slides). These forces are typically small compared to first order wave forces, but need to be kept in mind when investigating small waves.

One of the objectives during development of the new measuring device was that the mass of the slides is as low as possible. The mass of the heave rods acts directly on the ship displacement and can be taken into account when ballasting the ship. However, the mass of the nested slide system is moving along with the ship motions in horizontal directions and should therefore be as small as possible. In order to reduce the weight of the slides, ultralight aluminium profiles have been used. The mass contribution in longitudinal direction due to both $\Delta x$-slides is 11.56 kg while the mass contribution to the transverse direction is 33.32 kg due to the complete nested slide system.

A complete elimination of these effects is not possible. It is therefore important to assure that the bearings are freely running and not jammed. Furthermore, a regular lubrication of the bearings and a cleaning of the rail needs to be done. However, caution should be taken when lubricating the bearings. After applying the lubricant it is important to manually move the slides and clean the rails from the excessive lubricant. This has been checked by deflecting the individual slides approx. 15 cm and releasing them to

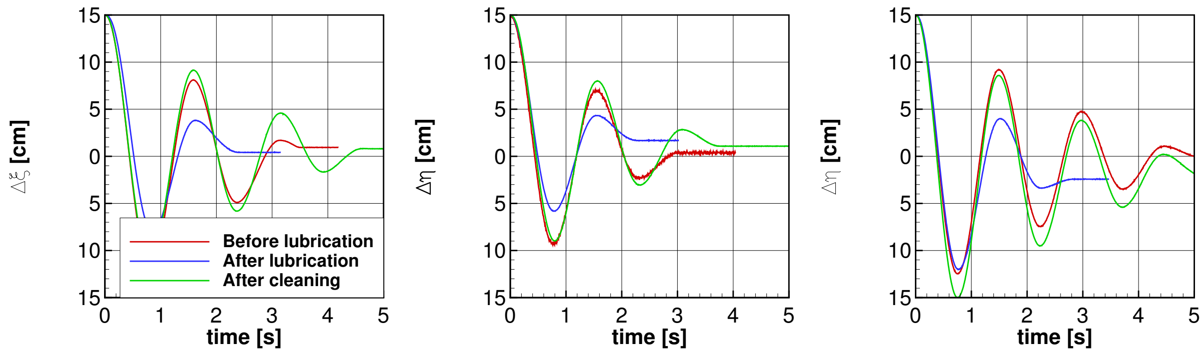


**(a)** $\Delta x$-slide back **(b)** $\Delta y$-slide back **(c)** $\Delta y$-slide front

**Figure 4.9.:** Influence on motion of slides after lubrication of bearings

oscillate until coming to a halt. This motion has been measured and is shown for each condition in figure 4.9a to 4.9c. It can be seen, that directly after lubricating, the slides move much worse than before, but removal of excessive lubricants improves the overall motion again. Also note the difference between the front and aft $\Delta y$-slide. As both are identically constructed and hence should move similar, differences can only be explained due to jamming of the bearings, which might have been slightly worse in case of the aft $\Delta y$-slide.

### Influence of spring rates

As already explained, the horizontal motions and the yaw motion are kept at a mean position using a spring system. One can argue, that these springs will affect the motion in the respective degrees of freedom. Lengwinat & Cura Hochbaum [49] investigated the influence of spring rates and mass of the slides theoretically, using the potential based panel method WAMIT (Wave Analysis Massachusetts Institute of Technology). Therein, it was shown that the RAO for surge increased with springs attached, while it decreased if the mass of the slides were added to the ship mass. Hence, both effects may cancel each other out, if the correct spring rate is chosen. However, a significant difference only occurred for relative wave lengths of $\lambda_W/L_{PP} > 1.0$.

An experimental investigation of the influence of different spring rates was conducted within this work. The main focus was on the motion amplitude of the water inside the moonpool, and if different spring rates are affecting it. The chosen spring rates are listed in table 4.4. The experiments have been performed for quartering head seas ($\mu_W = 45°$), as all degrees of freedoms are excited. Due to the choice of wave direction, the tests have been only performed for zero forward velocity.

**Table 4.4.:** Variation of spring rates for surge, sway and yaw

| configuration | surge | sway | yaw |
|---|---|---|---|
| k0 | 373.4 N/m | 792.0 N/m | 5.40 Nm/° |
| k1 | 185.5 N/m | 374.1 N/m | 2.55 Nm/° |
| k2 | 92.8 N/m | 187.0 N/m | 1.28 Nm/° |

Figure 4.10 shows a comparison of the mean oscillating amplitude inside the moonpool for all three investigated spring rates. It can be seen, that the amplitudes are almost identical in all cases, with a slight exception for configuration k1. This deviation is however in the range of accuracy as can be seen on the red error bar at $\lambda_W/L_{PP} = 1$ and $\lambda_W/L_{PP} = 0.5$, which represents the deviation of configuration k0 to a repeating test. As the deviation of k1 is never larger than the error bar it is assumed that the chosen spring rates have no influence on the moonpool oscillation amplitude.

The mean drift forces, and yaw moment in figure 4.11 show larger deviations for the different spring rate configurations. As no clear trend between the different spring rates can be identified, it is assumed that the deviation can be assigned to measuring uncertainties. Especially the longitudinal force should be taken with care, as the values are of less than 0.6 N and hence more difficult to determine accurately. The transverse drift force shows a more similar behaviour between the spring rates with an exemption for k1 at $\lambda_W/L_{PP} = 0.5$ and k0 at $\lambda_W/L_{PP} = 1$. The yaw moment shows a slightly better agreement. Repeating test would have gained some more insight if the mentioned deviations are due to force gauge sensitivity and hence in the range of accuracy, due to imprecise measurements, or if the mean forces have been indeed accurately captured.

Figure 4.12 and 4.13 show the dominant rotating respectively translating amplitudes of motion. All degrees of freedom are almost identical for different spring rates. Slight deviations occur at the longest relative wave length $\lambda_W/L_{PP} = 1.25$. This is in agreement with Lengwinat & Cura Hochbaum [49] which showed that the spring rates are having a slight influence on the RAO's for $\lambda_W/L_{PP} > 1$.

Concluding from this investigation, it seems to be of less importance, which spring rate is chosen, as the ship motions and the oscillation amplitude inside the moonpool are almost identical for all investigated configurations. Single deviating events are more probably related to postprocessing differences, rather than due to the chosen spring rate.

The surge motions are much higher if a forward velocity is applied, especially when accelerating or decelerating the ship. In order to prevent the force gauges from damage due to high peak loads if the slides are reaching the maximum amplitudes, the highest spring rates (k0) are chosen for the remaining experiments.

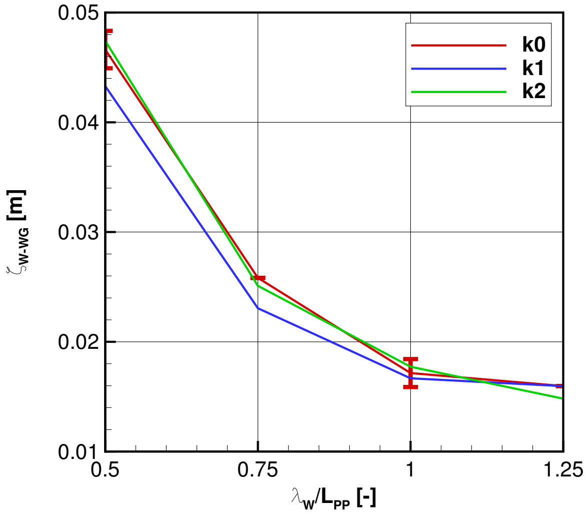


**Figure 4.10.:** Mean moonpool oscillation amplitude for different spring rates

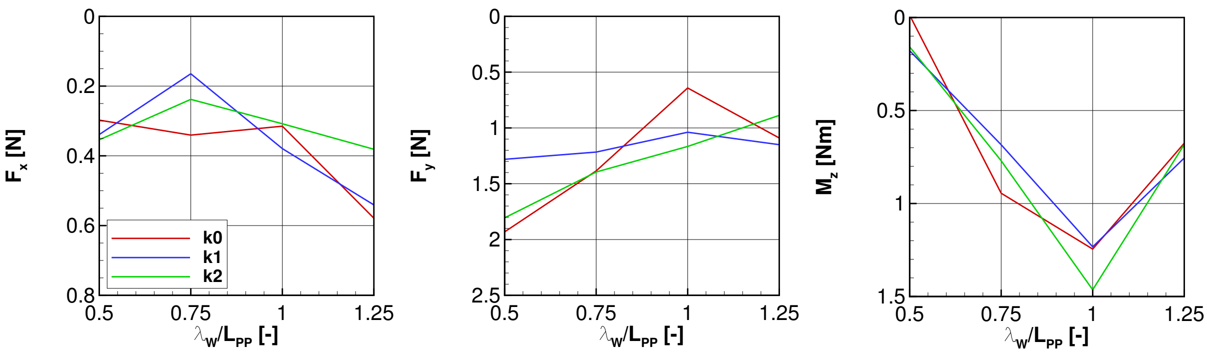


**(a)** Mean longitudinal drift force

**(b)** Mean transversal drift force

**(c)** Mean yaw moment

**Figure 4.11.:** Mean moonpool oscillation amplitude and Mean drift force in x- and y-direction and yaw moment for different spring rates

It should be noted that an investigation on the influence of different spring rates for a ship with forward velocity in waves has been numerically performed in Cura Hochbaum et al. [17]. A stronger dependency of the surge motion on the spring rates was detected, than in this work. This can also be assigned to the fact, that a much wider range of spring rates was investigated, than practically possible in the experiments. Their investigation

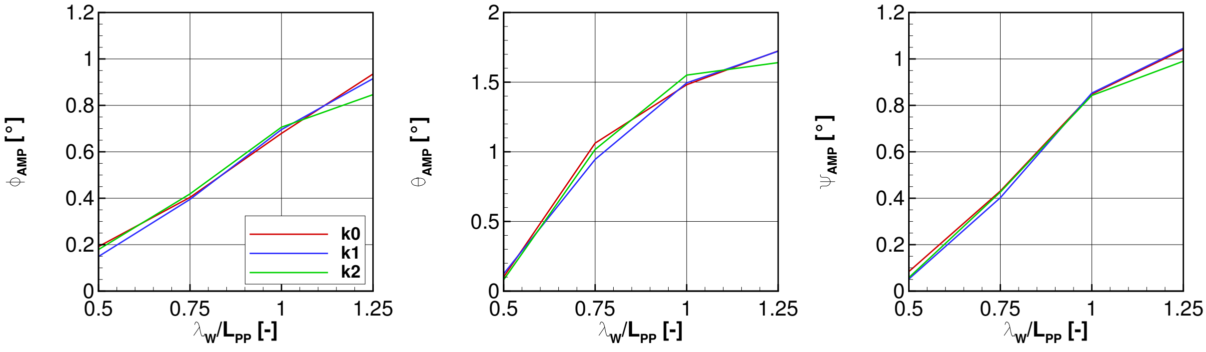


**(a)** Roll amplitude **(b)** Pitch amplitude **(c)** Yaw amplitude

**Figure 4.12.:** Amplitude of rotating motions for different spring rates

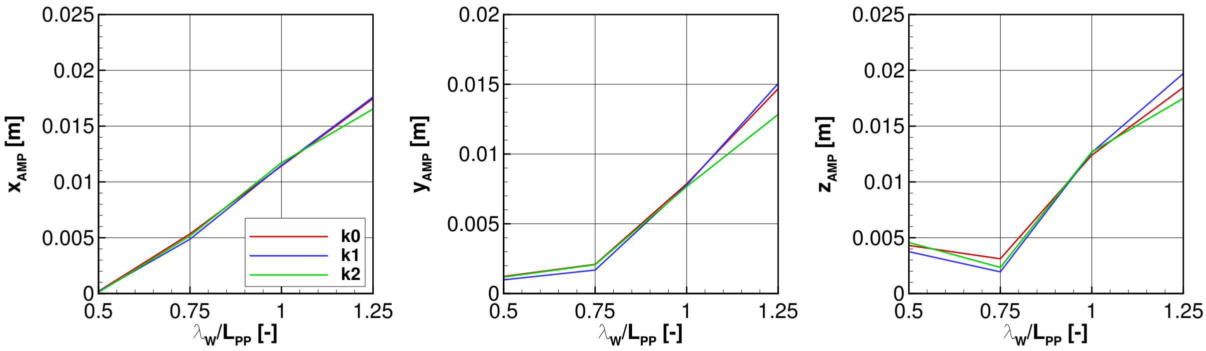


**(a)** Surge amplitude **(b)** Sway amplitude **(c)** Heave amplitude

**Figure 4.13.:** Amplitude of translating motions for different spring rates

showed, that the surge motion was significantly influenced with increasing spring rates. However, the added resistance in waves was almost identical for all investigated spring rates, as the pure hydrodynamic forces remained the same despite an increasing force due to the spring system.

## 4.3.2. Force determination

As already mentioned, two force gauges are installed in the ship to measure the ship fixed forces and moments. Although being capable of measuring in all 6 degrees of freedom (DOF), only the longitudinal and transversal forces of both gauges are used. This is due to the free motion of the ship inside the measuring device. If all DOF are restricted, then all 6DOF forces respectively moments can be analysed. Furthermore, by knowledge of the distance between the fore and aft force gauge, the yaw moment can be determined from the transversal forces of each force gauge. The total longitudinal and transversal forces can simple be determined by the sum of each longitudinal and transversal force gauge component.

During development of the new device, accurate measurement of mean forces were the biggest objective. A detailed analysis of the individual force components has been therefore conducted. This is e.g. shown in detail in [17, 16, 49, 78]. As the focus of this investigation is on moonpool hydrodynamics, mean forces are of somewhat minor importance but will be compared as well. When comparing forces of experimental and numerical sources, their respective components should be identical in order to avoid deviating results. The output of numerical simulations are usually solely the integrated stresses on the hull and hence pure hydrodynamic forces and moments. Further, gravitational forces may be included as well.

When conducting experiments, not only hydrodynamic forces, but also gravitational and inertia forces are measured. As some of the inertia forces are not zero when averaging over one wave period, they should be e.g. subtracted from the experimental data before comparing to numerical. A brief review of the force and moment components is given in the following:

As mentioned, the forces are determined in a ship fixed frame of reference. The relevant equations of motion for surge, sway and yaw are shown in equation (87),(88) and (89). These equations are stated for the centre of gravity $(x_G, y_G, z_G)$ and cartesian velocity components of the origin $(U_0, V_0, W_0)$, respectively their time derivatives. The mass of the system is denoted by $m$ and $I_{ij}$ are the inertia products. The superscripts *hydro*, *grav* and *meas* are representing components due to pure hydrodynamic forces on the hull, gravitational contribution and the total measured force respectively.

$$
\begin{aligned}
F_x^{meas} = & - m \left[ \left( \dot{U}_0 + \underbrace{qW_0 - rV_0}_{\neq 0} \right) - \underbrace{x_G \left(q^2 + r^2\right)}_{\neq 0} - y_G \left(\dot{r} - pq\right) + z_G \left( \dot{q} + \underbrace{pr}_{\neq 0} \right) \right] \\
& + F_x^{hydro} + F_x^{grav} \qquad (87) \\
F_y^{meas} = & - m \left[ \left( \dot{V}_0 + \underbrace{pW_0 - rU_0}_{\neq 0} \right) - x_G \left( \dot{r} - \underbrace{pq}_{\neq 0} \right) - \underbrace{y_G \left(p^2 + r^2\right)}_{\neq 0} + z_G \left( \dot{p} + \underbrace{qr}_{\neq 0} \right) \right] \\
& + F_y^{hydro} + F_y^{grav} \qquad (88) \\
M_z^{meas} = & - [\; I_{zz}\dot{r} - \underbrace{\left(I_{xx} - I_{yy}\right) pq}_{\neq 0} - I_{xy} \left(p^2 - q^2\right) - I_{yz} \left(\dot{q} + pr\right) \\
& - I_{xz} \left(\dot{p} - qr\right) + m x_G \left( \dot{V}_0 - \underbrace{pW_0 + rU_0}_{\neq 0} \right) - m y_G \left( \dot{U}_0 + qW_0 - rV_0 \right) \;] \\
& + M_z^{hydro} + M_z^{grav} \qquad (89)
\end{aligned}
$$

The inertial components in all three equations are the terms inside the squared brackets. Assuming harmonically oscillating conditions, the average value over full wave periods of the translating and rotating velocities and accelerations become zero ($\overline{U_{0i}} = \overline{\dot{U}_{0i}} = \overline{\omega}_i = \overline{\dot{\omega}}_i = 0$, with $U_{0i}$ representing the three cartesian velocity components of the origin and $\omega_i$ representing the three ship fixed angular velocity components). Furthermore, due to symmetry conditions the following products of inertia become zero or small: $I_{xy} = I_{xz} = I_{yz} = 0$. Inertia components which can be zero for certain conditions but are not generally zero are marked in equations (87)-(89).

The following force and momentum components will be compared in the subsequent chapters: The mentioned inertial components will be subtracted from the measured experimental data in a postprocessing step The gravitational component remains included. This component can have substantial magnitude for large motions, which increases the source of errors when having a time lag or imprecise motion measurements. The numerical data consists of the pure hydrodynamic forces (which can be differentiated between frictional and pressure components), as well as gravitational components. Following this procedure, both forces can be directly compared with each other.

Uharek & Cura Hochbaum [78] further mentioned a time lag between the experimentally determined ship motions and forces. This lag of the experimental force can be determined from Cura Hochbaum et al. [17] with approximately 0.35 s. The exact source of this time lag has not yet been found, but will be due to the measuring chain, respectively the data processing. Therefore, it should be kept in mind that time series need to be corrected for that time lag, if comparison between numerical and experimental time traces are conducted.

### 4.3.3. Calibration

A brief description of the calibration of each measuring equipment is given in the following paragraphs. The measuring software has been developed in Cura Hochbaum et al. [17] and Cura Hochbaum & Lengwinat [16] and slightly modified to accommodate three additional wave gauges, which are placed inside the moonpool. The software is based on *LabView* and features calibration of each signal. In total 30 signals, shown in table 4.5, are processed through the software.

**Table 4.5.:** Measuring signals

| channel | signal | channel | signal |
|---|---|---|---|
| 0 | Force gauge 1-1 | 15 | Cable sensor W4 |
| 1 | Force gauge 1-2 | 16 | Cable sensor W5 |
| 2 | Force gauge 1-3 | 17 | Cable sensor W6 |
| 3 | Force gauge 1-4 | 18 | Cable sensor W7 |
| 4 | Force gauge 1-5 | 19 | Cable sensor W8 |
| 5 | Force gauge 1-6 | 20 | Cable sensor W9 |
| 6 | Force gauge 2-1 | 21 | Cable sensor W1 |
| 7 | Force gauge 2-2 | 22 | Wave WG1 |
| 8 | Force gauge 2-3 | 23 | Wave WG2 |
| 9 | Force gauge 2-4 | 24 | Wave WG3 |
| 10 | Force gauge 2-5 | 25 | Moonpool WG1 |
| 11 | Force gauge 2-6 | 26 | Moonpool WG2 |
| 12 | Cable sensor W1 | 27 | Moonpool WG3 |
| 13 | Cable sensor W2 | 28 | Wave generator |
| 14 | Cable sensor W3 | 29 | Carriage speed |

The two force gauges (channel 0-11) mounted at the model have fixed calibration factors, which are included in the measuring software.

The cable sensors (channel 12-21) typically only require a calibration at the start of the test campaign. This is done manually by deflecting each cable and assuming a linear behaviour of deflection to voltage.

Most sensitive are the wave gauges and their calibration. Both for wave and moonpool, two wire resistance wave gauges are used. It is strongly advised to turn on the amplifier of the wave gauge signals approx. 30 min before measuring, as these are heating up, which can cause a drift of the signal. Each wave gauge is placed at the desired location and depth and the digital amplifier adjusted, such that the voltage is approx. 0 V at rest and the maximum expected wave does not exceed a voltage of ±10 V. Once the digital amplifier is correctly adjusted, the gauges are calibrated using the measuring software by lifting each gauge and defining the distance to a certain voltage change. Again this assumes linear behaviour. This procedure has been repeated every day, as the amplifier and wave gauges tend to be sensitive to environmental conditions.

Before starting of every test run, a new offset of all signals has been taken. This feature is included in the measuring software and is advised to use, as the slides may come to a halt at a different location after each run. Note that this function only sets a possible offset to zero, but calibration factors are not affected.

## 4.4. Inclining experiment

An inclining experiment has been performed in order to determine if the correct metacentric height $\overline{GM}$ is reached through ballasting of the model. The model was fully equipped and weights distributed in order to reach the desired initial vertical centre of gravity of $\overline{KG} = 0.252\,\text{m}$ and the desired gyradii $k_{xx} = 0.288\,\text{m}$ and $k_{yy} = k_{zz} = 0.761\,\text{m}$. Different additional weights have been initially placed midships and 0.3 m above keel. This weight has then been shifted 0.3 m to portside and the heeling angle $\phi$ measured.

From simple stability theory, the heeling moment $M_h$ and stabilising moment $M_{st}$ can be determined. Using both equation (91) and (92), the metacentric height can be determined. The results are shown in table 4.6. It can bee seen that the deviation of the measured metacentric height is only 1.5% from the desired value.

**Table 4.6.:** Results of inclining experiment

| Ballast | Weight | $\overline{KG}$ | $h_l$ | $\phi$ | $\overline{GM}$ |
|---|---|---|---|---|---|
| 1.05 kg | 251.92 kg | 0.2513 m | −0.3 m | 0.60° | 0.1194 m |
| 2.00 kg | 252.87 kg | 0.2515 m | −0.3 m | 1.15° | 0.1182 m |
| 3.05 kg | 253.92 kg | 0.2519 m | −0.3 m | 1.80° | 0.1147 m |
| 3.99 kg | 254.86 kg | 0.2522 m | −0.3 m | 2.35° | 0.1145 m |
| Mean | | | | | 0.1167 m |
| Target | | | | | 0.1150 m |
| Deviation | | | | | 1.48 % |

$$M_h = m \cdot g \cdot h_l \tag{90}$$

$$M_{st} = \rho \cdot g \cdot V \cdot \overline{GM} \cdot \sin(\phi) \tag{91}$$

$$\overline{GM} = \frac{m \cdot h_l}{\rho \cdot V \cdot \sin(\phi)} \tag{92}$$

## 4.5. Test matrix

The test matrix consisted of approx. 230 tests, which have been performed experimentally. The complete table of conducted tests can be found in the appendix B. Figure 4.14 explains the abbreviation for the individual denotion of tests. Note that this figure shows a complete list of investigated values for each individual parameter, but not all possible combinations have been tested. An obvious example is the wave direction $\mu_W$, which can only be set to quartering or beam seas, when being at rest ($Fr = 0$), due to the breadth limitations of the facility.

Generally speaking, different moonpool configurations have been tested in calm water and regular waves with forward velocity, to investigate transit conditions. Furthermore, operational conditions, with $Fr = 0$ were tested for regular waves with varying wave directions. The wave height has been adjusted according to the wave length, such that a constant wave steepness defined by wave height to wave length of $H_W/\lambda_W = 2\%$ has been reached. A detailed description of the wave characteristics is shown in table 4.7.

**Table 4.7.:** Wave characteristics

| | $\lambda_W/L_{PP}$ | $h/\lambda_W$ | $k_w$ | $\omega_W$ | T | $\zeta_W$ |
|---|---|---|---|---|---|---|
| deep water | 0.50 | $0.\overline{66}$ | 4.189 | 6.410 rad/s | 0.980 s | 1.50 cm |
| transitional water | 0.75 | $0.\overline{44}$ | 2.793 | 5.234 rad/s | 1.200 s | 2.25 cm |
| | 1.00 | $0.\overline{33}$ | 2.094 | 4.431 rad/s | 1.418 s | 3.00 cm |
| | 1.25 | $0.2\overline{6}$ | 1.676 | 3.890 rad/s | 1.615 s | 3.75 cm |

While most of the tests performed were repeated numerically in order to validate the result against each other, both experimental and numerical test matrices contain some investigations which have not been conducted in the other. In the experimental test matrix a variation of Froude number for the ship in waves has been conducted, while the Froude number in the numerics has been kept constant at $Fr = 0.15$, due to computational time effort. On the other hand, a variation of moonpool length to breadth ratio $l_{mp}/b_{mp}$ has been investigated only numerically, as this would have required an additional manufacturing of moonpool insertions for the experiments.

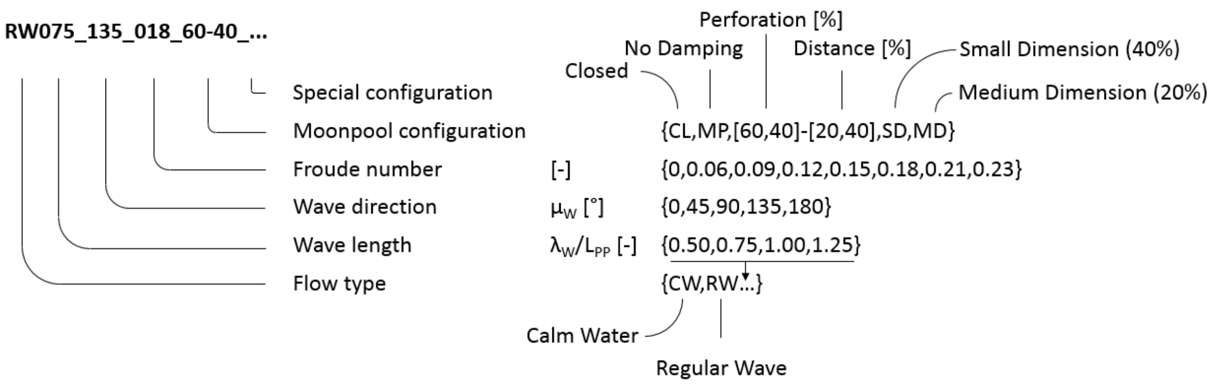


**Figure 4.14.:** Description of test name abbreviation

# 5. Numerical simulations

This chapter contains a description of the numerical grids, as well as initial investigations such as time step and grid dependencies. Furthermore, some general observations are presented, which are of importance when performing simulations with moonpools.

## 5.1. Ship model

A rendering of the model is shown in figure 5.1. Note that the origin of coordinates is different than used in the experiments in chapter 4.2. The origin of coordinates is at the forward perpendicular, midships and at the waterline with $x$-axis pointing towards the stern, $y$ to starboard and $z$ upwards. Motions are determined for the centre of gravity, which is located 1 % in front of the midship section. As mentioned, this coincides with the origin of coordinates used in the experiments, making the motions of both methods directly comparable.


**(a)** Side view

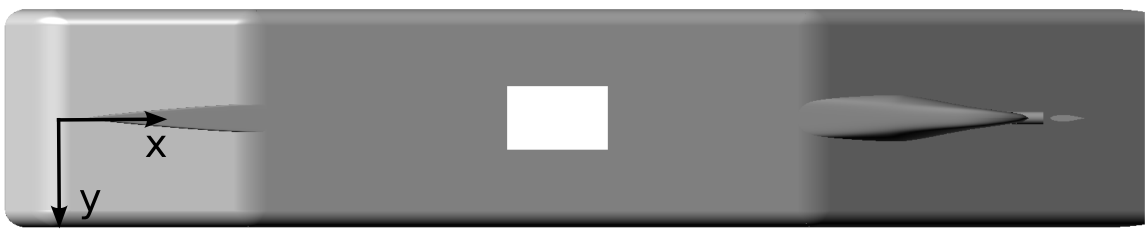


**(b)** Bottom view

**Figure 5.1.:** Rendered model with moonpool (MP)

### 5.1.1. Moonpool dimensions for numerical investigations

In total five different moonpool geometries have been investigated numerically. All moonpools are being placed midships. The moonpool geometries are listed in table 5.1. The size of 'MP' has been determined from van 't Veer & Tholen [80] by averaging the moonpool lengths and breadths listed in their publication and re-sizing them according to the real ship length and breadth respectively. This ensures that an average ratio of ship length to moonpool length and ship breadth to moonpool breadth is used. The ratio of length to breadth ($l_{mp}/b_{mp}$) is approx. 1.59. MP has been scaled down by 20% ('MD') and 40% ('SD') respectively in length and breadth. They therefore have the same ratio of length to breadth as MP, but smaller sizes. Another variation of MP has been done by changing $l_{mp}/b_{mp}$. 'lb1' has a ratio of $l_{mp}/b_{mp} = 1$ by keeping the breadth identical as for MP and 'lb2' of $l_{mp}/b_{mp} = 2$ by keeping the length identical as MP. MP, MD and SD have been build for the respective experiments, while lb1 & lb2 have only been investigated numerically.

**Table 5.1.:** Main dimensions of moonpools

| | | Full scale | Model scale | Unit |
|---|---|---|---|---|
| MP | $l_{mp}$ | 19.50 | 0.300 | m |
| | $b_{mp}$ | 12.30 | 0.189 | m |
| MD | $l_{mp}$ | 15.60 | 0.240 | m |
| | $b_{mp}$ | 9.83 | 0.151 | m |
| SD | $l_{mp}$ | 11.70 | 0.180 | m |
| | $b_{mp}$ | 7.37 | 0.113 | m |
| lb1 | $l_{mp}$ | 12.30 | 0.189 | m |
| | $b_{mp}$ | 12.30 | 0.189 | m |
| lb2 | $l_{mp}$ | 19.50 | 0.300 | m |
| | $b_{mp}$ | 9.75 | 0.150 | m |

## 5.2. Numerical grids

To ensure high quality grids, the whole model has been separated into smaller parts to create individual body-fitted grids. Therefore, parts as e.g. the forefoot or stern bulb are collar grids, which coincide with the hull surface in this instance. When oversetting the grids using *Suggar++*, these grids are being assembled and a continuous grid is being formed. The program *usurp* (Boger & Dreyer [5]) is then used to define panel weights for the cells located at wall boundaries. These weights range from 0 to 1. If two panels from different grids are at the same location of the surface, a factor between 0 and 1 is applied to them. This ensures that integral quantities such as forces are treated correctly. A visualisation of the assembled grid with detailed views is shown in figure 5.2 to 5.4.

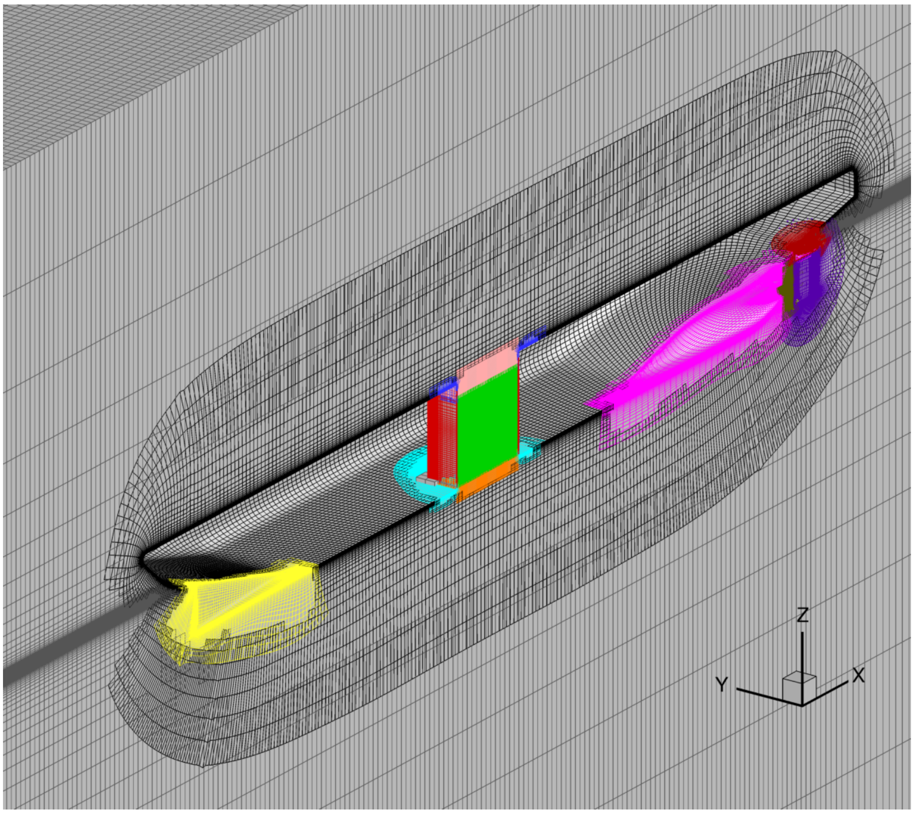


**Figure 5.2.:** Assembled grid after running *Suggar++*

The representation of the moonpool consists of several individual grids. Primarily, there is a grid, forming the inner part of the moonpool (red) going from deck to keel and ensuring $y^+ < 1$ at the wall. Another grid (green) with the same dimensions is used to refine the inner part of the moonpool, while disregarding a wall resolution of $y^+ < 1$. In order to prevent coarser cells at the wall due to the refinement grid, the first cell is blanked when creating the assembled grid. Splitting the moonpool into two grids, as has been described, has been done to reduce the number of cells. A ring at the bottom (cyan) and top (blue) of the moonpool provides a connection of the hull and moonpool and also ensures $y^+ < 1$ at the walls. At last, a rectangular box at the bottom (orange) and top (peach) ensures a vertical elongation of the moonpool, without having a wall refinement. The latter was necessary, as a sufficient overlapping region between the moonpool and the hull grid needed to be created, while avoiding a sudden accumulation of cells along the $x-$ and $y-$axis in the freestream area. A detailed view of the grids representing the moonpool is shown in figure 5.3. Furthermore, figure 5.4 shows a detailed view of the surface grid for the bow and stern section. Note that the propeller shaft grid has been designed, such that body force simulations could have been performed. However, no self propulsion simulations have been conducted within this work.

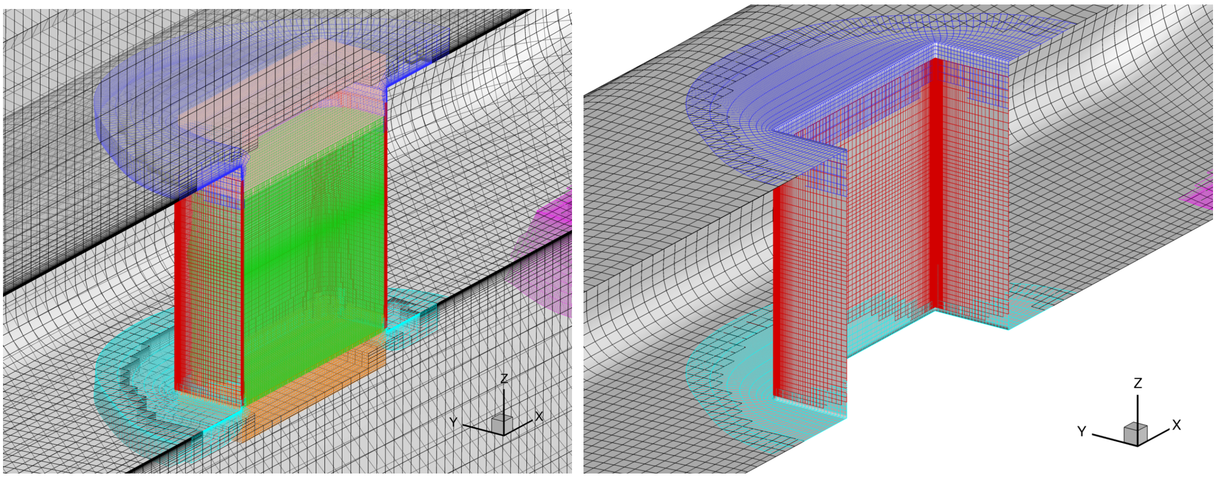


**(a)** Perspective view of volume grid

**(b)** Perspective view of the surface grid

**Figure 5.3.:** Grid of the moonpool for grid #2

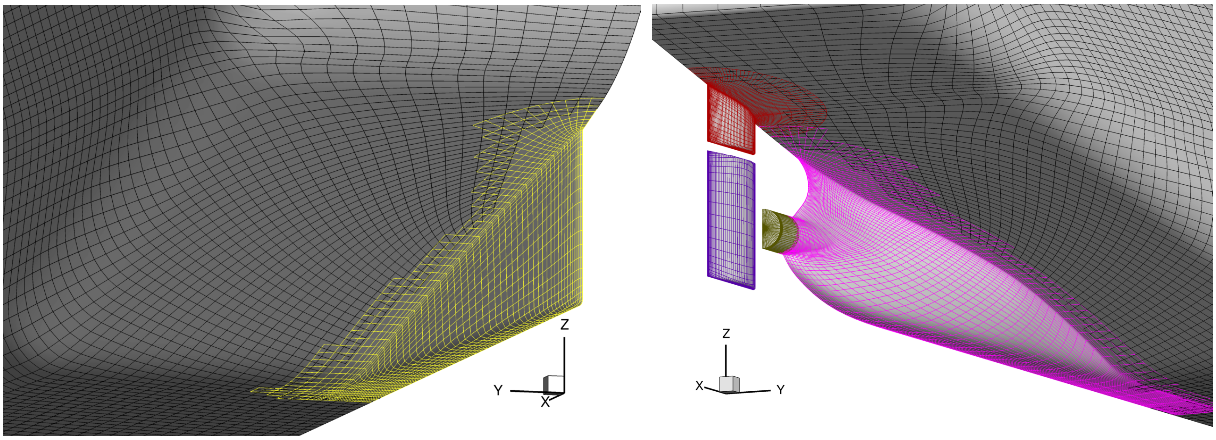


**(a)** Perspective view of the bow section

**(b)** Perspective view of the stern section

**Figure 5.4.:** Surface grid at bow and stern section for grid #2

The grids have been constructed as body-fitted single block structured grids using a hyperbolic grid generator. The simulations have been performed without making use of wall functions, although these have been later on investigated, as discussed in chapter 5.6.1. The equation defining the first cell layer thickness $y_1$ is:

$$\frac{y_1}{L_{ref}} = \frac{5.5}{Re^{0.9}} \tag{93}$$

This yields for a Reynolds number of $Re = 3.288 \cdot 10^6$, which corresponds to the highest investigated Froude number of $Fr = 0.23$, $\frac{y_1}{L_{ref}} = 7.5 \cdot 10^{-6}$. To ensure, that a dimensionless wall distance of $y^+ < 1$ is reached also when coarsening the grid, a distance of $\frac{y_1}{L_{ref}} = 2 \cdot 10^{-6}$ has been chosen for the finest grid (grid #1).

The finest grid has been initially constructed and afterwards coarsened twice using a refinement ratio of:

$$r_G = \frac{\Delta x_{G,2}}{\Delta x_{G,1}} = \frac{\Delta x_{G,3}}{\Delta x_{G,2}} = \sqrt{2}, \tag{94}$$

with $\Delta x_G$ representing the individual cell spacing in each direction. Table 5.2 contains the detailed information about each block structured grid, for the medium size grid (#2). The blocks of the finer (#1) and coarser (#3) grid have each the same number of points with a factor $\sqrt{2}$ increased respectively decreased. Total number of cells and the vertical and longitudinal cell resolution of the smallest wave is shown for all three grids in table 5.3.

**Table 5.2.:** List of individual block structured grids for medium grid, using symmetry condition at $\eta' = 0$

| # | Description | points in $i, j, k$ | total cells |
|---|---|---|---|
| 1 | Hull | 170 49 83 | 665,814 |
| 2 | Moonpool (wall resolution) | 170 99 48 | 778,414 |
| 3 | Moonpool refinement | 144 36 146 | 725,725 |
| 4 | Ring top | 21 29 143 | 79,520 |
| 5 | Ring bottom | 21 29 143 | 79,520 |
| 6 | Box top | 85 36 29 | 82,320 |
| 7 | Box bottom | 85 36 29 | 82,320 |
| 8 | Forefoot | 54 45 35 | 79,288 |
| 9 | Sternbulb | 85 49 44 | 173,376 |
| 10 | Propeller shaft | 48 53 36 | 85,540 |
| 11 | Rudder dome | 39 34 64 | 79,002 |
| 12 | Spade rudder | 49 56 33 | 84,480 |
| 13 | Background | 417 60 84 | 2,037,152 |
| | Total | | 5,031,841 |

**Table 5.3.:** Grid size for grids using symmetry condition at $\eta'$=0

| | Number of cells | $H_W/\Delta\zeta$ | $\lambda_W/\Delta\xi$ |
|---|---|---|---|
| (#1) fine | 14,532,716 | 32 | 94 |
| (#2) medium | 5,031,841 | 24 | 66 |
| (#3) coarse | 1,737,000 | 16 | 47 |

## 5.3. Computational domain

The computational domain is defined by the dimensions of the background grid. In general there are two types of simulations, where the computational domain needs to be adapted to.

1. **Domain type 1**: Simulations for head seas ($\mu_W$ =0°) and following seas ($\mu_W$ =180°), with or without forward velocity (no drift).

2. **Domain type 2**: Simulations with oblique waves, with or without forward velocity.

For the first domain type, a symmetry condition at $\eta' = 0$ can be assumed and only one half of the domain build. The ship is hence only performing motions within the $\xi - \zeta$-plane (surge, heave, pitch). The corresponding domain is shown in figure 5.5a, where also the boundary conditions are visualised. Note that the top and bottom boundary have a far-field respectively very far field boundary condition applied, as is described in chapter 2.6.

As *REX* is using a non-dimensional form to solve the Navier-Stokes equations, the length of the ship is used to scale the model dimensions to $L_{PP} = 1$. The forward perpendicular is placed at $\xi' = 0$ the aft perpendicular at $\xi' = 1$ and the centre of the moonpool at $\xi' = 0.5$. The vertical origin is always placed at the calm water line. The domain reaches in longitudinal direction from $\xi' = -1.5$ to $\xi' = 2.5$, in transversal direction from $\eta' = 0$ to $\eta' = 1$ and in vertical direction from $\zeta' = -1$ to $\zeta' = 0.5$. A very slight elongation of grid cells in longitudinal direction is applied from $\xi' > 1$. It is however still fine enough to capture the ship wave system behind the ship as well as allows simulations in following seas ($\mu_W = 180°$).

The second domain type is used for oblique waves where the ship is allowed to move in all DOF. Therefore, no symmetry condition can be applied and the computational domain needs to capture the complete surrounding of the model. The model is again placed in longitudinal direction between $\xi' = 0$ and $\xi' = 1$ and midships at $\eta' = 0$. The domain starts in longitudinal direction at $\xi' = -1.25$ and ends at $\xi' = 4.25$. The cells are

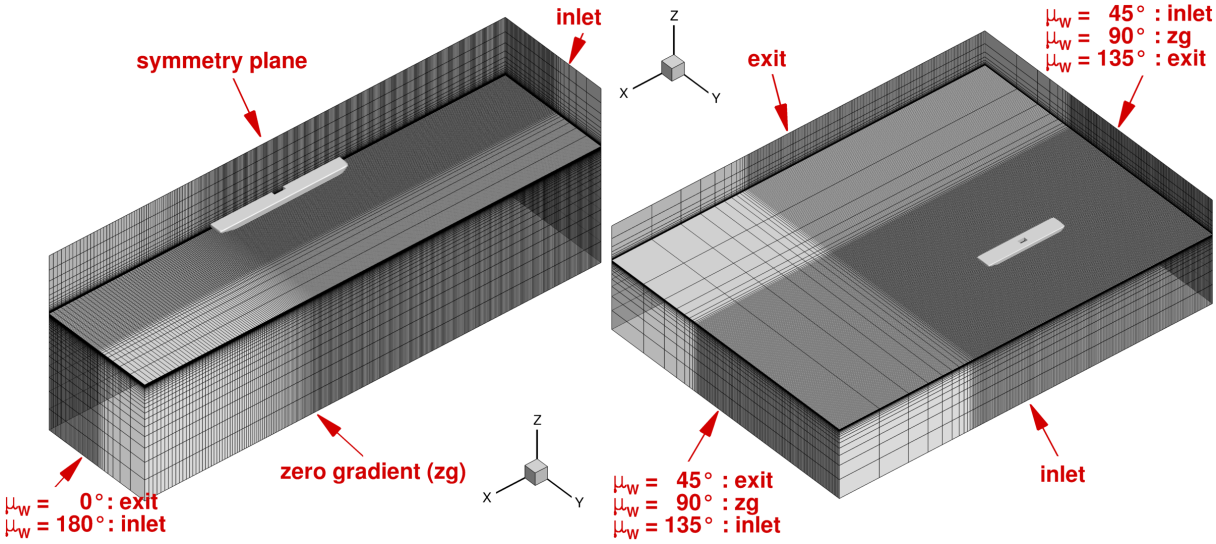


**(a)** Domain type 1 (grid #2) **(b)** Domain type 2

**Figure 5.5.:** Domain, boundary conditions and cell distribution

homogeneously distributed from $-1.25 \leq \xi' \leq 2.25$ and afterwards elongated to increase the wave damping. In transversal direction the domain starts at $\eta' = -2.75$ and ends at $\eta' = 1.25$, with a homogeneous cell distribution between $-1.25 \leq \eta' \leq 1.25$. The dimensions in vertical direction are identical to domain type 1. Note that the number of points for domain type 2 has been reduced in order to save computational time. The cell size within the fine resolved area around the ship equals the cell size of the coarse background grid in grid #3. As can be seen in chapter 5.4, this grid already reaches a wave quality of 94 %. The number of points for all other blocks creating the model are identical as in domain type 1. To build a complete ship model without having a symmetry plane, most of the blocks have been mirrored and then assembled using *Suggar++*, which then consist of two blocks (port and starboard side) sharing an averaged multi-block boundary condition. When reducing the number of blocks, the number of processors needed is reduced, as has been explained in chapter 2.5. Hence, if possible, blocks such as the moonpool have been mirrored and joined within the grid generator and exported as one block.

## 5.4. Grid dependency

A grid dependency study has been performed using three different grids, as shown in table 5.3. Remember that the dimensionless wall distance $y^+$ was smaller than 1 for all three grids, but is slightly changing due to grid coarsening. The study has been performed in calm water conditions and in regular waves. The individual simulations considered within this study ensured a reduction of residuals by several orders of magnitude. The results of the grid study can be seen in table 5.4 to 5.5. The convergence study has been determined following the recommended procedures by Stern et al. [73]. The change in solution between the two grids ($\epsilon_G$) is defined by the difference of them ($\hat{S}_G$):

$$\epsilon_{G,21} = \hat{S}_{G,2} - \hat{S}_{G,1} \tag{95}$$

$$\epsilon_{G,32} = \hat{S}_{G,3} - \hat{S}_{G,2} \tag{96}$$

The convergence ratio $R_G$ on the other hand is defined as the rate of the change:

$$R_{G,1-3} = \frac{\epsilon_{G,21}}{\epsilon_{G,32}} \tag{97}$$

There are three classes of convergence:

i) $0 < R_G < 1$: Monotonic convergence

ii) $R_G < 0$: Oscillatory convergence

iii) $R_G > 1$: Divergence

The grid dependency analysis has been done for two different cases. Once for the fixed ship with moonpool in calm water and once for the ship with moonpool free to heave and pitch in waves, to include the accuracy of the generated waves and the motions. The non-dimensional time step of $\Delta t' = 0.002$ has been kept constant for all investigated grids.

Table 5.4 shows results for the ship with moonpool MP in calm water at $Fr = 0.15$ and with no motions allowed. The total resistance reaches an oscillatory convergence. The frictional component is monotonically converging while the pressure component shows a diverging behaviour. It is known that grid coarsening leads to numerical diffusion and hence an increasing pressure resistance. Furthermore, flow separation at the relatively strong hull curvature at the ship shoulders could further increase the separation. The diverging pressure component can be seen as unfavourable, but the following grid study for wave conditions will show better behaviour.

The mean oscillation of water column inside the moonpool has been investigated as well, which is an important parameter for this work. It shows slightly oscillatory, but still satisfying behaviour. The coarse grid overestimates the amplitude, while medium and fine grid have almost identical magnitudes.

Figure 5.6 shows the pressure distribution on the hull, as well as the surface elevation for all three grids. One can see that the free surface is still not fully developed for the medium grid. This is also due to the low Froude number of 0.15, where only small ship waves are being produced. As the grids are designed to analyse waves rather than calm water conditions, small ship waves are less accurately resolved. This has to be taken as a compromise. As the focus of this work is on analysing moonpool characteristics and grid #2 already has a converged moonpool oscillation amplitude, this deficiency is accepted.

**Table 5.4.:** Resistance coefficients for total resistance ($_T$), frictional ($_F$) and pressure ($_P$) and mean oscillation amplitude ($\zeta_{0-WG}$) in MP for calm water

| | coarse | medium | fine | $\epsilon_{G,21}$ | $\epsilon_{G,32}$ | $R_{G,1-3}$ |
|---|---|---|---|---|---|---|
| $C_T$ | $6.455 \cdot 10^{-3}$ | $6.530 \cdot 10^{-3}$ | $6.504 \cdot 10^{-3}$ | $0.026 \cdot 10^{-3}$ | $-0.075 \cdot 10^{-3}$ | -0.347 |
| $C_F$ | $3.508 \cdot 10^{-3}$ | $3.647 \cdot 10^{-3}$ | $3.758 \cdot 10^{-3}$ | $-0.111 \cdot 10^{-3}$ | $-0.139 \cdot 10^{-3}$ | 0.799 |
| $C_P$ | $2.947 \cdot 10^{-3}$ | $2.883 \cdot 10^{-3}$ | $2.746 \cdot 10^{-3}$ | $0.137 \cdot 10^{-3}$ | $0.064 \cdot 10^{-3}$ | 2.141 |
| $\zeta_{0-WG}$ [m] | $2.121 \cdot 10^{-3}$ | $1.788 \cdot 10^{-3}$ | $1.813 \cdot 10^{-3}$ | $-0.025 \cdot 10^{-3}$ | $0.333 \cdot 10^{-3}$ | -0.075 |

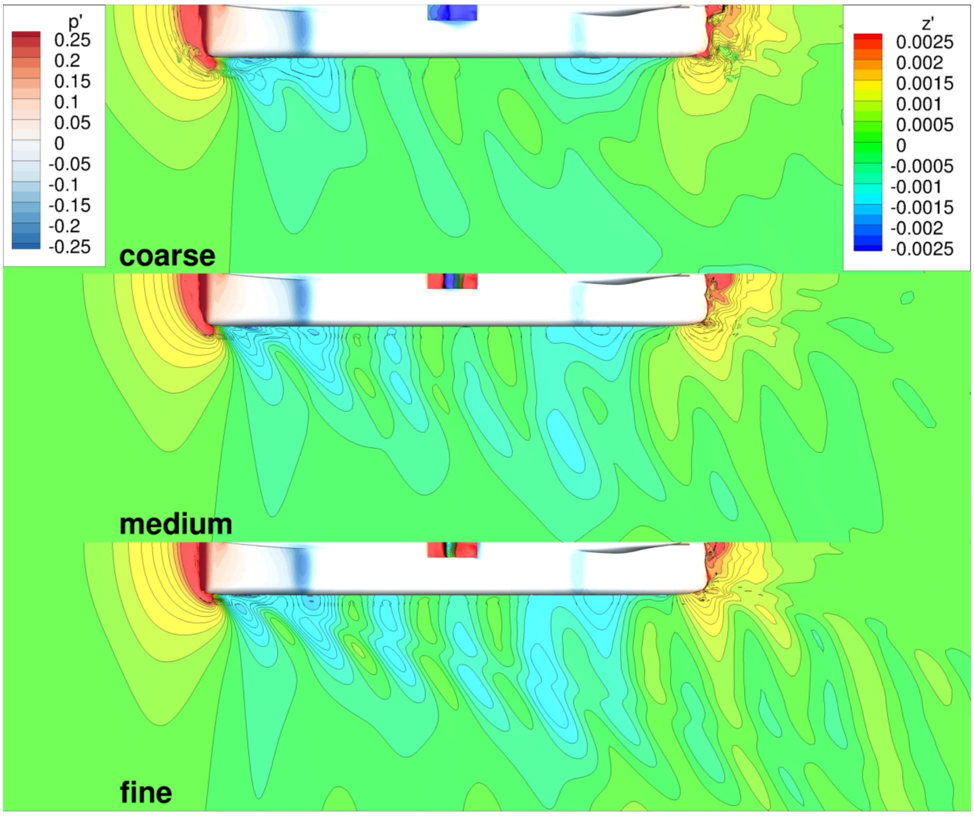


**Figure 5.6.:** Free surface and pressure distribution on hull for grid dependency analysis

The accuracy of wave amplitude has been determined additionally to the previously investigated resistance coefficients and oscillation amplitude for the grid dependency of the ship with moonpool in regular waves of $\lambda_W/L_{PP} = 0.5$ coming from $\mu_W = 0°$ (head waves) in table 5.5. The oscillation amplitude is further distinguished between the amplitude at piston mode resonant frequency and at wave frequency. Although the total resistance and pressure component show an oscillatory convergence, the convergence ratio is small and the results are satisfying. The frictional resistance component converges again monotonically. The amplitude at piston mode frequency decreases for the finest grid, causing a divergence of that parameter. The amplitudes at wave frequency are relatively small, but still converge monotonically. The same applies for the wave accuracy, which produces already for the coarse grid a non-dimensional amplitude of 0.94 and which improves up to 0.97 for grid #1. The resolved amplitude of the incoming wave has been analysed the following way. A Fourier-transformation of the free surface parallel to the ship and at $\eta' = 0.9$ (no/minor influences of the ship wave system) has been performed and analysed over one wave period. Afterwards, the first amplitude of the Fourier transform has been averaged over the length of the ship and made non-dimensional with the incoming wave amplitude. Figure 5.7 further shows a comparison of the instantaneous free surface elevation and velocity vector field of superposed orbital velocities and ship velocity for the numerical result (blue) and according to linear wave theory (red). The data from the numerical simulation has been extracted from the same slice as for the Fourier-transformation and for the last computed time step for grid #2. One can see a very good agreement between the analytical and computed wave characteristics. Note that the evaluation of wave quality has been done extensively for head seas (and following seas, as discussed in chapter 6.1.5). The waves for quartering and beam seas should be of similar quality, due to the homogeneous cell distribution (shown in figure 5.5b) and are hence not specifically analysed.

**Table 5.5.:** Resistance coefficients for total resistance ($_T$), frictional ($_F$) and pressure ($_P$), mean oscillation amplitudes ($\zeta_{WG}$) in MP and wave accuracy $\zeta_W/\zeta_{target}$

| | coarse | medium | fine | $\epsilon_{G,21}$ | $\epsilon_{G,32}$ | $R_{G,1-3}$ |
|---|---|---|---|---|---|---|
| $C_T$ | $6.976{\cdot}10^{-3}$ | $7.338{\cdot}10^{-3}$ | $7.305{\cdot}10^{-3}$ | $0.033{\cdot}10^{-3}$ | $-0.362{\cdot}10^{-3}$ | -0.091 |
| $C_F$ | $3.500{\cdot}10^{-3}$ | $3.635{\cdot}10^{-3}$ | $3.704{\cdot}10^{-3}$ | $-0.069{\cdot}10^{-3}$ | $-0.135{\cdot}10^{-3}$ | 0.511 |
| $C_P$ | $3.477{\cdot}10^{-3}$ | $3.703{\cdot}10^{-3}$ | $3.601{\cdot}10^{-3}$ | $0.102{\cdot}10^{-3}$ | $-0.226{\cdot}10^{-3}$ | -0.451 |
| $\zeta_{0-WG}$ [m] | $1.774{\cdot}10^{-2}$ | $1.839{\cdot}10^{-2}$ | $1.579{\cdot}10^{-2}$ | $0.26{\cdot}10^{-2}$ | $-0.065{\cdot}10^{-2}$ | -4.000 |
| $\zeta_{W-WG}$ [m] | $1.228{\cdot}10^{-3}$ | $2.006{\cdot}10^{-3}$ | $2.594{\cdot}10^{-3}$ | $-0.588{\cdot}10^{-3}$ | $-0.778{\cdot}10^{-3}$ | 0.746 |
| $\zeta_W/\zeta_{target}$ | 0.94 | 0.96 | 0.97 | -0.01 | -0.02 | 0.500 |

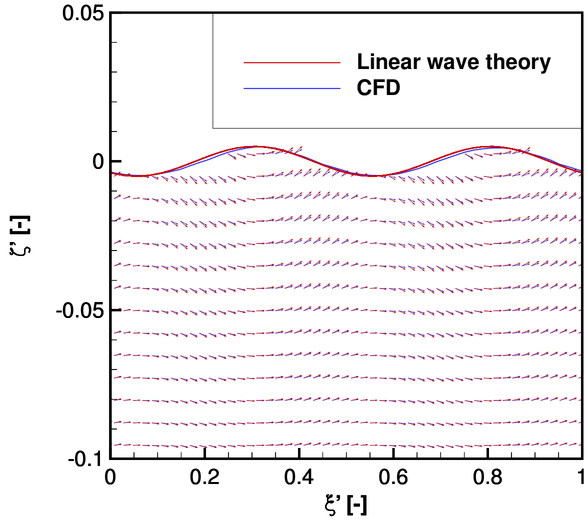


**Figure 5.7.:** Comparison of analytical and numerical wave characteristics at $\eta' = 0.9$ and $0 \leq \xi' \leq 1$

A symmetry plane was used at $\eta' = 0$ for the grid dependency analysis (domain type 1). For further computations with e.g. beam seas, the size of the individual grids at least doubles (domain type 2), which increases the necessary computational time. Furthermore, the accuracy of the resolved amplitude is already very satisfactory for grid #2 with 96%. The resolved wave system for the calm water case is satisfactory as well for grid #2 and the resistance components of the individual grid dependency analyses seem to be of a high enough accuracy. Taking into account all these circumstances and making a compromise between accuracy and computational time, grid #2 will be used for all further simulations.

## 5.5. Time step dependency

A time step dependency has been performed for the ship with moonpool in calm water, as well as in waves. The most important results, which need to show a time step convergence are 1) the oscillating amplitudes inside the moonpool $\zeta_{WG}$, 2) resistance coefficients of the ship ($C_T$, $C_P$, $C_F$) and 3) the incoming wave amplitude $\zeta_W$. Time step convergence study is equally done as for the grid convergence.

The oscillation inside the moonpool can be caused by flow separation in calm water conditions, or excited through waves, as has been already discussed in chapter 1. One can assume that a sufficient accuracy of wave amplitude will cause an oscillation inside the moonpool in any case. Hence, it needs to be shown that the oscillation also occurs

**Table 5.6.:** Resistance coefficients for total resistance ($_T$), frictional ($_F$), pressure ($_P$) components and mean dominant amplitude for moonpool 'SD' in calm water

| $\Delta t'$ | 0.0005 | 0.001 | 0.002 | 0.005 | 0.01 |
|---|---|---|---|---|---|
| $C_T$ | $5.882 \cdot 10^{-3}$ | $5.895 \cdot 10^{-3}$ | $5.957 \cdot 10^{-3}$ | $6.052 \cdot 10^{-3}$ | $6.157 \cdot 10^{-3}$ |
| $C_F$ | $3.907 \cdot 10^{-3}$ | $3.895 \cdot 10^{-3}$ | $3.882 \cdot 10^{-3}$ | $3.887 \cdot 10^{-3}$ | $3.881 \cdot 10^{-3}$ |
| $C_P$ | $1.975 \cdot 10^{-3}$ | $2.000 \cdot 10^{-3}$ | $2.075 \cdot 10^{-3}$ | $2.165 \cdot 10^{-3}$ | $2.276 \cdot 10^{-3}$ |
| $\zeta_{0-WG}$ [m] | $1.744 \cdot 10^{-2}$ | $1.725 \cdot 10^{-2}$ | $1.840 \cdot 10^{-2}$ | $2.517 \cdot 10^{-2}$ | $3.366 \cdot 10^{-2}$ |

**Table 5.7.:** Verification of time step convergence for moonpool 'SD' in calm water

| | $\epsilon_{t,21}$ | $\epsilon_{t,32}$ | $\epsilon_{t,43}$ | $\epsilon_{t,54}$ | $R_{t,1-3}$ | $R_{t,2-4}$ | $R_{t,3-5}$ |
|---|---|---|---|---|---|---|---|
| $C_T$ | $0.013 \cdot 10^{-3}$ | $0.062 \cdot 10^{-3}$ | $0.095 \cdot 10^{-3}$ | $0.105 \cdot 10^{-3}$ | 0.210 | 0.653 | 0.905 |
| $C_F$ | $-0.012 \cdot 10^{-3}$ | $-0.013 \cdot 10^{-3}$ | $0.005 \cdot 10^{-3}$ | $-0.006 \cdot 10^{-3}$ | 0.923 | -2.600 | -0.833 |
| $C_P$ | $0.025 \cdot 10^{-3}$ | $0.075 \cdot 10^{-3}$ | $0.090 \cdot 10^{-3}$ | $0.111 \cdot 10^{-3}$ | 0.333 | 0.833 | 0.810 |
| $\zeta_{0-WG}$ [m] | $-0.019 \cdot 10^{-3}$ | $0.115 \cdot 10^{-2}$ | $0.677 \cdot 10^{-2}$ | $0.849 \cdot 10^{-2}$ | -0.165 | 0.170 | 0.797 |

in calm water conditions and that this is independent of the chosen time step. Table 5.6 shows results of the time step dependency for the calm water case and table 5.7 the corresponding convergence ratios, both for the ship with moonpool 'SD'.

The overall time step convergence can be seen as very good. The pressure resistance component converges monotonically with decreasing time step. The convergence ratios of the frictional resistance component are less distinct, although it should be mentioned that the respective differences $\epsilon$ are of very small magnitude. The total resistance component converges strong monotonically for all time steps. The mean dominant amplitude inside the moonpool converges monotonically for the larger time steps and oscillatory for the smallest.

Furthermore, a time step dependency analysis has been done for the ship with moonpool 'MP' in waves. The focus in this case laid on the investigation of the wave amplitude. Moreover, this case has additionally to the oscillating amplitude at piston mode frequency $\zeta_{0-WG}$ an amplitude corresponding to the wave frequency $\zeta_{W-WG}$. The smallest investigated wave has been used for this analysis, which has a non-dimensional wave length of $\lambda_W/L_{PP} = 0.5$ and a non-dimensional amplitude of $\zeta'_W = 5 \cdot 10^{-3}$. The non-dimensional time step $\Delta t' = 0.01$ has been to large and caused divergence within the first time iteration. Therefore, only time steps between $\Delta t' = 0.005$ and 0.00025 are shown. Table 5.8 contains the resistance coefficients, oscillation amplitude due to piston and wave frequency and the accuracy of wave amplitude. The time step $\Delta t' = 0.005$ had some problems with convergence and had to be run with an increased artificial diffusion coefficient for the level

**Table 5.8.:** Resistance coefficients for total resistance ($_T$), frictional ($_F$), pressure ($_P$) components, mean dominant amplitude for moonpool 'MP' in regular waves of $\lambda_W/L_{PP} = 0.5$ and wave accuracy $\zeta_W/\zeta_{target}$

| $\Delta t'$ | 0.00025 | 0.0005 | 0.001 | 0.002 | *0.005* |
|---|---|---|---|---|---|
| $C_T$ | $7.135 \cdot 10^{-3}$ | $7.170 \cdot 10^{-3}$ | $7.264 \cdot 10^{-3}$ | $7.338 \cdot 10^{-3}$ | $\mathit{6.878 \cdot 10^{-3}}$ |
| $C_F$ | $3.652 \cdot 10^{-3}$ | $3.654 \cdot 10^{-3}$ | $3.652 \cdot 10^{-3}$ | $3.635 \cdot 10^{-3}$ | $\mathit{3.672 \cdot 10^{-3}}$ |
| $C_P$ | $3.484 \cdot 10^{-3}$ | $3.517 \cdot 10^{-3}$ | $3.612 \cdot 10^{-3}$ | $3.703 \cdot 10^{-3}$ | $\mathit{3.206 \cdot 10^{-3}}$ |
| $\zeta_{0-WG}$ [m] | $1.786 \cdot 10^{-2}$ | $1.800 \cdot 10^{-2}$ | $1.838 \cdot 10^{-2}$ | $1.839 \cdot 10^{-2}$ | $\mathit{1.308 \cdot 10^{-2}}$ |
| $\zeta_{W-WG}$ [m] | $2.275 \cdot 10^{-3}$ | $2.342 \cdot 10^{-3}$ | $2.227 \cdot 10^{-3}$ | $2.006 \cdot 10^{-3}$ | $\mathit{5.253 \cdot 10^{-4}}$ |
| $\zeta_W/\zeta_{target}$ | 0.96 | 0.96 | 0.96 | 0.96 | *0.78* |

**Table 5.9.:** Verification of time step convergence for moonpool 'MP' in regular waves of $\lambda_W/L_{PP} = 0.5$

| | $\epsilon_{t,21}$ | $\epsilon_{t,32}$ | $\epsilon_{t,43}$ | $\epsilon_{t,54}$ | $R_{t,1-3}$ | $R_{t,2-4}$ | $R_{t,3-5}$ |
|---|---|---|---|---|---|---|---|
| $C_T$ | $0.035 \cdot 10^{-3}$ | $0.094 \cdot 10^{-3}$ | $0.074 \cdot 10^{-3}$ | $-0.460 \cdot 10^{-3}$ | 0.372 | 1.270 | -1.609 |
| $C_F$ | $0.002 \cdot 10^{-3}$ | $-0.002 \cdot 10^{-3}$ | $-0.017 \cdot 10^{-3}$ | $0.037 \cdot 10^{-3}$ | -1 | 0.118 | -0.459 |
| $C_P$ | $0.033 \cdot 10^{-3}$ | $0.095 \cdot 10^{-3}$ | $0.091 \cdot 10^{-3}$ | $-0.497 \cdot 10^{-3}$ | 0.347 | 1.044 | -0.183 |
| $\zeta_{0-WG}$ [m] | $0.014 \cdot 10^{-3}$ | $0.038 \cdot 10^{-2}$ | $0.001 \cdot 10^{-2}$ | $-0.531 \cdot 10^{-2}$ | 0.368 | 38 | -0.002 |
| $\zeta_{W-WG}$ [m] | $0.067 \cdot 10^{-3}$ | $-0.115 \cdot 10^{-3}$ | $-0.221 \cdot 10^{-3}$ | $-1.481 \cdot 10^{-3}$ | -0.583 | 0.520 | 0.149 |
| $\zeta_W/\zeta_{target}$ | 0 | 0 | 0 | -0.18 | $\infty$ | $\infty$ | 0 |

set transport equation. Therefore, the wave accuracy is poor and all other parameters are affected. For all other results it can be seen that especially the frictional resistance component is very similar and barely changes. The pressure resistance component decreases slightly with decreasing time step and hence does the total resistance component. The respective convergence ratios are listed in table 5.9 and show a good convergence for the three smallest time steps ($R_{t,1-3}$) and a satisfactory behaviour for the medium three time steps ($R_{t,2-4}$). Total and pressure resistance coefficient are however diverging, yet with small magnitude. The same applies for both oscillation amplitudes, which remain of very similar magnitude from $\Delta t' = 0.002$ on. The wave accuracy is already at 96% for $\Delta t' = 0.002$ and is not improving further with decreasing time step. Convergence ratios for the discussed amplitudes should be taken with care, as the absolute change is small.

Although a convergence towards the smallest time step is indicated from the time step analysis in waves, a compromise had to be found between accuracy of the individual results and computational time. Therefore, $\Delta t' = 0.002$ has been chosen for all further simulations. Especially the oscillating amplitudes and wave amplitudes are already of satisfactory convergence at $\Delta t' = 0.002$.

At last, a comparison of cases with a constant non-dimensional time step $\Delta t'$ and a constant dimensional time step $\Delta t$ has been conducted for different Froude numbers. Results are shown in figure 5.8 and 5.9. For constant non-dimensional time steps, $\Delta t' = 0.002$ was used for all Froude numbers investigated. The dimensional time step $\Delta t$ was kept identical with the non-dimensional time step for the case of $Fr = 0.15$ and adjusted accordingly with changing Froude numbers, as is shown in figure 5.8a. The mean piston mode amplitudes and frequencies inside moonpool MP are compared. One can observe, that the mean amplitude remains identical over almost all Froude numbers. The largest deviation occurs for $Fr = 0.21$ with a deviation of 14 %. The simulation for constant dimensional Froude number at $Fr = 0.23$ diverged and is therefore not included.

A disagreement can be seen when comparing the respective frequencies. The agreement is still good at $Fr = 0.12$. For $Fr = 0.09$ and $Fr = 0.06$ the results are somewhat more ambiguous, although it should be mentioned that their respective oscillation amplitudes are small and hence of less significance. For both Froude numbers, the frequency of around 1.4 Hz dominate over a smaller frequency for the constant dimensional time step. The opposite behaviour occurs for the constant non-dimensional time step, where the higher frequency is not visible, respectively less pronounced. This higher frequency is close to the first sloshing mode of $f_1 = 1.61$ Hz (refer to chapter 6.1.1 for description) and visualisation of the free surface in the numerics and experiments confirmed a sloshing type behaviour for these Froude numbers. The time series at WG3 for both time step approaches for $Fr = 0.09$ are exemplary shown in figure 5.9a. The occurrence of the sloshing frequency cannot be directly explained by the decreasing time step. The frequency of $f_{0-WG} = 1.38$ Hz equals a period of approx. 0.7 s. The dimensional time step equals $\Delta t \approx 0.01$ s and is hence 70 times smaller than the period to be detected. As the experiments confirmed a sloshing type behaviour, the constant dimensional time yields better results for the lowest Froude numbers, than the non-dimensional constant time step.

The above described disagreement could not be detected for higher Froude numbers, as can be exemplary seen in figure 5.9b, showing the time series at WG3 for $Fr = 0.18$. Amplitudes are almost identical and only a slight shift in frequency is visible.

Note also from figure 5.8b that the influence on resistance coefficients is negligible for this study.

Concluding from this study, it is better to decrease the non-dimensional time step according to figure 5.8a for the lowest Froude numbers of $Fr = 0.06$ and $Fr = 0.09$, in order to resolve the oscillation inside the moonpool correctly. For higher Froude numbers than $Fr = 0.12$ it is of less importance which time step is kept constant, as the results are not affected significantly.

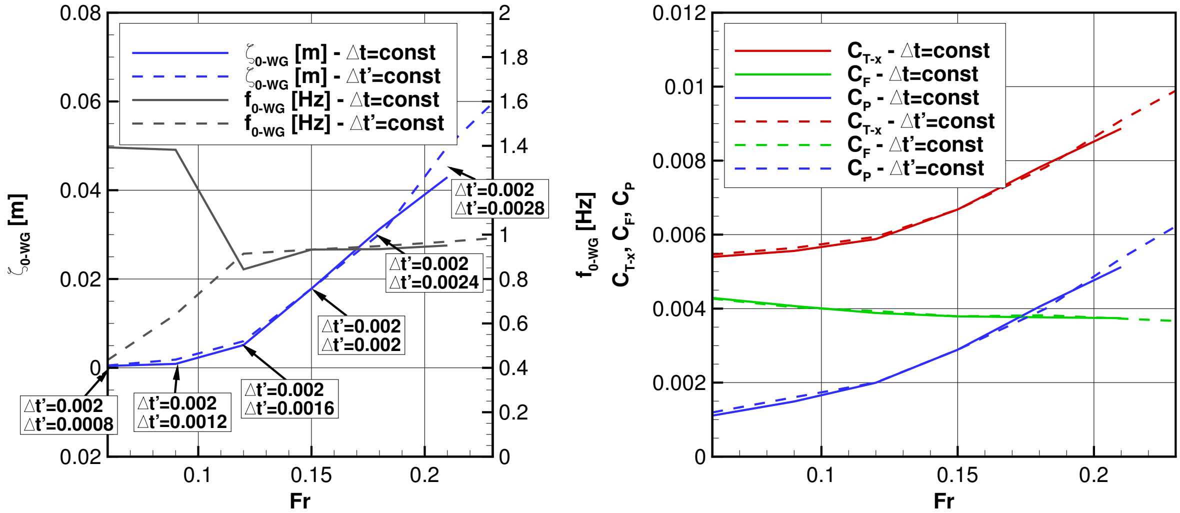


**(a)** Mean amplitude and frequencies **(b)** Resistance coefficients

**Figure 5.8.:** Comparison of constant dimensional and constant non-dimensional time step

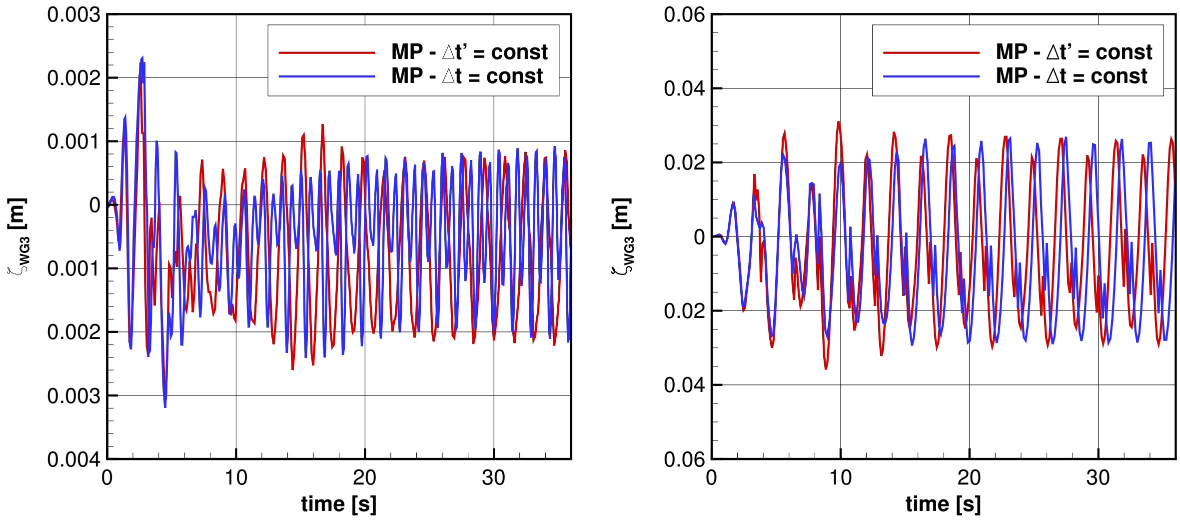


**(a)** Oscillation for $Fr = 0.09$ **(b)** Oscillation for $Fr = 0.18$

**Figure 5.9.:** Comparison of time series at WG3 with constant dimensional and constant non-dimensional time step

## 5.6. Influence of turbulence model

This section briefly describes the influence of different turbulence models, which have been investigated in this work. There have been done simulations with two different turbulence models, namely a RANS and a DDES model, both based on the $k$-$\omega$-$SST$ model. Furthermore, the RANS model has been used with and without wall functions. The general characteristics of these models have been already explained in detail in chapter 2.2. Table 5.10 shows the differences between those two models using no wall functions. The simulations have been conducted on the same grid, whose cell resolution is appropriate for both turbulence models. It can bee seen, that the resistance increases slightly using DDES, compared to RANS simulations. This is mainly due to the increased pressure resistance, resulting from a more detailed vorticity in the moonpool. The increase in computational time would be acceptable with approximately 6%. The different resolution in the vorticity can bee seen in figure 2.2 on page 20 which shows the same time step once for a RANS simulation (left) and a DDES simulation (right). Furthermore, a slightly higher three-dimensionality of the free surface can be seen for the DDES simulation compared to the RANS simulation.

The time step dependency from chapter 5.5 has been repeated for the DDES model. Figure 5.10a shows the comparison of the mean free surface oscillation amplitude inside the moonpool for both turbulence models. While the RANS model has a very good time step convergence towards the experimental value (shown in orange), DDES shows a strong divergence. The oscillation inside the moonpool almost vanishes for decreasing time steps. This also affects the pressure resistance component and hence the total resistance component, which are shown in figure 5.10b. While the RANS model shows a good convergence (as has already been discussed in chapter 5.5), the resistance components diverge, when using DDES with a decreasing time step.

This result is somewhat surprising, as no direct reason has been found for divergence of DDES. Although this does not explain the time step divergence, it should be noted that the grid in front of the leading edge of the moonpool has a value for $\Delta \approx \delta_{99}/5$,

**Table 5.10.:** Comparison of resistance coefficient components between RANS and DDES

| | RANS | DDES | $\Delta_{RANS}$ |
|---|---|---|---|
| $C_T$ | $5.957 \cdot 10^{-3}$ | $6.123 \cdot 10^{-3}$ | +2.8% |
| $C_F$ | $3.882 \cdot 10^{-3}$ | $3.875 \cdot 10^{-3}$ | −0.2% |
| $C_P$ | $2.075 \cdot 10^{-3}$ | $2.248 \cdot 10^{-3}$ | +8.3% |

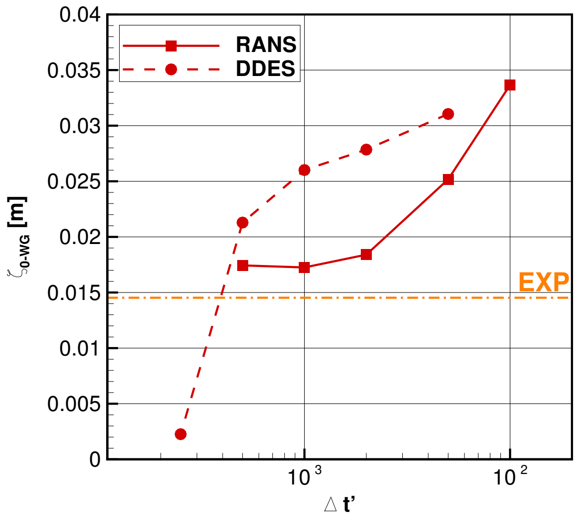


**(a)** Mean wave gauge amplitude in moonpool

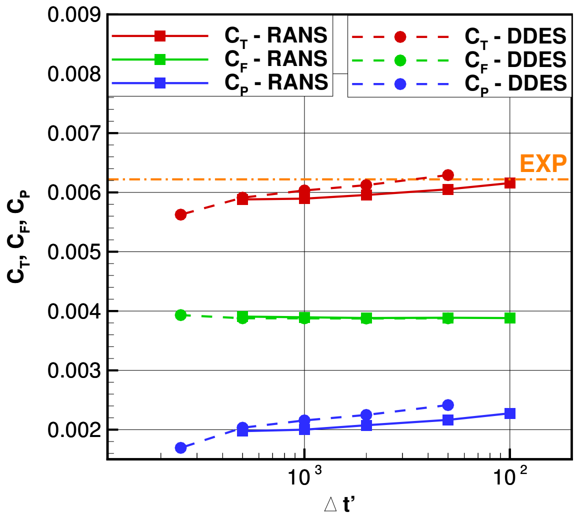


**(b)** Restistance components

**Figure 5.10.:** Time step dependency for moonpool 'SD' comparing RANS and DDES

defined through the grid spacing in longitudinal direction and is hence lower than recommended values, as mentioned on page 21. These ambiguous grids should however be treated correctly using DDES instead of DES, as has been used in this work and would not explain the divergence. The grid inside the moonpool can be seen as isotropic and hence ideal for LES mode in DDES. In order to further investigate the reason for divergence of DDES, the following recommendations are given. With the change from DES to DDES, the turbulence model became time dependent. This is due to the dependency on the boundary layer, whereas DES has been solely dependent on the grid size. The time step dependency could be repeated using DES to check if divergence occurs again. Two vortices originating from the forefoot are contracting the boundary layer in front of the moonpool, as will be explained in chapter 5.8. The time step dependency could hence be repeated without the forefoot to investigate if this boundary layer contraction is influencing the turbulence model behaviour. At last, the grid could be adapted to fulfil the above mentioned recommendations of cell length to boundary layer thickness. This could also give an insight, if Courant numbers are playing an import role on DES respectively DDES models.

It was expected that both models, DDES and RANS, would yield the same convergence with slight differences in resistance components due to higher resolution of vortices using DDES. Due to that finding, it was decided to disregard DDES and use the RANS model for all simulations instead.

### 5.6.1. Wall functions

It was tested, if use of wall functions would be feasible for this study. New grids were generated, which mainly differed in the cell distribution in wall-normal direction. However, some other cell distributions needed to be adapted, in order for the hyperbolic grid generator to produce valid grids. These changes were kept to a minimum, to ensure best comparability with the grids without use of wall functions. The dimensionless wall distance was set to $y^+ \approx 80$. When using the settings for *REX* from the simulations without wall functions, a problem with the free surface occurred. The parameter `wav_blank` is used to define a distance from the wall, within which the points are blanked and solutions taken from the next neighbouring point. If not blanked, the no-slip condition at the wall ($\dot{\xi}_i = 0$) would be used for the transport of the level set equation. This would lead to a free surface, which does not move were being in contact with a wall. Until now, `wav_blank` was set to $3 \cdot 10^{-4}$, marked with the black dotted line in figure 5.11. The solid red line shows the mean wave gauge amplitude inside the moonpool for the case using wall functions for different `wav_blank` parameters. One can see that a small `wav_blank` parameter reduces the free surface oscillation to a minimum. This is due to the effect that the free surface remains at $z = 0$ were being in contact with a wall. This suppresses the deflection of the free surface almost completely as is shown on the left side in figure 5.11a for the free surface in the moonpool. If `wav_blank` is increased the contact problem vanishes and the free surface oscillates as expected (shown on the right side in figure 5.11a). The red dashed line shows the mean wave gauge amplitude which has been determined from simulations without wall functions. Figure 5.11b shows the same investigation for the resistance components. The solid lines show the case for wall functions which remains quite constant for small `wav_blank` parameters and drops when increasing `wav_blank` above $10^{-3}$ until the simulation diverges. Dashed lines again show the respective values when using no wall functions.

As the grid resolution in wall-normal direction has been decreased when using wall functions, `wav_blank` smaller than $10^{-3}$ lead to no cell blanking, as the first cell thickness is approx. $7 \cdot 10^{-4}$. This is causing the contact problems, as the zero velocity at the walls are used for the transport of level set equation. This parameter should hence be greater than the smallest cell layer thickness. However, `wav_blank` also affects the determination of forces, which is why a drop in resistance coefficients occurs for larger `wav_blank` parameters.

To overcome the uncertainty of choosing an appropriate value for `wav_blank`, a new parameter `nblank` was implemented into *REX*, which uses a fixed number of points from

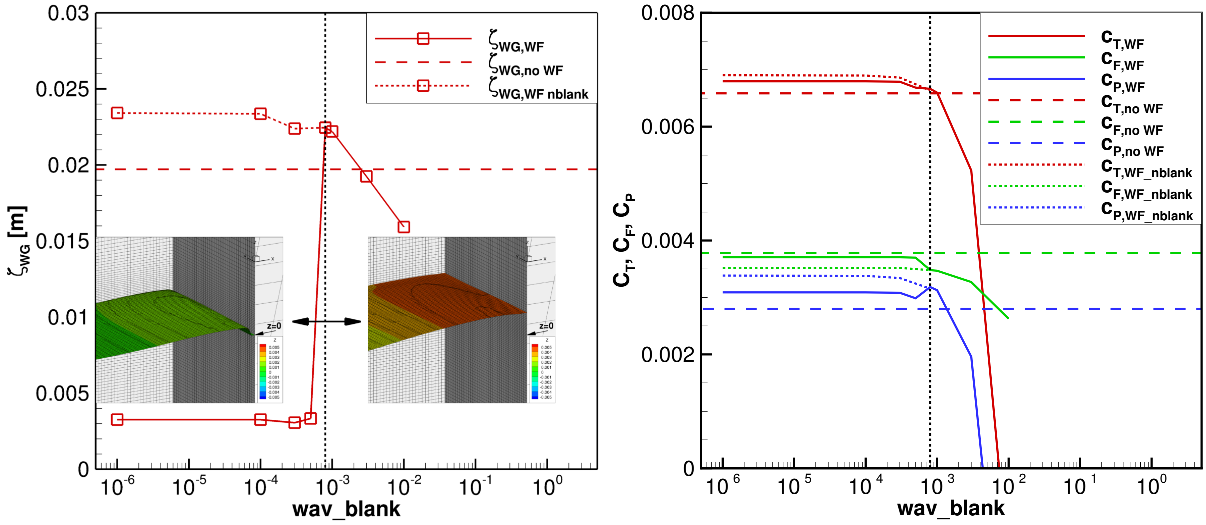


**(a)** Mean wave gauge amplitude **(b)** Restistance components

**Figure 5.11.:** Influence of parameter `wav_blank` when using wall functions

the wall being blanked, instead of a distance. The result is shown in the dotted lines in figure 5.11. Using the parameter `nblank` to blank the first cell at the walls, one can choose small values for `wav_blank`, to maintain constant resistance coefficients. Although the total resistance component is almost identical to the case without wall functions, the frictional and pressure resistance deviate a little, but counteract each other.

A grid dependency analysis has been conducted using the parameter `nblank` and `wav_blank` of $3 \cdot 10^{-4}$ as has been set when using no wall functions. Unfortunately, this analysis showed a diverging behaviour of the pressure and hence total resistance component, as can be seen in figure 5.12a. The oscillation frequency and mean wave gauge amplitude inside the moonpool remain similar, which is shown in figure 5.12b.

Analysing of the pressure component for all three grids individually for the hull and moonpool is shown in figure 5.13 for a short time span. The left figure shows the pressure coefficient which is acting solely on the moonpool. One can see that a change in phase and amplitude occurs from coarse to medium grid, but no significant changes happen when using the fine grid. This leads to the conclusion that the grid resolution would be fine enough to predict the pressure acting on the moonpool using the medium grid. The right figure shows the pressure coefficient acting on the hull (excluding the moonpool surfaces). Here, a significant difference can be seen between all three grids.

A significant change in pressure from medium to fine grid occurs somewhere at the hull. One possibility would be a separation at the stern region which has not been captured

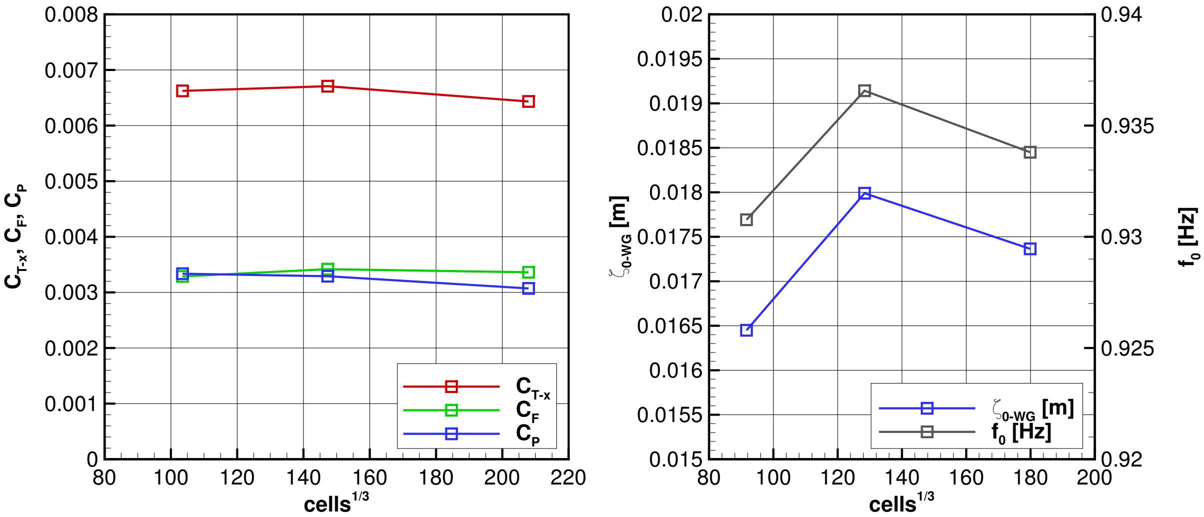


**(a)** Restistance components

**(b)** Mean wave gauge amplitude and piston mode frequency

**Figure 5.12.:** Grid dependency for resistance components and mean oscillation amplitude and frequency inside the moonpool 'MP'

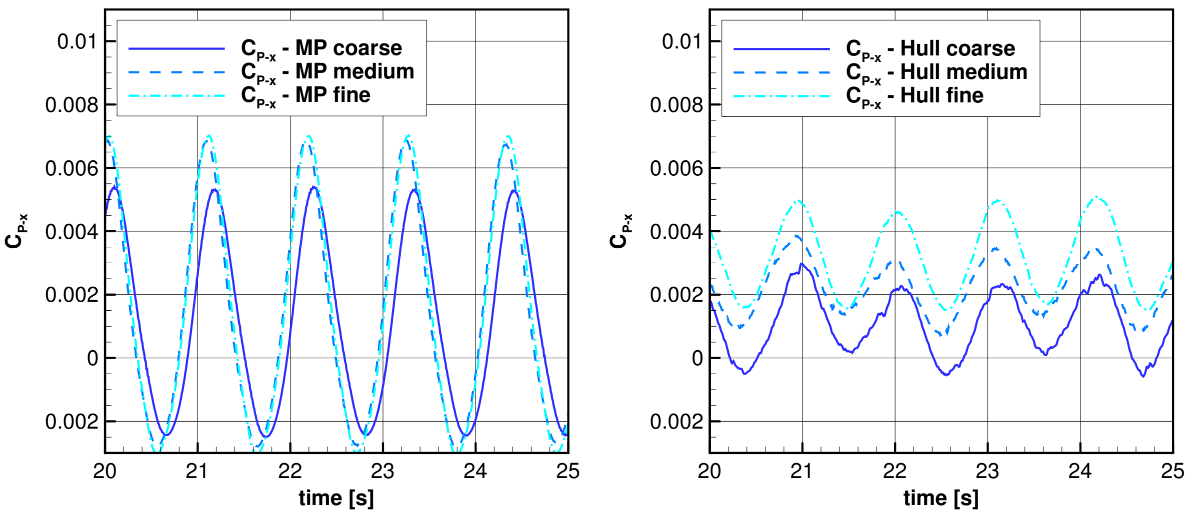


**(a)** Pressure component acting on the moonpool

**(b)** Pressure component acting on the hull

**Figure 5.13.:** Pressure components on moonpool and hull for grid dependency analysis

until using the fine grid. To overcome this, further refinement would probably solve the issue.

Due to these findings it was decided to use the RANS model without wall functions, as this showed a clear time step and grid convergence and therefore the highest reliability.

## 5.7. Influence of motion restrictions

This section deals with the effects of restraining individual degrees of freedom. It is especially of interest for numerical simulations to know which degree of freedom has strong influences on the results, not only on resistance or coupled motions, but in this case also on the moonpool characteristics. Several tests, numerically and experimentally, have been performed. The experiments have been conducted with the ship at rest and a wave encountering angle of $\mu_W = 45°$. Due to the measuring platform, the DOF that could be restrained were heave & pitch combined, yaw and roll. Note that a restriction of surge would have been feasible as well, but has not been included into this matrix. The model was exposed to regular waves. Forces, moment, motions and oscillation amplitudes have been measured. Comparison is made with the same situations, where no restriction of DOF is applied and the model is kept at place using springs.

Heave and pitch could only be investigated combined, as the heave rods were fixed using brackets, which restrains both motions. Yaw motion was suppressed by connecting the fore and aft $\Delta y$-slide. Most problematic was the suppression of roll motion. It is originally allowed through the rod ends. These are further able to leave the pitch motion unrestrained to a certain limit. To suppress the roll motion, the rod ends were turned by 90°, which lead to a completely unrestrained pitch motion and roll motion being allowed to certain limits. The latter was tried to suppress using spacer. This approach was only successful to a certain limit, as the spacer caused an increasing friction in pitch motion and could not completely suppress the roll motion. A new rod end construction would have been necessary, to accurately restrain rolling. As it was not possible to suppress the roll motion in a satisfactory way, the results are excluded and only the investigation of heave & pitch as well as yaw is shown for the experimental part. The results in terms of RAO for moonpool oscillation are shown in figure 5.14. The longitudinal and transversal force amplitudes, as well as the yaw moment amplitudes are shown in figure 5.15. At last, motions are presented in figure 5.16, where an influence of suppression of individual DOF was detected. Other DOF which were not affected are listed in appendix C.1. The results for each DOF are discussed together with the numerical analysis in the following

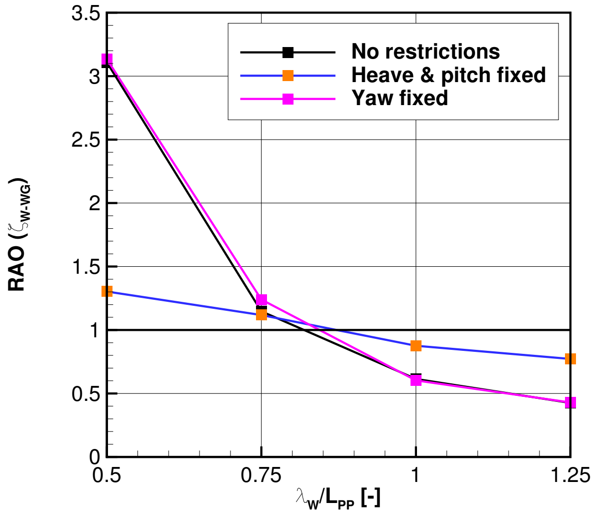


**Figure 5.14.:** Influence of motion restriction on moonpool oscillation amplitude

subsections.

The numerical investigation focused on analysing the influence of restraining motions at forward velocity. Simulations were conducted at $Fr = 0.15$ and wave encountering angles of $\mu_W = 0°$ to investigate suppression of surge, heave and pitch, $\mu_W = 45°$ for yaw and $\mu_W = 90°$ for roll and sway. Figure 5.17 is showing the RAO's of oscillation amplitudes due to piston mode frequency (dashed lines) and wave frequency (solid lines) inside the moonpool for the three different wave angles and their respective restrained motions. The black lines represent the case without motion restraining and the coloured lines each individual restrained DOF. The longitudinal force amplitudes for $\mu_W = 0°$, transversal force amplitudes for $\mu_W = 90°$ and yaw moment amplitudes for $\mu_W = 45°$ are shown in figure 5.18. Note that the forces for the case of restrained yaw motion have a similar agreement as the moment and are therefore not shown. At last, figure 5.19 presents individual motions, where a restraining of DOF had an effect on. All other motion parameters, which did not show significant differences between the unrestrained and restrained case are listed in appendix C.1.

### Surge

Restraining the surge motion has no effect on the moonpool characteristics. Its influence on motions is little as well. Only at $\lambda_W/_{PP} = 1.25$ can be seen a slight deviation in heave amplitude (see figure 5.19a). This is probably also the reason for a slight deviation in longitudinal force in figure 5.18a. Other wave lengths show exactly identical mean forces. This agrees with findings from Uharek & Cura Hochbaum [78],

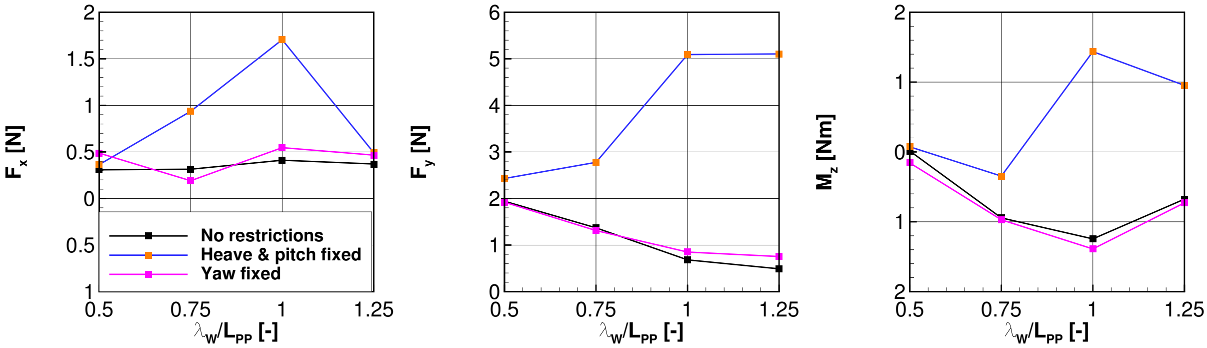


(a) Longitudinal force (b) Transversal force (c) Yaw moment

**Figure 5.15.:** Influence of motion restriction on force and moment amplitudes

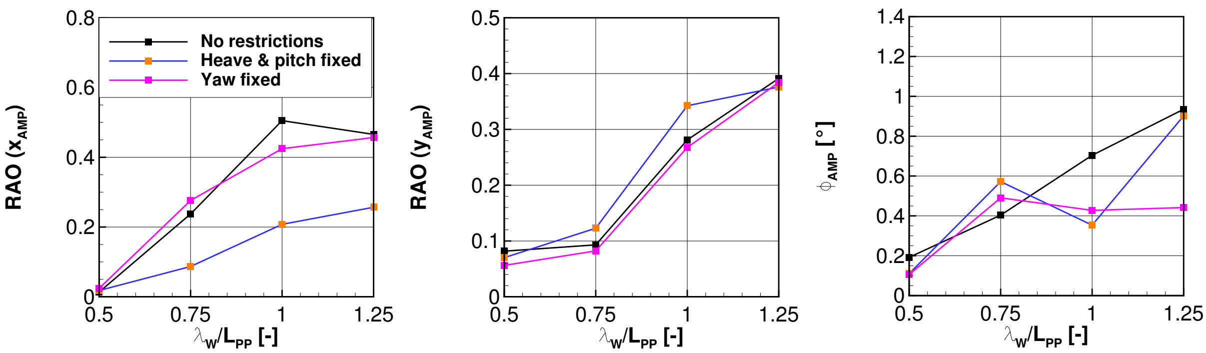


(a) Surge motion (b) Sway motion (c) Roll motion

**Figure 5.16.:** Influence of motion restriction on other DOF

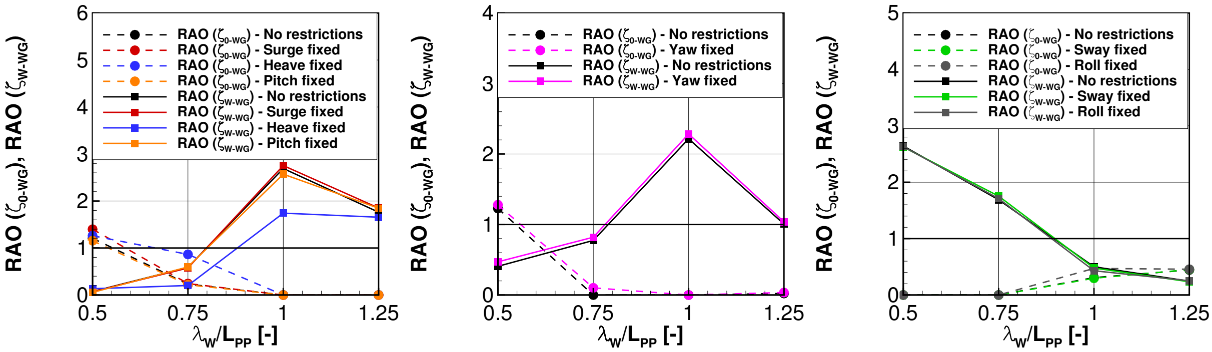


**(a)** Restriction of surge, heave and pitch at $\mu_W = 0°$

**(b)** Restriction of yaw at $\mu_W = 45°$

**(c)** Restriction of sway and roll at $\mu_W = 90°$

**Figure 5.17.:** Influence of motion restriction on moonpool oscillation amplitude at piston and wave frequency

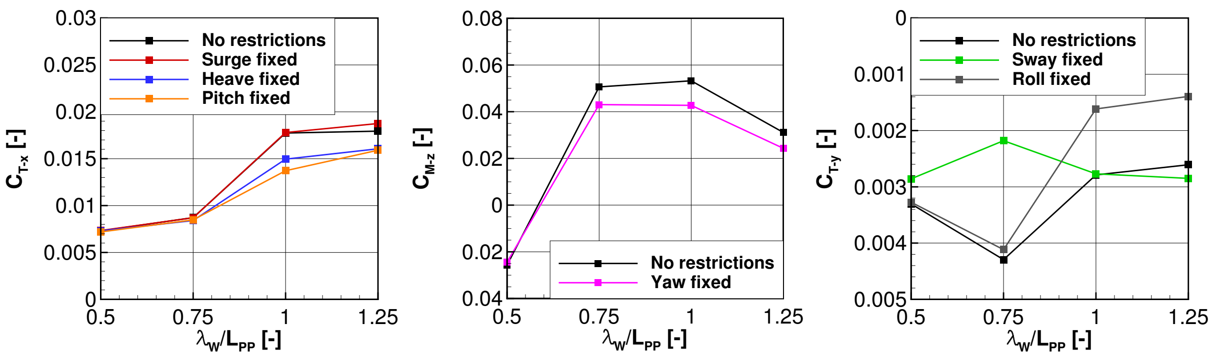


**(a)** Restriction of surge, heave and pitch at $\mu_W = 0°$

**(b)** Restriction of yaw at $\mu_W = 45°$

**(c)** Restriction of sway and roll at $\mu_W = 90°$

**Figure 5.18.:** Influence of motion restriction on force and moment amplitudes

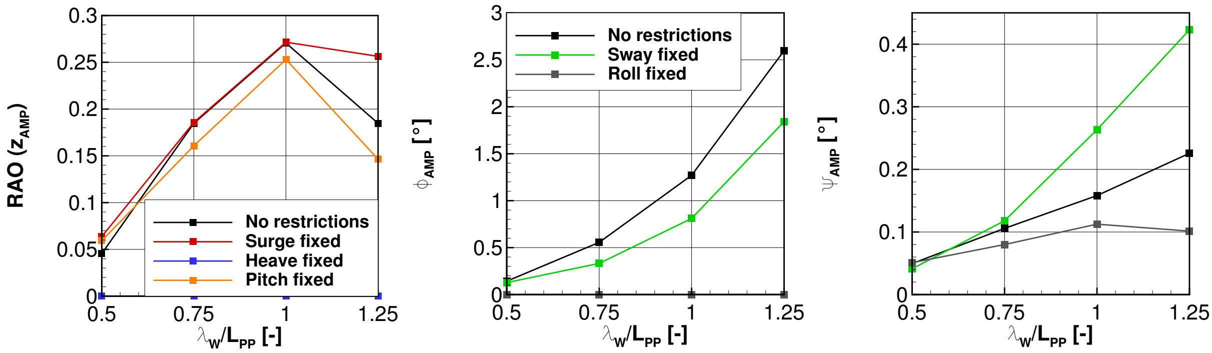


**(a)** Restriction of surge, heave and pitch at $\mu_W = 0°$

**(b)** Restriction of sway and roll at $\mu_W = 90°$

**(c)** Restriction of sway and roll at $\mu_W = 90°$

**Figure 5.19.:** Influence of motion restriction on other DOF

where different restoring forces have been investigated and no influence on mean forces was observed.

### Sway

The moonpool characteristic is not changed if swaying is suppressed. It seems to affect however the roll and yaw amplitude at longer waves (see figure 5.19b and 5.19c). As this case has been done at $\mu_W = 90°$, the magnitudes of yaw motion are small and hence the inaccuracy through restraining of sway negligible. The roll motion is showing a more clear dependency on the correct swaying behaviour. A major deviation of the side force when restraining swaying can only be detected for $\lambda_W/L_{PP} = 0.75$ (see figure 5.18c), whereas it agrees well with the unrestrained cases for all other wave lengths.

### Heave

The heave amplitude has a major influence, as can be seen in the experimental investigation (which is combined with a restriction of pitching). The RAO of wave induced oscillation inside the moonpool is significantly lower for $\lambda_W/L_{PP} = 0.5$, than without any restriction for the ship at rest and $\mu_W = 45°$ (figure 5.14). This effect will be further investigated in chapter 6.2. The RAO is then slightly overestimated for the two longest waves. For the case at $Fr = 0.15$ the amplitude induced by wave frequency is underestimated for almost all wave lengths (figure 5.17a). Only the amplitude at piston mode frequency for $\lambda_W/_{PP} = 0.75$ is overestimated. Suppression of heave influenced the surge and roll amplitude for the ship at rest (figure 5.16a and

5.16c). Only a minor influence can be seen for the swaying motion (figure 5.16b). An effect on other DOF through restriction of heaving has not been detected by the conducted investigations. The influence on forces and moment when restraining heave can be seen from the experimental cases in figure 5.15 (remember, these figures show a combined heave & pitch restriction) and for the longitudinal force for a pure heave restriction in figure 5.18b. Despite for the shortest wave, a clear dependence on the correct heave motion can be seen for all forces and the yaw moment, as was expected.

### Roll

No influence can be detected on oscillating amplitudes inside the moonpool when restricting the roll motion. Neither are other motions significantly affected (as can be further seen in appendix C.1). When investigating the side force at $\mu_W = 90°$, reduced magnitudes are observed for the two longest waves (figure 5.18c), when restraining the roll motion.

### Pitch

As pitching was restrained in the experimental investigation combined with heave, no clear effect of pitching can be determined from this investigation. By comparing the numerical results for restricted pitch motion with no restriction, it seems however that pitching does not have any effect on the moonpool characteristics (figure 5.17a). A minor coupling effect can be seen for the heave motion, which is slightly underestimated for the longest wave (figure 5.19a). A clear dependency on the correct pitch motion can be detected from experimental results of force and yaw moment amplitudes (figure 5.15) and numerical results for the longitudinal force amplitudes (figure 5.18a).

### Yaw

Restraining the yaw motion has barely any effect on other parameters. The moonpool oscillation is not affected at all, as can bee seen in figure 5.14 and 5.17b. The same applies for the other DOF which are not affected if yaw is suppressed. Only exemption might be rolling, which is similar from numerical simulations at forward speed, but shows a slight deviation for longer waves in the experimental data at rest (figure 5.16c). The forces and yaw moment are neither affected in the experimental, nor in the numerical investigation, by a restrained yaw motion.

Concluding from the previous discussed results heave and pitch motion are most important to correctly predict moonpool characteristics, forces and yaw moment. The surge and yaw motion on the other hand can be restrained without causing inaccuracies in the results. The sway and roll motion are not of importance for the moonpool oscillations, but might play a role for correct determination of forces or coupled motions and should hence be unrestrained if possible. Note that Gaillard & Cotteleer [34] reported that surge motion promotes the development of sloshing modes inside the moonpool. Their recommendation is to perform tests under self-propelled conditions in order to correctly consider the surge motion. Such an effect has not been detected in this work. It might occur if moonpools with a higher ratio of length to breadth are investigated.

## 5.8. Influence of vortices

It was observed during the numerical simulations that two pronounced vortices are formed below the keel. These vortices originate from the forefoot and extend until the moonpool opening. Their transverse location, when reaching the moonpool, is approximately at the side walls of the moonpool. The severe oscillation inside the moonpool usually causes a breakdown of the vortical structures behind the moonpool. These vortices are shown in figure 5.20, where the iso-Q surface is coloured in the velocity magnitude. The turning direction of the vortices can be seen in figure 5.21a. The differences in the flow field, compared to a simulation without forefoot (figure 5.21b) can be clearly seen. A longitudinal and transverse plane visualise the longitudinal velocity component $u$. The transverse plane is placed right in front of the moonpool leading edge and shows the velocity vector plot in this plane. The longitudinal plane further highlights the boundary layer thickness, which is marked with $\delta_{99}$. The strong vertical and transverse velocities due to the two vortices lead to a compression of the boundary layer in between them. The reduction of boundary layer is of approx. 60%. Furthermore, the inner part of the leading edge experiences a vertical velocity component, while the outer part an even stronger transverse velocity component.

It was investigated if the different flow conditions due to the vortices have a significant influence on the ship and moonpool performance. Figure 5.22 shows the results of simulations in calm water for different Froude numbers with the forefoot (dashed lines) and without (solid lines). The resistance components for both cases are shown in figure 5.22a. The overall performance is pretty similar. The frictional component (green) is slightly reduced when disregarding the forefoot. This however is not due to a smaller

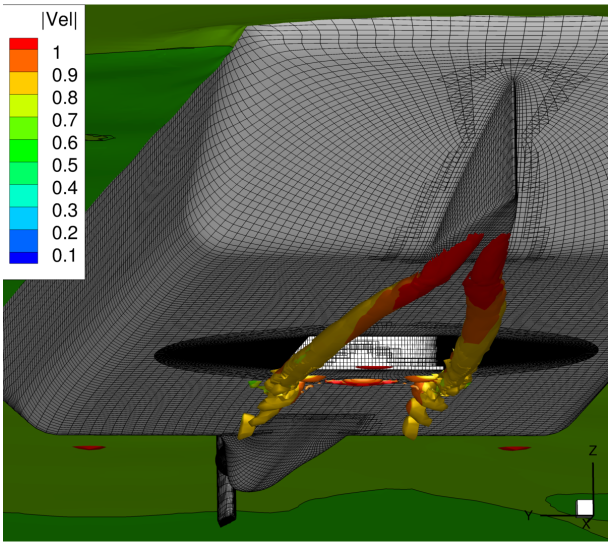


**Figure 5.20.:** Vortices below the keel

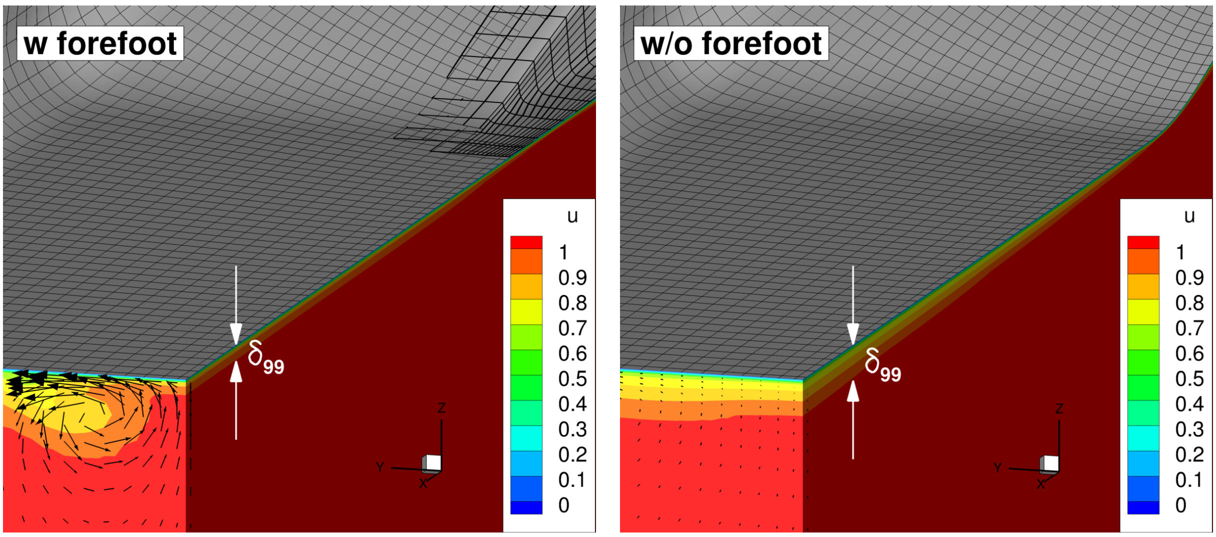


**(a)** Simulation with forefoot **(b)** Simulation without forefoot

**Figure 5.21.:** Boundary layer development and vector plot with and without forefoot

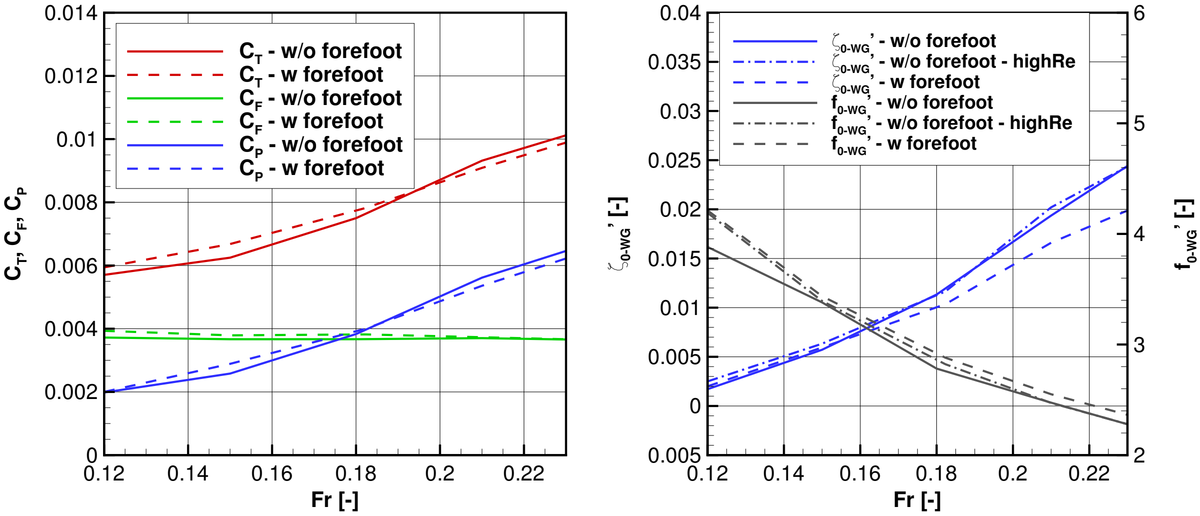


**(a)** Resistance components

**(b)** Mean oscillating amplitude and frequency inside the moonpool

**Figure 5.22.:** Comparison of simulations with and without forefoot

wetted area, as both forces are non-dimensionalised with their respective wetted areas. It is therefore most likely that this effect occurs due to induced velocities through the vortices. The pressure component for the case with forefoot is quite similar for low Froude numbers or slightly higher than without forefoot. Hence, the total resistance component is slightly higher in case of considering a forefoot. This behaviour changes for higher Froude numbers. As can be seen in figure 5.22b the mean amplitude of oscillation inside the moonpool increases if the forefoot is disregarded. The non-dimensional frequency is only slightly lower if no forefoot is present, with a larger drop for $Fr = 0.12$. It should be noted that the ship motions are negligible small and similar in all cases and hence not source of the change in oscillation amplitude.

In order to understand if the boundary layer thickness or the transverse and vertical velocity components are causing this behaviour, further simulations with a higher Reynolds number have been conducted for the ship without forefoot. Those simulations could be performed using no wall functions as well, as the grid allowed increasing $y^+$ values. The maximum Reynolds number until reaching a $y^+ = 1$ for $Fr = 0.23$ was $Re = 3.294 \cdot 10^7$ with $L_{ref} = 14.35\,\mathrm{m}$ compared to $Re = 3.288 \cdot 10^6$ for $L_{ref} = 3\,\mathrm{m}$. Even higher Reynolds numbers and hence smaller boundary layers would have been only achieved, when changing the turbulence model to wall functions and simulating the full scale ship. Due to the above mentioned uncertainties with grid dependence for wall functions, this option was disregarded. The conducted simulations with a 'medium scale ship' lead to a reduction in boundary layer of approx. 26%. Although this equals only half of the reduction compared to the case with forefoot, an indication if the boundary layer has an influence on the moonpool characteristics should be visible. Figure 5.22b shows the non-dimensional oscillation amplitude and frequencies for the case with high Reynolds number with the dashed-dotted lines. Those follow the solid lines, which represent the same simulations with lower Reynolds number and hence larger boundary layer, for almost every situation. The amplitude for higher Froude numbers is not reduced for the case of high Reynolds numbers, as happens for the ship with forefoot. It can therefore be concluded that the source of drop in amplitude is not the boundary layer, but the strong vertical and transverse velocities caused by the vortices originating from the forefoot.

## 5.9. Numerical roll decay test

As already mentioned in chapter 4.3.1, a roll decay test has been performed experimentally. The influence of cable actuated distance sensors on the roll amplitude has been shown by comparison with a roll decay test using an IMU.

The roll decay test was repeated numerically in order to determine the accuracy of roll motion, which will be of importance when simulating beam sea conditions. Neither the experimental model, nor the numerical model had bilge keels attached. The mass, gyradii and initial heel angle were identical as in the experiment. Note that some heaving, pitching and other motions might have occurred in the experiments, but were not taken into account as exact starting conditions in the numerical simulations.

Several parameters had a significant influence on the roll characteristic in the numerical simulations and will be discussed in the following.

A major influence on the numerical results was found in the time step integration method, which is used to determine the ship motions out of the resulting forces respectively accelerations. Figure 5.23a shows a comparison of the different investigated methods for the first roll periods.

The black dashed line represents the experimental roll decay amplitude from the IMU. The first order explicit method (red line) is typically used to find a steady state for sinkage and trim simulations. This is because the method is either 4 point or 8 point averaged, meaning that for the determination of the current time step velocities, the previous four or eight accelerations are included and averaged. Therefore, this method yields increasing roll amplitudes (approximately 1° after 2 roll periods), as the chosen time step is quite

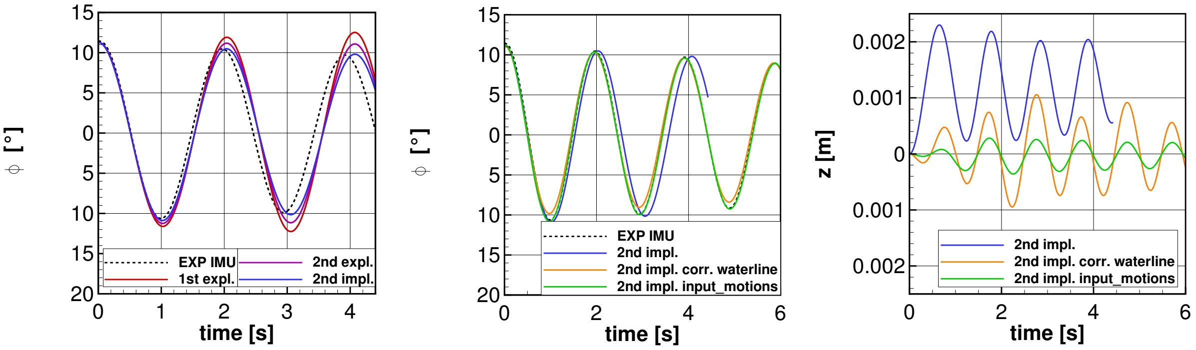


**(a)** Influence of time integration method

**(b)** Influence of initial condition

**(c)** Heave amplitude depending on initial condition

**Figure 5.23.:** Influencing parameters on roll decay test

large ($\Delta t' = 0.002$) and hence the change of motion at the peaks is damped to much, leading to an overshoot.

Afterwards higher order methods were tested. A second order explicit method (purple line) showed some improvements as the roll amplitude did not increase any more, but was kept steady, leading to no significant roll motion reduction. Implicit methods of second order (blue line) and second order using the least-squares method (not shown in the diagram) lead to further improvements. The second order implicit method showed a clear reduction in roll motion amplitude, almost coinciding with the experimental data regarding the amplitudes. The least-squares method lead to identical results as the second order implicit method.

The second order implicit method has the best accuracy, while being significantly faster than the least-squares method and has hence been chosen for all further simulations. Explicit methods and lower order methods were disregarded, due to their poor performance in dynamic roll motion behaviour. Their advantage is a significantly shorter computational time.

A clear deviation in roll period is visible in figure 5.23a. This was reduced by adjusting the numerical grid in vertical direction, as the initial buoyancy did not match the mass. The improvement can be seen in figure 5.23b and 5.23c when comparing the roll motion and heave motion for the uncorrected case (blue line) with the corrected (orange line). The oscillation in heave motion took place around a non-zero value before correction. At last the grid inclination approach has been changed. In the first approach *Suggar++* was used to incline the grid already during the phase of grid generation. This lead to unsymmetrical rolling, which could not be explained. Afterwards, the grid without an initial inclination was used and a heeling achieved using a prescribed motion for roll. When the desired heeling angle was reached, the simulation was restarted with all DOF free to move. This approach is shown in green in figure 5.23b and 5.23c.

Finally a good agreement between numerical and experimental results was achieved as can be seen by comparing the green dotted line (experiment) with the solid green line (numerics) in figure 5.24.

The majority of experiments where rolling will occur is done with the experimental set-up as discussed in chapter 4.3. There, cable distance sensors are connected to the model to determine all motions. These distance sensors significantly increase the roll damping.

If numerical simulations where rolling occurs are to be compared to experimental data, an additional damping due to the effect of cable distance sensors needs to be applied in the numerical approach. A general description for the equation of motion is:

$$m\frac{d^2x}{dt^2} + c\frac{dx}{dt} + k \cdot x = 0, \tag{98}$$

where $c$ describes the damping coefficient, $k$ the spring coefficient, $m$ is the mass and $x$ the translation of motion. The damping coefficient can be expressed using the damping ratio $\zeta_d = \frac{c}{c_c}$, where $c_c = 2m\omega_n$ is the critical damping and $\omega_n$ the natural frequency. A damping ratio of zero corresponds to an undamped system, $0 < \zeta_d < 1$ to an underdamped system which is still oscillating but decaying in amplitude, $\zeta_d = 1$ is the critical damping and $\zeta_d > 1$ corresponds to an overdamped system which does not oscillate any more. The damping ratio is related to the logarithmic decrement $\Lambda$ by:

$$\zeta_d = \frac{\Lambda}{2\pi} \tag{99}$$

with the definition of the logarithmic decrement

$$\Lambda = \frac{1}{n} ln \left( \frac{\zeta(t_i)}{\zeta(t_{i+n})} \right), \tag{100}$$

with $\zeta(t_i)$ being the amplitude of the peak at time $t_i$ and $\zeta(t_{i+n})$ the amplitude $n$-periods away. A dimensionless damping coefficient for finite difference methods can hence be described by:

$$c' = \frac{2\Lambda}{T_n} \frac{L_{ref}}{u_{ref}}, \tag{101}$$

where the natural Period $T_n$ has been used instead of the natural frequency $\omega_n$ and $L_{ref}$ and $u_{ref}$ are the characteristic length and velocity to non-dimensionalise all equations.

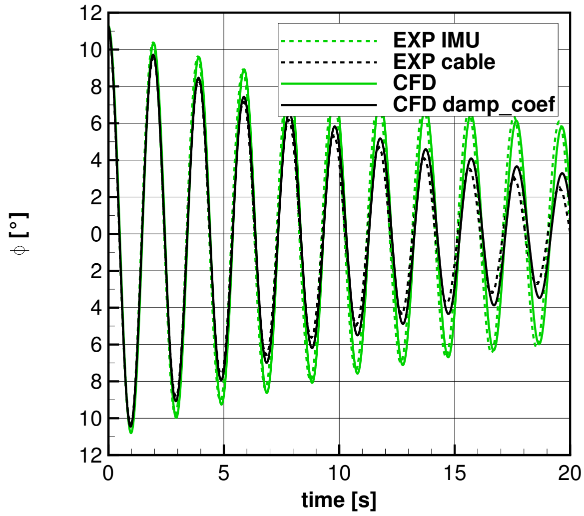


**Figure 5.24.:** Roll decay amplitude for undamped (green) and damped (black) experiments (dashed line) and numerical simulations (solid line)

The logarithmic decrement, which is necessary to mimic the damping effect of cable distance sensors in the numerical simulations, is the difference of the logarithmic decrement from the experiments with cable sensors (black dashed line in figure 5.24) and the logarithmic decrement of the undamped numerical simulation (green solid line in figure 5.24). The numerical simulation with the applied damping coefficient is shown in figure 5.24 with the solid black line and corresponds well with the experimental data with cable distance sensors. A slight deviation in natural frequency of 0.8% can be seen for both numerical simulations, which is acceptable. The damped amplitude is slightly underestimated but also of sufficient accuracy. Table 5.11 summarises the natural frequency and logarithmic decrement of all four cases, shown in figure 5.24.

**Table 5.11.:** Natural frequency and logarithmic decrement of roll decay tests

| | EXP IMU | CFD | deviation | EXP cable | $CFD_{damp\_coef}$ | deviation |
|---|---|---|---|---|---|---|
| $\omega_n$ | 3.215 | 3.199 | -0.5% | 3.219 | 3.193 | -0.8% |
| $\Lambda$ | 6.232E-2 | 6.723E-3 | +7.9% | 1.473E-1 | 1.246E-1 | -15.4% |

The determined additional roll damping coefficient has been used in all further simulations, where rolling was allowed for. Certain simulations have been repeated using no additional roll damping coefficient, in order to determine the influence on the roll amplitude in wave excited conditions. Figure 5.25 is showing the time series (left) and the corresponding Fourier transformation (middle) of the roll amplitude for case RW075_-

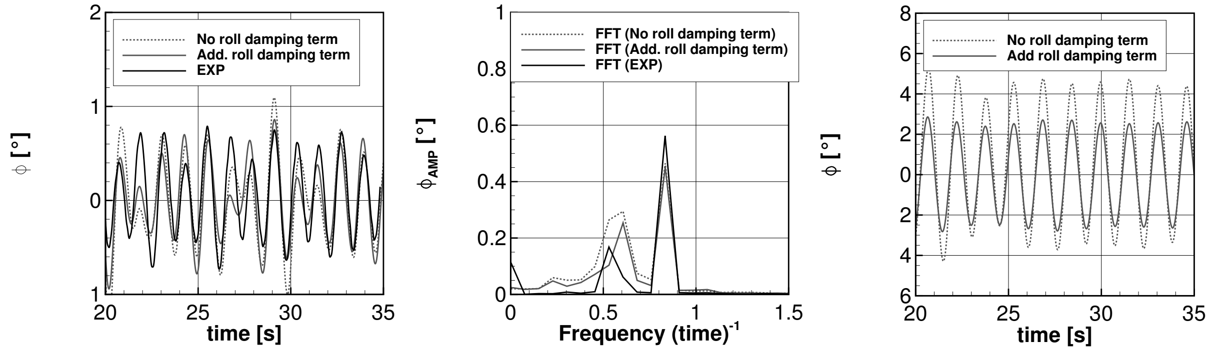


**(a)** Time series RW075_90_-0_MP **(b)** Fourier transformation RW075_90_0_MP **(c)** Time series RW125_90_-015_MP

**Figure 5.25.:** Effect of additional roll damping for $\mu_W = 90°$

90_0_MP. The solid grey line represents the case with additional roll damping coefficient applied, the dashed grey line the one without and the solid black line the experimental result. The experimental result has been determined using the new measurement device and is hence being affected by additional damping due to the presence of cable distance sensors. Both, experimental and numerical results are composed by a superposition of a roll amplitude corresponding to the wave frequency (at $f_W = 0.81\,\mathrm{Hz}$) and a lower frequency at approximately $f \approx 0.55\,\mathrm{Hz}$. The latter corresponds to the natural roll frequency. The amplitude at the natural roll frequency is slightly higher in numerical simulations, albeit it is declining over time. Longer simulation times might lead to better comparison of experimental and numerical methods regarding the amplitude at natural roll frequency. Comparing the numerical results for additional and no additional damping coefficients reveals slightly higher natural roll amplitudes if the additional damping term is missing. The roll amplitude corresponding to the wave frequency is however not significantly affected. Figure 5.25c is showing the time series of a different case with longer wave lengths ($\lambda_W/L_{PP} = 1.25$) and at forward speed. Note that no experimental data is available for the case of beam seas and forward speed, due to seakeeping basin limitations. A stronger dependency on the additional roll damping term can be seen in these results. The roll amplitude is about 1.3° higher, if no additional roll damping is applied. The wave frequency is in close proximity to the natural roll frequency, which is why first, high amplitudes are occurring and second, the signal is oscillating at only one frequency, rather than two superposed frequencies.

This leads to the conclusion that an additional numerical damping coefficient to mimic the damping effect of cable distance sensors is of importance, when investigating the amplitude at natural roll frequency. It should therefore be applied when comparing numerical results with experimental data of the chosen measuring device. It seems to be however of less importance if the wave excitation frequency differs from the natural roll frequency and comparison of roll amplitudes is done for the wave excitation frequency.

# 6. Results

This chapter contains the summary of numerical and experimental results for different moonpool configurations and environmental circumstances. Chapter 6.1 contains all relevant results for the ship in transit condition, while chapter 6.2 all results for operational conditions.

## 6.1. Transit condition

With 'transit condition' it is referred to the ship with different moonpool configurations at forward velocities and sailing in calm water or waves of different direction and length. No operations would normally take place in the moonpool during transit conditions. It is however of interest to reduce the oscillation inside the moonpool in order to reduce the resistance but also to increase safety by avoiding green water on deck. The following sections contain different investigated aspects for transit conditions.

### 6.1.1. Oscillation frequencies

Although the purpose of a moonpool is to increase the operability by providing a secured place with reduced water motions, oscillations of the water will take place in almost any case. This applies to transit, but also to operational condition. These oscillations can be described, as any fluctuating time signal, by one or more frequencies and respective amplitudes. These frequencies can be, in case of a moonpool, distinguished between the following:

1. Shedding frequencies

2. Wave frequencies

3. Moonpool resonant frequencies

#### Shedding frequencies

With shedding frequencies it is referred to an oscillation, typically of low amplitude, which is initiated solely by the separation at the leading edge of the moonpool at forward velocities. If no severe shear-layer rollup is taking place, the disturbance inside the moonpool will be at a minimum. This makes shedding frequencies most difficult to determine as the recorded signal is mainly covered by noise and hence rather ambiguous. A clear observance of shedding frequencies is discussed in chapter 6.1.7, where the moonpool is closed at the free surface. No oscillation of the water column takes place and the pressure fluctuation at the leading edge of the moonpool corresponds solely to vortex shedding.

### Wave frequencies

The frequency of environmental waves can prescribe the oscillation frequency inside the moonpool. As will be shown later, this does not have to be the case for all waves, as the moonpool might predominantly oscillate at its resonance frequency although the only source of disturbances is coming from waves of a different frequency. Often, the recorded signal consists of two main frequencies, being the wave and moonpool resonant frequency, leading to inharmonic time series.

### Moonpool resonant frequencies

Each moonpool has its own resonant frequency, mainly being defined by its dimensions. It is common practice to distinguish between piston mode motions and sloshing mode motions. In the piston mode, the entire water surface inside the moonpool rises and sinks. No, respectively minimum phase shifts will be detected, when recording the elevation at different locations. This is not the case for sloshing modes, which is characterised by a wave travelling between the moonpool walls and hence phase shifts between signals at different locations.

The natural frequency of a piston mode motion can be estimated by describing the water column enclosed by the moonpool as an undamped mass-spring system. The resonant frequencies for such systems are known to be

$$\omega = \sqrt{\frac{c}{m + m_{add}}}. \tag{102}$$

$c$ is a restoring coefficient, $m$ the mass of the enclosed water and $m_{add}$ the added mass coefficient, resulting from effects proportional to the acceleration of the water column. The restoring coefficient can be formulated by $c = \rho g A$ and the mass with $m = \rho A T$. $A$ describes the horizontal area of the moonpool and $T$ the draught of the moonpool, typically coinciding with the draught of the ship. Note that the index $_{mp}$ will be skipped in order to simplify the following equations, although all dimensions in this chapter refer to moonpool dimensions. Equation (102) simplifies to

$$\omega = \sqrt{\frac{g}{T + T_{add}}} \tag{103}$$

This equation is simple to use and understand, as one can directly see a main parameter influencing the piston mode frequency, namely the draught $T$. The difficulty is in accurately determining the 'added draught' coefficient $T_{add}$.

A widely used method to determine the added draught has been proposed by Molin [56], whose approach has already been introduced in chapter 1. Remember that his theory is based on linearised potential flow theory and a motionless barge with no forward velocity. Molin's approach yields the following description for the piston mode frequency:

$$\omega_0 \approx \sqrt{\frac{g}{T + bf_3}} \quad \text{with,} \tag{104}$$

$$f_3 = \frac{1}{\pi}\left[\sinh^{-1}\left(\frac{l}{b}\right) + \frac{l}{b}\sinh^{-1}\left(\frac{b}{l}\right) + \frac{1}{3}\left(\frac{b}{l} + \frac{l^2}{b^2}\right) - \frac{1}{3}\left(1 + \frac{l^2}{b^2}\right)\sqrt{\frac{b^2}{l^2} + 1}\right] \tag{105}$$

From equation (105) it can be seen that the breadth and length of the moonpool are the other important parameters which define the resonant frequency. Fukuda [32] gave an even simpler estimation of the added draught with $T_{add} = 0.41\sqrt{A}$. A similar recommendation is given from DNV-GL [22] with the added draught defined as $T_{add} = \kappa\sqrt{A}$ and $\kappa$ being depended on the shape and aspect ratio, ranging between 0.45 - 0.48.

Fukuda [32] also mentioned the formulation for sloshing modes with

$$\omega_m = \sqrt{\frac{m\pi g}{l}}, \tag{106}$$

whereas the formulation for sloshing modes by Molin [56] is more complex and requires numerical integration. Index $m$ denotes the sloshing mode and starts with 1 for a standing wave in the moonpool with a crest on one wall and a trough at the other wall. van't Veer & Tholen [80] showed that the approaches of Molin and Fukuda yield similar sloshing frequencies for different moonpool geometries.

Some general findings of Molin were that piston mode frequencies are always lower than the first sloshing mode frequency. The latter increase unboundedly with decreasing ratios of $T/l$ and $b/l$.

When running calm water simulations, the water column of the moonpool will oscillate at its resonant frequency, or sometimes at the shedding frequency. When performing

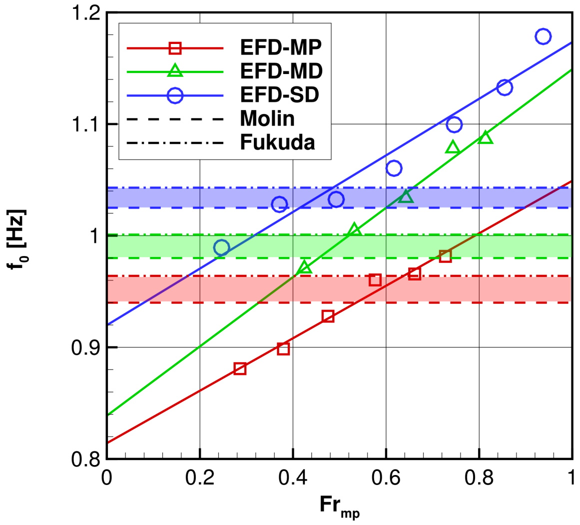


**Figure 6.1.:** Moonpool oscillation frequencies over Froude numbers

the simulations and experiments, it turned out that the piston mode frequency was not constant but gradually increased for increasing Froude numbers. The approach of Molin does not take account of forward velocities and the author is not aware of any other source dealing with the influence of forward ship speed on the natural piston mode frequency. van't Veer & Tholen [80] mentioned non-constant Strouhal numbers for the moonpool ($Sr_{mp} = f_0 \cdot l_{mp}/v$) in the range of 0.2 to 0.4, but did not further specify the progress of frequencies. A slightly wider range of Strouhal numbers has been found within this work, as can be seen in table 6.1. The non-constant resonant frequencies are shown in figure 6.1 for the three moonpools MP, MD and SD. The coloured symbols represent the individual dominating frequencies inside the moonpool, which have been determined by experiments. The respective coloured dashed lines show the approximated piston mode frequency by Molin and the dashed-doted line by Fukuda for each moonpool dimension. The coloured solid lines are a linear fit of the experimental values. A similar behaviour of all moonpool dimensions can be seen, although a linear trend is not the best fit. Note that the frequencies do not converge towards the approximated frequencies by Molin or Fukuda for low Froude numbers. Fukuda reported similar findings, where the frequency drops below the natural frequency, depending on the forward velocity (Fukuda [32] and Fukuda & Yoshii [33]).

For the case of moonpool SD, the differences in resonant frequency are shown in table 6.1. The natural piston mode frequency, e.g. determined by equation (104)-(105) leads to $f_0 = 1.025$ Hz. The relative wave length $\lambda_W/L_{PP}$, which would lead at that

**Table 6.1.:** Experimental results of frequencies for moonpool SD

| u [m/s] | Fr [-] | $Fr_{mp}$ [-] | $Sr_{mp}$ [-] | $f_0$ [Hz] | $\lambda_W/L_{PP}$ [-] $f_0$=var. | $\lambda_W/L_{PP}$ [-] $f_0$=const. | $\Delta\lambda_W/L_{PP}$ [-] |
|---|---|---|---|---|---|---|---|
| 0.328 | 0.06 | 0.247 | 0.54 | 0.989 | **0.74** | **0.69** | **-0.05** |
| 0.493 | 0.09 | 0.371 | 0.38 | 1.028 | **0.78** | **0.78** | **0.00** |
| 0.655 | 0.12 | 0.493 | 0.28 | 1.033 | **0.86** | **0.87** | **0.01** |
| 0.820 | 0.15 | 0.617 | 0.23 | 1.060 | **0.90** | **0.96** | **0.06** |
| 0.992 | 0.18 | 0.747 | 0.20 | 1.099 | **0.93** | **1.04** | **0.11** |
| 1.136 | 0.21 | 0.855 | 0.18 | 1.133 | **0.96** | **1.11** | **0.15** |
| 1.246 | 0.23 | 0.938 | 0.17 | 1.178 | **0.95** | **1.17** | **0.22** |

specific Froude number to a resonant behaviour inside the moonpool has been calculated once for the observed variable frequency and once for the constant frequency.

One can see that depending on the chosen velocity of the ship, relative wave lengths between 0.74 up to 0.95 will result in a resonant behaviour in case of head seas. For a fictitious full scale ship with $L_{PP}$ = 195 m, these would correspond to wave lengths between $\lambda_W$ =144 m and 185 m. The differences in wave length between using a constant and variable frequency are small for lower Froude numbers but become with $\Delta\lambda_W/L_{PP}$ = 0.22 quite large for the highest investigated Froude number. This should emphasise the importance of knowledge of exact resonant frequency at forward speed. With a better knowledge of the exact velocity dependent resonant frequency, the ship could be more safely operated during respective sea states, by adjusting the ship speed to avoid resonant conditions. Therefore, the following work has been done in order to predict the resonant frequency, including a dependency of the ship speed.

### 6.1.2. Empirical approach for velocity dependent resonant frequency

The following chapter presents an empirical approach to determine a velocity dependent resonant frequency of the moonpool, based on experimental and numerical results. Calm water tests have been performed for various moonpool geometries in order to include the different lengths and breadths of the moonpool. Note that no variation of the draught has been conducted. It should be also mentioned at this point already that this approach is up to now only valid for the model investigated. A wider database of models with moonpools would enhance the empirical formulation of the velocity dependent resonant frequency.

Experimental investigations have been conducted for the moonpools MP, MD and SD. The same geometries and additionally lb1 and lb2 have been simulated numerically. The Froude number of the ship has been varied between $0.06 \leq Fr \leq 0.23$.

Figure 6.2 shows the experimental results for the non-dimensional resonant frequency $f_0' = f_0 \cdot l_{mp}/u_{\text{ref}}$ over the moonpool Froude number $Fr_{mp} = u_{\text{ref}}/\sqrt{l_{mp} \cdot g}$. The black symbols represent the exact experimental value and the black line the power fit curve through these values. The red symbols (respectively blue for lb2) represent the numerical results and again the coloured curves the power fit. One can see that the non-dimensional frequencies match very well between experiments and numerics. Each figure shows the equation of the respective power fit curves. The lowest goodness of fit is of 0.998 and hence all curve fits can be seen as accurate enough. Linear and exponential curve fitting showed less good agreements between numerical and experimental values and had lower goodness of fit values and were hence disregarded.

The determined curve fittings were further analysed in order to state a general equation for all geometries. The general power equation can be written as:

$$f_0' = \exp\left[A \cdot \ln\left(Fr_{mp}\right) + B\right] \tag{107}$$

Factor $A$ is relatively constant for all geometries and will be determined by averaging the respective coefficients of the individual curve fits. Factor $B$ shows a more clear tendency between the different geometries. A linear dependency of $B$ on the moonpool length was found, as figure 6.3a shows with a goodness of fit of 0.887. Therefore, $B$ is divided into

$$B = B_1 + B_2 \cdot l_{mp} \tag{108}$$

Equation (107) hence turns to

$$f_0' = \exp\left[A \cdot \ln\left(Fr_{mp}\right) + B_1 + B_2 \cdot l_{mp}\right] \tag{109}$$

When processing the curves shown in figure 6.2, the following coefficients could be determined,

- $A_1 = -8.9835$
- $B_1 = -2.1379$
- $B_2 = 1.3564\text{m}^{-1}$,

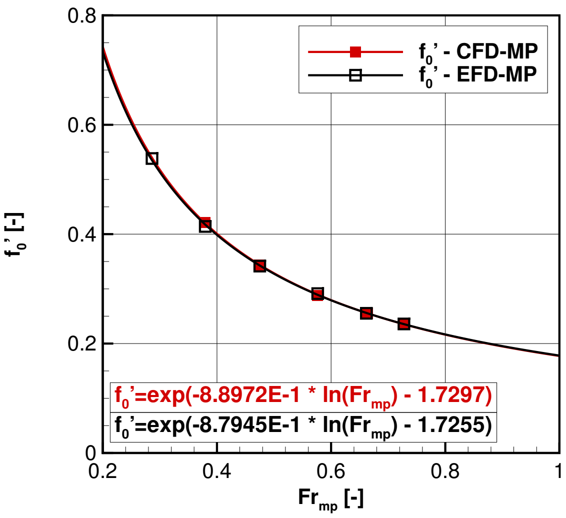


**(a)** Exp. and numerical power fit of MP

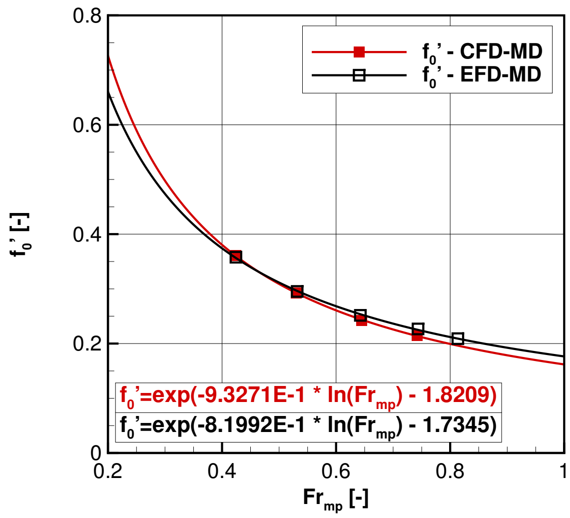


**(b)** Exp. and numerical power fit of MD

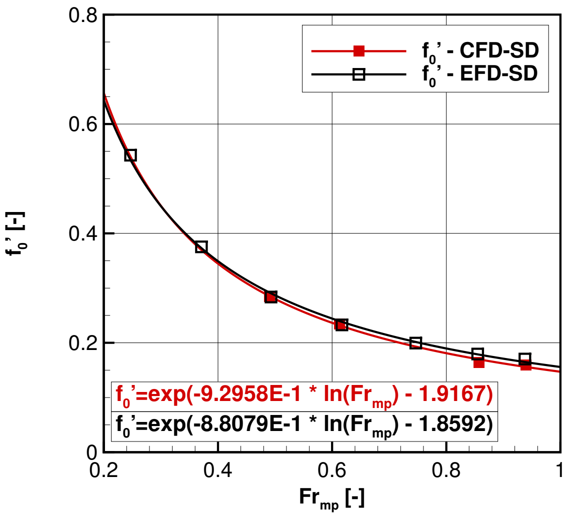


**(c)** Exp. and numerical power fit of SD

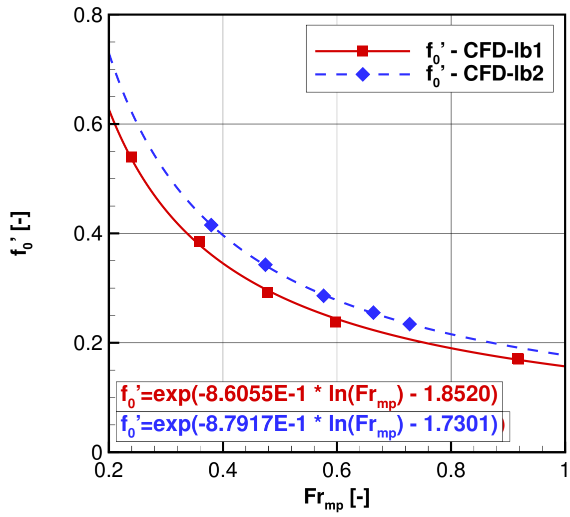


**(d)** Numerical power fit of lb1 and lb2

**Figure 6.2.:** Power fit of non-dimensional resonant frequencies for MP, MD, SD, lb1 and lb2

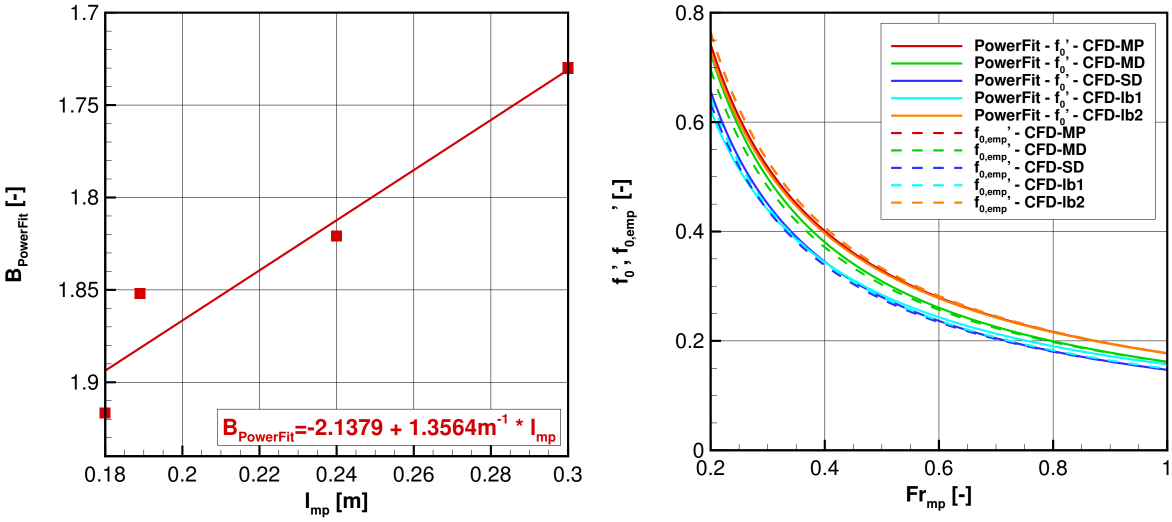


**(a)** Linear fit of factor $B$ for MP, MD, SD, lb1 and lb2

**(b)** Power fit of MP, MD, SD, lb1 and lb2 and respective general fit using equation (110)

**Figure 6.3.:** Linear fit of factor $B$ and Power fit of original and empirical approach

and the general equation can be stated as:

$$f'_{0,\text{emp}} = \exp\left[-8.9835 \cdot \ln\left(Fr_{mp}\right) + \left(-2.1379 + 1.3564 \cdot l_{mp}\right)\right] \tag{110}$$

Figure 6.3b shows the original power fit in solid lines and the general function using equation 110 in dashed lines. The respective lines show a good agreement. Note that this figure only shows the numerical power fit curves and their approximation using equation (110). Comparison to the experimental power fit curves shows similar results.

In order to exclude the dependency of the moonpool draught, equation (110) is substituted in equation (103) which yields a description for the added draught $T_{add}$ using the above mentioned approach

$$T_{add} = \frac{g}{\omega^2_{0,\text{emp}}} - T, \tag{111}$$

with $\omega_{0,\text{emp}} = 2\pi \cdot f_{0,\text{emp}}$.

This approach yields velocity dependent dimensional resonant frequencies for MP, MD, SD, lb1 and lb2, as can be seen in figure 6.4. The filled black symbols represent frequencies, which have been excluded from the power fitting approach due to the following reasons:

As already discussed in chapter 5.5, the lowest Froude numbers sometimes show an ambiguous behaviour in resonant frequency, as their dominant frequency sometimes corresponds to sloshing modes or to the second harmonic of the piston mode. When looking at MP in figure 6.4a, two frequencies at $Fr_{mp} < 0.35$, show much higher values than the rest. These frequencies are due to sloshing type motions and are hence excluded, as this approach is only valid for piston type motions. The two lowest moonpool-Froude numbers in MD and SD (figure 6.4b and 6.4c) show decreased frequencies, compared to the other results. This decreasing cannot be explained until now. One frequency at SD and two at lb1 are excluded for higher moonpool-Froude numbers, as they decrease to around $f_0 \approx 0.4\,\mathrm{Hz}$. The oscillation amplitude at these Froude numbers is extremely small (as will be shown in section 6.1.3) and hence no clear frequencies can be determined for these cases. At last, the two lowest Froude numbers of lb2 are excluded. The frequency of the lowest Froude number cannot be explained, while the one of the second lowest correlates to the second harmonic of the piston type motion.

This approach covered a wide range of Froude numbers for the ship. As the non-dimensional frequency $f_0'$ has been used for the power fitting and $u_{ref}$ was used for non-dimensionalisation, this approach is not valid for $u \to 0$, as $f_0' \to \infty$. The approach has been tested for one ship with several different moonpool geometries. Therefore, the database is too small to make equation 110 applicable to all types of ships and moonpools without further validation. A broader range of input data would enhance the equation and could also detect other dependencies than the ones used.

### 6.1.3. Oscillation amplitudes

The oscillation amplitudes at transit condition appear due to the moonpool resonant frequency. The results of all three wave gauges for the numerically and experimentally analysed oscillation amplitudes are shown in figure 6.5. WG2 is located at the centre of the moonpool, WG1 4.5 cm in longitudinal direction towards the leading edge and WG3 4.5 cm towards the trailing edge. All shown amplitudes are due to piston mode oscillations, except for the frequencies discussed in the previous chapter. One can immediately see that the longer moonpools (MP, lb2 and MD) undertake much stronger amplitudes than the shorter ones (lb1, SD). If the amplitudes are stronger, the free surface performs the highest oscillation at WG3 and the lowest at WG1. This is due to a strong vortex which is deflected upwards at the trailing wall and pushes the water up. This rises the free surface in the aft half, which then leads to a motion of the fluid towards the leading wall. Although having similar behaviour of a sloshing motion, this cycle repeats with the dominating piston mode and is hence of lower frequency than the first sloshing motion according to equation (106). An exemplary cycle has been shown in figure 1.1. For the

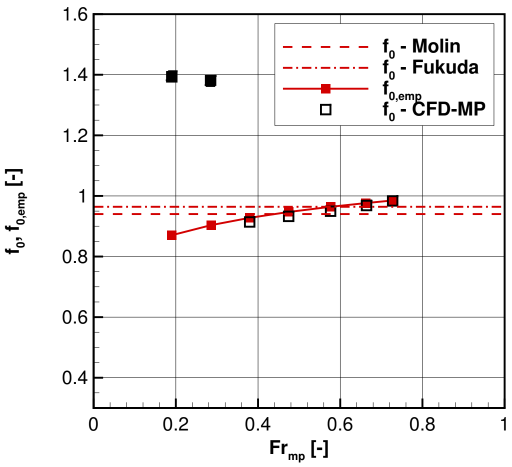


**(a)** Comparison of different approaches for MP

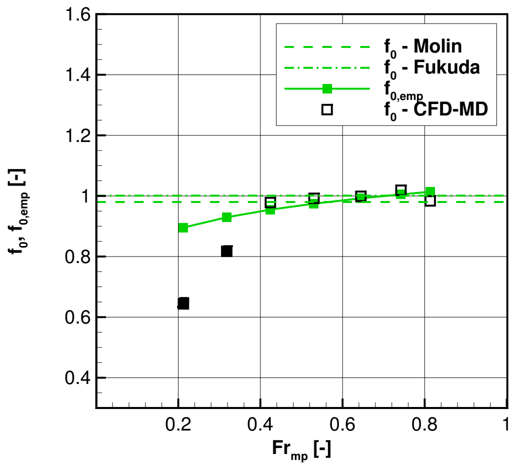


**(b)** Comparison of different approaches for MD

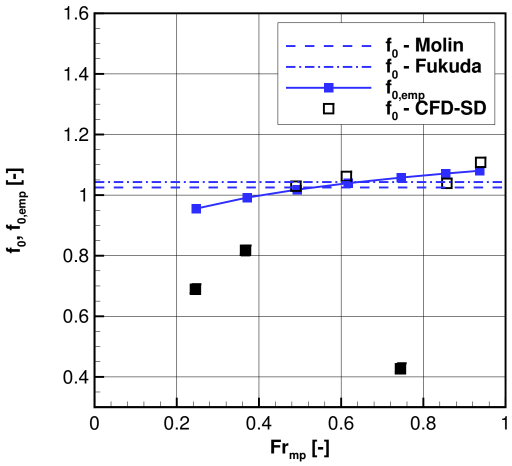


**(c)** Comparison of different approaches for SD

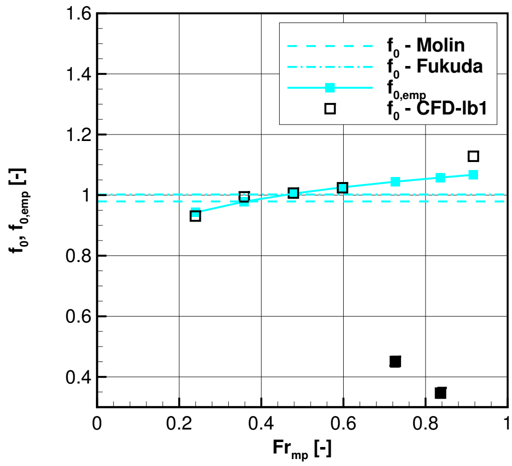


**(d)** Comparison of different approaches for lb1

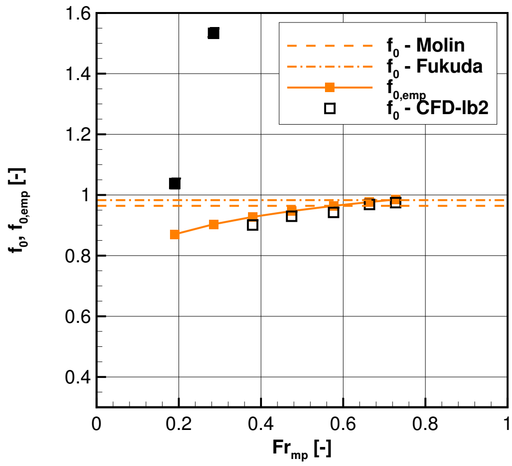


**(e)** Comparison of different approaches for lb2

**Figure 6.4.:** Resonant frequencies from numerics and empirical approach for MP, MD, SD, lb1 and lb2

more moderate free surface motions of SD and lb1, all three wave gauges show mostly similar amplitudes. The free surface hence rises and sinks at all locations with the same amplitude and no, respectively little inclination of the free surface occurs. An observation that can be made though, is that the free surface is for these geometries often a little higher at the front and aft wall of the moonpool and lower in the centre.

Comparing the numerical results (coloured lines and symbols) in figure 6.5 with the experimental (black symbols) reveals some discrepancies. For MP, the agreement is satisfying until a moonpool Froude number of $Fr_{mp} \approx 0.58$ corresponding to $Fr = 0.18$. The amplitudes of the two highest Froude numbers seem however over-predicted in the numerical simulations. In both, numerics and experiments, the amplitudes keep constantly rising with increasing Froude number. It should be noted that the wave gauges are not placed at the front respectively aft wall, where the maximum amplitudes would occur. A placement of WG1 & WG3 closer to the walls might have improved the agreement due to more distinguished signals.

The largest discrepancy occurs for MD, where the numerics predict much higher amplitudes than the experiments. The amplitudes drop for the highest Froude number in the numerics and already for $Fr_{mp} > 0.53$ in the experiments. Reason for that different behaviour has not been found. It should be borne in mind that the experimental setup consisted of moonpool insertions, which reduced the size of the original moonpool MP. This comes at the cost of additional edges, which are not present in the numerical grid. Although it is not believed that additional vortex generation due to unwanted edges in the experiments caused this severe reduction, it might be part of an explanation. More likely could be a different development of shear-layer rollup and propagation of this vortex in numerics and experiments. If the separated vortex is more upward directed in the numerical simulations than experiments, deflection at the trailing wall could be stronger and cause more severe oscillations in the simulations, while being shed mostly under the keel in experiments and hence limiting the oscillation amplitude. Further investigation of this theory would require the experimental determination of the velocity field inside the moonpool. This however is highly complicated, time and data consuming and has hence not been conducted within this work. The theory would be supported by the fact that oscillations for the longer moonpool MP and shorter moonpool SD agree satisfactory, where the vortex propagation might be more clearly, whereas moonpool MD might represent an ambiguous case.

Moonpool SD shows again a fairly good agreement between experimental and numerical results. Only $Fr_{mp} \approx 0.74$ has still significant amplitudes in the experiments, while they already vanished in the numerics, as is the case for all higher Froude numbers. It was

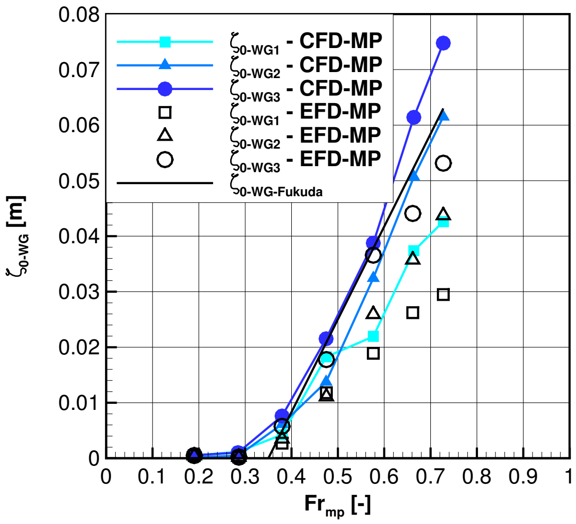


**(a)** Numerical and experimental amplitudes for MP

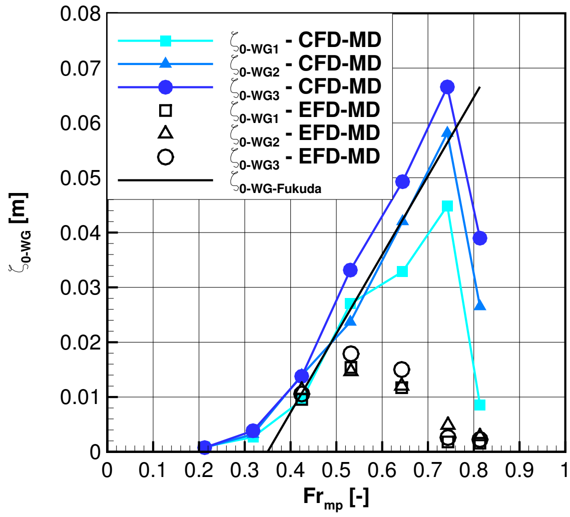


**(b)** Numerical and experimental amplitudes for MD

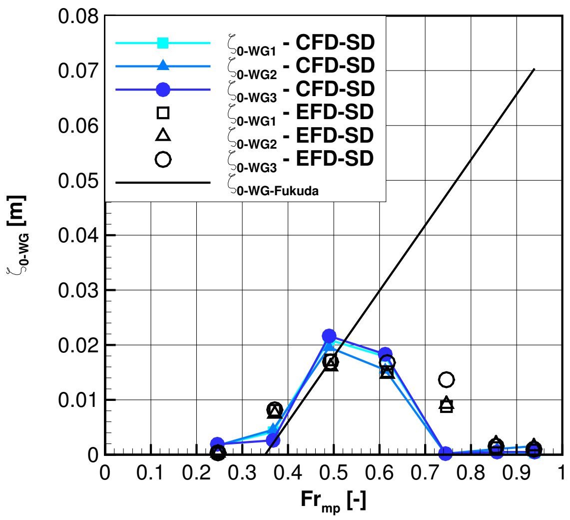


**(c)** Numerical and experimental amplitudes for SD

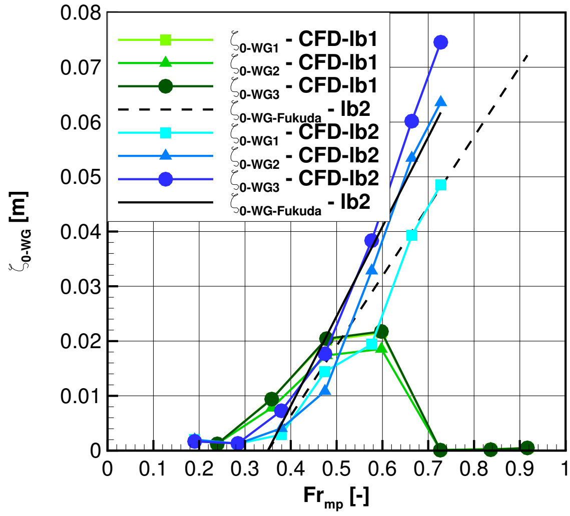


**(d)** Numerical amplitudes for lb1 and lb2

**Figure 6.5.:** Wave gauge amplitudes for MP, MD, SD, lb1 and lb2

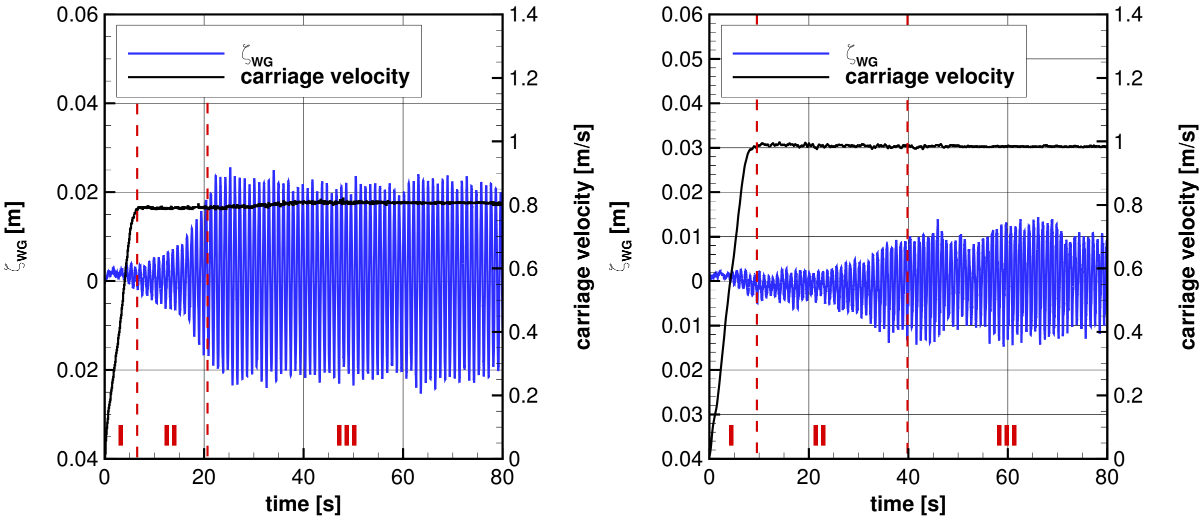


(a) $Fr = 0.15$

(b) $Fr = 0.18$

**Figure 6.6.:** Experimental mean wave gauge amplitude for SD

not clear, if the experimental oscillation for $Fr_{mp} \approx 0.74$ resulted from vibrations of the measuring platform/carriage, causing additional disturbances and hence moonpool oscillations. To further investigate this, experiments in the large towing tank have been conducted, whose carriage runs much smoother and at very constant speed. Furthermore, all DOF were restricted to check if motions are causing the higher moonpool oscillations. Figure 6.6 shows the mean oscillating amplitude and the carriage velocity at $Fr = 0.15$ (left) and $Fr = 0.18$ (right), corresponding to $Fr_{mp} \approx 0.61$ respectively 0.74. The figures are split into three regions, I) being the acceleration phase of the carriage, II) the development of oscillating amplitudes and III) the fully developed oscillating amplitudes. Comparing both figures leads to the conclusion that while at $Fr = 0.15$ the amplitude develops quite rapidly, it takes much longer to develop at $Fr = 0.18$ and further has less steady amplitudes. Although the numerical simulation for $Fr = 0.18$ has been run longer to check if the oscillation develops at a later stage, no significant oscillating amplitudes established. The rapid collapse in oscillating amplitude seems to occur around $Fr_{mp} = 0.75$ for all investigated moonpool geometries (check figure 6.5). For higher moonpool Froude numbers, the vortices separated from the leading edge, break up at the trailing edge and are mostly carried below the keel and barely enter the moonpool any more.

The length of lb2 and MP is identical, as is lb1 and SD. The only varying parameter is the respective breadth. As lb2 and lb1 show a very similar behaviour as MP and SD, it can be concluded that the breadth has no significant influence on the oscillation amplitude at transit conditions in calm water.

Fukuda [32] gave an estimation of oscillation amplitude during transit conditions in calm water, using the current ship speed $u$ and the velocity at which oscillations start to develop $u_{start}$. The latter needs to be measured and gives room for discussions. Gaillarde & Cotteleer [34] suggest to use a method by Covert [15]. The equation Fukuda yielded is

$$\frac{\zeta_{0-WG-\text{Fukuda}}}{l_{mp}} = \frac{3\pi}{16} \cdot \frac{u - u_{start}}{l_{mp} \cdot \omega_0} \tag{112}$$

The exact definition of amplitude is not specifically mentioned. Applying equation (112) on the geometries investigated and using $Fr_{mp} = 0.35$ to calculate $u_{start}$, the amplitudes predicted by Fukuda could be determined. These amplitudes are shown in figure 6.5 with the respective black lines and agree well with the results obtained in this work.

### 6.1.4. Added resistance due to moonpool oscillations

The oscillations inside the moonpool cause an increase in ship resistance, which is generally a function of the oscillation amplitude, as will be shown. van't Veer & Tholen [80] investigated the effect of moonpools on the resistance and proposed a simple model for the added resistance, based on experiments. The added resistance coefficient $\Delta C_{mp}$ can be defined by the difference between the non-dimensional resistance of the ship with ($C_{T,w}$) and without moonpool ($C_{T,wo}$)

$$\Delta C_{mp} = C_{T,w} - C_{T,wo}, \tag{113}$$

where the coefficients are each determined with the respective wetted surface in hydrostatic condition.

The numerical simulations have been performed with sinkage and trim free and all other DOF restrained. The simulations for the ship without moonpool ('CL') have been performed for $0.12 \leq Fr \leq 0.21$, whereas all other simulations and experiments for a wider range of $0.06 \leq Fr \leq 0.23$. Figure 6.7 shows the results for MP, MD, SD, lb1 and lb2 each compared to CL. The coloured lines and symbols represent numerical simulations, whereas the black symbols represent experimental results. Only resistance coefficients in longitudinal direction are shown. The red lines represent the total resistance coefficient, the green lines the frictional resistance and the blue lines the pressure resistance coefficient. The orange lines have been determined from equation (113) and visualise the increase of resistance due to presence of the moonpool.

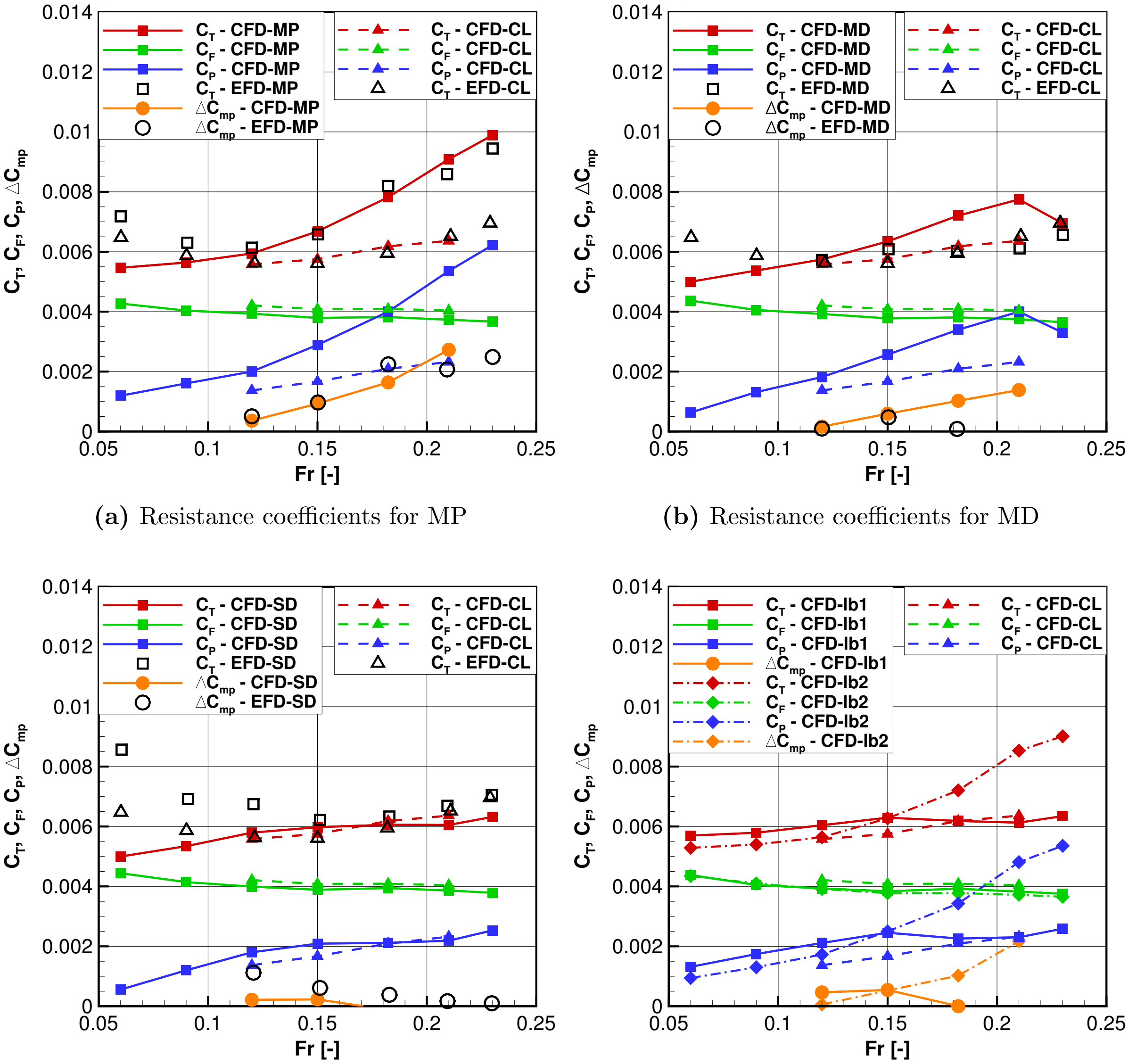


**(a)** Resistance coefficients for MP

**(b)** Resistance coefficients for MD

**(c)** Resistance coefficients for SD

**(d)** Resistance coefficients for lb 1 and lb2

**Figure 6.7.:** Numerical and experimental resistance coefficients for MP, MD, SD, lb1, lb2 and CL

The experimental results predict higher total resistance coefficients for $Fr = 0.06$ and 0.09 for all moonpool geometries than the numerical results. It is believed that the experiments are over-predicted, probably due to laminar boundary layers and consequential higher separation. The Reynolds numbers are very small, especially for the lowest Froude numbers and due to the limited model length of $L_{PP} = 3\,\mathrm{m}$. This effect cannot occur in the numerical simulations, as the turbulence model is prescribing a fully turbulent boundary layer. Another general observation is the lower frictional resistance of all moonpool configurations, compared to CL. This is due to the missing shear forces at the moonpool opening, which are not compensated by the shear inside the moonpool, where velocity gradients are generally much smaller. The added resistance coefficients solely result from an increase in pressure resistance, in presence of the moonpool. This can be explained by vortex separation at the leading edge causing a pressure low at the front wall and an impingement of vortices at the trailing edge causing a pressure high at the aft wall.

The overall agreement between numerical and experimental results for MP (figure 6.7a) is very good. The experimental results tend to fluctuate a little for the highest Froude numbers, whereas the numerical results show a steady increase. This deviation is acceptable though. The added resistance also agrees well between experiments and numerics and is steadily increasing with increasing Froude numbers.

Figure 6.7b shows the results for MD. Experiments and numerics agree for $Fr = 0.12$ and 0.15, whereas they are deviating for higher Froude numbers. The numerical total resistance coefficient increases up to $Fr = 0.21$, whereas the experimental coefficient even drops below the baseline of CL. It should be mentioned that the dimensional resistance is still slightly higher in presence of the moonpool, but the larger wetted surface reduces the coefficient, such that it can be smaller than for the case without moonpool. The added resistance coefficient is steadily increasing for the numerical simulations, while it is turning negative for the two highest Froude numbers in the experiments.

Moonpool SD (figure 6.7c) has a different behaviour for the highest Froude numbers, than MD. The numerical results sink below CL while remaining almost identical to CL in the experiments. This causes a slight negative added resistance in the numerics and almost no added resistance in the experiments.

lb1 in figure 6.7d shows a very similar behaviour as SD and lb2 as MP. Again, the breadth does not seem to have any influence on the resistance.

An obvious observation is the connection between the progress of the resistance coefficient and the moonpool oscillation amplitude. When comparing figure 6.5 with 6.7, a direct connection between both can be made. This circumstance also explains the occurrence of negative added resistance coefficients, which appears when the oscillation

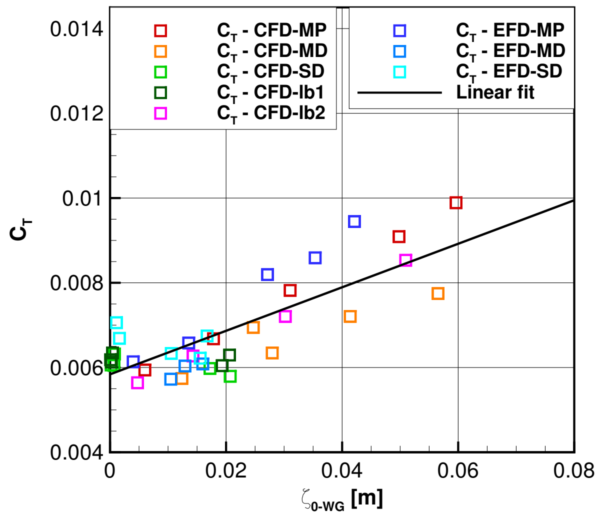


**Figure 6.8.:** Correlation of resistance coefficient and oscillation amplitude

amplitude vanishes. The dimensional resistance is then of similar magnitude, while the non-dimensional coefficient might be lower, due to the larger wetted surface of the ship with moonpool.

Figure 6.8 shows the total resistance coefficient $C_T$ over the mean dominating oscillation amplitudes $\zeta_{0-WG}$ for all numerical and experimental results. Similar findings have been shown by van't Veer & Tholen [80], who distinguished the added resistance coefficients for piston and sloshing mode motions. As no pure sloshing motion occurred during this investigation, only piston mode motions are shown in this diagram. The linear increase, shown with the black line, is clearly visible. It is hence of interest to reduce the oscillation amplitude by suitable measures, in order to avoid an increase in ship resistance during transit condition.

## 6.1.5. Influence of incoming waves

Until now, only calm water tests have been shown. This chapter is describing the results of the ship sailing in waves and their effect on the moonpool characteristics. Therefore, regular waves of $\lambda_W/L_{PP} = 0.50, 0.75, 1.00$ and $1.25$ have been investigated. The wave steepness has been kept constant at $2\zeta_W/\lambda_W = 2\,\%$ leading to wave amplitudes in model scale of $\zeta_W = 0.015, 0.0225, 0.03$ and $0.0375\,\mathrm{m}$. All numerical simulations have been done for $Fr = 0.15$ and different wave headings of $\mu_W = 0°, 45°, 90°, 135°$ and $180°$. Additionally, investigations for $Fr = 0.18$, $\mu_W = 0°$ and a slightly wider range of wave lengths are shown in Löhrmann et al. [51]. Conclusions are similar and will not be repeated here.

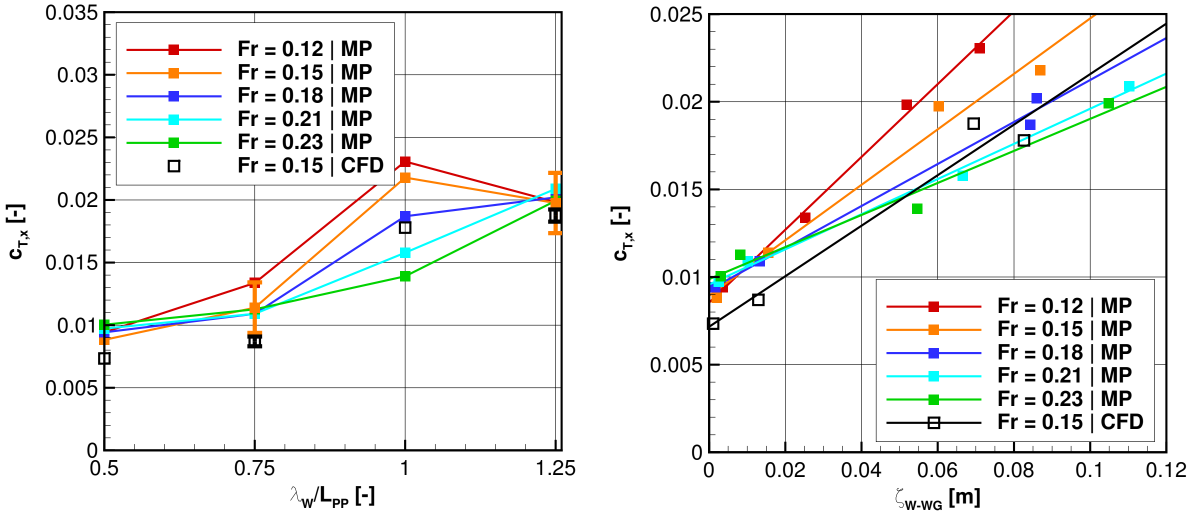


**(a)** Total resistance coefficient for MP

**(b)** Total resistance coefficient over mean oscillating amplitude at wave frequency

**Figure 6.9.:** Total resistance coefficient

Experiments have been conducted for Froude numbers of $Fr = 0.12, 0.15, 0.18, 0.21$ and $0.23$, but only head seas ($\mu_W = 0°$) and following seas ($\mu_W = 180°$) could be investigated, due to limitations of the seakeeping basin. The numerical and experimental tests have been conducted for the moonpool geometries MP, MD and SD.

### Head seas

The following figures contain results for head seas, which are discussed for the case of MP. Note that especially the ship motions are very similar for the other investigated moonpool geometries. Only the resistance coefficients show some differences between MP, MD and SD. All remaining results are shown in appendix C.2. For figure 6.9 to 6.12, the coloured lines represent different Froude numbers and all results are shown for varying relative wave lengths. The black symbols respectively lines represent the results from numerical simulations, which have been only conducted for $Fr = 0.15$.

Figure 6.9a shows the total resistance coefficient. At first, a clear difference of the investigated Froude numbers can be seen at $\lambda_W/L_{PP} = 1$, whereas the coefficients are quite similar at other wave lengths. This wave length correlates to the resonant case, where the frequency of wave and piston mode are close to each other. Interestingly, the resistance coefficient at $\lambda_W/L_{PP} = 1$ is highest for the lowest Froude number and vice versa. This correlates to the order of highest RAO of moonpool oscillations as can be seen

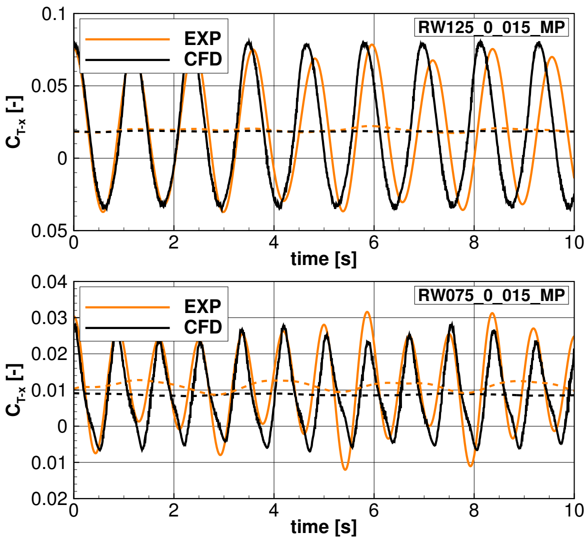


**Figure 6.10.:** Experimental and numerical force signal for $\lambda_W/L_{PP} = 0.75$ and $\lambda_W/L_{PP} = 1.25$

in figure 6.12a, with an exemption for $Fr = 0.12$. A combination of both, force coefficient and oscillating amplitude at wave frequency is shown in figure 6.9b. The gradient of resistance coefficient is highest for lowest Froude numbers and vice versa. This behaviour is identical for the other moonpool geometries.

The black symbols in figure 6.9a represent the numerical results and need to be compared with the orange line. One can see, that both methods match very well for the longest wave, but deviate slightly for the shorter ones. The largest difference of 24% occurs at $\lambda_W/L_{PP} = 0.75$. The force time signals at two wave lengths are investigated in detail in figure 6.10 to understand the reason of deviation. Remember that the experimental measurement has been filtered and inertia forces subtracted in order to make a comparison with the pure hydrodynamic and gravitational forces from the numerical code. The upper figure shows the force signal for $\lambda_W/L_{PP} = 1.25$ and the lower for $\lambda_W/L_{PP} = 0.75$. The periods match for $\lambda_W/L_{PP} = 0.75$ but deviate for $\lambda_W/L_{PP} = 1.25$, as the longest waves are influenced by shallow water in the experiments, whereas only deep water waves were investigated in the numerics. The upper figure shows quite constant amplitudes oscillating at the wave frequency, with a slightly stronger non-periodicity in the experimental data. The lower figure shows more non-periodicities in both methods. This is due to the effect, that a pronounced amplitude at the resonant piston mode and wave frequency is present, whereas the amplitude at wave frequency was dominating over the one at piston mode frequency for $\lambda_W/L_{PP} = 1.25$. This periodicity has been visualised using the moving average $m(t)$, plotted in the respective dashed lines. The normal moving average is calculated by

$$m(t) = \frac{1}{n}\sum_{i=0}^{n-1} C_{T-x}(t-i), \tag{114}$$

with $n$ being the data points within one period. This method calculates the average value at every point for a certain time range, e.g. the wave period. If the signal oscillates solely at the wave frequency, this parameter should be ideally constant. Disturbances would result in an oscillating moving average. If however the time signal oscillates not only due to the wave frequency but also with the resonant piston mode frequency, the moving average cannot turn constant. Theoretically, it should then ideally oscillate harmonically with the piston mode frequency. Both signals have therefore been averaged twice, once using the data points for the respective wave period $n_W$ and once for the piston mode period $n_0$.

$$m(t) = \frac{1}{n_0}\sum_{i=0}^{n_0-1}\left[\frac{1}{n_W}\sum_{i=0}^{n_W-1} C_{T-x}(t-i)\right](t-i), \tag{115}$$

The moving average for both wave length is very constant for the numerical simulations, whereas especially at $\lambda_W/L_{PP} = 0.75$ it oscillates strongly in the experiments. This emphasises the importance of choosing the time span for averaging. It appears less critical in the numerical results, but more critical in the experiments. The time signal at $\lambda_W/L_{PP} = 0.75$ still oscillates non-harmonically and with an approximate frequency of 0.4 Hz. This frequency can be found in the surge and pitch signal, albeit of only minor amplitude. It might therefore be associated to one of these motions, respectively the characteristics of the measurement platform allowing these motions, such as the $\Delta x$-slide. The uncertainty when averaging the discussed time signals has been plotted in figure 6.9a for the mentioned wave lengths with error bars. The size of the error bars corresponds to the amplitude of the moving average.

The motions in figure 6.11 show a good agreement between experiments and numerics. The response amplitude operator (RAO) for heave shows a deviation of 27% at $\lambda_W/L_{PP} = 1$ between experiments and numerics, which however correlates to an amplitude difference of 0.2 cm. All other results for heave agree very well. The maximum deviation in pitch motion occurs at $\lambda_W/L_{PP} = 1$ with 19%, which correlates to a difference of 0.2° and can be seen as satisfying too. Note that both motions do not reach their maximum at $\lambda_W/L_{PP} = 1$ but $\lambda_W/L_{PP} = 1.25$, which was not expected and might be due to the barge

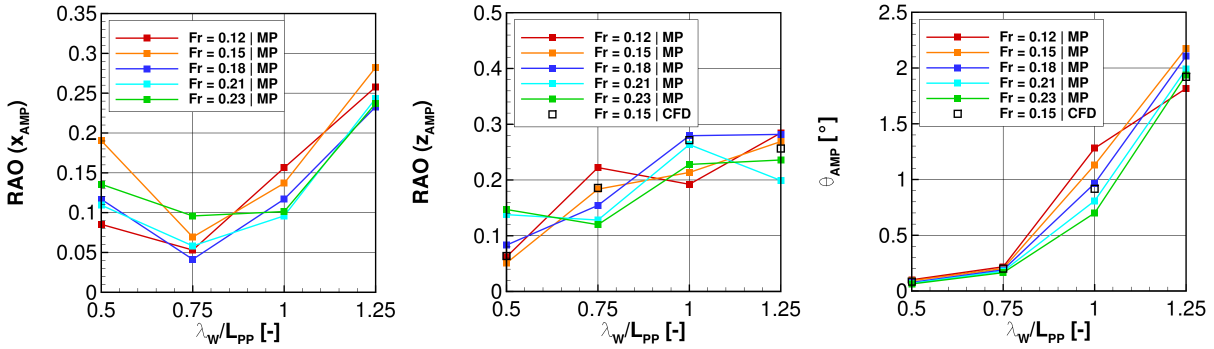


**(a)** Surge amplitude for MP **(b)** Heave amplitude for MP **(c)** Pitch amplitude for MP

**Figure 6.11.:** Surge, heave and pitch amplitude for MP at $\mu_W = 0°$

type form of the ship. The surge motion amplitude is shown in figure 6.11a. Note that the surge motion was restrained for head seas in the numerical simulations, which did not affect the results, as has been discussed in chapter 5.7.

Sway, roll and yaw are not shown, as they are of negligible magnitude for head seas.

Figure 6.12 shows the RAO's of the mean oscillation amplitudes at piston mode frequency (dashed lines and circular symbols) and wave frequency (solid lines and square symbols) for MP, MD and SD. Again, the respective black symbols represent the numerical result at $Fr = 0.15$. The results agree extremely well for all moonpool geometries. The encounter wave frequency is of similar magnitude as the piston mode frequency for $\lambda_W/L_{PP} = 1$ and 1.25. It is then not possible to distinguish between both and only one amplitude can be determined, which is assigned to the wave frequency. Note that these amplitudes might also contain some energy due to the piston mode frequency or vice versa.

A general observation is that the RAO's are greater than 1 for almost any case, when sailing at forward speed and have even a maximum value of 3.72. Some exemptions occur for the shortest wave lengths, especially for MD but also at some Froude numbers for MP and SD.

As expected, the amplitudes at wave frequency are relatively small for short waves, compared to the amplitudes at piston mode frequency. They increase however drastically for longer waves ($\lambda_W/L_{PP} > 0.75$). This shift from dominating piston mode frequencies to wave frequencies has been already mentioned by Löhrmann et al. [51].

Figure 6.12a shows the RAO's for MP. The largest RAO's occur for the two highest Froude numbers and are of similar magnitude over all $\lambda_W/L_{PP}$. Especially the low Froude numbers show only small RAO's at short wave lengths and a peak at $\lambda_W/L_{PP} = 1$. Note

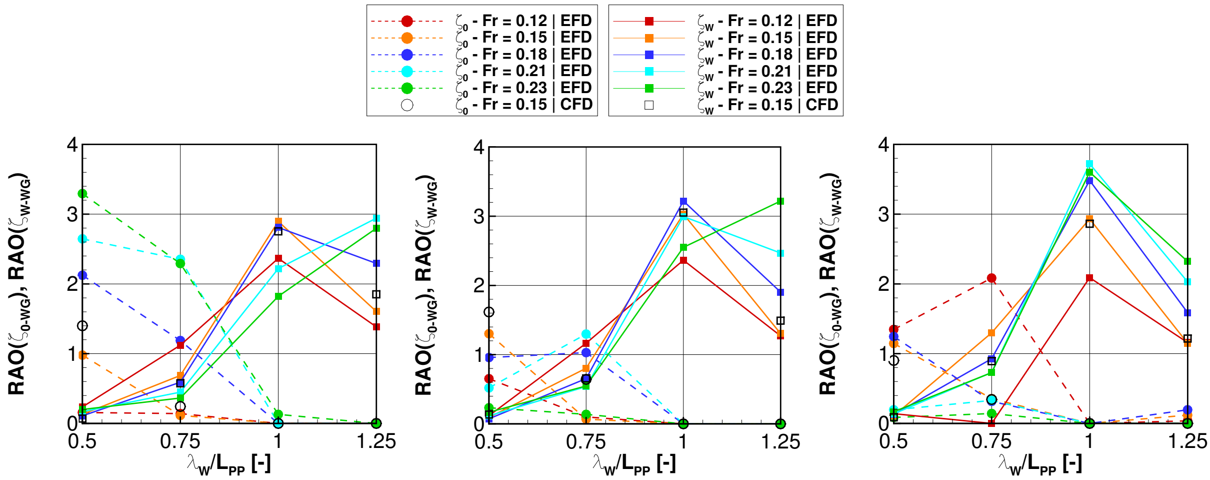


**(a)** RAO's of moonpool oscillation amplitudes for MP

**(b)** RAO's of moonpool oscillation amplitudes for MD

**(c)** RAO's of moonpool oscillation amplitudes for SD

**Figure 6.12.:** RAO's of oscillation amplitude due to piston mode and wave frequency at $\mu_W = 0°$

that numerical and experimental results for both RAO's agree very well.

The results for MD are shown in figure 6.12b. The Froude numbers have less influence in this case and RAO's generally increase with increasing wave length. Note that for $Fr = 0.23$ and $\lambda_W/L_{PP} = 1.25$, the highest amplitudes have been measured. The water motion was exceeding the wave gauge lengths, and severe green water has been recorded during the experiments. The amplitudes at piston mode frequency are relatively small compared to MP. The agreement between numerical and experimental results is again very good with a minor exemption for the piston mode amplitude at $\lambda_W/L_{PP} = 0.75$.

Figure 6.12c shows the results for SD. It is visible, that the peak shifts for the lowest Froude number from $\lambda_W/L_{PP} = 0.75$ towards $\lambda_W/L_{PP} = 1$ for higher Froude numbers. This agrees well, with the potential resonant wave lengths for head seas in table 6.1, which have been determined based on the velocity dependent piston mode frequencies. The amplitudes assigned to the piston mode frequencies are generally small with the exemption at $Fr = 0.12$ and $\lambda_W/L_{PP} = 0.75$. Again numerics and experiments agree very well.

A higher resolution in relative wave lengths would have probably better highlighted the shift in RAO peak towards longer wave lengths for higher Froude numbers. This is especially visible at MP and MD when looking at $Fr = 0.21$ and 0.23.

Figure 6.13 is showing an instantaneous visualisation of the free surface for the four investigated wave lengths, when the wave crest is approx. at the forward perpendicular.

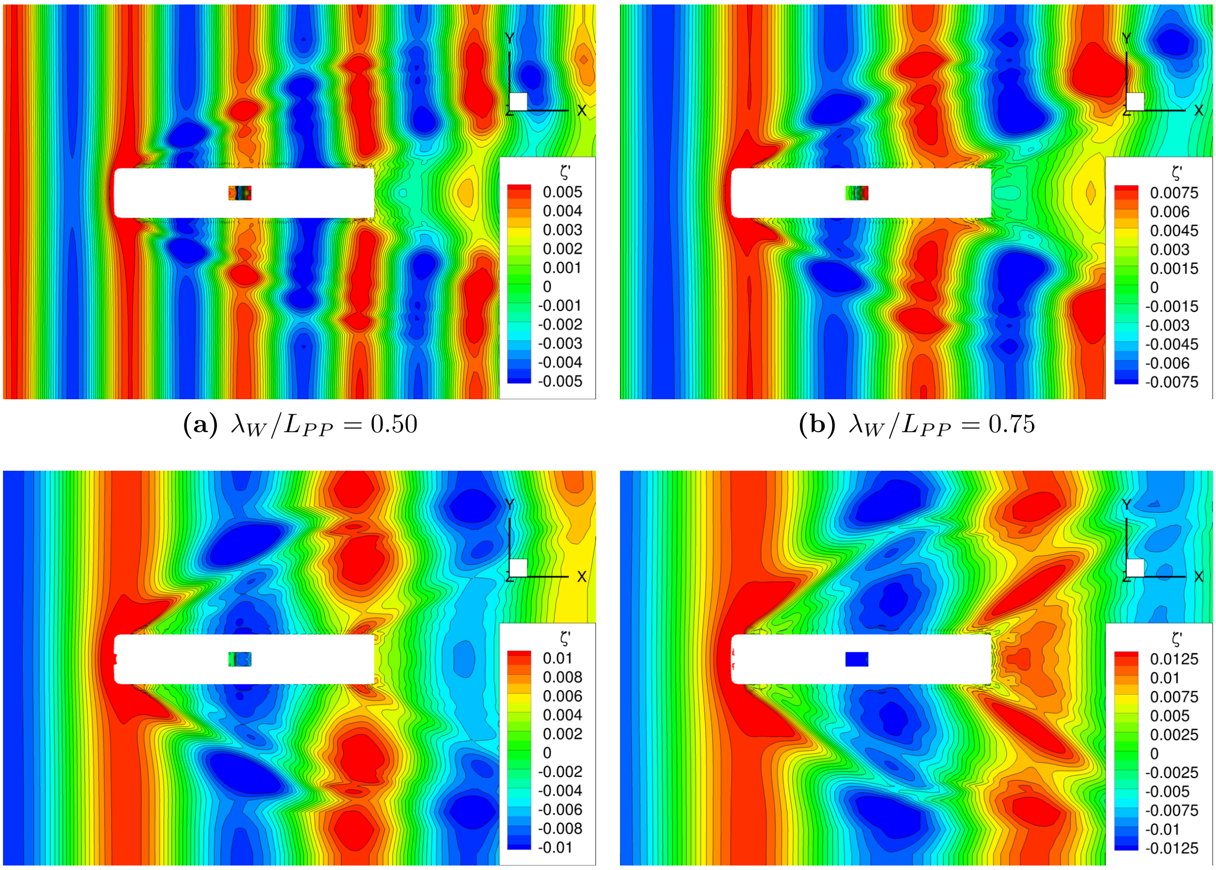


**(a)** $\lambda_W/L_{PP} = 0.50$ **(b)** $\lambda_W/L_{PP} = 0.75$

**(c)** $\lambda_W/L_{PP} = 1.00$ **(d)** $\lambda_W/L_{PP} = 1.25$

**Figure 6.13.:** Wave system for $Fr = 0.15$, $\mu_W = 0°$ and different wave lengths

The ship is disturbing the wave field for the two longest waves even further away in transverse direction. The accuracy of the wave quality has been determined at a transverse direction, outside of the shown area, in order to reach an undisturbed wave. The wave quality for the four waves in head seas are equally of $\zeta_W/\zeta_{target} \approx 0.95$.

### Quartering & beam seas

Numerical simulations have been performed to study the effect of beam and quartering seas on moonpool characteristics. The ship was able to move in every direction and springs of equal strength as in the experimental setup were applied on surge, sway and yaw motion. Simulations were conducted for $Fr = 0.15$ and wave directions of $\mu_W = 45°, 90°$ and $135°$. This study has only been done for MP.

The six DOF motions are shown in figure 6.14. The highest amplitudes in surge, roll and yaw occur for $\mu_W = 135°$. Pitch amplitude is highest at $\mu_W = 45°$ and sway and heave

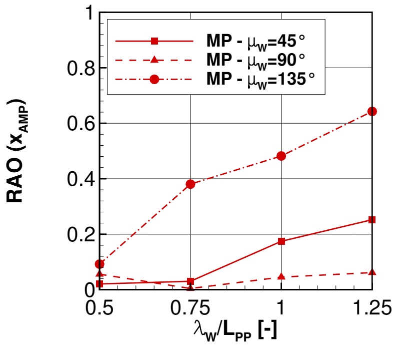


**(a)** RAO of surge motion for MP

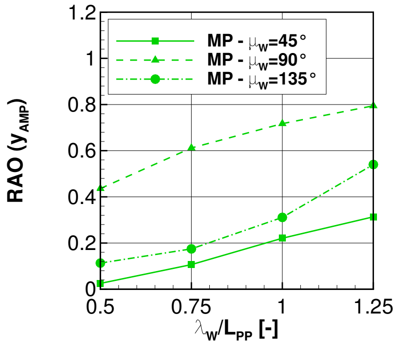


**(b)** RAO of sway motion for MP

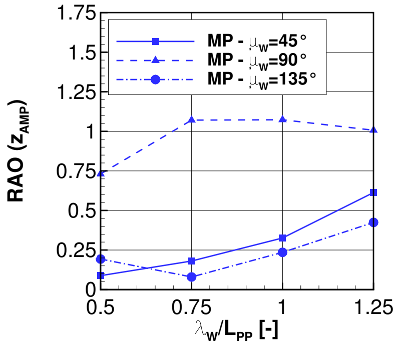


**(c)** RAO of yaw motion for MP

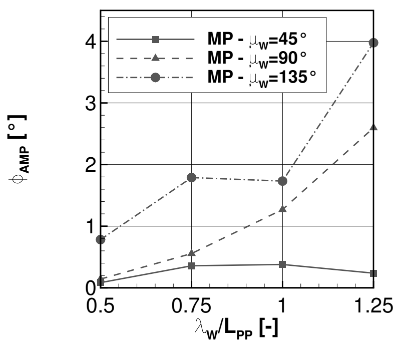


**(d)** Roll motion amplitude for MP

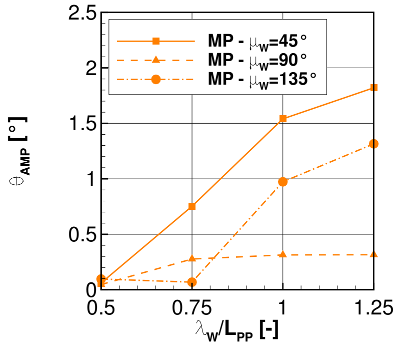


**(e)** Pitch motion amplitude for MP

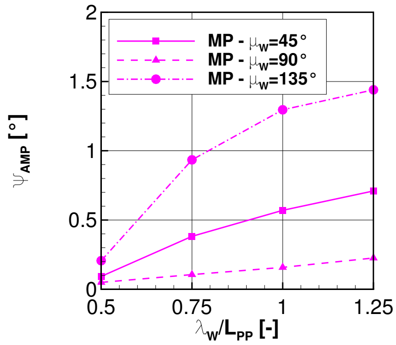


**(f)** Yaw motion amplitude for MP

**Figure 6.14.:** RAO's of translational motions and motion amplitudes of rotational motions for quartering and beam seas

for $\mu_W$ =90°.

Figure 6.15 shows the RAO of mean amplitudes at piston mode (solid lines) and wave frequency (dashed lines) as well as the respective frequencies for the three wave directions. A clear peak for $\mu_W$ =45° at $\lambda_W/L_{PP} = 1$ can be seen for the mean amplitude assigned to the wave frequency. This peak also correspond to the highest dimensional amplitude measured. The highest RAO is reached for $\mu_W$ =90° at $\lambda_W/L_{PP} = 0.5$ and can be assigned to the piston mode frequency. $\mu_W$ =135° shows generally low RAO's. This behaviour can be clearly explained by the progression of frequencies, shown in figure 6.15b. The piston mode frequency (solid lines) is quite constant around $0.95 \leq f_0 \leq 1.05$, whereas the encounter wave frequency changes with encountering angle $\mu_W$ and wave length $\lambda_W/L_{PP}$. For $\mu_W$ =45° the encountering frequency matches the wave frequency at $\lambda_W/L_{PP} \approx 1$, which causes resonant behaviour and hence the peak in amplitude. For $\mu_W$ =90° this effect occurs at $\lambda_W/L_{PP} \approx 0.5$. The encountering frequencies of $\mu_W$ =135° are below the

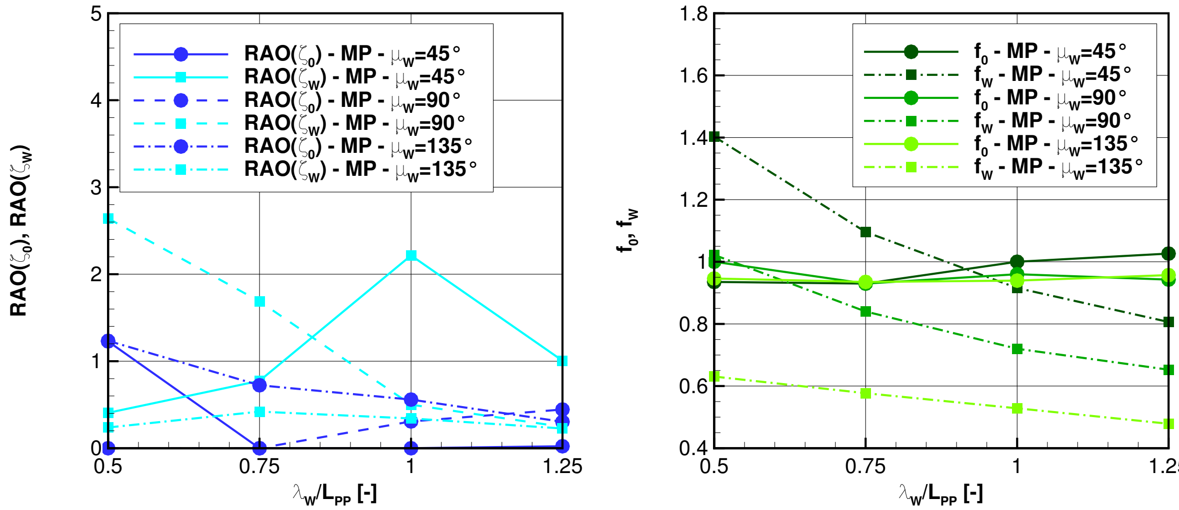


**(a)** RAO of mean amplitude at piston mode and wave frequency

**(b)** Piston mode and wave frequencies

**Figure 6.15.:** Moonpool characteristics for quartering and beam seas

piston mode frequency at all times, which is reason for the generally low mean amplitudes.

Comparison with results from head seas shows that the RAO of the oscillation amplitudes can be decreased significantly, when changing the course. This effect is mainly due to the change in encountering frequency.

Longitudinal forces (figure 6.16a) are as expected highest for $\mu_W = 45°$ and almost constant for $\mu_W = 90°$ and $\mu_W = 135°$. The side force is largest for beam seas and hence plausible as well. At last the non-dimensional moments are similar for $\mu_W = 45°$ and $\mu_W = 90°$, whereas it oscillates around zero for $\mu_W = 135°$.

Figure 6.17 shows instantaneous free surface elevations for head-, beam- and quartering seas of $\lambda_W/L_{PP} = 1$ with the wave crest approx. at the bow.

### Following seas

The simulations for following seas were conducted slightly different than for head seas. If no damping approach is used in the background domain, severe wave reflection occurs at the domain inlet (in front of the ship) and the wave amplitude decreases.

This problem was overcome by damping the waves at the domain inlet and outlet towards the undisturbed wave field. Damping at the domain outlet (behind the ship) ensures stable waves of correct amplitude, which overtake the ship. Furthermore, possible

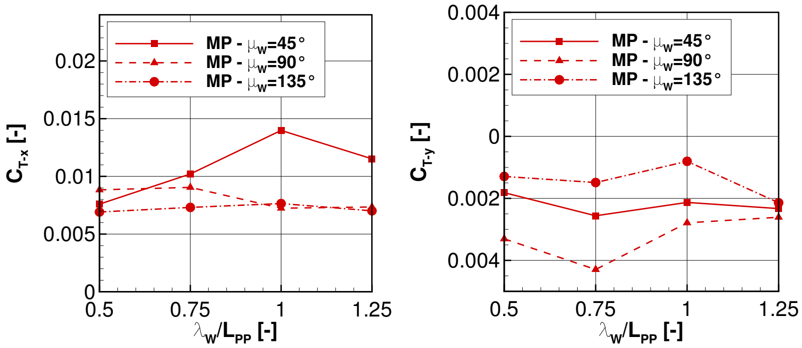


**(a)** Longitudinal force coefficient **(b)** Transversal force coefficient **(c)** Yaw moment coefficient

**Figure 6.16.:** Non-dimensional forces and moments for different wave encounter angles

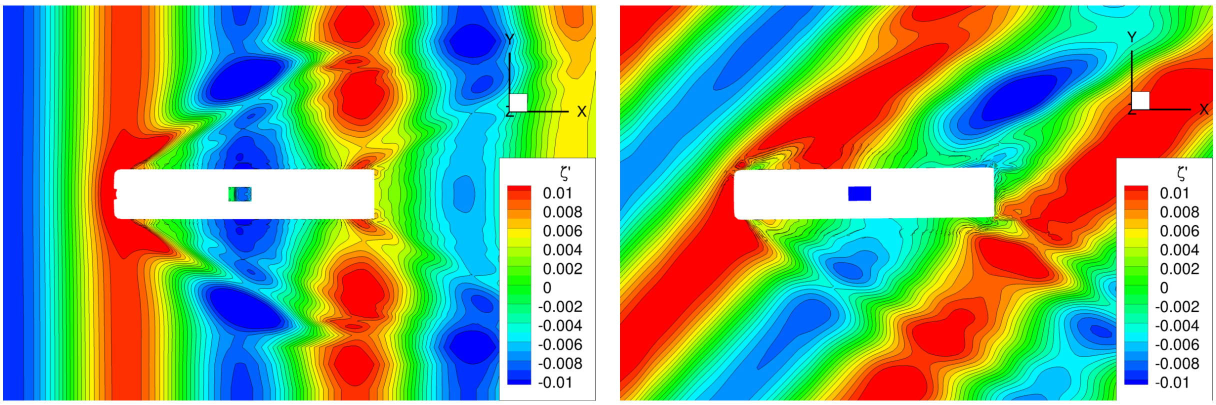


**(a)** $\mu_W = 0°$ **(b)** $\mu_W = 45°$

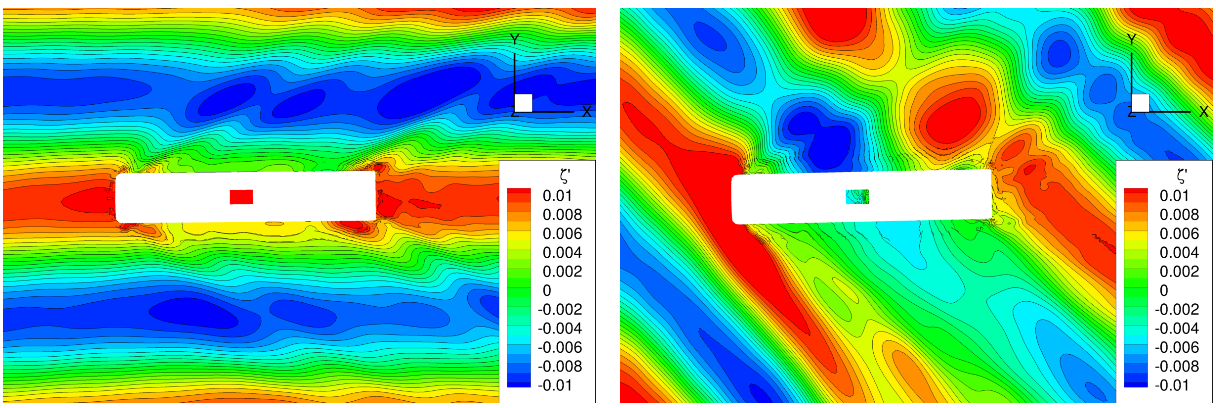


**(c)** $\mu_W = 90°$ **(d)** $\mu_W = 135°$

**Figure 6.17.:** Wave system for $Fr = 0.15$, $\lambda_W/L_{PP} = 1.0$ and different encounter angles

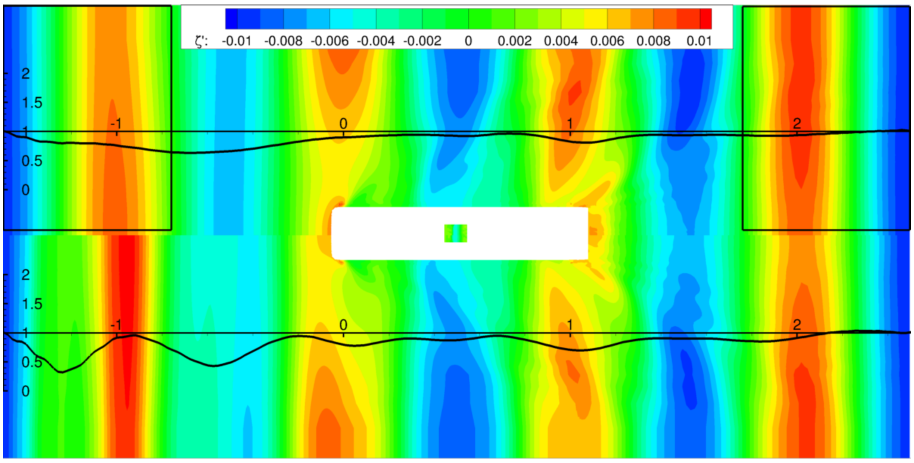


**Figure 6.18.:** Comparison of wave quality for damped (top) and non-damped case (bottom)

ship wave systems are damped and cannot be reflected at the outlet. Damping at the domain inlet mainly prevents wave reflection.

The wave fields for the damped and non-damped approach are shown in figure 6.18 for $\lambda_W/L_{PP} = 1$. The top figure shows the damped case, where the sponge layers are visualized at the domain inlet and outlet with a black rectangle. The graph represents the non-dimensional amplitude of the first harmonic after Fourier analysing the last wave period on a slice at $\eta = 0.9$. As the correct wave conditions are given at the inlet and outlet through the boundary conditions, the graph reaches an amplitude of 1 on both ends. The ship is located between $0 < \xi < 1$ and a good accuracy of amplitude can be seen for that region ($\zeta_W/\zeta_{target} = 0.93$). The amplitude drops to $\zeta_W/\zeta_{target} = 0.63$ in front of the ship, which is not critical, as these are waves which already passed the ship and should not affect the results. This low in amplitude could arise naturally as the ship is influencing the waves, but might also be due to numerical dissipation or due to the sponge layer at the domain inlet.

The case without damping is shown in the lower part of figure 6.18. The waves travelling towards the ship (on the right side of the figure) are of similar quality, although the amplitude decreases further than when applying the sponge layer at the domain outlet, which 'preserves' the waves a little longer. The accuracy of amplitude in the area of interest ($0 < \xi < 1$) is however only $\zeta_W/\zeta_{target} = 0.86$. More problematic is the wave reflection at the domain inlet, which can be identified by the oscillating amplitude of the first harmonic, shown in the lower graph. This happens, as waves which passed the ship and travel towards the domain inlet, reach the domain boundary at a different phase, than the generated wave at that face.

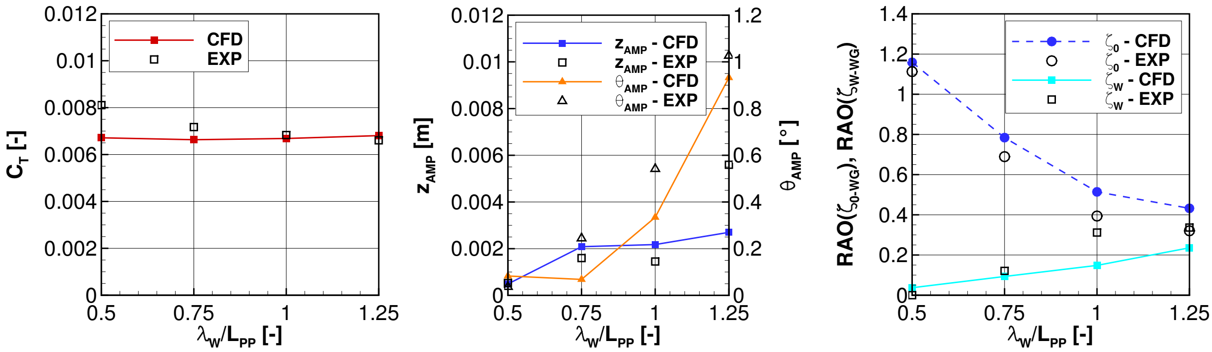


**(a)** Longitudinal resistance coefficient

**(b)** Heave and pitch amplitude

**(c)** RAO of oscillating amplitude at piston mode frequency

**Figure 6.19.:** Results for resistance, motions and RAO's of oscillation amplitude at $Fr = 0.15$ and $\mu_W = 180°$

Following seas condition has been tested numerically and experimentally at $Fr = 0.15$ and for MP. Although the above described damping approach has been used in the numerical simulations, the wave quality is lower than for head or quartering seas, with the lowest wave accuracy of $\zeta_W/\zeta_{target} = 0.86$ for $\lambda_W/L_{PP} = 0.75$. The results are shown in figure 6.19. The resistance coefficients in figure 6.19a match satisfactory between numerical and experimental solutions. Slightly decreasing coefficients can be identified in the experiments, whereas the numerics predict almost constant values. Largest deviation occurs for the shortest wave with a 17% lower numerical resistance. The heave and pitch motion is shown in figure 6.19b and has again satisfactory agreement between numerics and experiments. Numerical solutions predict lower values for heave at $\lambda_W/L_{PP} = 1.25$ and for pitch at the two medium wave lengths. Finally, the RAO's for oscillation amplitude in figure 6.19c have a good agreement in both the amplitudes due to piston mode (blue dashed line) and wave frequency (turquoise solid line). All investigated wave frequencies are well below the piston mode resonance frequency, due to the encountering angle of $\mu_W = 180°$. Therefore, only modest RAO's occur, with a maximum reached for the shortest wave. The signals are dominated by the amplitude at piston mode frequency and amplitudes at wave frequency are slowly increasing with increasing wave length. Compared to results of head seas condition, these oscillations are however of generally low amplitude.

### 6.1.6. Influence of damping

The damping approach, discussed in chapter 2.8.3, has been applied to investigate the effect of perforated bulkheads in calm water and head seas. Numerical results are compared with experimental data. Two layouts of perforated bulkheads have been analysed. The first has the moonpool dimensions of 'MD' and is compared to the experimental case '60-20' (refer to table 4.3 on page 59). The second has dimension of 'SD' and is compared to '60-40'. The cases where the numerical damping approach was applied will be denoted with index $_c$. The investigated cases differ only in the dimension of the damping chamber behind the bulkhead, which is relatively large in case of $SD_c$ and smaller for $MD_c$. Previous experimental investigations with insertion 60-40 and 40-40 revealed no significant differences in damping behaviour for 60%, respectively 40% porosities and equal damping chamber size, as has been reported in Löhrmann et al. [51]. The numerical grid had to be adapted to be comparable with the insertions used in the experiments. These insertions reduce the size of the moonpool bottom opening according to the damping chamber size. The bottom opening is an import factor for the flow entering the moonpool and must hence be made comparable between experiments and numerics. Therefore, the numerical grids have been adapted by adding a plate with no-slip boundary condition at the moonpool opening, as is shown in figure 6.20. The left figure shows the plate (in red) for case $MD_c$ and the right figure for $SD_c$. The sponge layers are than applied vertically above these plates, as has been illustrated in figure 2.6b. The advantage of this approach is that the numerical grid is, with the exemption of a simple grid for the plate, not changed. Considering the exact geometry of the perforated bulkheads through a numerical grid would lead to a huge increase in cell size. Furthermore, as *REX* uses structured grids, these grids would have to be composed due to its complexity by multiple block structured grids and then assembled through the overset grid approach. This would also increase the amount of necessary processors, as has been discussed in chapter 2.5 and would hence be highly ineffective

After defining the sponge layer boundaries according to the size of insertions in the experiments, the only remaining parameter to be chosen is the numerical damping constant $c$. It was originally tried to find a correlation between the experimental porosity and numerical damping constant, probably also depending on the size of the damping chamber. Due to the almost identical experimental results for the two investigated porosities, this was unfortunately not possible. It might also be that the damping constant is only dependent on the sponge layer length and not of porosity. More variations of experimental insertion layouts in porosity and chamber size would have been necessary to conduct a

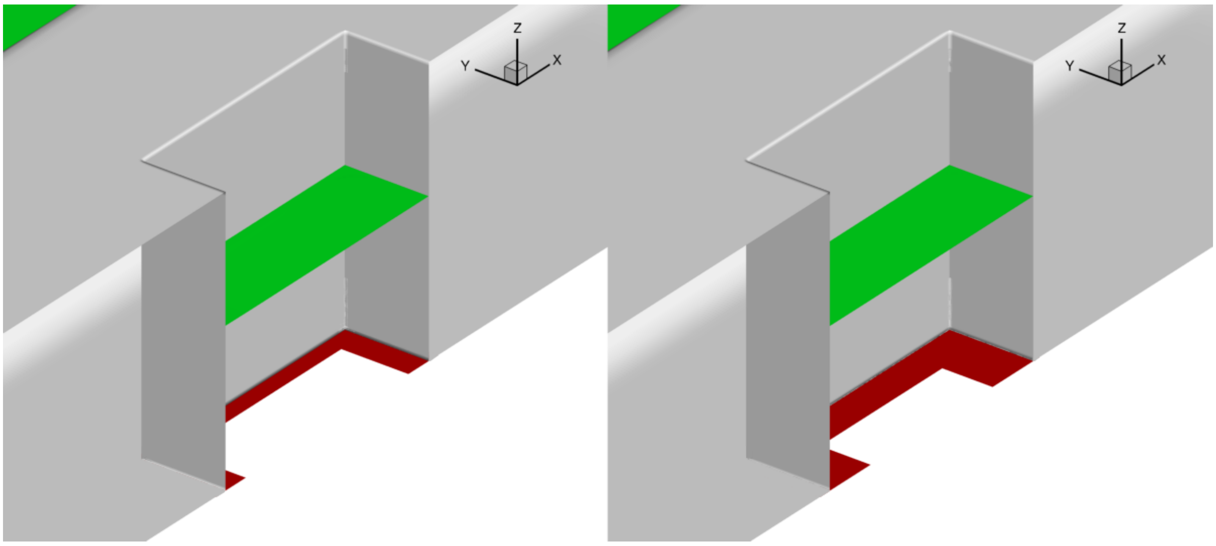


**Figure 6.20.:** Numerical model with plates at moonpool bottom opening for $MD_c$ (left) and $SD_c$ (right)

more reliable analysis, but was not possible within the scope of this work. Instead, the damping constant was varied for both cases ($MD_c$ and $SD_c$) individually, in order to find a comparable damping behaviour with the experimental results. This analysis is shown in figure 6.21 and has been done for the calm water case at $Fr = 0.15$ for $MD_c$ and $SD_c$. The blue and black dotted lines represent the non-damped moonpool oscillations from experiments respectively numerical results. The damping constant $c = 0$ represents the case with no sponge layer applied but with the plate at bottom opening being present. The damping constants had to be relatively large in order to reach the oscillation amplitudes of the respective experimental damped cases, the latter being shown in the green dotted line. In case of $MD_c$ a damping constant of $c = 20\,\mathrm{s}^{-1}$ lead to comparable oscillation amplitudes as in the experiments. For case $SD_c$, which has a larger damping chamber and hence longer sponge layer length, a damping constant of $c = 10\,\mathrm{s}^{-1}$ yielded similar oscillation amplitudes, as in the experiment.

Note the relatively small magnitude of oscillation amplitudes in the damped cases. These amplitudes were often not possible to determine using Fourier analysis, as no dominant frequency existed and resulting amplitudes would have been very unreliable. Instead, the variance $\sigma$ of the time signal has been determined and with the relation of significant wave height to variance $H_s = 4\sigma$, the (significant) amplitude determined.

Results for the numerical damping approach in calm water and different Froude numbers are shown in figure 6.22. The green lines with squared symbols represent the case

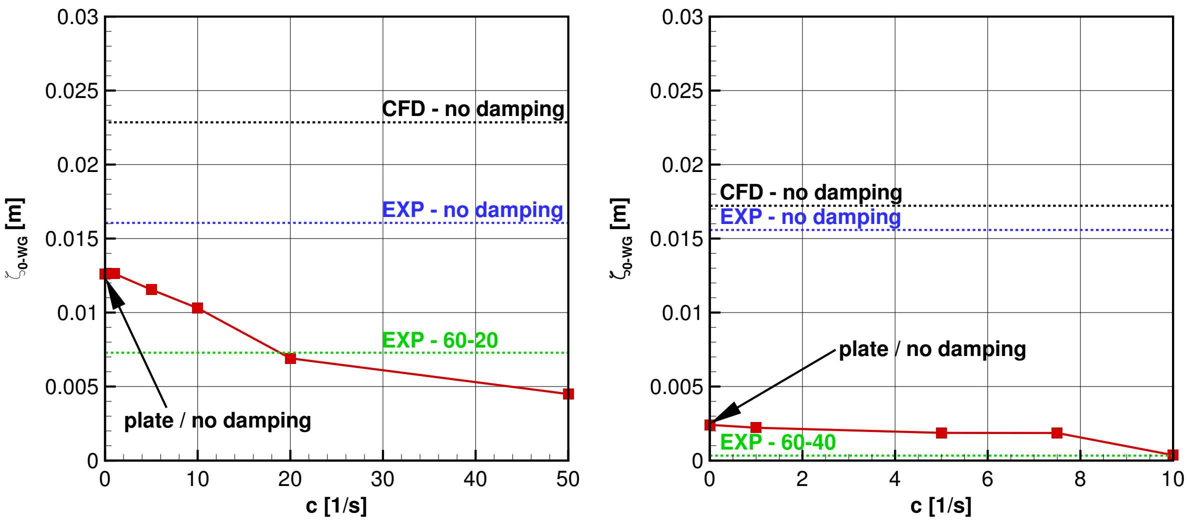


**(a)** $\mathrm{MD}_c$ **(b)** $\mathrm{SD}_c$

**Figure 6.21.:** Investigation of damping constant $c$

with no damping applied (MD respectively SD). The hollow black symbols represent the experimental cases. The orange line indicates the reduced moonpool oscillations for only having a plate at the moonpool bottom opening and no sponge layer applied. Note that no comparable experimental cases have been conducted for this condition. At last, the red lines with circular symbols represent the damped moonpool oscillations by applying a sponge layer with $c = 20\,\mathrm{s}^{-1}$ for $\mathrm{MD}_c$, respectively $c = 10\,\mathrm{s}^{-1}$ for $\mathrm{SD}_c$. Using the numerical damping approach to mimic the effect of perforated bulkheads leads to a significant reduction in moonpool oscillations, which agrees well with the experimental data. Although the non-damped amplitudes disagree for MD, as has already been discussed, the damped amplitudes match very well with the experimental values from insertion 60-20. The oscillating amplitudes for SD are already low and the damping approach further reduces the oscillations to a minimum. Both, experiments and numerics predict amplitudes below $\zeta_{0-WG} = 0.002$m. The only exemption occurs for $Fr = 0.12$, where the numerical simulation predicts slightly higher amplitudes than the experimental result. The oscillating amplitude can be reduced by up to 57% for $\mathrm{MD}_c$ respectively 85% for $\mathrm{SD}_c$, compared to applying only a plate at the bottom opening. The amplitude at the non-damped case is especially at higher Froude numbers and shorter moonpool openings decreasing rapidly. The damped cases show hence as well almost no surface oscillation for both, experiments and numerics at these Froude numbers.

Figure 6.23 shows results of the damping approach for head seas condition at $Fr = 0.15$.

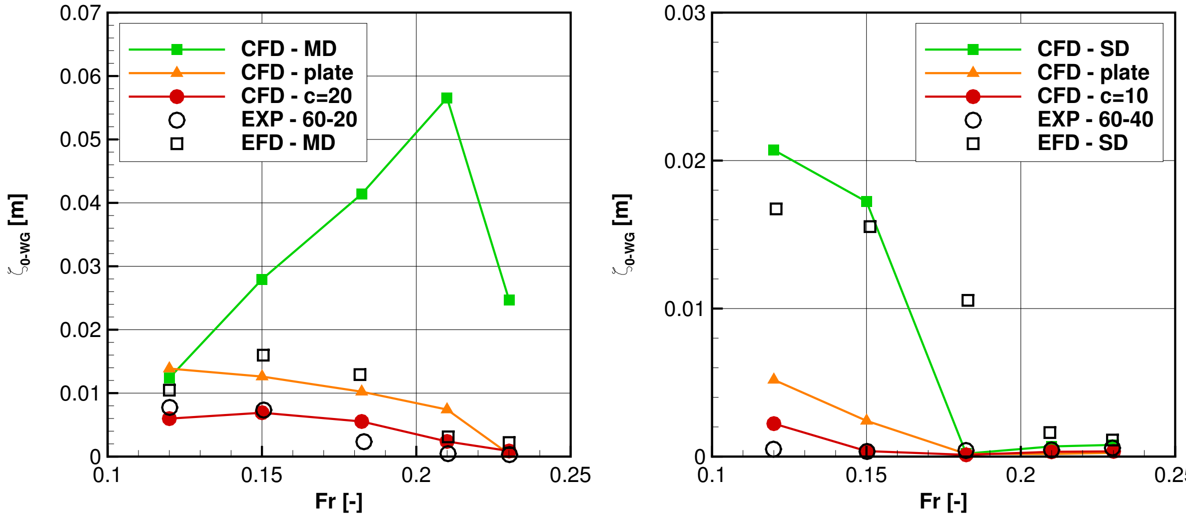


**(a)** $\mathrm{MD}_c$ **(b)** $\mathrm{SD}_c$

**Figure 6.22.:** Damping of oscillating amplitudes for calm water condition

The oscillation amplitude is now distinguished between the amplitudes corresponding to the piston mode frequency (represented by dashed lines) and wave frequency (solid lines). The investigation with applying only a plate and no sponge layer has not been conducted for head seas. Case $\mathrm{MD}_c$ works reasonably well, as both amplitudes match in the experiments and numerical simulations. Only the amplitude at wave frequency and $\lambda_W/L_{PP} = 1.0$ disagrees, as the numerics only predict approx. 50% of the experimental RAO. The numerical results yield a reduction in peak amplitude of 64% and the experiments of 47%. Despite of that, all other amplitudes are very satisfying. The agreement between experimentally and numerically damped oscillations for case $\mathrm{SD}_c$ is very good. Both oscillating amplitudes are reduced by the same amount in the numerical and experimental case. The peak amplitude can be reduced by approx. 75%. A general observation is that the amplitude at piston mode frequency is damped significantly and the remaining amplitude correspond almost solely to the wave frequency.

The effect of perforated bulkheads in head seas at different Froude numbers was only investigated experimentally. Results can be seen in figure 6.24, which is comparing the RAO of oscillating amplitudes at wave frequency of damped case 60-20 (solid lines) with non-damped case MD (dashed lines) for different Froude numbers (different colours). The amplitudes at piston mode frequency are not shown for sake of clarity, as their magnitude at $\lambda_W/L_{PP} = 0.5$ was below $RAO\,(\zeta_{0-WG}) = 0.5$ and vanished completely for longer wave lengths. The perforated bulkhead proved to work efficiently for wave

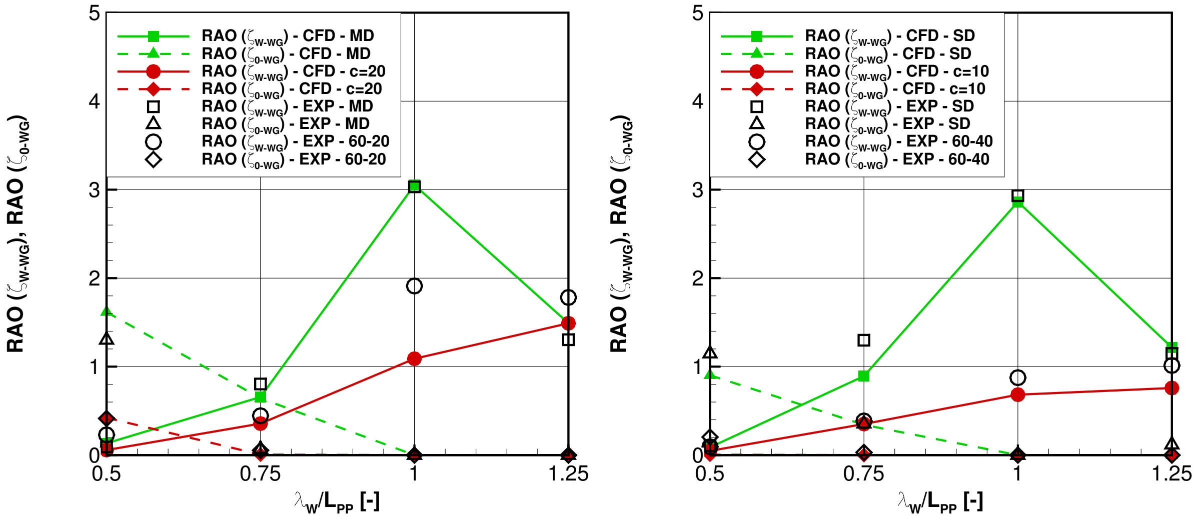


**(a)** $\mathrm{MD}_c$ **(b)** $\mathrm{SD}_c$

**Figure 6.23.:** Damping of oscillating amplitudes for head seas condition

lengths up to the resonant wave length, which is approx. around $\lambda_W/L_{PP} = 1$. Except for the highest Froude number, this wave length produces the largest RAO, which can be reduced by 16-51% using a perforated bulkhead. Most interesting is the behaviour at $\lambda_W/L_{PP} = 1.25$. For $Fr = 0.12 - 0.18$, the RAO of oscillation amplitude is higher for 60-20 than MD. It could not be determined from the experiments, which effect causes an increasing in oscillating amplitude with perforated bulkheads at this wave length. The RAO at $Fr = 0.21$ is very similar between 60-20 and MD. For $Fr = 0.23$ a reduction in RAO still takes place, compared to the non-damped case. Note that at $\lambda_W/L_{PP} = 1.25$ and $Fr = 0.23$ severe green water occurred during the experiments for case MD, as is shown in figure 6.25.

It can be concluded that the numerical damping approach works relatively well to mimic the effect of perforated bulkheads while avoiding complex grids. Additional computational time due to the numerical damping is negligible, as is the increase in cell size due to the grid for the bottom plate. This approach yields qualitatively comparable results and could hence be used to conduct simulations with e.g. a body being handled inside a moonpool with perforated bulkheads. There are however disadvantages, the biggest being until now the random choice of numerical damping constant $c$ to yield comparable results as in the experiments. A bigger experimental variation of perforation and damping chamber size would enable to set up a more sophisticated model of correlating damping constants. Furthermore, the numerical approach cannot reproduce effects such as wall

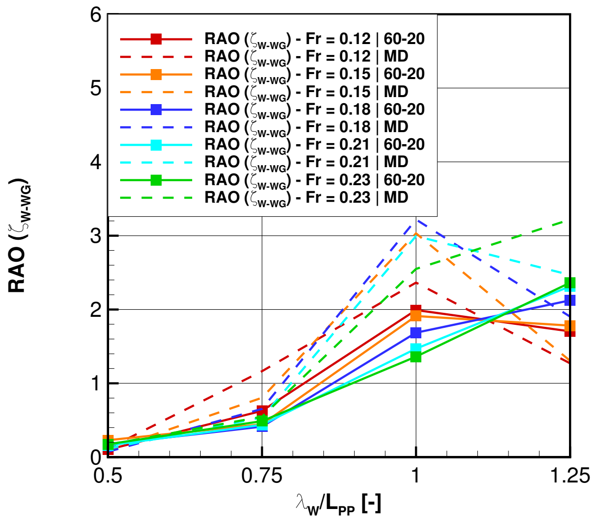


**Figure 6.24.:** Experimental results for damping in head seas condition for different Froude numbers

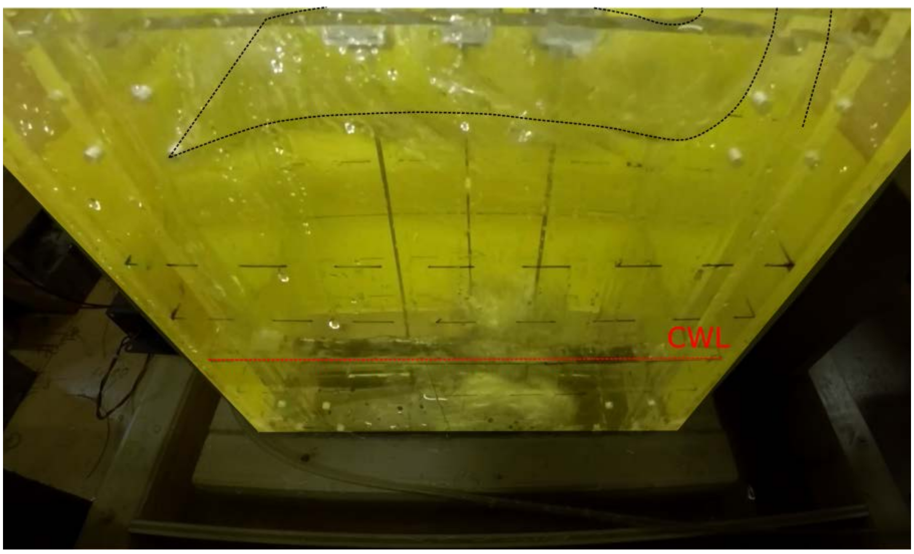


**Figure 6.25.:** Extreme oscillating event with green water at $\lambda_W/L_{PP} = 1.25$ and $Fr = 0.23$

reflection, which would partly happen at perforated bulkheads. It remains unknown though, how much influence such physical effects have and how pronounced they are. Complex experiments with a technique to measure the instantaneous velocities inside the moonpool could give an answer. These are however even with techniques such as Particle Image Velocimetry (PIV) difficult to perform as well as time and data intensive. The author is not aware of any efforts of measuring the flow field inside the moonpool.

### 6.1.7. Closed moonpool

After analysing damping devices in moonpools, it is now investigated what effects occur when closing the moonpool. This has been done solely numerically for calm water at different speeds and for head seas at $Fr = 0.15$. The moonpool grids have been splitted in the free surface at rest in an upper and lower part. The face at the height of the free surface has been defined as wall and forces on that plate measured separately.

A general and expected observation is that no oscillation of the water column takes place any more, as the moonpool can be seen as numerically sealed and no pressure balance can take place. This implies that no resonant piston motion sets in. However, small oscillations in e.g. force signals can be observed, as is shown in figure 6.26c, where the hydrodynamic force component is shown for the hull (red) and moonpool (green) individually. These are due to vortex shedding at much higher frequency, which appears at the leading edge of the moonpool, visualised in figure 6.26a for a random time instance. The black surface represents the closing lid of the moonpool. The shedding frequencies, which have been determined by Fourier analysing a pressure signal, recorded close to the moonpool leading edge, are shown in table 6.2. One can immediately see that the shedding frequencies are much higher than piston or even sloshing type frequencies. A large vortex is formed in the after part of the moonpool as can be seen in the streamlines in figure 6.26b. This vortex also remains for simulations in waves. The non-dimensional velocity magnitude plotted in this figure has been averaged over 7.37 s using 100 time steps. One can see the generally low velocity in the moonpool front part, due to missing water column oscillations. A medium upward directed velocity at the trailing wall is generated through the shear-layer rollup.

Figure 6.27 contains results of resistance coefficients for the ship with closed moonpool at the free surface (FS - solid lines), compared to the ship without moonpool (CL - dashed-dotted lines) and the ship with open moonpool (MP - dashed lines). Figure 6.27a shows the analysis for calm water condition and different Froude numbers. Only the longitudinal components are shown for total resistance coefficients (red), frictional coefficient (green)

**Table 6.2.:** Shedding frequencies for MP closed at free surface

| u [m/s] | Fr [-] | $f_{\text{shedding}}$ [Hz] | $Sr_{mp}$ [-] |
|---|---|---|---|
| 0.651 | 0.12 | 3.628 | 1.672 |
| 0.814 | 0.15 | 4.599 | 1.695 |
| 0.989 | 0.18 | 5.477 | 1.661 |
| 1.139 | 0.21 | 6.093 | 1.605 |
| 1.248 | 0.23 | 6.535 | 1.571 |

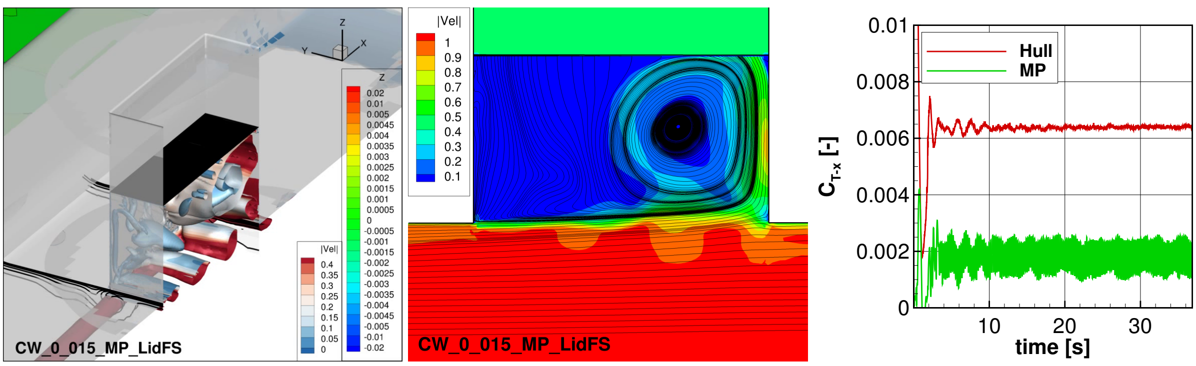


**(a)** Iso-Q surfaces of vortex shedding

**(b)** Streamtraces in longitudinal plane inside the moonpool

**(c)** Total longitudinal hydrodynamic forces on hull and moonpool surfaces

**Figure 6.26.:** Vortices inside closed moonpool MP and resulting hydrodynamic force signal

and pressure coefficient (blue). The lowest resistance is achieved for the ship without moonpool, as was expected. Closing the moonpool at the FS results in a quite constant increase in pressure resistance over Froude number. The frictional resistance is reduced compared to CL, as has been explained already. Interestingly, the pressure resistance of MP is lower than the closed moonpool at FS for small Froude numbers ($Fr < 0.18$) and higher for larger Froude numbers ($Fr > 0.18$). This is can be explained when investigating the pressure field inside the moonpool, which is shown in the appendix C.3. The pressure field does not change for increasing Froude numbers, when the moonpool is closed at the free surface. This is due to a steady mean vortex at all Froude numbers, which is formed, as shown in figure 6.26b. The leading wall always experiences a low pressure field, whereas the trailing wall a high pressure field. The highest pressures can be measured at the trailing edge, where separated vortices hit the trailing wall. The result is a constantly and relatively high pressure resistance. Especially the leading wall pressure field however changes for different Froude numbers, if the moonpool is not closed. At low Froude numbers, a high pressure field also exists at the leading wall, as the mean location of the vortex is at the moonpool centre. This causes a reduction in pressure resistance, when comparing with the moonpool closed at FS. Higher Froude numbers also lead to higher moonpool oscillations, as has been shown. As explained at the beginning, the vortex separation coincides with the upward motion of the free surface. This results in an 'upward suction' of the vortex for severe oscillations and hence a shift of the mean vortex position towards the leading wall. Therefore, a strong low pressure field at the leading wall for high Froude numbers respectively high oscillations occurs and leads to a drastically increasing pressure resistance.

As a conclusion, closing of the moonpool at the FS is hence only favourable in terms of resistance reduction for higher Froude numbers. The open moonpool configuration would be beneficial for an assumed design Froude number of $Fr = 0.15$, where oscillations are relatively low.

Figure 6.27b is showing the same investigation, but for a constant Froude number of $Fr = 0.15$ and different relative wave lengths. Comparing CL with FS shows an identical behaviour as for calm water. The pressure resistance is increased for the ship with the moonpool closed at the free surface. When comparing FS and MP it appears that only at $\lambda_W/L_{PP} = 1$ the resistance for the ship with open moonpool is higher, than for the closed moonpool at free surface. The frequency of that wave length corresponds to the resonant piston mode frequency, producing high oscillations and hence high resistance coefficients. For wave lengths not corresponding to the resonant piston mode, the total resistance coefficients are lower, as was already the case for $Fr = 0.15$ in calm water

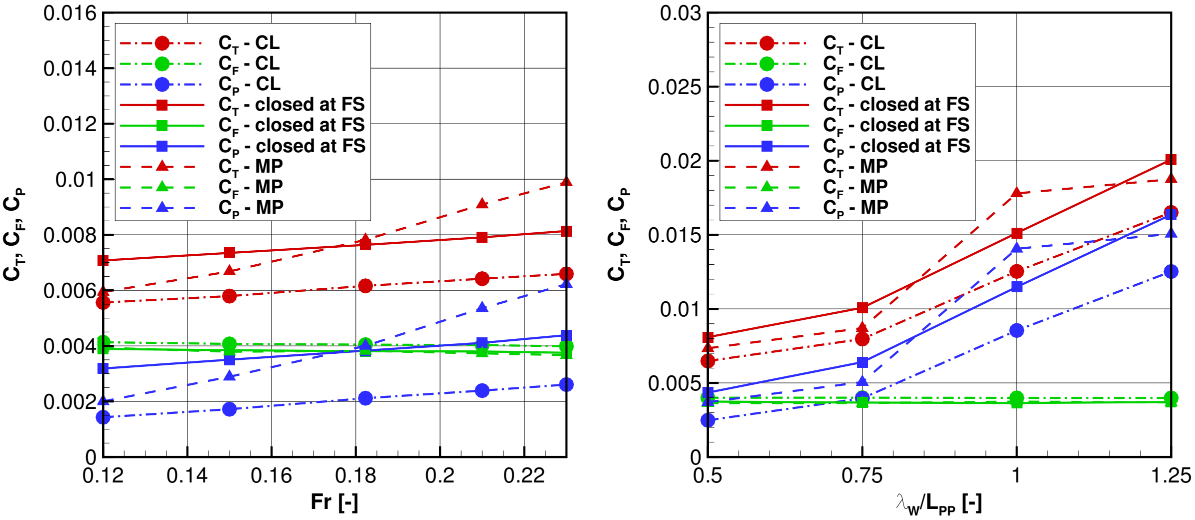


**(a)** Longitudinal resistance coefficients for calm water

**(b)** Longitudinal resistance coefficients in waves

**Figure 6.27.:** Resistance analysis of the ship with closed moonpool at free surface (FS) condition.

The hydrodynamic forces on the plate which closes the moonpool at the FS has been calculated separately in order to get an understanding of its contribution and occurring full scale forces. Figure 6.28 shows the results of this investigation for calm water (left) and waves (right). The vertical forces increase with increasing speed. As frictional forces can be neglected when analysing vertical forces, the remaining components are hydrostatic and dynamic pressure components. Note that the resulting forces shown in figure 6.28 are only a fraction of the hydrostatic force due to the sinkage of the ship, as the dynamic pressure force is counteracting. The hydrostatic force would be almost one order of magnitude higher. Note, that the resistance coefficients are made non-dimensional using the wetted surface of the model and not the area of the plate. The force (shown on the right axis) is made dimensional for the full scale ship (with scale of $\lambda = 65$) and for the full ship (no symmetry).

The same investigation has been done for the case with different wave lengths and is shown in figure 6.28b. The mean force (dashed line) even reduces towards the longest waves, while the force amplitude due to the oscillating wave, shown in the error bars, increases drastically. This was expected, as increasing waves yield an increase in pressure fluctuation at the plate. However, the force amplitude is of reasonable magnitude, compared to the mean force value. A maximum force at $\lambda_W/L_{PP} = 1$ of of approx. 150 kN

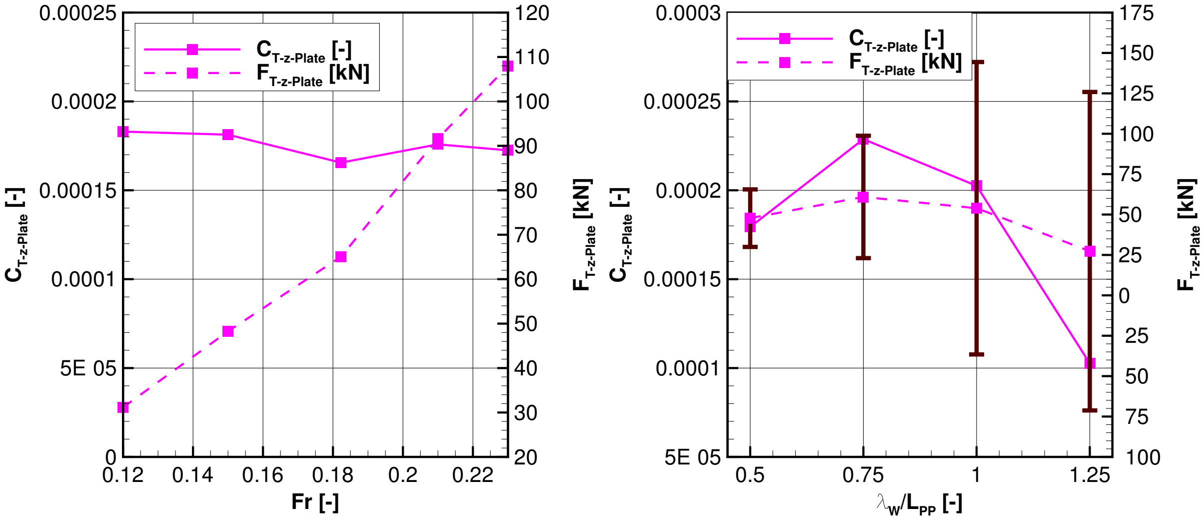


**(a)** Vertical resistance coefficient and force in calm water

**(b)** Vertical resistance coefficient, force and amplitudes in waves

**Figure 6.28.:** Vertical force on plate and force amplitude (error bars)

corresponds to approximately 15 t which seems to be feasible in terms of a mechanical engineering point of view.

## 6.2. Operational condition

This chapter contains results for operational conditions, meaning the ship having no forward velocity and being exposed to waves of different length and direction. Experimental and numerical tests have been conducted for these conditions with a varying wave length of $\lambda_W/L_{PP} = 0.50, 0.75, 1.00$ and 1.25 and encountering angles of $\mu_W = 0°, 45°$ and $90°$. Due to the quite symmetric ship, encountering angles of $\mu_W = 135°$ and $180°$ were skipped. All DOF were unrestrained in both, experiments and numerical simulations, with the exemption of surge, sway and yaw, which were held at a mean position using springs. The spring stiffness were of equal magnitude in experiments and numerics.

One difficulty in performing these measurement is dealing with reflected waves. The case with quartering and beam seas have obviously the highest reflection. Reflection develops in the experiments, as waves travel from the wave maker towards the ship and when reached, are being reflected backwards towards the wave maker again. This can be seen as comparable to real conditions, although reflected waves are being 'channelled' in the seakeeping basin, whereas they are able to take any direction in real condition.

Re-reflected waves from the wave maker should be avoided though in the measurements. Problems might arise if the waves hit the object at an angle (e.g. $\mu_W = 45°$) and are reflected between the walls of the basin. This might lead to not ideally long crested waves, which arrive at the model. Note that no sideways wave absorber has been installed during the experiments, which might prevent side wall reflection.

The simulations face a different problem. Waves arriving at the model are being reflected similar to the experimental case. Although the domain boundaries are not defined as solid walls, numerical re-reflection at the boundaries can, but do not have to arise and is generally difficult to examine. The problem is, that possible re-reflection would happen much faster, as the domain boundaries are much closer to the model, due to practical limitations in grid sizes. Reflecting waves are visualised in figure 6.29, where figure 6.29a is showing the waves after initialisation of the simulation, figure 6.29b the waves after reflection at the ship and figure 6.29c the solution where possible re-reflection might have occurred. Note that this problem mainly arises at zero or low ship velocities. The loss of long-crested waves starts already in figure 6.29b, is fully developed in figure 6.29c and can be mainly assigned due to radiation and diffraction effects. The general wave travelling direction is from top to bottom of the figure and a sponge layer zone can be seen at the bottom, where the amplitude is effectively damped.

The numerical simulations have been performed by damping the waves at the outlet of the domain (depending on the wave direction). This prevented waves to reflect at the domain outlet. Possible re-reflection could not be circumvented using this approach. One possible solution is to apply a sponge layer at all domain boundaries and damp towards the undisturbed wave. This should theoretically prevent reflection of waves at the domain outlet and possible re-reflection of waves at the domain inlet. Normal reflection of waves at the ship would be allowed and hence a similar situation as in the experimental setup being ensured. This approach has been tested for the wave length of $\lambda_W/L_{PP} = 0.5$ and wave direction of $\mu_W = 90°$. The results in motion, forces and moment are almost identical as to the previous damping approach. The same applies for the oscillation behaviour inside the moonpool. Figure 6.29d is showing the corresponding wave field. Comparison with figure 6.29c reveals that the disturbances towards the domain boundaries decreases, which indicates that possible re-reflection would have been prevented. It needs to be mentioned that the wave crest is slightly overestimated and the trough underestimated. This might result on one hand from the coarse grid at the bottom of the figure, which was initially designed to dissipate waves, whereas in this damping approach, the waves are numerically preserved. On the other hand, the chosen boundary conditions of wave type at every vertical domain face for the new damping approach might have been not ideal. It

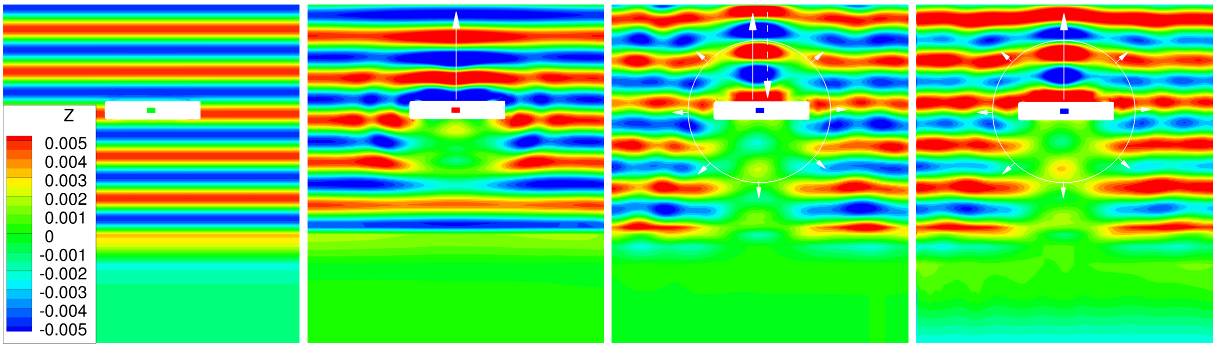


**(a)** Initial wave field **(b)** Reflected waves from model **(c)** Radiated, diffracted and possible re-reflected waves **(d)** Radiated and diffracted waves

**Figure 6.29.:** Effect of reflection at zero speed in numerical simulations

can nevertheless be concluded that numerical re-reflection probably did not influence the results, as they are still of very similar magnitude as for the previous damping approach, where possible re-reflection could have occurred.

The following figures show the results for operational conditions. Translational motions are presented in figure 6.31, rotational motions in figure 6.32. Forces in longitudinal and transverse direction, as well moment around the vertical axis is given in figure 6.33. Finally, figure 6.34 shows the mean wave gauge amplitudes. The coloured lines represent results from numerical simulations and the respective black hollow symbols the experimental results. Solid lines and squared symbols are results from head sea conditions, dashed lines and deltas for quartering seas and dashed-dotted lines with circles represent beam sea conditions.

Overall agreement of motions can be seen as good, but there are some exemptions worth mentioning. The surge and sway motion show some discrepancies between experimental and numerical results. This uncertainty can be assigned to two reasons. First, sidewall reflection in the experiments might have influenced the results more severely than expected. Second, both motions have no restoring forces despite the virtual spring system attached to it. Especially the surge motion takes long time to be damped from its resonant frequency towards a motion responding solely to the wave frequency. Deviating motion magnitudes might have been determined, when running the simulation much longer. The slowly converging signals are shown in figure 6.30a with the red line representing the surge amplitude and the green line sway amplitude for case RW100_45_0_MP. Roll and yaw motion are converging slightly faster in this case towards a harmonic oscillation. Heave

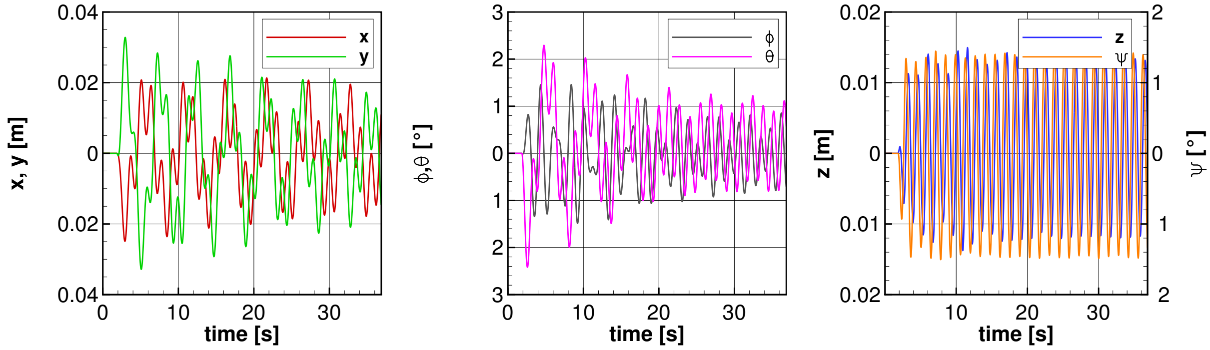


**(a)** Surge and sway motion **(b)** Roll and yaw motion **(c)** Heave and pitch motion

**Figure 6.30.:** Time traces of translational motion and rotational motion for RW100_45_-0_MP

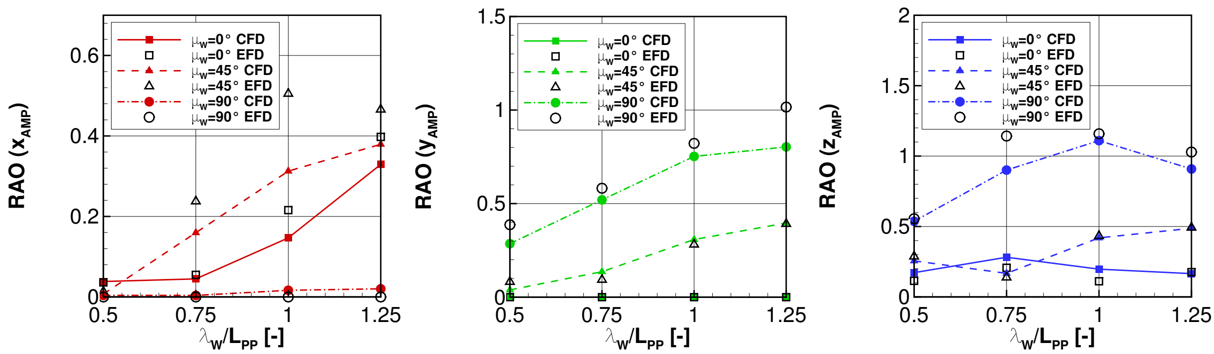


**(a)** Surge motion **(b)** Sway motion **(c)** Heave motion

**Figure 6.31.:** Translational motions

and pitch are due to its strong restoring forces of constant amplitude after a very short time and hence least time critical.

The amplitude shown in the figures refers to the respective wave frequency, although some numerical simulations had higher amplitudes in surge motion, but for the resonant frequency of the spring system. This effect may influence the determination of the amplitude at wave frequency.

The sway motion is, despite a discrepancy of 23% for beam seas at $\lambda_W/L_{PP} = 1.25$, agreeing very well between numerics and experiments.

The same applies for the heave motion, where the largest disagreement occurs at $\lambda_W/L_{PP} = 0.75$ with approximately 21%. All other points match very well.

Rotational motions also agree very well between numerics and experiments. The pitch

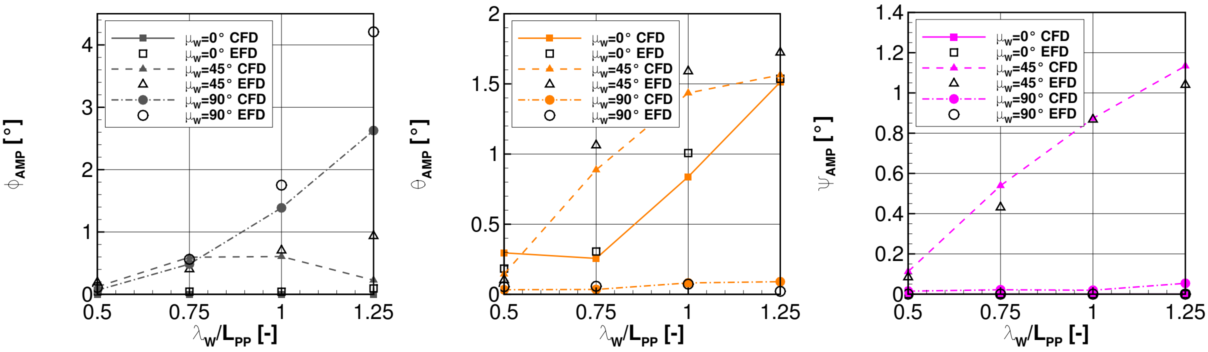


**(a)** Roll motion **(b)** Pitch motion **(c)** Yaw motion

**Figure 6.32.:** Rotational motions

and yaw motions are almost identical in all cases. The largest differences occur for the roll motion at $\lambda_W/L_{PP} = 1.25$. The numerical results show much lower amplitudes for $\mu_W = 45°$ and $90°$ than the experiments.

The force coefficients in longitudinal and transversal direction, as well as the non-dimensional yaw moment are shown in figure 6.33. Note that the fictitious velocity corresponding to $Fr = 0.15$ has been used to determine the non-dimensional force coefficients for the ship at rest. It was decided against introducing new non-dimensional coefficients for operational conditions depending on e.g. $\rho g \zeta_W^2 L$, which are often used for these type of experiments.

The progression of curves for the different wave encountering angles between experiments and numerics have similar trends, but are deviating partly severely. Reason for this is most probably found in different reflection behaviour in the wave basin and the numerical domain and the generally very low magnitude of forces and moment. Most deviating is the longitudinal force for $\mu_W = 45°$ and transversal force for $\mu_W = 90°$. These encountering angles are troublesome in terms of reflection, as was mentioned. Repetition of numerical simulations with no-slip wall conditions representing the seakeeping basin walls could give more insight if reflection is indeed reason for the deviating forces. The yaw moment shown in figure 6.33c agrees reasonable well for long waves but deviates slightly between experiment and numerics for short waves.

In order to avoid reflections it might be beneficial to conduct the simulations with a sponge layer at every domain boundary, damping the field towards the undisturbed wave and to conduct the experiments with sideways installed wave absorbers.

The RAO's of mean oscillation amplitude inside the moonpool are shown in figure 6.34. The progression of all curves match well between experiments and numerics. Small dis-

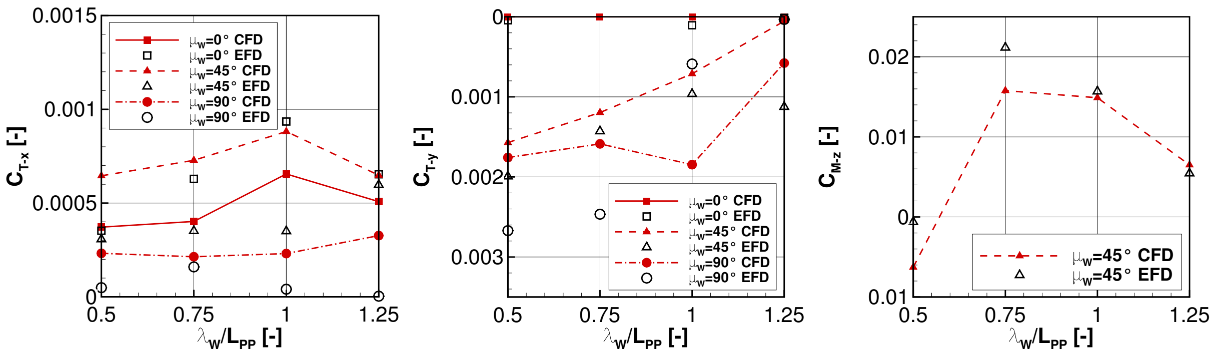


**(a)** Longitudinal force coefficient

**(b)** Transversal force coefficient

**(c)** Vertical moment coefficient

**Figure 6.33.:** Forces and moment coefficients

crepancies are found at shorter wave lengths, which are however acceptable. The amplitudes are all corresponding to the respective wave frequencies and not to the piston mode frequency. The wave frequency at $\lambda_W/L_{PP} = 0.5$ is $f_W \approx 1\,\mathrm{Hz}$ and drops towards $f_W \approx 0.65\,\mathrm{Hz}$ for $\lambda_W/L_{PP} = 1.25$. Hence, only the smallest investigated wave is in the vicinity of the resonant piston mode frequency, whereas all other waves have significantly lower frequencies. The RAO for this wave length at $\mu_W = 0°$ reaches values between 0.5 and 0.9 and is hence of similar magnitude as in transit conditions for low Froude numbers. Interestingly, the RAO for $\mu_W = 45°$ and 90° is significantly higher and reaches values of approx. 3. As shown in figure 5.14, restraining of heave and pitch motion at $\mu_W = 45°$ lead to a severe reduction in RAO. Hence, reason for increasing RAO's can be found in undesirable phase shifts between ship motion, wave elevation and moonpool water column elevation. The time series and phase shifts for all three wave directions are shown in appendix C.4. The phase shift between the wave elevation $\zeta_W$ and heave motion $\zeta$ at $\mu_W = 45°$ is $\epsilon = 180°$ and hence exactly out of phase, leading to an amplification of moonpool water column oscillation. For $\mu_W = 90°$, this phase shift is only $\epsilon = 44°$. However, the moonpool water column oscillates with a phase shift of approx. $\epsilon = 135°$ with regard to the wave elevation $\zeta_W$, leading again to high RAO of moonpool oscillation.

For waves longer than $\lambda_W/L_{PP} = 1$ the RAO for quartering and beam seas show lower values than for head seas, although only slightly.

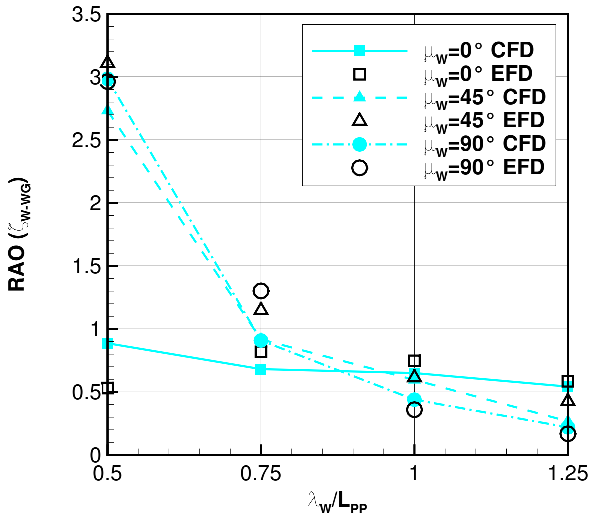


**Figure 6.34.:** Mean oscillation amplitudes inside moonpool MP

## 6.2.1. Influence of damping in operational condition

It has been experimentally investigated, which effect perforated bulkheads have in operational condition. This has been done for wave direction of $\mu_W = 0°$ and 45°. The comparison is made between MD and 60-20. Both have the same moonool opening at the bottom of the ship, while MD has solid walls and 60-20 a perforation of 60%.

Figure 6.35 shows the RAO's for these conditions. Note that the frequencies again all correspond to the respective wave frequencies and not the piston mode frequency. The solid lines represent the case without damping and the dashed lines with damping. The progression of the non-damped case MD is similar as for MP, which was discussed in figure 6.34. Constantly lower RAO's than 1 are reached for $\mu_W = 0°$, while a high peak is observed at $\lambda_W/L_{PP} = 0.5$ for $\mu_W = 45°$. The perforated bulkheads have a significant influence on short waves of $\lambda_W/L_{PP} = 0.5$, where a reduction in oscillation amplitude of approx. 80% and 60% are reached for $\mu_W = 0°$ respectively $\mu_W = 45°$. This is a significant enhancement of operational conditions at these wave lengths. When looking at longer waves, this advantage diminishes, as the RAO for the case with damping is slightly larger than without damping. The peak of RAO for cases with damping is reached at $\lambda_W/L_{PP} = 0.75$ where an increase of approx. 60% and 40% is observed. This increasing amplitude drops again for longer waves and converges towards the amplitudes of MD, where differences between damped and non-damped case tend to get negligible.

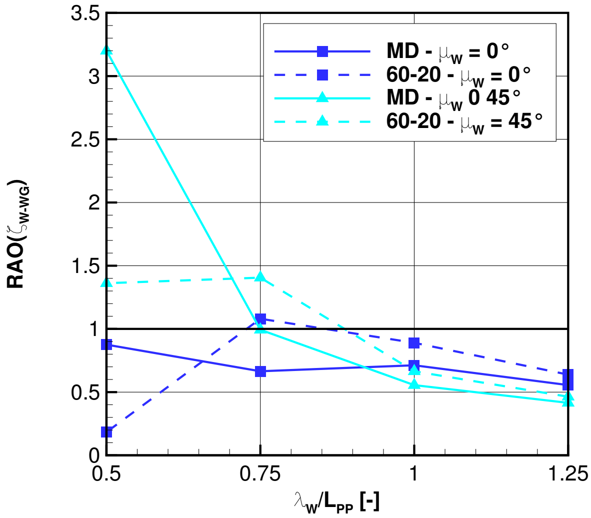


**Figure 6.35.:** Experimental RAO's of mean oscillation inside MD and 60-20 for different wave encountering angles

# 7. Conclusions

This work dealt with the investigation of different flow phenomena inside moonpools. Therefore, numerical simulations have been performed for a ship with different moonpool geometries. The investigated moonpools varied in size (MP, MD and SD) and in length to breadth ratio (lb1 and lb2). Tests were conducted in calm water for varying Froude numbers, regular waves of different wave length and direction and for the ship at rest. Furthermore, the performance of damping devices inside the moonpool was analysed. Main focus of all investigations was the oscillation behaviour of the water column inside the moonpool. The procedure for the analysis was to Fourier transform the wave gauge time signal and determine the spectral amplitudes at the frequencies of interest. These frequencies were usually the natural piston mode frequency and, if present, the wave frequency. In order to validate the numerical results, experiments have been conducted in a seakeeping basin at the Technical University of Berlin with a newly developed measuring device. The following conclusion can be drawn from the investigation:

The numerical method used is generally able to predict ship and especially moonpool characteristics accurately. The water column motion of the moonpool usually agrees well with experimentally determined results. This applies in particular when investigating the ship in waves, where the water column oscillation is influenced by the presence of waves. The spectral amplitude due to the piston mode motion in the moonpool is generally dominating for small wave lengths compared to the spectral amplitude, which belongs to the wave frequency. Increasing wave lengths however leads to a shift of dominant amplitude from piston towards wave frequency. Coinciding piston mode frequencies and wave frequencies lead to resonant behaviour. These situations should be avoided as response amplitude operators for the free surface oscillation of $RAO(\zeta_{WG}) > 3$ might occur and thereby a strong amplification of the water column oscillation. This generally leads to a drastic increase in resistance and can also cause green water on deck. The oscillation behaviour at calm water condition is more difficult to predict than in regular waves. Some discrepancies between experimental and numerical results occurred for that condition, although general agreement can be seen as satisfactory. One discrepancy is e.g. the mean oscillation amplitudes for moonpool MD, which were relatively high in numerical simulations, compared to the experimental results. Reason for this deviation is not clear. One influencing factor might have been the usage of insertions in the experiments, which produced additional edges in front of the moonpool leading edge. These edges are not present in the numerical model and might have produced artificial vortices, leading to an increased damping in the experiments. Comparison of vortex generation and propagation between numerical and experimental tests would be necessary to further investigate this discrepancy. This would imply the experimental measurement of the velocity field inside the moonpool, being very data and time consuming and which could hence not be conducted within this work. The agreement of amplitudes for SD and MP were satisfactory, although the numerical results predicted slightly higher amplitudes for MP at highest Froude numbers, than the experiments. The oscillating amplitude collapsed for higher Froude numbers and almost no oscillation could be measured any more for these velocities. The point of collapse can be roughly estimated at moonpool Froude number of $Fr_{mp} = v/\sqrt{l_{mp}g} = 0.75$.

Perforated bulkheads are commonly used to damp the oscillation amplitude inside moonpools. Considering the exact geometry of perforated bulkheads leads to highly complex grids and a drastic increase in computational costs. A new method has been developed, where a numerical damping approach has been successfully implemented into the flow solver in order to mimic the effect of perforated bulkheads. This approach avoids the necessity of complex grids and hence reduces significantly the number of grid cells and, in case of *REX*, also the amount of processors due to a reduced number of blocks. The derived numerical oscillation amplitudes agreed very well with experimental data, where the moonpool has been investigated with an exact geometry of a perforated bulkhead. This new approach can hence be used to conduct highly accurate numerical simulations under consideration of damping effects due to perforated bulkheads, without further increasing grid complexity. Further valuable insight into the flow behaviour with perforated bulkheads would be achieved, if numerical simulations for the exact represented geometry would be conducted. This should however be done using a flow solver with unstructured grids in order to keep the additional computational costs reasonable. The perforated bulkheads investigated in this work reduced the oscillation amplitude by up to 85% and hence clearly improved the performance, especially during transit conditions. It should be noted that experiments revealed slightly higher oscillation amplitudes for perforated bulkheads in operational conditions and waves of $\lambda_W/L_{PP} \geq 0.75$, than without the perforated bulkheads. This phenomenon could unfortunately not be further investigated, due to the lack of information on the flow field during experimental tests. Perforated bulkheads however reduced the oscillation amplitude drastically for short waves of $\lambda_W/L_{PP} = 0.5$.

Closing the moonpool at the free surface leads to a complete suppression of water column oscillation. The influence on resistance components changes for varying Froude numbers. The viscous pressure resistance increases for all Froude numbers compared to the ship without moonpool, due to a steady vortex in the aft half of the moonpool. If the moonpool is not closed, this increase is up to 16% lower for small Froude numbers and 22% higher for larger Froude numbers. Closing of the moonpool is hence only beneficial for higher Froude numbers. Typical design Froude numbers of such ships are in the area of $Fr = 0.18$, which is were both approaches, open moonpool and moonpool closed at the free surface, have similar resistance coefficients. If waves are being present, the resistance of the open moonpool increases for $Fr = 0.15$ by 18% at point of resonance, where the moonpool experiences strong oscillation amplitudes. For other wave frequencies, the resistance increase/decrease remains similar as in the calm water case. A detailed operational velocity profile of the ship including typical encounter wave spectra would be necessary to determine, if closure of the moonpool at the free surface is advantageous. If the ship is however seldom sailing at higher speeds than $Fr = 0.18$, the resistance would be lower if the moonpool remains open. Naturally, the lowest resistance would be achieved when closing the moonpool at the keel, which would however lead to sloshing events if the water column remains in the moonpool.

Almost all measured oscillations of the moonpool could be assigned to the natural piston mode frequency or wave frequency if present. Clear sloshing frequencies seldom occurred. A strong dependency of the natural piston mode frequency on the ship speed was detected during this investigation. Knowledge of the correct piston mode frequency can lead to better avoidance of resonant behaviour in sea states, as has been shown. Therefore, an empirical approach has been developed within this work, based on the moonpool length $l_{mp}$ and moonpool Froude number $Fr_{mp}$. This method is able to predict the velocity dependent piston mode frequencies accurately and can hence improve the correct determination of the exact resonant point. Current methods can only be applied for zero speed conditions and hence deviate partly severely from real resonant frequencies at forward speed. Especially for very low moonpool Froude numbers and collapsed oscillations due to moonpool Froude numbers higher than $Fr_{mp} = 0.75$, these frequencies may however deviate severely from the natural piston mode frequency. This newly developed empirical method should be therefore applied with care for these conditions. More data from other ship geometries and their moonpool oscillation behaviour would significantly improve the empirical method and might also determine better dependencies from geometrical properties.

The wave direction has a strong influence on the oscillation amplitude inside the moonpool. This can be explained by two reasons. First, the encountering frequency changes in transit condition, when changing the wave direction. This leads to resonant effects at different wave lengths. A change of heading would hence lead to a different encounter wave frequency, which could then avoid high oscillating amplitudes due to a coinciding frequency with the natural piston mode motion. Second, undesirable phase shifts between the wave elevation, heave motion and moonpool water column oscillation can lead to further amplification of the oscillating amplitude inside the moonpool. The individual phase shifts vary for different wave directions and lengths. Strong amplification due to phase shifts occurred in operational condition (at zero speed) for the shortest investigated wave at $\mu_W = 45°$ and $90°$.

One additional important finding of this work has been the difference in results from the turbulence models RANS and DDES. Although DDES provides a much higher vortex resolution and is expected to lead to more accurate results, a severe time step divergence occurred. This has not been the case for the RANS model. Reason for divergence has unfortunately not been found and should be further investigated. As mentioned, DDES is time dependent due to the definition of length scale in dependence on the boundary layer. This is not the case for DES. A comparison should hence be conducted if DES leads to similar time step divergence, as DDES did. Due to the dependence of DDES on the boundary layer, the influence of vortices originating from the forefoot and contracting the boundary layer should also be included in the investigation. At last, the grid resolution in the area of vortex generation could be adapted according to the recommendations given in chapter 2.2.4, which could give an answer if Courant numbers are playing an important role for DDES simulations.

Deviating forces between experiments and numerical simulations were found for operational conditions (ship at rest). Influence of possible re-reflection was investigated by damping towards the undisturbed wave at all domain boundaries. This approach should avoid re-reflection but yielded similar results as when damping towards a free stream condition. It is hence not believed that numerical re-reflection was causing the deviating results. It is more likely that side-wall reflection was disturbing the experiments. This should be avoided by installing perforated sheets next to the model in the seakeeping basin. Consideration of side-walls in numerical simulations could confirm this assumption. The grid had to be adapted and new simulations conducted. These would probably need to be of longer simulation time in order to achieve a similar reflection behaviour as in the experiments and would be hence time consuming. Furthermore to possible reflection issues, the friction in bearings of the measuring frame might be influencing the force measurements. This especially applies for zero speed conditions, as the measured mean forces are extremely low. At last, the surge and sway motion in the numerical simulations is converging slowly, taking into account the attached springs. Hence, simulations should be run much longer for these situations, or active damping in the respective DOF could be applied, which however might tamper the results.

Biggest drawback of the numerical simulations has been the long computational time. This especially applies for simulations with quartering or beam seas, where the domain doubles in size. Viscous effects are only of interest in vicinity of the ship respectively moonpool. This suggests the usage of either coupled potential theory and viscous methods, or usage of e.g. SWENSE (Spectral Wave Explicit Navier Stokes Equations). Both methods make use of the simple and accurate determination of waves using potential theory, which is significantly faster. As mentioned, the coupled method developed in [47, 30, 31] yielded a reduction in computational time of three magnitudes.

Extensive research has been conducted in the field of moonpool flow analysis, providing valuable data for different configurations of moonpool geometries and environmental conditions. Both, the experimental and numerical methods were complex, above state of the art and yielded for highest possible accuracy. Especially the numerical simulations have until now been seldom conducted in such detail, complexity and extent for moonpool analyses. Some important findings have been made and new approaches for numerical consideration of perforated bulkheads and more accurate determination of natural piston mode frequencies developed. As only one ship could be investigated, these approaches should be further refined using additional data from other geometries.

# Appendix A.

# Reflection coefficient

## A.1. 2-point-method

Using Fourier transformation, equation 58 can be expressed for both probes at the locations $x_1$ respectively $x_2$ through the respective Fourier series with the Fourier coefficients $A_{1,j}, B_{1,j}, A_{2,j}$ and $B_{2,j}$

$$\zeta_1(t) = \sum_{j=1}^{N} [A_{1,j} \cos(\omega_{W,j} t) + B_{1,j} \sin(\omega_{W,j} t)] \tag{116}$$

$$\zeta_2(t) = \sum_{j=1}^{N} [A_{2,j} \cos(\omega_{W,j} t) + B_{2,j} \sin(\omega_{W,j} t)] \,, \tag{117}$$

with

$$A_{1,j} = \zeta_{I,j} \cos(\Phi_{I,j}) + \zeta_{R,j} \cos(\Phi_{R,j}) \tag{118}$$

$$B_{1,j} = \zeta_{I,j} \sin(\Phi_{I,j}) + \zeta_{R,j} \sin(\Phi_{R,j}) \tag{119}$$

$$A_{2,j} = \zeta_{I,j} \cos(k_{W,j} \Delta x + \Phi_{I,j}) + \zeta_{R,j} \cos(k_{W,j} \Delta x + \Phi_{R,j}) \tag{120}$$

$$B_{2,j} = \zeta_{I,j} \sin(k_{W,j} \Delta x + \Phi_{I,j}) - \zeta_{R,j} \sin(k_{W,j} \Delta x + \Phi_{R,j}), \tag{121}$$

where $\Delta x = x_2 - x_1$ is the distance between the two probe locations.

Correlation between (116) & (117) and ultimately (137) & (138) has been explained by Riekert [61] and will be only repeated here:

Fourier analysis of a signal leads to the following imaginary form:

$$P_j = x_j + i \cdot y_j = C_j e^{(i\Phi_j)} = C_j \cos(\Phi_j) + iC_j \sin(\Phi_j) \tag{122}$$

The signal can then be written as:

$$\zeta_j(t) = C_j \cos(\omega_{W,j} t + \Phi_j) \tag{123}$$
$$= C_j \left[\cos(\omega_{W,j} t) \cos(\Phi_j) - \sin(\omega_{W,j} t) \sin(\Phi_j)\right] \tag{124}$$
$$= x_j \cos(\omega_{W,j} t) + (-y_j) \sin(\omega_{W,j} t) \tag{125}$$

with $x_j = C_j \cos(\Phi_j)$ and $y_j = C_j \sin(\Phi_j)$. The coefficients in equation (116) & (117) are hence identical to the real respectively negative imaginary part of the complex Fourier spectrum. To determine equations (62)-(63) and (116)-(121) the relationship shown in equation (116) & (117) is used for the signal of probe 1 and 2 individually. The coordinate systems is placed at probe 1 and the angle sum of trigonometric functions $\sin(\alpha + \beta) = \sin(\alpha)\cos(\beta) + \cos(\alpha)\sin(\beta)$ as well as $\cos(\alpha + \beta) = \cos(\alpha)\cos(\beta) - \sin(\alpha)\sin(\beta)$ is used.

$$\begin{aligned}
\zeta_1(x,t) = \quad & \zeta_I(0,t) + \zeta_R(0,t) \\
= & \sum_{j=1}^{N} \left[\zeta_{I,j} \cos(-\omega_{W,j} t + \Phi_{I,j}) + \zeta_{R_j} \cos(\omega_{W,j} t + \Phi_{R,j})\right] \\
= & \sum_{j=1}^{N} \zeta_{I,j} \left[\cos(-\omega_{W,j} t) \cos(\Phi_{I,j}) + \sin(\omega_{W,j} t) \sin(\Phi_{I,j})\right] \\
& + \zeta_{R,j} \left[\cos(\omega_{W,j} t) \cos(\Phi_{R,j}) - \sin(\omega_{W,j} t) \sin(\Phi_{R,j})\right]
\end{aligned}$$

$$
\begin{aligned}
&= \sum_{j=1}^{N} \underbrace{\left[\zeta_{I,j}\cos(\Phi_{I,j}) + \zeta_{R,j}\cos(\Phi_{R,j})\right]}_{A_{1,j}} \cos(\omega_{W,j}t) \\
&\quad + \underbrace{\left[\zeta_{I,j}\sin(\Phi_{I,j}) - \zeta_{R,j}\sin(\Phi_{R,j})\right]}_{B_{1,j}} \sin(\omega_{W,j}t) \qquad (126)
\end{aligned}
$$

$$
\begin{aligned}
\zeta_2(x,t) =& \quad \zeta_I(\Delta x, t) + \zeta_R(\Delta x, t) \\
=& \sum_{j=1}^{N} \left[\zeta_{I,j}\cos(k_{W,j}\Delta x - \omega_{W,j}t + \Phi_{I,j}) + \zeta_{R_j}\cos(k_{W,j}\Delta x + \omega_{W,j}t + \Phi_{R,j})\right] \\
=& \sum_{j=1}^{N} \zeta_{I,j}\left[\cos(-\omega_{W,j}t)\cos(k_{W,j}\Delta x + \Phi_{I,j}) + \sin(\omega_{W,j}t)\sin(k_{W,j}\Delta x + \Phi_{I,j})\right] \\
& + \zeta_{R,j}\left[\cos(\omega_j t)\cos(k_{W,j}\Delta x + \Phi_{R,j}) - \sin(\omega_{W,j}t)\sin(k_{W,j}\Delta x + \Phi_{R,j})\right] \\
=& \sum_{j=1}^{N} \underbrace{\left[\zeta_{I,j}\cos(k_{W,j}\Delta x + \Phi_{I,j}) + \zeta_{R,j}\cos(k_{W,j}\Delta x + \Phi_{R,j})\right]}_{A_{2,j}} \cos(\omega_{W,j}t) \\
& + \underbrace{\left[\zeta_{I,j}\sin(k_{W,j}\Delta x + \Phi_{I,j}) - \zeta_{R,j}\sin(k_{W,j}\Delta x + \Phi_{R,j})\right]}_{B_{2,j}} \sin(\omega_{W,j}t) \qquad (127)
\end{aligned}
$$

To determine equation (137) & (138), equations (120) and (121) need to be rewritten:

$$
\begin{aligned}
A_{2,j} =& \quad \zeta_{I,j}\cos(k_{W,j}\Delta x + \Phi_{I,j}) + \zeta_{R,j}\cos(k_{W,j}\Delta x + \Phi_{R,j}) \qquad (128) \\
=& \quad \zeta_{I,j}\left[\cos(k_{W,j}\Delta x)\cos(\Phi_{I,j}) - \sin(k_{W,j}\Delta x)\sin(\Phi_{I,j})\right] \\
& + \zeta_{R,j}\left[\cos(k_{W,j}\Delta x)\cos(\Phi_{R,j}) - \sin(k_{W,j}\Delta x)\sin(\Phi_{R,j})\right] \\
=& \quad \left[\zeta_{I,j}\cos(\Phi_{I,j}) + \zeta_{R,j}\cos(\Phi_{R,j})\right]\cos(k_{W,j}\Delta x) \\
& - \left[\zeta_{I,j}\sin(\Phi_{I,j}) + \zeta_{R,j}\sin(\Phi_{R,j})\right]\sin(k_{W,j}\Delta x) \\
=& \quad A_{1,j}\cos(k_{W,j}\Delta x) - \left[\zeta_{I,j}\sin(\Phi_{I,j}) + \zeta_{R,j}\sin(\Phi_{R,j})\right]\sin(k_{W,j}\Delta x)
\end{aligned}
$$

$$
A_{2,j} - A_{1,j}\cos(k_{W,j}\Delta x) = \left[\zeta_{I,j}\sin(\Phi_{I,j}) + \zeta_{R,j}\sin(\Phi_{R,j})\right]\sin(k_{W,j}\Delta x) \qquad (129)
$$

and similar operations lead to

$$
B_{2,j} - B_{1,j}\cos(k_{W,j}\Delta x) = \left[\zeta_{I,j}\cos(\Phi_{I,j}) + \zeta_{R,j}\cos(\Phi_{R,j})\right]\sin(k_{W,j}\Delta x) \qquad (130)
$$

In a second step, the derived equations are multiplied with equation (120) respectively (118):

$$A_{2,j}B_{1,j} - A_{1,j}B_{1,j}\cos(k_{W,j}\Delta x) = -\left[\zeta_{I,j}^2\sin^2(\Phi_{I,j}) - \zeta_{R,j}^2\sin^2(\Phi_{R,j})\right]\sin(k_{W,j}\Delta x) \quad (131)$$

$$A_{1,j}B_{2,j} - A_{1,j}B_{1,j}\cos(k_{W,j}\Delta x) = \left[\zeta_{I,j}^2\cos^2(\Phi_{I,j}) - \zeta_{R,j}^2\cos^2(\Phi_{R,j})\right]\sin(k_{W,j}\Delta x) \quad (132)$$

Subtraction of those two equations results in:

$$\zeta_{I,j}^2 - \zeta_{R,j}^2 = \frac{A_{1,j}B_{2,j} - A_{2,j}B_{1,j}}{\sin(k_{W,j}\Delta x)} \quad (133)$$

Equation (118) and (119) respectively (129) and (130) squared and summed up yield

$$A_{1,j}^2 + B_{1,j}^2 = \zeta_{I,j}^2 + 2\zeta_{I,j}\zeta_{R,j}\cos(\Phi_{I,j} + \Phi_{R,j}) + \zeta_{R,j}^2 \quad (134)$$

$$\zeta_{I,j}^2 - 2\zeta_{I,j}a_{R,j}\cos(\Phi_{I,j} + \Phi_{R,j}) + \zeta_{R,j}^2 = \frac{[A_{2,j} - A_{1,j}\cos(k_{W,j}\Delta x)]^2 + [B_{2,j} - B_{1,j}\cos(k_{W,j}\Delta x)]^2}{\sin^2(k_{W,j}\Delta x)} \quad (135)$$

Summation of the last two equations yields

$$\zeta_{I,j}^2 + \zeta_{R,j}^2 = \frac{(A_{1,j}^2 + B_{1,j}^2)\sin^2(k_{W,j}\Delta x) + [A_{2,j} - A_{1,j}\cos(k_{W,j}\Delta x)]^2 + [B_{2,j} - B_{1,j}\cos(k_{W,j}\Delta x)]^2}{2\sin^2(k_{W,j}\Delta x)} \quad (136)$$

Equation (133) and (136) can both be used to state the final expression for $\zeta_{I,j}$ respectively $\zeta_{R,j}$

$$\zeta_{I,j} = \frac{\sqrt{(A_{2,j} - A_{1,j}\cos(k_{W,j}\Delta x) - B_{1,j}\sin(k_{W,j}\Delta x))^2 + (B_{2,j} + A_{1,j}\sin(k_{W,j}\Delta x) - B_{1,j}\cos(k_{W,j}\Delta x))^2}}{2|\sin(k_{W,j}\Delta x)|} \quad (137)$$

$$\zeta_{R,j} = \frac{\sqrt{(A_{2,j} - A_{1,j}\cos(k_{W,j}\Delta x) + B_{1,j}\sin(k_{W,j}\Delta x))^2 + (B_{2,j} - A_{1,j}\sin(k_{W,j}\Delta x) - B_{1,j}\cos(k_{W,j}\Delta x))^2}}{2|\sin(k_{W,j}\Delta x)|} \quad (138)$$

Hence, the initial and reflected amplitudes can be expressed solely by the geometrical relationship of the two probes $\Delta x$ and the Fourier coefficients for every individual wave component $j$. To determine the reflection coefficient for every individual frequency, equation (61) can be used. An overall reflection coefficient can be described by first determining the initial and reflected amplitude spectra using

$$S_I(\omega_W) = \frac{\zeta_I(\omega_W)^2}{2 \cdot d\omega_W} \tag{139}$$

$$S_R(\omega_W) = \frac{\zeta_R(\omega_W)^2}{2 \cdot d\omega_W}. \tag{140}$$

With those, the energy of the spectra can be expressed as the integration of the amplitude spectra over the frequency range.

$$E_I = \int_{\omega_{min}}^{\omega_{max}} S_I(\omega_W) d\omega_W \tag{141}$$

$$E_R = \int_{\omega_{min}}^{\omega_{max}} S_R(\omega_W) d\omega_W \tag{142}$$

Goda & Suzuki [35] as well as Mansard & Funke [53] stress the following weaknesses of this method in their publications:

1. The denominator in equation (137) and(138) leads to indetermination of these equations, if the distance between the probes $\Delta x$ is such, that $x/\lambda_W = n/2$, with $n = 0, 1, 2, \ldots$ and $\lambda_W$ being the wave length.
2. The frequency range is limited as:
   a) The estimation gets less reliable if the coherency factor decreases, which happens if the distance between the probes is too large.
   b) The contrast in the cross spectral analysis is reduced, when the distance gets too small.

## A.2. 3-point-method

Similar to the 2-point-method, this chapter contains additional explanations about the derivation of the 3-point-method, which has been already explained in detail by Riekert [61] and will only be repeated here.

The probe signals are being Fourier transformed and written as:

$$\zeta_p(t) = \sum_{j=1}^{N} C_{p,j} \cos(\omega_{W,j} t + \Phi_{p,j}), \tag{143}$$

with $C_{p,j}$ being the Fourier coefficient for every component $j$ at every probe $p$. Note, that Mansard and Funke used a different notation of the general wave equations. Equation (143) can be written in polar or rectangular form

$$B_{p,j} = C_{p,j} e^{(i\Phi_{p,j})} \tag{144}$$

$$= \left[C_{p,j}\cos(\Phi_{p,j}) + iC_{p,j}\sin(\Phi_{p,j})\right]. \tag{145}$$

Again, the elevation of irregular waves can be written as a summation of discrete harmonic components, which is being composed of an incident wave and a reflected wave travelling in the opposite direction

$$\zeta(x,t) = \sum_{j=1}^{N}\left[\zeta_{I,j}\cos(\omega_{W,j}t - k_{W,j}x - \Phi_{I,j}) + \zeta_{R,j}\cos(\omega_{W,j}t + k_{W,j}x + \Phi_{R,j})\right] + \Omega(x,t), \tag{146}$$

with $\Omega$ being introduced as a noise signal considering the errors mentioned in the 2-point-method. If the origin of the coordinate system is placed at the position of the first probe, equation (146) results for three probes in

$$\zeta_1(0,t) = \sum_{j=1}^{N}\left[\zeta_{I,j}\cos(\omega_{W,j}t - \Phi_{I,j}) + \zeta_{R,j}\cos(\omega_{W,j}t + \Phi_{R,j})\right] + \Omega(0,t) \tag{147}$$

$$\zeta_2(x_{12},t) = \sum_{j=1}^{N}\left[\zeta_{I,j}\cos(\omega_{W,j}t - k_{W,j}x_{12} - \Phi_{I,j}) + \zeta_{R,j}\cos(\omega_{W,j}t + k_{W,j}x_{12} + \Phi_{R,j})\right] + \Omega(x_{12},t) \tag{148}$$

$$\zeta_3(x_{13},t) = \sum_{j=1}^{N}\left[\zeta_{I,j}\cos(\omega_{W,j}t - k_{W,j}x_{13} - \Phi_{I,j}) + \zeta_{R,j}\cos(\omega_{W,j}t + k_{W,j}x_{13} + \Phi_{R,j})\right] + \Omega(x_{13},t). \tag{149}$$

Equations (147)-(149) are Fourier transformed, written in polar form and conjugated, to achieve a similar expression as Mansard and Funke did:

$$B_{1,j} = \underbrace{\zeta_{I,j} e^{(i\Phi_{I,j})}}_{Z_{I,j}} + \underbrace{\zeta_{R,j} e^{(-i\Phi_{R,j})}}_{Z_{R,j}} + \underbrace{Y_{1,j} e^{(-i\phi_{1,j})}}_{\epsilon_{1,j}} \tag{150}$$

$$B_{2,j} = \underbrace{\zeta_{I,j} e^{(i(k_{W,j}x_{12}+\Phi_{I,j}))}}_{Z_{I,j}e^{(ik_{W,j}x_{12})}} + \underbrace{\zeta_{R,j} e^{(-i(k_{W,j}x_{12}+\Phi_{R,j}))}}_{Z_{R,j}e^{(ik_{W,j}x_{12})}} + \underbrace{Y_{2,j} e^{(-i\phi_{2,j})}}_{\epsilon_{2,j}} \tag{151}$$

$$B_{3,j} = \underbrace{\zeta_{I,j} e^{(i(k_{W,j}x_{13}+\Phi_{I,j}))}}_{Z_{I,j}e^{(ik_{W,j}x_{13})}} + \underbrace{\zeta_{R,j} e^{(-i(k_{W,j}x_{13}+\Phi_{R,j}))}}_{Z_{R,j}e^{(ik_{W,j}x_{13})}} + \underbrace{Y_{3,j} e^{(-i\phi_{3,j})}}_{\epsilon_{3,j}} \tag{152}$$

$Y_{p,j}$ and $\phi_{p,j}$ are the Fourier coefficient respectively the phase shift of the noise signal at probe $p$. $Z_{I,j}$ and $Z_{R,j}$ are introduced, to emphasise the relevant phase differences between the three probes and will be the variables, which need to be determined in order to define the reflection coefficient. $\epsilon_{p,j}$ represents the unknown errors, which need to be minimised through the least squares approach. The least squares method now requires, that the sum of the squared errors of all probes $p$ reaches a minimum. This happens, if the both partial derivatives are zero

$$\sum_{p=1}^{3} (\epsilon_{p,j})^2 = \text{minimum} \quad \Leftrightarrow \quad \frac{\partial \left[\sum_{p=1}^{3} (\epsilon_{p,j})^2\right]}{\partial Z_{I,j}} = \frac{\partial \left[\sum_{p=1}^{3} (\epsilon_{p,j})^2\right]}{\partial Z_{R,j}} = 0 \tag{153}$$

With

$$\begin{aligned}\sum_{p=1}^{3} (\epsilon_{p,j})^2 = \; & (B_{1,j} - Z_{I,j} - Z_{R,j})^2 \\ & + \left(B_{2,j} - Z_{I,j} e^{ik_{W,j}x_{12}} - Z_{R,j} e^{-ik_{W,j}x_{12}}\right)^2 \\ & + \left(B_{3,j} - Z_{I,j} e^{ik_{W,j}x_{13}} - Z_{R,j} e^{-ik_{W,j}x_{13}}\right)^2 \end{aligned} \tag{154}$$

we get after differentiating and some transformations the solution for $Z_{I,j}$ and $Z_{R,j}$, which solely depend on the Fourier coefficients $B_{p,j}$ and some trigonometrical dependencies between the probes:

$$Z_{I,j} = \frac{B_{1,j}(R1_j + iQ1_j) + B_{2,j}(R2_j + iQ2_j) + B_{3,j}(R3_j + iQ3_j)}{D_j} \tag{155}$$

$$Z_{R,j} = \frac{B_{1,j}(R1_j - iQ1_j) + B_{2,j}(R2_j - iQ2_j) + B_{3,j}(R3_j - iQ3_j)}{D_j}, \tag{156}$$

using the following abbreviations:

$$R1_j = \sin^2(k_{W,j}x_{12}) + \sin^2(k_{W,j}x_{13}) \tag{157}$$

$$Q1_j = \sin(k_{W,j}x_{12})\cos(k_{W,j}x_{12}) + \sin(k_{W,j}x_{13})\cos(k_{W,j}x_{13}) \tag{158}$$

$$R2_j = \sin(k_{W,j}x_{13})\sin(k_{W,j}(x_{13} - x_{12})) \tag{159}$$

$$Q2_j = \sin(k_{W,j}x_{13})\cos(k_{W,j}(x_{13} - x_{12})) - 2\cdot\sin(k_{W,j}x_{12}) \tag{160}$$

$$R3_j = -\sin(k_{W,j}x_{12})\sin(k_{W,j}(x_{13} - x_{12})) \tag{161}$$

$$Q3_j = \sin(k_{W,j}x_{12})\cos(k_{W,j}(x_{13} - x_{12})) - 2\cdot\sin(k_{W,j}x_{13}) \tag{162}$$

$$D_j = 2\cdot\left(\sin^2(k_{W,j}x_{12}) + \sin^2(k_{W,j}x_{13}) + \sin^2(k_{W,j}(x_{13} - x_{12}))\right). \tag{163}$$

The reflection coefficient and the spectral densities of the incident and reflected waves can then be defined as already explained in the 2-point-method using equations (139) to (64).

From equation (155), (156) and (163) it can be seen that, unlike the 2-point method, it is less likely that the method gets indeterminate by the denominator. This happens when the expressions are a multiple of $\pi$ and hence

1. the distance $x_{12}$ equals $n \cdot \lambda_W/2$ with $n = 1, 2, \ldots$
2. <u>and</u> the distance $x_{13}$ is a multiple of $x_{12}$.

# Appendix B.

# Test Matrix

This section contains the list of conducted experimental tests. Green highlighted entries refer to test, which were also conducted numerically.

| Test-Name | Test run of day | Date | Flow type | Direction | Froude number | MP configuration | Towing Tank | Remarks |
|---|---|---|---|---|---|---|---|---|
| CW_0_006_SD | 7 | 25.11.2016 | CW | 0 | 0.06 | SD | SW | poti=0.799 |
| CW_0_009_SD | 6 | 25.11.2016 | CW | 0 | 0.09 | SD | SW | poti=1.235 |
| CW_0_012_SD | 5 | 25.11.2016 | CW | 0 | 0.12 | SD | SW | poti=1.66 |
| CW_0_015_SD | 4 | 25.11.2016 | CW | 0 | 0.15 | SD | SW | poti=2.11 |
| CW_0_018_SD | 3 | 25.11.2016 | CW | 0 | 0.18 | SD | SW | poti=2.59 |
| CW_0_021_SD | 2 | 25.11.2016 | CW | 0 | 0.21 | SD | SW | poti=3.00 |
| CW_0_023_SD | 0 & 1 | 25.11.2016 | CW | 0 | 0.23 | SD | SW | poti=3.315 |
| CW_0_012_SD | 10 | 28.12.2016 | CW | 0 | 0.12 | SD | DW | nominal value tow carraige v=0.685 |
| CW_0_015_SD | 9 | 28.12.2016 | CW | 0 | 0.15 | SD | DW | nominal value tow carraige v=0.856 |
| CW_0_018_SD | 8 | 28.12.2016 | CW | 0 | 0.18 | SD | DW | nominal value tow carraige v=1.041 |
| CW_0_021_SD | 7 | 28.12.2016 | CW | 0 | 0.21 | SD | DW | nominal value tow carraige v=1.183 |
| CW_0_023_SD | 6 | 28.12.2016 | CW | 0 | 0.23 | SD | DW | nominal value tow carraige v=1.297 |
| CW_0_006_CL | 12 & 13 | 16.11.2016 | CW | 0 | 0.06 | CL | SW | test run 12: poti=0.822; test run 13: poti=0.799 |
| CW_0_009_CL | 10 & 11 | 16.11.2016 | CW | 0 | 0.09 | CL | SW | test run 10: poti=1.245; test run 11: poti=1.235 |
| CW_0_012_CL | 9 | 16.11.2016 | CW | 0 | 0.12 | CL | SW | poti=1.688 |
| CW_0_015_CL | 7 & 8 | 16.11.2016 | CW | 0 | 0.15 | CL | SW | test run poti=2.137; test run 6: poti=2.11 |
| CW_0_018_CL | 5 & 6 | 16.11.2016 | CW | 0 | 0.18 | CL | SW | test run poti=2.628; test run 6: poti=2.59 |
| CW_0_021_CL | 4 | 16.11.2016 | CW | 0 | 0.21 | CL | SW | poti=3.03 |
| CW_0_023_CL | 3 | 16.11.2016 | CW | 0 | 0.23 | CL | SW | poti=3.315 |
| CW_0_006_009_MD | 6 | 19.12.2017 | CW | 0 | 0.06 & 0.09 | MD | SW | poti=0.794 and 1.235 |
| CW_0_012_MD | 5 | 17.08.2017 | CW | 0 | 0.12 | MD | SW | poti=1.66 |
| CW_0_015_MD | 4 | 17.08.2017 | CW | 0 | 0.15 | MD | SW | poti=2.11 |
| CW_0_018_MD | 3 | 17.08.2017 | CW | 0 | 0.18 | MD | SW | poti=2.57 |
| CW_0_021_MD | 2 | 17.08.2017 | CW | 0 | 0.21 | MD | SW | poti=3.00 |
| CW_0_023_MD | 0 & 1 | 17.08.2017 | CW | 0 | 0.23 | MD | SW | poti=3.315, Run 0 had water on board and was repeated |
| CW_0_012_MD | 4 | 18.12.2017 | CW | 0 | 0.12 | MD | SW | Repeating test of previous test period |
| CW_0_015_MD | 3 | 18.12.2017 | CW | 0 | 0.15 | MD | SW | Repeating test of previous test period |
| CW_0_018_MD | 2 | 18.12.2017 | CW | 0 | 0.18 | MD | SW | Repeating test of previous test period |
| CW_0_021_MD | 1 | 18.12.2017 | CW | 0 | 0.21 | MD | SW | Repeating test of previous test period |
| CW_0_023_MD | 0 | 18.12.2017 | CW | 0 | 0.23 | MD | SW | Repeating test of previous test period |
| CW_0_006_MP | 6 | 23.11.2016 | CW | 0 | 0.06 | MP | SW | poti=0.799 |
| CW_0_009_MP | 5 | 23.11.2016 | CW | 0 | 0.09 | MP | SW | poti=1.235 |
| CW_0_012_MP | 4 | 23.11.2016 | CW | 0 | 0.12 | MP | SW | poti=1.66 |
| CW_0_015_MP | 3 | 23.11.2016 | CW | 0 | 0.15 | MP | SW | poti=2.11 |
| CW_0_018_MP | 2 | 23.11.2016 | CW | 0 | 0.18 | MP | SW | poti=2.59 |
| CW_0_021_MP | 1 | 23.11.2016 | CW | 0 | 0.21 | MP | SW | poti=3.00 |

| Test-Name | Test run of day | Date | Flow type | Direction | Froude number | MP configuration | Towing Tank | Remarks |
|---|---|---|---|---|---|---|---|---|
| CW_0_023_MP | 0 | 23.11.2016 | CW | 0 | 0.23 | MP | SW | poti=3.315 |
| CW_0_012_MP | 5 | 28.12.2016 | CW | 0 | 0.12 | MP | DW | nominal value tow carraige v=0.685 |
| CW_0_015_MP | 4 | 28.12.2016 | CW | 0 | 0.15 | MP | DW | nominal value tow carraige v=0.856 |
| CW_0_018_MP | 2 & 3 | 28.12.2016 | CW | 0 | 0.18 | MP | DW | nominal value tow carraige: test run 2: v=1.027; test run 3: v=1.041 |
| CW_0_021_MP | 1 | 28.12.2016 | CW | 0 | 0.21 | MP | DW | nominal value tow carraige v=1.183 |
| CW_0_023_MP | 0 | 28.12.2016 | CW | 0 | 0.23 | MP | DW | nominal value tow carraige v=1.297 |
| CW_0_006_40-40 | 7 | 22.11.2016 | CW | 0 | 0.06 | 40-40 | SW | poti=0.799 |
| CW_0_009_40-40 | 6 | 22.11.2016 | CW | 0 | 0.09 | 40-40 | SW | poti=1.235 |
| CW_0_012_40-40 | 4 & 5 | 22.11.2016 | CW | 0 | 0.12 | 40-40 | SW | test run 4: poti=1.63; test run 5: poti=1.66 second run, velocity too low |
| CW_0_015_40-40 | 3 | 22.11.2016 | CW | 0 | 0.15 | 40-40 | SW | poti=2.10 |
| CW_0_018_40-40 | 2 | 22.11.2016 | CW | 0 | 0.18 | 40-40 | SW | poti=2.59 |
| CW_0_021_40-40 | 1 | 22.11.2016 | CW | 0 | 0.21 | 40-40 | SW | poti=3.00 |
| CW_0_023_40-40 | 0 | 22.11.2016 | CW | 0 | 0.23 | 40-40 | SW | |
| CW_0_006_60-40 | 14 | 23.11.2016 | CW | 0 | 0.06 | 60-40 | SW | poti=0.799 |
| CW_0_009_60-40 | 13 | 23.11.2016 | CW | 0 | 0.09 | 60-40 | SW | poti=1.235 |
| CW_0_012_60-40 | 12 | 23.11.2016 | CW | 0 | 0.12 | 60-40 | SW | poti=1.66; |
| CW_0_015_60-40 | 11 | 23.11.2016 | CW | 0 | 0.15 | 60-40 | SW | poti=2.11 |
| CW_0_018_60-40 | 10 | 23.11.2016 | CW | 0 | 0.18 | 60-40 | SW | poti=2.59 |
| CW_0_021_60-40 | 9 | 23.11.2016 | CW | 0 | 0.21 | 60-40 | SW | poti=3.00 |
| CW_0_023_60-40 | 8 | 23.11.2016 | CW | 0 | 0.23 | 60-40 | SW | poti=3.315 |
| CW_0_012_40-20 | 4 | 15.08.2017 | CW | 0 | 0.12 | 40-20 | SW | poti=1.66 |
| CW_0_015_40-20 | 3 | 15.08.2017 | CW | 0 | 0.15 | 40-20 | SW | poti=2.11 |
| CW_0_018_40-20 | 2 & 6 | 15.08.2017 | CW | 0 | 0.18 | 40-20 | SW | poti=2.59 Repeated (run 6), but identical result |
| CW_0_021_40-20 | 1 & 5 | 15.08.2017 | CW | 0 | 0.21 | 40-20 | SW | poti=3.00 Repeated (run 5, more plausible resistance compared to Fr 0.23 & 0.18) |
| CW_0_023_40-20 | 0 | 15.08.2017 | CW | 0 | 0.23 | 40-20 | SW | poti=3.315 |
| CW_0_012_SD_0DOF | 3 | 02.08.2017 | CW | 0 | 0.12 | SD | DW | |
| CW_0_015_SD_0DOF | 4 & 5 & 6 & 7 | 02.08.2017 | CW | 0 | 0.15 | SD | DW | test run 2: high acceleration; test run 3: low acceleration |
| CW_0_0165_SD_0DOF | 9 | 02.08.2017 | CW | 0 | 0.16 | SD | DW | |
| CW_0_018_015_SD_0DOF | 8 | 02.08.2017 | CW | 0 | 0.18 - 0.15 | SD | DW | slowing down from Fr=0.18 to Fr=0.15 |
| CW_0_018_SD_0DOF | 0 | 02.08.2017 | CW | 0 | 0.18 | SD | DW | |
| CW_0_021_SD_0DOF | 1 | 02.08.2017 | CW | 0 | 0.21 | SD | DW | |
| CW_0_023_SD_0DOF | 2 | 02.08.2017 | CW | 0 | 0.23 | SD | DW | |

| Test-Name | Test run of day | Date | Flow type | Direction | Froude number | MP configuration | Towing Tank | Remarks |
|---|---|---|---|---|---|---|---|---|
| RW050_0_0_SD | 14 | 05.12.2017 | RW050 | 0 | 0.0 | SD | SW | z0=-0,1cm |
| RW075_0_0_SD | 13 | 05.12.2017 | RW075 | 0 | 0.0 | SD | SW | z0=-0,1cm |
| RW100_0_0_SD | 12 | 05.12.2017 | RW100 | 0 | 0.0 | SD | SW | z0=-0,1cm |
| RW125_0_0_SD | 11 | 05.12.2017 | RW125 | 0 | 0.0 | SD | SW | z0=-0,1cm |
| RW050_0_0_MD | 6 | 05.12.2017 | RW050 | 0 | 0.0 | MD | SW | z0=-1,3cm |
| RW075_0_0_MD | 5 & 19 | 05.12.2017 | RW075 | 0 | 0.0 | MD | SW | z0=-1,3cm (repeated in run 19) |
| RW100_0_0_MD | 4 | 05.12.2017 | RW100 | 0 | 0.0 | MD | SW | z0=-1,3cm |
| RW125_0_0_MD | 3 | 05.12.2017 | RW125 | 0 | 0.0 | MD | SW | z0=-1,3cm |
| RW050_0_0_MP | 10 | 05.12.2017 | RW050 | 0 | 0.0 | MP | SW | z0=-0,1cm |
| RW075_0_0_MP | 9 | 05.12.2017 | RW075 | 0 | 0.0 | MP | SW | z0=-0,1cm |
| RW100_0_0_MP | 8 | 05.12.2017 | RW100 | 0 | 0.0 | MP | SW | z0=-0,1cm |
| RW125_0_0_MP | 7 | 05.12.2017 | RW125 | 0 | 0.0 | MP | SW | z0=-0,1cm |
| RW050_45_0_SD | 5 | 08.12.2017 | RW050 | 45 | 0.0 | SD | SW | Wave amp slightly too high? -> prob. Reflection |
| RW075_45_0_SD | 6 | 08.12.2017 | RW075 | 45 | 0.0 | SD | SW | |
| RW100_45_0_SD | 7 | 08.12.2017 | RW100 | 45 | 0.0 | SD | SW | |
| RW125_45_0_SD | 8 | 08.12.2017 | RW125 | 45 | 0.0 | SD | SW | |
| RW050_45_0_MD | 9 | 08.12.2017 | RW050 | 45 | 0.0 | MD | SW | Wave amp slightly too high? -> prob. Reflection |
| RW075_45_0_MD | 10 | 08.12.2017 | RW075 | 45 | 0.0 | MD | SW | |
| RW100_45_0_MD | 11 | 08.12.2017 | RW100 | 45 | 0.0 | MD | SW | |
| RW125_45_0_MD | 12 | 08.12.2017 | RW125 | 45 | 0.0 | MD | SW | |
| RW050_45_0_MP | 13 | 08.12.2017 | RW050 | 45 | 0.0 | MP | SW | Repeated on 12.12.17 run 5 |
| RW075_45_0_MP | 14 | 08.12.2017 | RW075 | 45 | 0.0 | MP | SW | |
| RW100_45_0_MP | 15 | 08.12.2017 | RW100 | 45 | 0.0 | MP | SW | Repeated on 12.12.17 run 4 |
| RW125_45_0_MP | 16 | 08.12.2017 | RW125 | 45 | 0.0 | MP | SW | |
| RW050_45_0_MP_6 | 3 | 11.12.2017 | RW050 | 45 | 0.0 | MP | SW | No yaw |
| RW075_45_0_MP_6 | 2 | 11.12.2017 | RW075 | 45 | 0.0 | MP | SW | No yaw |
| RW100_45_0_MP_6 | 1 | 11.12.2017 | RW100 | 45 | 0.0 | MP | SW | No yaw |
| RW125_45_0_MP_6 | 0 | 11.12.2017 | RW125 | 45 | 0.0 | MP | SW | No yaw |
| RW075_45_0_MP_4 | 3 & 4 | 14.12.2017 | RW075 | 45 | 0.0 | MP | SW | No roll. *1* |
| RW100_45_0_MP_4 | 1 & 2 | 14.12.2017 | RW100 | 45 | 0.0 | MP | SW | No roll. *1* |
| RW125_45_0_MP_4 | 0 | 14.12.2017 | RW125 | 45 | 0.0 | MP | SW | No roll. *1* |
| RW050_45_0_MP_35 | 0 | 12.12.2017 | RW050 | 45 | 0.0 | MP | SW | No heave / pitch. Heavy vibration of measuring |
| RW075_45_0_MP_35 | 1 | 12.12.2017 | RW075 | 45 | 0.0 | MP | SW | No heave / pitch. Wave amp too small? |
| RW100_45_0_MP_35 | 2 | 12.12.2017 | RW100 | 45 | 0.0 | MP | SW | No heave / pitch |
| RW125_45_0_MP_35 | 3 | 12.12.2017 | RW125 | 45 | 0.0 | MP | SW | No heave / pitch |

*1 Slight rolling was possible. Prob. strong friction in pitching*

| Test-Name | Test run of day | Date | Flow type | Direction | Froude number | MP configuration | Towing Tank | Remarks |
|---|---|---|---|---|---|---|---|---|
| RW050_45_0_MP_kx1 | 6 | 12.12.2017 | RW050 | 45 | 0.0 | MP | SW | Soft springs, Cy=8*46.67N/m, Cx=8*23.19N/m |
| RW075_45_0_MP_kx1 | 7 | 12.12.2017 | RW075 | 45 | 0.0 | MP | SW | Soft springs, Cy=8*46.67N/m, Cx=8*23.19N/m |
| RW100_45_0_MP_kx1 | 8 | 12.12.2017 | RW100 | 45 | 0.0 | MP | SW | Soft springs, Cy=8*46.67N/m, Cx=8*23.19N/m |
| RW125_45_0_MP_kx1 | 9 | 12.12.2017 | RW125 | 45 | 0.0 | MP | SW | Soft springs, Cy=8*46.67N/m, Cx=8*23.19N/m |
| RW050_45_0_MP_kx2 | 14 | 12.12.2017 | RW050 | 45 | 0.0 | MP | SW | Soft springs, Cy=4*46.67N/m, Cx=4*23.19N/m |
| RW075_45_0_MP_kx2 | 13 | 12.12.2017 | RW075 | 45 | 0.0 | MP | SW | Soft springs, Cy=4*46.67N/m, Cx=4*23.19N/m |
| RW100_45_0_MP_kx2 | 12 | 12.12.2017 | RW100 | 45 | 0.0 | MP | SW | Soft springs, Cy=4*46.67N/m, Cx=4*23.19N/m |
| RW125_45_0_MP_kx2 | 10 & 11 | 12.12.2017 | RW125 | 45 | 0.0 | MP | SW | Soft springs, Cy=4*46.67N/m, Cx=4*23.19N/m |
| RW050_45_0_40-20 | 7 | 11.12.2017 | RW050 | 45 | 0.0 | 40-20 | SW | |
| RW075_45_0_40-20 | 6 | 11.12.2017 | RW075 | 45 | 0.0 | 40-20 | SW | |
| RW100_45_0_40-20 | 5 | 11.12.2017 | RW100 | 45 | 0.0 | 40-20 | SW | |
| RW125_45_0_40-20 | 4 | 11.12.2017 | RW125 | 45 | 0.0 | 40-20 | SW | No Video |
| RW050_90_0_SD | 12 | 06.12.2017 | RW050 | 90 | 0.0 | SD | SW | *1* |
| RW075_90_0_SD | 13 | 06.12.2017 | RW075 | 90 | 0.0 | SD | SW | *1* |
| RW100_90_0_SD | 14 | 06.12.2017 | RW100 | 90 | 0.0 | SD | SW | *1* |
| RW125_90_0_SD | 15 | 06.12.2017 | RW125 | 90 | 0.0 | SD | SW | *1* |
| RW050_90_0_SD | 1 | 08.12.2017 | RW050 | 90 | 0.0 | SD | SW | Repeated with yaw free. Wave amp ok. *2* |
| RW075_90_0_SD | 2 | 08.12.2017 | RW075 | 90 | 0.0 | SD | SW | Repeated with yaw free. Wave amp too low? *2* |
| RW100_90_0_SD | 3 | 08.12.2017 | RW100 | 90 | 0.0 | SD | SW | Repeated with yaw free. Wave amp ok. *2* |
| RW125_90_0_SD | 4 | 08.12.2017 | RW125 | 90 | 0.0 | SD | SW | Repeated with yaw free. Wave amp ok. *2* |
| RW050_90_0_MD | 7 | 06.12.2017 | RW050 | 90 | 0.0 | MD | SW | *3* |
| RW075_90_0_MD | 4 | 06.12.2017 | RW075 | 90 | 0.0 | MD | SW | *3* |
| RW100_90_0_MD | 5 | 06.12.2017 | RW100 | 90 | 0.0 | MD | SW | *3* |
| RW125_90_0_MD | 6 | 06.12.2017 | RW125 | 90 | 0.0 | MD | SW | *3* |
| RW050_90_0_MP | 8 | 06.12.2017 | RW050 | 90 | 0.0 | MP | SW | *3* |
| RW075_90_0_MP | 9 | 06.12.2017 | RW075 | 90 | 0.0 | MP | SW | *3* |
| RW100_90_0_MP | 10 | 06.12.2017 | RW100 | 90 | 0.0 | MP | SW | *3* |
| RW125_90_0_MP | 11 | 06.12.2017 | RW125 | 90 | 0.0 | MP | SW | *3* |
| RW050_0_0_40-20 | 18 | 05.12.2017 | RW050 | 0 | 0.0 | 40-20 | SW | z0=-0,1cm |
| RW075_0_0_40-20 | 17 | 05.12.2017 | RW075 | 0 | 0.0 | 40-20 | SW | z0=-0,1cm |
| RW100_0_0_40-20 | 16 | 05.12.2017 | RW100 | 0 | 0.0 | 40-20 | SW | z0=-0,1cm |
| RW125_0_0_40-20 | 15 | 05.12.2017 | RW125 | 0 | 0.0 | 40-20 | SW | z0=-0,1cm |

*1 Measuring of wave amp problematic due to reflection. Position of wave gauge #3 18.5m before midship, WG#1 12.58m behind midships*

*2 Position of wave gauge #3 18.5m before midship, WG#1 12.58m behind midships*

*3 Measuring of wave amp problematic due to reflection. Position of wave gauge #3 18.5m before midship, WG#1 12.58m behind midships*

| Test-Name | Test run of day | Date | Flow type | Direction | Froude number | MP configuration | Towing Tank | Remarks |
|---|---|---|---|---|---|---|---|---|
| RW050_0_012_SD | 15 | 10.01.2018 | RW050 | 0 | 0.12 | SD | SW | Insertion mounted approx. 0.5cm to high |
| RW050_0_015_SD | 16 | 10.01.2018 | RW050 | 0 | 0.15 | SD | SW | Insertion mounted approx. 0.5cm to high |
| RW050_0_018_SD | 17 | 10.01.2018 | RW050 | 0 | 0.18 | SD | SW | Insertion mounted approx. 0.5cm to high |
| RW050_0_021_SD | 18 | 10.01.2018 | RW050 | 0 | 0.21 | SD | SW | Insertion mounted approx. 0.5cm to high |
| RW050_0_023_SD | 19 | 10.01.2018 | RW050 | 0 | 0.23 | SD | SW | Insertion mounted approx. 0.5cm to high |
| RW075_0_012_SD | 10 | 10.01.2018 | RW075 | 0 | 0.12 | SD | SW | Insertion mounted approx. 0.5cm to high |
| RW075_0_015_SD | 11 | 10.01.2018 | RW075 | 0 | 0.15 | SD | SW | Insertion mounted approx. 0.5cm to high |
| RW075_0_018_SD | 12 | 10.01.2018 | RW075 | 0 | 0.18 | SD | SW | Insertion mounted approx. 0.5cm to high |
| RW075_0_021_SD | 13 | 10.01.2018 | RW075 | 0 | 0.21 | SD | SW | Insertion mounted approx. 0.5cm to high |
| RW075_0_023_SD | 14 | 10.01.2018 | RW075 | 0 | 0.23 | SD | SW | Insertion mounted approx. 0.5cm to high |
| RW100_0_012_SD | 5 | 10.01.2018 | RW100 | 0 | 0.12 | SD | SW | Insertion mounted approx. 0.5cm to high |
| RW100_0_015_SD | 6 | 10.01.2018 | RW100 | 0 | 0.15 | SD | SW | Insertion mounted approx. 0.5cm to high |
| RW100_0_018_SD | 7 | 10.01.2018 | RW100 | 0 | 0.18 | SD | SW | Insertion mounted approx. 0.5cm to high |
| RW100_0_021_SD | 8 | 10.01.2018 | RW100 | 0 | 0.21 | SD | SW | Insertion mounted approx. 0.5cm to high |
| RW100_0_023_SD | 9 | 10.01.2018 | RW100 | 0 | 0.23 | SD | SW | Insertion mounted approx. 0.5cm to high |
| RW125_0_012_SD | 0 | 10.01.2018 | RW125 | 0 | 0.12 | SD | SW | Insertion mounted approx. 0.5cm to high |
| RW125_0_015_SD | 1 | 10.01.2018 | RW125 | 0 | 0.15 | SD | SW | Insertion mounted approx. 0.5cm to high |
| RW125_0_018_SD | 2 | 10.01.2018 | RW125 | 0 | 0.18 | SD | SW | Insertion mounted approx. 0.5cm to high |
| RW125_0_021_SD | 3 | 10.01.2018 | RW125 | 0 | 0.21 | SD | SW | Insertion mounted approx. 0.5cm to high |
| RW125_0_023_SD | 4 | 10.01.2018 | RW125 | 0 | 0.23 | SD | SW | Insertion mounted approx. 0.5cm to high |
| RW050_0_012_MD | 0 | 19.12.2017 | RW050 | 0 | 0.12 | MD | SW | |
| RW050_0_015_MD | 1 | 19.12.2017 | RW050 | 0 | 0.15 | MD | SW | |
| RW050_0_018_MD | 2 & 3 | 19.12.2017 | RW050 | 0 | 0.18 | MD | SW | Repeated in run 3 (Name.: RW050_0_018_2_MD) |
| RW050_0_021_MD | 4 | 19.12.2017 | RW050 | 0 | 0.21 | MD | SW | |
| RW050_0_023_MD | 5 | 19.12.2017 | RW050 | 0 | 0.23 | MD | SW | |
| RW075_0_012_MD | 0 | 20.12.2017 | RW075 | 0 | 0.12 | MD | SW | |
| RW075_0_015_MD | 1 | 20.12.2017 | RW075 | 0 | 0.15 | MD | SW | |
| RW075_0_018_MD | 2 | 20.12.2017 | RW075 | 0 | 0.18 | MD | SW | |
| RW075_0_021_MD | 3 | 20.12.2017 | RW075 | 0 | 0.21 | MD | SW | |
| RW075_0_023_MD | 4 | 20.12.2017 | RW075 | 0 | 0.23 | MD | SW | |
| RW100_0_012_MD | 5 | 20.12.2017 | RW100 | 0 | 0.12 | MD | SW | |
| RW100_0_015_MD | 6 | 20.12.2017 | RW100 | 0 | 0.15 | MD | SW | |
| RW100_0_018_MD | 7 | 20.12.2017 | RW100 | 0 | 0.18 | MD | SW | |
| RW100_0_021_MD | 8 | 20.12.2017 | RW100 | 0 | 0.21 | MD | SW | |
| RW100_0_023_MD | 9 | 20.12.2017 | RW100 | 0 | 0.23 | MD | SW | |

| Test-Name | Test run of day | Date | Flow type | Direction | Froude number | MP configuration | Towing Tank | Remarks |
|---|---|---|---|---|---|---|---|---|
| RW125_0_012_MD | 10 | 20.12.2017 | RW125 | 0 | 0.12 | MD | SW | |
| RW125_0_015_MD | 11 | 20.12.2017 | RW125 | 0 | 0.15 | MD | SW | Green water on bow due to high pitching |
| RW125_0_018_MD | 12 | 20.12.2017 | RW125 | 0 | 0.18 | MD | SW | Green water on bow due to high pitching |
| RW125_0_021_MD | 13 | 20.12.2017 | RW125 | 0 | 0.21 | MD | SW | Green water on bow due to high pitching |
| RW125_0_023_MD | 14 | 20.12.2017 | RW125 | 0 | 0.23 | MD | SW | Green water on bow due to high pitching |
| RW050_0_012_MP | 1 | 21.12.2017 | RW050 | 0 | 0.12 | MP | SW | Named in TDMS files with ID 0, but should be ID 1. Converted data is called ID 1 |
| RW050_0_015_MP | 11 | 21.12.2017 | RW050 | 0 | 0.15 | MP | SW | |
| RW050_0_018_MP | 12 | 21.12.2017 | RW050 | 0 | 0.18 | MP | SW | |
| RW050_0_021_MP | 13 | 21.12.2017 | RW050 | 0 | 0.21 | MP | SW | |
| RW050_0_023_MP | 14 & 15 | 21.12.2017 | RW050 | 0 | 0.23 | MP | SW | Repeated as MP-Amp did develop late (but maybe only due to capturing of model?) |
| RW075_0_012_MP | 0 | 11.01.2018 | RW075 | 0 | 0.12 | MP | SW | |
| RW075_0_015_MP | 1 | 11.01.2018 | RW075 | 0 | 0.15 | MP | SW | |
| RW075_0_018_MP | 2 | 11.01.2018 | RW075 | 0 | 0.18 | MP | SW | |
| RW075_0_021_MP | 3 | 11.01.2018 | RW075 | 0 | 0.21 | MP | SW | |
| RW075_0_023_MP | 4 | 11.01.2018 | RW075 | 0 | 0.23 | MP | SW | |
| RW100_0_012_MP | 6 | 21.12.2017 | RW100 | 0 | 0.12 | MP | SW | |
| RW100_0_015_MP | 7 | 21.12.2017 | RW100 | 0 | 0.15 | MP | SW | |
| RW100_0_018_MP | 8 | 21.12.2017 | RW100 | 0 | 0.18 | MP | SW | |
| RW100_0_021_MP | 9 | 21.12.2017 | RW100 | 0 | 0.21 | MP | SW | |
| RW100_0_023_MP | 10 | 21.12.2017 | RW100 | 0 | 0.23 | MP | SW | |
| RW125_0_012_MP | 0 | 21.12.2017 | RW125 | 0 | 0.12 | MP | SW | |
| RW125_0_015_MP | 2 | 21.12.2017 | RW125 | 0 | 0.15 | MP | SW | |
| RW125_0_018_MP | 3 | 21.12.2017 | RW125 | 0 | 0.18 | MP | SW | |
| RW125_0_021_MP | 4 | 21.12.2017 | RW125 | 0 | 0.21 | MP | SW | Heavy green water from MP. Wave gauge measurement inside MP probably insufficient |
| RW125_0_023_MP | 5 | 21.12.2017 | RW125 | 0 | 0.23 | MP | SW | Heavy green water from MP. Wave gauge measurement inside MP probably insufficient |
| RW050_0_015_MP | 5 | 12.01.2018 | RW050 | 180 | 0.15 | MP | SW | Measurement of wave amp influenced by ship wave system. Velocity slightly too high |
| RW075_0_015_MP | 6 | 12.01.2018 | RW075 | 180 | 0.15 | MP | SW | Measurement of wave amp influenced by ship wave system. Velocity slightly too high |
| RW100_0_015_MP | 7 | 12.01.2018 | RW100 | 180 | 0.15 | MP | SW | |
| RW125_0_015_MP | 8 | 12.01.2018 | RW125 | 180 | 0.15 | MP | SW | |
| RW050_0_012_40-20 | 5 | 11.01.2018 | RW050 | 0 | 0.12 | 40-20 | SW | |
| RW050_0_015_40-20 | 6 | 11.01.2018 | RW050 | 0 | 0.15 | 40-20 | SW | |

| Test-Name | Test run of day | Date | Flow type | Direction | Froude number | MP configuration | Towing Tank | Remarks |
|---|---|---|---|---|---|---|---|---|
| RW050_0_018_40-20 | 7 | 11.01.2018 | RW050 | 0 | 0.18 | 40-20 | SW | |
| RW050_0_021_40-20 | 8 | 11.01.2018 | RW050 | 0 | 0.21 | 40-20 | SW | |
| RW050_0_023_40-20 | 9 | 11.01.2018 | RW050 | 0 | 0.23 | 40-20 | SW | |
| RW075_0_012_40-20 | 10 | 11.01.2018 | RW075 | 0 | 0.12 | 40-20 | SW | |
| RW075_0_015_40-20 | 11 | 11.01.2018 | RW075 | 0 | 0.15 | 40-20 | SW | |
| RW075_0_018_40-20 | 12 | 11.01.2018 | RW075 | 0 | 0.18 | 40-20 | SW | |
| RW075_0_021_40-20 | 13 | 11.01.2018 | RW075 | 0 | 0.21 | 40-20 | SW | |
| RW075_0_023_40-20 | 14 | 11.01.2018 | RW075 | 0 | 0.23 | 40-20 | SW | |
| RW100_0_012_40-20 | 15 | 11.01.2018 | RW100 | 0 | 0.12 | 40-20 | SW | |
| RW100_0_015_40-20 | 16 | 11.01.2018 | RW100 | 0 | 0.15 | 40-20 | SW | |
| RW100_0_018_40-20 | 17 | 11.01.2018 | RW100 | 0 | 0.18 | 40-20 | SW | |
| RW100_0_021_40-20 | 18 | 11.01.2018 | RW100 | 0 | 0.21 | 40-20 | SW | |
| RW100_0_023_40-20 | 19 | 11.01.2018 | RW100 | 0 | 0.23 | 40-20 | SW | |
| RW125_0_012_40-20 | 20 | 11.01.2018 | RW125 | 0 | 0.12 | 40-20 | SW | |
| RW125_0_015_40-20 | 21 | 11.01.2018 | RW125 | 0 | 0.15 | 40-20 | SW | |
| RW125_0_018_40-20 | 22 | 11.01.2018 | RW125 | 0 | 0.18 | 40-20 | SW | |
| RW125_0_021_40-20 | 23 | 11.01.2018 | RW125 | 0 | 0.21 | 40-20 | SW | |
| RW125_0_023_40-20 | 24 | 11.01.2018 | RW125 | 0 | 0.23 | 40-20 | SW | |
| RW050_0_015_40-40 | 0 & 1 | 12.01.2018 | RW050 | 0 | 0.15 | 40-40 | SW | Problem with wave gauge 3, repeated in run 1 |
| RW075_0_015_40-40 | 2 | 12.01.2018 | RW075 | 0 | 0.15 | 40-40 | SW | |
| RW100_0_015_40-40 | 3 | 12.01.2018 | RW100 | 0 | 0.15 | 40-40 | SW | |
| RW125_0_015_40-40 | 4 | 12.01.2018 | RW125 | 0 | 0.15 | 40-40 | SW | |

# Appendix C.

# Results

This chapter contains remaining results of the conducted investigations, which have not been shown yet in the main part of this thesis.

## C.1. Influence of motion restriction

The DOF, which are not affected by motion restriction and therefore not shown in the main part are listed in figure C.1 for results from the experimental investigation at zero speed and $\mu_W = 45°$ and in figure C.2 and C.3 for the numerical investigations at $Fr = 0.15$ and different wave encounter angles.

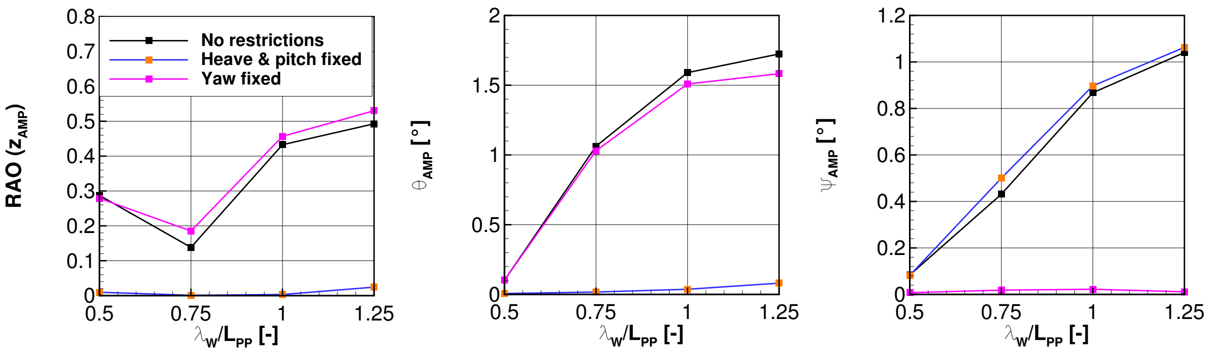


**(a)** Influence on heave motion **(b)** Influence on pitch motion **(c)** influence on yaw motion

**Figure C.1.:** Influence of motion restriction at zero speed and $\mu_W = 45°$

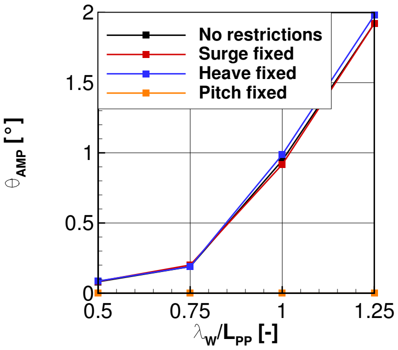


**(a)** Influence on pitch motion at $\mu_W = 0°$

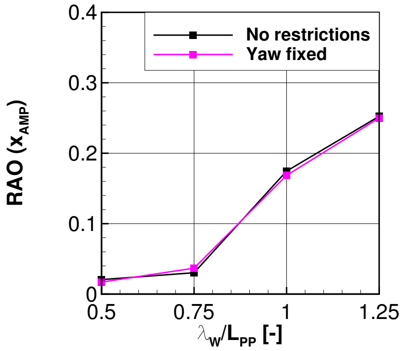


**(b)** Influence on surge motion at $\mu_W = 45°$

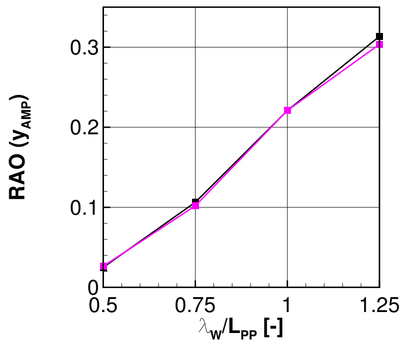


**(c)** influence on sway motion at $\mu_W = 45°$

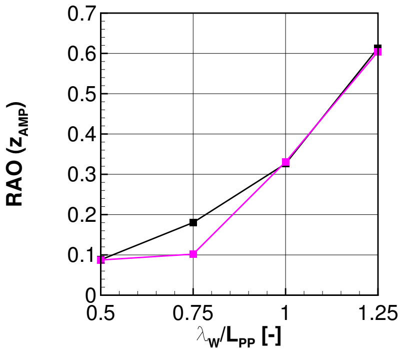


**(d)** Influence on heave motion at $\mu_W = 45°$

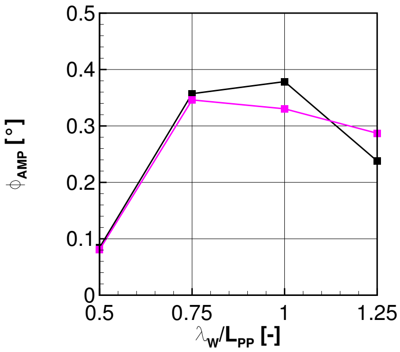


**(e)** Influence on roll motion at $\mu_W = 45°$

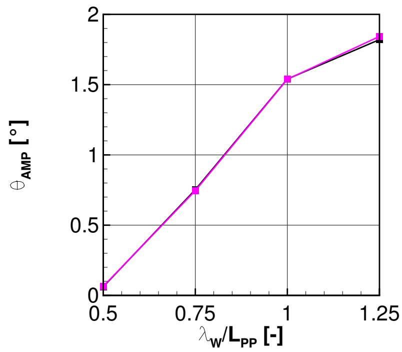


**(f)** influence on pitch motion at $\mu_W = 45°$

**Figure C.2.:** Influence of motion restriction at $Fr = 0.15$ and $\mu_W = 0°$ and $\mu_W = 45°$

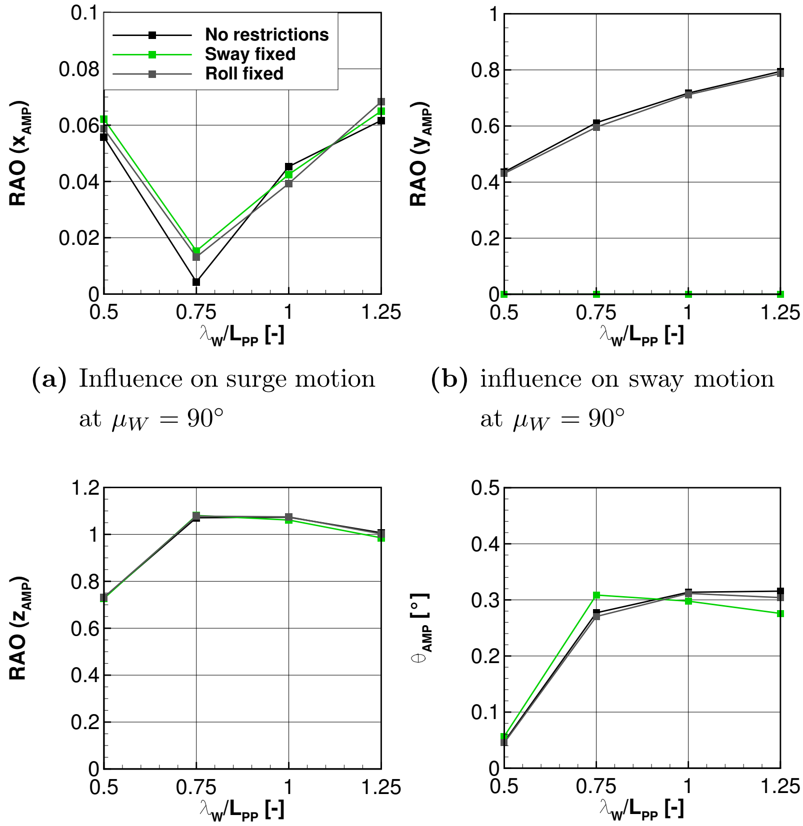


**(a)** Influence on surge motion at $\mu_W = 90°$

**(b)** influence on sway motion at $\mu_W = 90°$

**(c)** Influence on heave motion at $\mu_W = 90°$

**(d)** influence on pitch motion at $\mu_W = 90°$

**Figure C.3.:** Influence of motion restriction at $Fr = 0.15$ and $\mu_W = 90°$

# C.2. Head seas

This section contains results from numerical simulations (black squares) and experimental tests (coloured lines) which have not been shown in the main part.

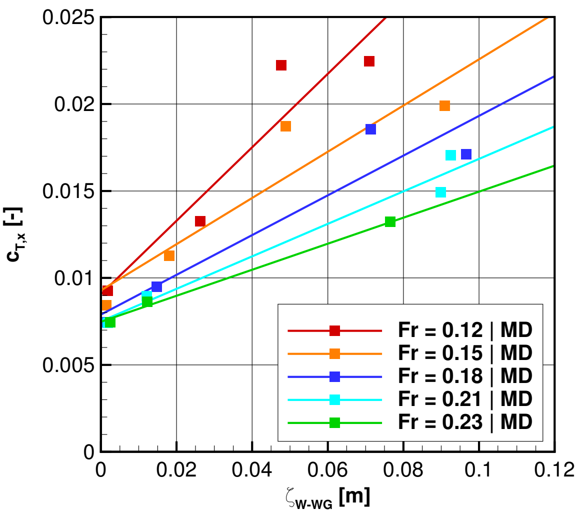


**(a)** Total resistance coefficient over mean oscillating amplitude at wave frequency for MD

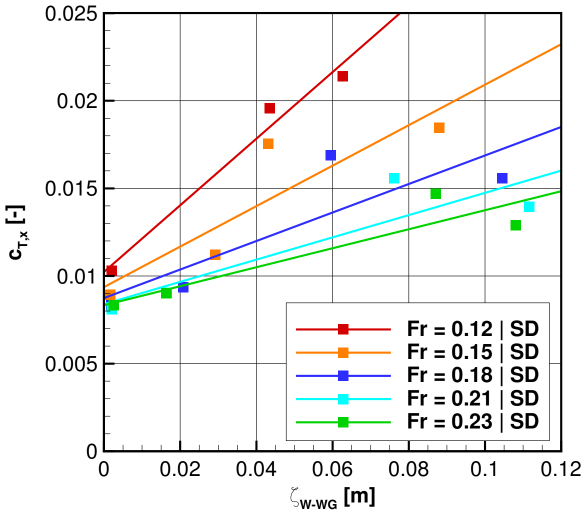


**(b)** Total resistance coefficient over mean oscillating amplitude at wave frequency for SD

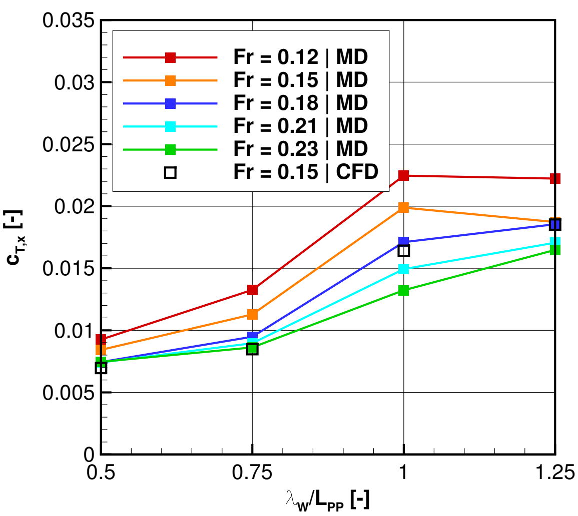


**(c)** Total resistance coefficient for MD

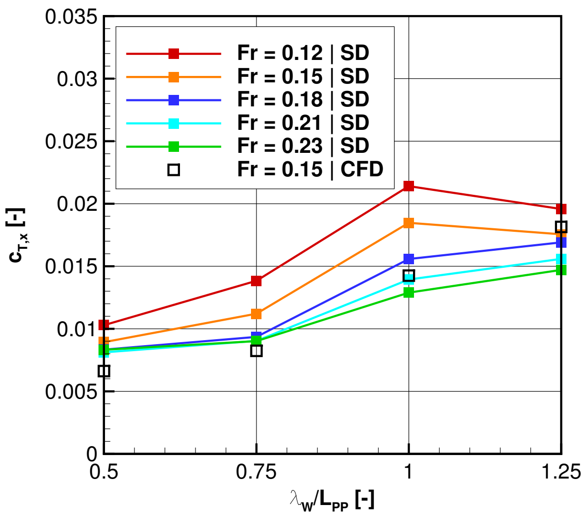


**(d)** Total resistance coefficient for SD

**Figure C.4.:** Total resistance coefficients for MD and SD

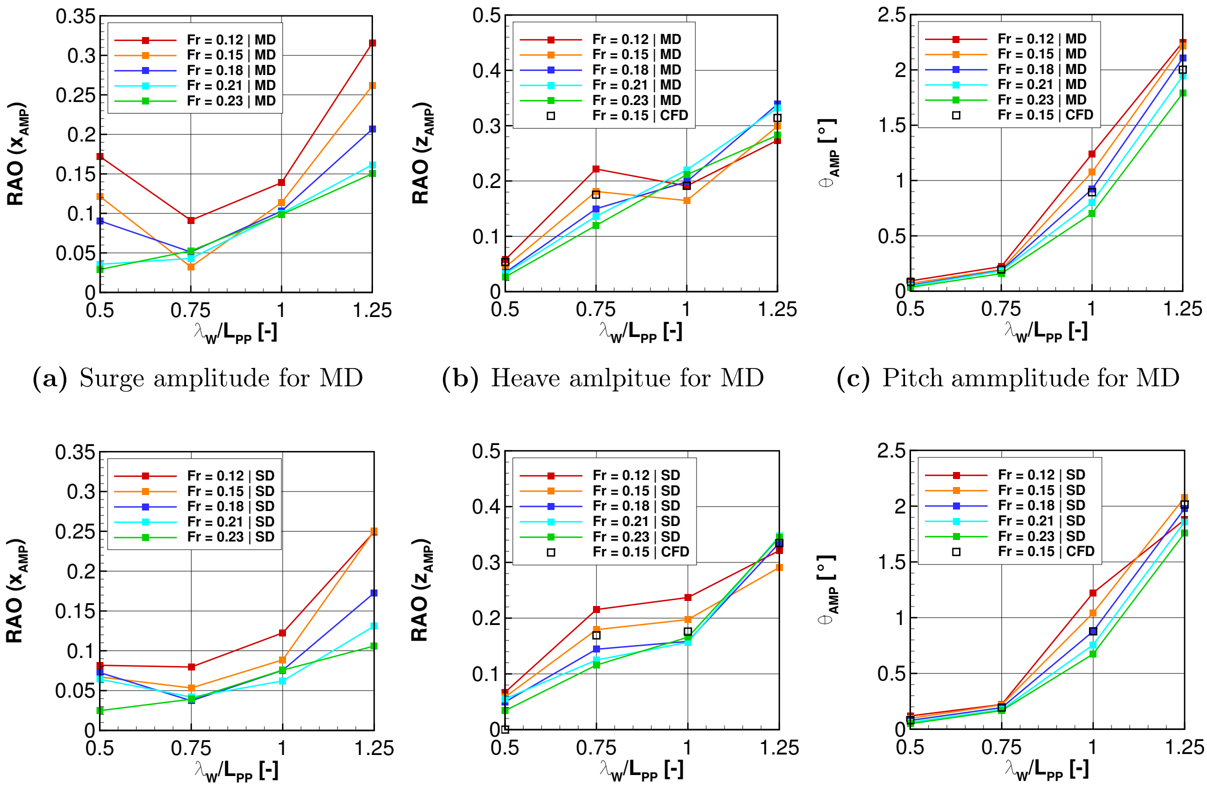


**(a)** Surge amplitude for MD **(b)** Heave amlpitue for MD **(c)** Pitch ammplitude for MD

**(d)** Surge amplitude for SD **(e)** Heave amlpitue for SD **(f)** Pitch ammplitude for D

**Figure C.5.:** Total resistance coefficients for MD and SD

# C.3. Closed Moonpool

The following figures show the pressure field of a slice in longitudinal direction inside the moonpool. The slice is located at the centre of the moonpool in longitudinal direction. Shown is the non-dimensional pressure field $Pavg$, which has been averaged over full oscillation cycles.

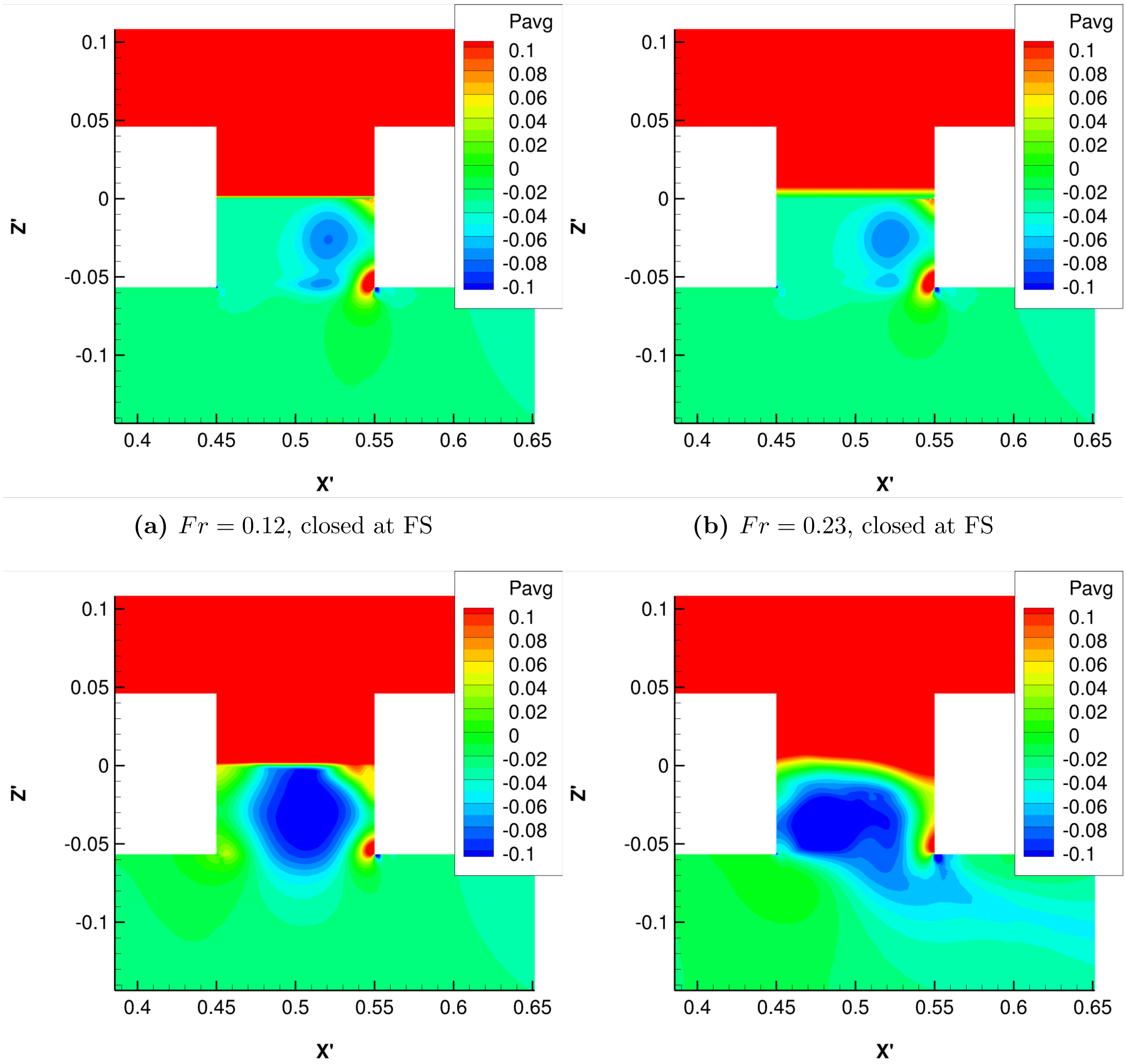


(a) $Fr = 0.12$, closed at FS

(b) $Fr = 0.23$, closed at FS

(c) $Fr = 0.12$, MP

(d) $Fr = 0.23$, MP

**Figure C.6.:** Non-dimensional mean pressure field at low and high Froude numbers for the moonpool closed at FS and open moonpool (MP)

## C.4. Operational condition

The following figures show the time series of the wave elevation $\zeta_W$ in red, heave motion $\zeta$ in blue and moonpool water column oscillation amplitude $\zeta_{W-WG}$ in green for $\lambda_W/LPP = 0.5$ at three different wave directions $\mu_W = 0°$ (figure C.7a), $\mu_W = 45°$ (figure C.7b) and $\mu_W = 90°$ (figure C.7c).

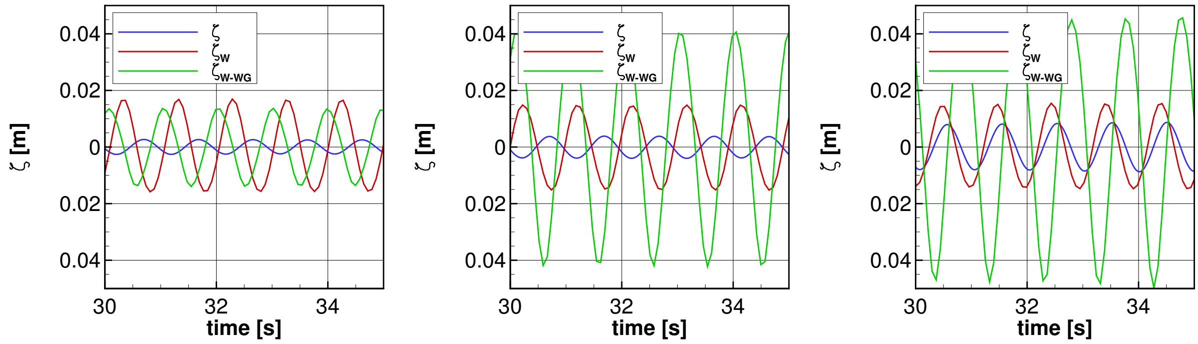


**(a)** $\mu_W = 0°$ **(b)** $\mu_W = 45°$ **(c)** $\mu_W = 90°$

**Figure C.7.:** Phase shift between wave elevation $\zeta_W$, heave motion $\zeta$ and moonpool water column oscillation $\zeta_{W-WG}$ for $\lambda_W/LPP = 0.5$

# Bibliography


[1] A. B. Aalbers. The water motions in a moonpool. *Ocean Engineering*, 11(6):557–579, 1984.

[2] J. Bell, L. Howell, and P. Colella. An efficient second-order projection method for viscous incompressible flow. In *10th Computational Fluid Dynamics Conference*, page 1560, 24 June 1991 - 26 June 1991.

[3] S. Bhushan, T. Xing, P. M. Carrica, and F. Stern. Model- and full-scale URANS simulations of Athena resistance, powering, seakeeping, and 5415 maneuvering. *Journal of Ship Research*, 53(4):179–198, 2009.

[4] J. Blazek. *Computational fluid dynamics: Principles and applications.* Elsevier, Amsterdam and New York, 1st ed edition, 2001.

[5] D. A. Boger and J. J. Dreyer. Prediction of Hydrodynamic Forces and Moments for Underwater Vehicles Using Overset Grids: AIAA 2006-1148. In *44th AIAA Aerospace Sciences Meeting and Exhibit*, 2006.

[6] J. Boussinesq. *Essai sur la théorie des eaux courantes*. Impr. Nationale, Paris, France, 1877.

[7] P. M. Carrica, R. V. Wilson, R. W. Noack, and F. Stern. Ship motions using single-phase level set with dynamic overset grids. *Computers & Fluids*, 36(9):1415–1433, 2007.

[8] P. M. Carrica, R. V. Wilson, and F. Stern. Unsteady RANS simulation of the ship forward speed diffraction problem. *Computers & Fluids*, 35(5):545–570, 2006.

[9] P. M. Carrica, R. V. Wilson, and F. Stern. An unsteady single-phase level set method for viscous free surface flows. *International Journal for Numerical Methods in Fluids*, 53(2):229–256, 2007.

[10] B. Caruelle. *Simulations d'écoulements instationnaires turbulents en aérodynamique*. Phd, Institut national polytechnique, France, 2000.

[11] D. Chalkias and J. W. Krijger. Moonpool behaviour of a stationary vessel in waves and a method to increase operability. In *36th International Conference on Ocean, Offshore and Arctic Engineering*, 2017.

[12] R. K.-C. Chan. Two-dimensional time-dependent calulations of large-amplitude surface gravity waves due to a surface disturbance. In J. W. Schot, editor, *Proceedings, First International Conference on Numerical Ship Hydrodynamics*, pages 315–331, Bethesda, Maryland, USA, 1975.

[13] M. S. Chong, A. E. Perry, and B. J. Cantwell. A general classification of three-dimensional flow fields. *Physics of Fluids A: Fluid Dynamics*, 2(5):765, 1990.

[14] G. F. Clauss and Y. Chen. Reduction of tank wall effects by vertical side wall wave absorbers. *Proceedings of the ITTC*, pages 493–500, 1990.

[15] E. E. Covert. An approximate calculation of the onset velocity of cavity oscillations. *AIAA Journal*, 8(12):2189–2194, 1970.

[16] A. Cura Hochbaum and A. Lengwinat. Report on model tests at TUB: SHOPERA - Energy Efficient Ship Operations, Grant Agreement No. 605221: Devliverable D3.5.

[17] A. Cura Hochbaum, S. Uharek, and A. Lengwinat. Abschlussbericht des Teilvorhabens PROMANSEE: Progonose der Manövrierbarkeit von Schiffen im Seegang: Förderkennzeichen 03SX339E.

[18] A. Cura Hochbaum and M. Vogt. Towards the simulation of seakeeping and manoeuvring based on the computation of the free surface viscous ship flow. In *24th Symposium on Naval Hydrodynamics*, 2002.

[19] I. de Vries, Y. Roux, M. Naciri, and G. Bonnaffoux. Dynamics of entrapped water in large diameter turret moonpools. In *32nd International Conference on Ocean, Offshore and Arctic Engineering*, 9-14 Juni 2013.

[20] S. Deck. *Simulation numérique des charges latérales instationnaires sur des configurations de lanceur*. Phd, Université d'Orléans, France, 2002.

[21] S. Deck, E. Garnier, and P. Guillen. Turbulence modelling applied to space launcher configurations. *Journal of Turbulence*, 3:N57, 2002.

[22] Det Norske Veritas. Modelling and analysis of marine operations: DNV-RP-H103, April 2011.

[23] O. el Moctar, A. Brehm, and T. E. Schellin. Prediction of slamming loads for ship structural design using potential flow and RANSE codes. In *25th Symposium on Naval Hydrodynamics*, pages 116–129, 2004.

[24] J. W. English. A means of reducing oscillations in drillwells caused by vessels' forward speed. *The Naval Architect*, pages 88–90, May 1976.

[25] T. Esch and F. R. Menter. Heat transfer predictions based on two-equation turbulence models with advanced wall treatment. In *4th Int. Symposium, Turbulence, heat and mass transfer*, volume 4, New York, Wallingford, 2003. Begell House.

[26] O. M. Faltinsen and A. N. Timokha. *Sloshing.* Cambridge University Press, New York, 2009.

[27] O. M. Faltinsen and A. N. Timokha. On damping of two-dimensional piston-mode sloshing in a rectangular moonpool under forced heave motions. *Journal of Fluid Mechanics*, 772, 2015.

[28] J. H. Ferziger and M. Perić. *Computational methods for fluid dynamics.* Springer Berlin Heidelberg, Berlin, Heidelberg, s.l., third, rev. edition edition, 2002.

[29] T. I. Fossen. *Guidance and control of ocean vehicles.* John Wiley & Sons Ltd., Chichester, England, 1994.

[30] A. G. Fredriksen, T. Kristiansen, and O. M. Faltinsen. Experimental and numerical investigation of wave resonance in moonpools at low forward speed. *Applied Ocean Research*, 47:28–46, 2014.

[31] A. G. Fredriksen, T. Kristiansen, and O. M. Faltinsen. Wave-induced response of a floating two-dimensional body with a moonpool. *Phil. Trans. R. Soc. A*, 373, 2015.

[32] K. Fukuda. Behaviour of water in vertical well with bottom opening of ship, and its effects on ship-motion. *Journal of the Society of Naval Architects of Japan*, (141):107–122, 1977.

[33] K. Fukuda and Y. Yoshii. Flow calculation in vertical cavity with free surface and bottom opening to water stream. *Journal of the Japan Society of Naval Architects and Ocean Engineers*, (10):23–28, 2009.

[34] G. Gaillarde and A. Cotteleer. Water motion in moonpools: Emperical and theoretical approach. 2004.

[35] Y. Goda and Y. Suzuki. Estimation of incident and reflected waves in random wave experiments. *Coastal Engineering*, 15:828–845, 1976.

[36] G. Haller. An objective definition of a vortex. *Journal of Fluid Mechanics*, 525:1–26, 1999.

[37] Hunt, J. C. R., A. A. Wray, and P. Moin. Eddies, streams, and convergence zones in turbulent flows. *Proceedings of the Summer Program 1988*, pages 193–208, 1988.

[38] International Towing Tank Conference. ITTC - Recommended Procedures and Guidelines: Ship Models: 7.5-01-01-01.

[39] F. Ismail, P. M. Carrica, T. Xing, and F. Stern. Evaluation of linear and nonlinear convection schemes on multidimensional non-orthogonal grids with applications to KVLCC2 tanker. *International Journal for Numerical Methods in Fluids*, pages 850–886, 2009.

[40] M. Israeli and S. A. Orszag. Approximation of radiation boundary conditions. *Journal of Computational Physics*, 41(1):115–135, 1981.

[41] R. I. Issa. Solution of the implicitly discretised fluid flow equations by operator-splitting. *Journal of Computational Physics*, 62:40–65, 1985.

[42] N. G. Jacobsen, D. R. Fuhrman, and J. Fredsøe. A wave generation toolbox for the open-source CFD library: OpenFoam. *International Journal for Numerical Methods in Fluids*, 70(9):1073–1088, 2012.

[43] J. Jeong and F. Hussain. On the identification of a vortex. *Journal of Fluid Mechanics*, 285(-1):69, 1995.

[44] G. Kalitzin, G. Medic, G. Iaccarino, and P. Durbin. Near-wall behavior of RANS turbulence models and implications for wall functions. *Journal of Computational Physics*, 204(1):265–291, 2005.

[45] V. Kolář. Vortex identification: New requirements and limitations. *International Journal of Heat and Fluid Flow*, 28(4):638–652, 2007.

[46] J. W. Krijger and D. Chalkias. CFD driven drillship design. In *35th International Conference on Ocean, Offshore and Arctic Engineering*, Sunday 19 June 2016.

[47] T. Kristiansen, T. Sauder, and R. Firoozkoohi. Validation of a hybrid code combining potential and viscous flow with application to 3D moonpool. In *32nd International Conference on Ocean, Offshore and Arctic Engineering*, 9-14 Juni 2013.

[48] B. E. Launder and D. B. Spalding. The numerical computation of turbulent flows. *Computer Methods in Applied Mechanics and Engineering*, 3(2):269–289, 1974.

[49] A. Lengwinat and A. Cura Hochbaum. The influence of inertial effects on the mean forces and moments on a ship sailing in oblique waves: Part A: A new measurement device for wave forces. *Ocean Engineering*, 166:1–11, 2018.

[50] J. Li, A. M. Castro, and P. M. Carrica. A pressure-velocity coupling approach for high void fraction free surface bubbly flows in overset curviliniear grids. *International Journal for Numerical Methods in Fluids*, 79(7):343–369, 2015.

[51] J. Löhrmann, P. M. Carrica, and A. Cura Hochbaum. Numerical and Experimental Damping of Piston and Sloshing Motions in Moonpools. In *ASME 2017 36th International Conference on Ocean, Offshore and Arctic Engineering*, June 25-30, 2017.

[52] J. Löhrmann and A. Cura Hochbaum. Simulation of seakeeping tests using OpenFOAM. In R. E. Bensow, editor, *Proceedings of the 17th Numerical Towing Tank Symposium*, 2014.

[53] Mansard, E. P. D. and E. R. Funke. The measurement of incident and reflected spectra using a least squares method. In B. L. Edge, editor, *Proceedings of the Seventeenth Coastal Engineering Conference*, volume no. 5104 of *San Joaquin Valley Drainage*, pages 114–172, New York, 1980. American Society of Civil Engineers.

[54] F. R. Menter. Two-equation eddy-viscosity turbulence models for engineering applications. *AIAA Journal*, 32(8):1598–1605, 1994.

[55] F. R. Menter and M. Kuntz. Adaptation of eddy-viscosity turbulence models to unsteady separated flow behind vehicles. In F. Pfeiffer, P. Wriggers, R. McCallen, F. Browand, and J. Ross, editors, *The aerodynamics of heavy vehicles: Trucks, buses, and trains*, volume 19 of *Lecture Notes in Applied and Computational Mechanics*, pages 339–352. Springer Berlin Heidelberg, Berlin, Heidelberg, 2004.

[56] B. Molin. On the piston and sloshing modes in moonpools. *Journal of Fluid Mechanics*, 430:27–50, 2001.

[57] B. Molin. On natural modes in moonpools with recesses. *Applied Ocean Research*, 67:1–8, 2017.

[58] J. N. Newman. Progress in wave load computations on offshore structures, 2004.

[59] R. W. Noack, D. A. Boger, R. F. Kunz, and P. M. Carrica. Suggar++: An improved general overset grid assembly capability: AIAA 2009-3992. In *19th AIAA Computational Fluid Dynamics*, 2009.

[60] B. Plessers, J. Berlamont, and E. Huse. *Reduction of tank wall interference by slender vertical wave absorbers*. Leuven, Belgium, 1992.

[61] T. Riekert. Studienarbeit zu Berechnung von Reflexionskoeffizienten.

[62] D. Rockwell and E. Naudascher. Self-sustained oscillations of impinging free shear layers. *Annual Review of Fluid Mechanics*, pages 67–94, 1979.

[63] T. Sauder, T. Kristiansen, and A. Östman. Validation of a numerical method for the study of piston-like oscillations between a ship and a terminal. In *20th International Offshore and Polar Engineering Conference*, 2010.

[64] H. Schlichting. *Grenzschicht-Theorie*. G. Braun, Karlsruhe, 1951.

[65] J. Smagorinsky. General circulation experiments with the primitve equations: The basic Experiment. *Monthly Weather Review*, 91(3):99–164, 1963.

[66] A. Sommerfeld. *Partial differential equations in physics*. Academic Press, New York, 1949.

[67] H.-J. Son, S.-H. Choi, M.-H. Kim, and S.-M. Hwangbo. Drag reduction of recess type moonpool under vessel's forward speed. In *27th International Conference on Offshore Mechanics and Arctic Engineering*, pages 143–148, June 15–20, 2008.

[68] P. R. Spalart. A young person's guide to detached-eddy simulation grids. (NASA/CR-2001-211032), 2001.

[69] P. R. Spalart. Detached-eddy simulation. *Annual Review of Fluid Mechanics*, 41(1):181–202, 2009.

[70] P. R. Spalart and S. R. Allmaras. A one-equation turbulence model for aerodynamic flows. In *30th Aerospace Sciences Meeting and Exhibit*, 06 January 1992 - 09 January 1992.

[71] P. R. Spalart, S. Deck, M. L. Shur, K. D. Squires, M. K. Strelets, and A. Travin. A new version of detached-eddy simulation, resistant to ambiguous grid densities. *Theoretical and Computational Fluid Dynamics*, 20(3):181–195, 2006.

[72] P. R. Spalart, W.-H. Jou, M. Strelets, and S. R. Allmaras. Comments on the feasability of LES for wings, and on a hybrid RANS/LES approach. *Proceedings of the First AFOSR International Conference on DNS/LES*, pages 137–147, 1997.

[73] F. Stern, R. V. Wilson, and J. Shao. Quantitative V&V of CFD simulations and certification of CFD codes. *Int. Journal for Numerical Methods in Fluids*, 50(11):1335–1355, 2006.

[74] E. B. Thornton and R. J. Calhoun. Spectral resolution of breakwater reflected waves. *Journal of Waterway, Harbors and Coastal Engineering Devision*, 98(4):443–460, 1972.

[75] A. Travin, M. Shur, P. R. Spalart, and M. Strelets. On URANS solutions with LES-like behaviour. In P. Neittaanmäki, T. Rossi, K. Majava, and O. Prionneau, editors, *Congress on Computational Methods in Applied Sciences and Engineering*. Jyväskylä, 2004.

[76] A. Travin, M. Shur, M. Strelets, and P. R. Spalart. Detached-eddy simulations past a circular cylinder. *Flow, Turbulence and Combustion*, 63:293–313, 1999.

[77] A. Travin, M. Shur, M. Strelets, and P. R. Spalart. Physical and numerical upgrades in the detached-eddy simulation of complex turbulent flows. In R. Friedrich and W. Rodi, editors, *Advances in LES of complex flows*, volume 65 of *Fluid Mechanics and Its Applications*, pages 239–254. Kluwer Academic Publishers, Dordrecht, 2004.

[78] S. Uharek and A. Cura Hochbaum. The influence of inertial effects on the mean forces and moments on a ship sailing in oblique waves: Part B: Numerical prediction using a RANS code. *Ocean Engineering*, 165:264–276, 2018.

[79] H. van der Heiden, P. van der Plas, A. Veldman, R. Luppes, and R. Verstappen. Simulation of moonpool water motion. In B. Brinkmann and P. Wriggers, editors, *5th International Conference on Computation Methods in Marine Engineering*, 2013.

[80] R. van t Veer and H. J. Tholen. Added resistance of moonpools in calm water. In *27th International Conference on Offshore Mechanics and Arctic Engineering*, pages 153–162, Sunday 15 June 2008.

[81] D. C. Wilcox. *Turbulence modeling for CFD*. DCW Industries, La Cañada, Calif., 1st ed. edition, 1993.

[82] R. V. Wilson, P. M. Carrica, M. Hyman, and F. Stern. A steady and unsteady single-phase level set method for large amplitude ship motions and maneuvering. In *25th Symposium on Naval Hydrodynamics*, pages 88–104, 2004.

[83] R. V. Wilson, P. M. Carrica, and F. Stern. Unsteady RANS method for ship motions with application to roll for a surface combatant. *Computers & Fluids*, 35(5):501–524, 2006.

[84] T. Xing, P. M. Carrica, and F. Stern. Computational towing tank procedures for single run curves of resistance and proulsion. *Journal of Fluids Engineering*, 130(10):101102, 2008.

[85] T. Xing, M. Kandasamy, and F. Stern. Unsteady Free-Surface Wave-Induced Separation: Analysis of Turbulent Structures using Detached Eddy Simulation and Single-Phase Level Set. *Journal of Turbulence*, 8:N44, 2007.

[86] S. O. Yoo, H. J. Kim, D. Y. Lee, B. Kim, and S. H. Yang. Experimental and numerical study on the flow reduction in the moonpool of floating offshore structure. In *36th International Conference on Ocean, Offshore and Arctic Engineering*, 2017.

[87] J. Zhou, R. J. Adrian, S. Balachandar, and T. M. Kendall. Mechanisms for Generating Coherent Packets of Hairpin Vortices in Channel Flow. *Journal of Fluid Mechanics*, 387:353–396, 1999.